Infrared Spectroscopy of Buffer-Gas Cooled Molecules and Dynamics of Bose Gases in Spherical Symmetry

by

Cameron J. E. Straatsma

M.Sc., University of Alberta, 2011

B.Sc., University of Alberta, 2009

A thesis submitted to the

Faculty of the Graduate School of the

University of Colorado in partial fulfillment

of the requirements for the degree of

Doctor of Philosophy

Department of Electrical, Computer, and Energy Engineering

2018

This thesis entitled:
Infrared Spectroscopy of Buffer-Gas Cooled Molecules and Dynamics of Bose Gases in Spherical Symmetry
written by Cameron J. E. Straatsma
has been approved for the Department of Electrical, Computer, and Energy Engineering

Heather J. Lewandowski

Juliet T. Gopinath

Date

The final copy of this thesis has been examined by the signatories, and we find that both the content and the form meet acceptable presentation standards of scholarly work in the above mentioned discipline.

Straatsma, Cameron J. E. (Ph.D., Electrical Engineering)

Infrared Spectroscopy of Buffer-Gas Cooled Molecules and Dynamics of Bose Gases in Spherical Symmetry

Thesis directed by Heather J. Lewandowski

Infrared absorption spectroscopy is a highly sensitive technique for probing molecular structure, and when combined with cold molecular beam methods it provides unparalleled spectral resolution and absorption sensitivity to transitions in isolated gas-phase molecules. The first part of this dissertation investigates molecular beams of large polyatomic molecules produced via laser ablation of solid targets inside a buffer-gas cooling cell. Using matrix isolation spectroscopy to study the ablation products of graphite, we observe carbon clusters C_3 to C_{12} produced at a rate of approximately $10^{11} - 10^{12}$ molecules for every pulse of the ablation laser. In a similar fashion, we study the production of metal oxide molecules with a buffer-gas beam source by ablating pure metal in the presence of O_2 gas, and find consistent production of the WO molecule. Finally, we discuss efforts towards high resolution rotational-vibrational spectroscopy of WO in the gas phase.

The investigation of collective modes in ultracold atomic gases provides revealing information about the nature of interactions in these systems. Of particular interest is the interplay between a Bose-Einstein condensate and thermal excitations present at finite temperature, which effect the dynamics of collective modes by shifting mode frequencies and introducing damping. The second part of this dissertation investigates the dynamics of the monopole mode of a degenerate Bose gas in an isotropic harmonic trap recently developed at JILA. Through numerical simulations within the Zaremba-Nikuni-Griffin formalism, we identify the beating between two eigenmodes of the system, corresponding to in-phase and out-of-phase oscillations of the condensed and noncondensed portions of the gas. This beating leads to nonexponential collapse of the amplitude of the condensate oscillation, followed by a partial revival. Results of the simulations are shown to agree well with experimental data.

Acknowledgements

This dissertation represents the end to a rather interesting journey through graduate school that was possible due to the support and guidance of many amazing people. First and foremost, I am indebted to Heather Lewandowski for offering her unwavering support and constant encouragement, and allowing me a great deal of freedom while pursuing research goals. Heather's passion for interesting physics, infinite optimism, and dedication to her students made for a wonderful experience conducting research in her group. I also thank my other collaborators on the monopole mode project – Victor Colussi, Dan Lobser, Matthew Davis, Murray Holland, and Eric Cornell – from whom I learned a great deal about kinetic theory and cold Bose gases through many insightful discussions. Additionally, I thank Juliet Gopinath for acting as my titular adviser in ECEE, and for her support and flexibility over the past year.

I would also like to acknowledge the amazing people at JILA that not only keep things running smoothly, but readily offer their expertise to anyone in need. I thank the members of the instrument shop, electronics shop, computing group, supply office, and administrative support group for all their assistance over the years. In particular, I would like to thank Hans Green and Terry Brown, who have helped me with a wide variety of problems on countless occasions, and shared much of their wisdom with me. Their infinite patience, friendly demeanor, and curiosity are contagious.

Finally, none of this would have been possible without the love and support of my amazing family, and the wonderful friends and labmates who have helped make graduate school substantially more enjoyable. In particular, I am grateful for Carrie Weidner and Seth Caliga for providing

constant support and convincing this Canadian to finally play ice hockey, Brad Pelz for always being eager to meet up for breakfast, climbing, snowboarding, or pretty much any crazy outdoor activity, and for Paul Ackerman and Ana Mazan for sharing many dinners and interesting conversations over the years. Lastly, I am forever grateful for the love and constant encouragement from my partner Courtney Peck, who is always there for me and pushes me to be the best version of myself.

Contents

Chapter

Tables

Table

Figures

Figure

Part 1: Infrared Spectroscopy of Buffer-Gas Cooled Molecules

Chapter 1

Introduction to Part 1

Molecular structure has a profound influence on the properties of materials and their applications in the world around us. A rather striking example of this is given by the differences between diamond and graphite. Although both materials are composed entirely of elemental carbon, diamond is one of the hardest known materials, is electrically insulating, and is visually transparent. On the other hand, graphite is soft, electrically conducting, and visually opaque. Therefore, diamond is an excellent abrasive and an expensive, sought-after gemstone, while graphite can be used as a lubricant and is so cheap that it is used to make pencils. The reason for such disparate properties between these materials lies in differences of the underlying molecular structure.

In addition to material properties, molecular structure and bonding play a central role in the effect of drugs on the human body, the perceived scent and taste of different compounds, as well as in the dynamics of chemical reactions. In fact, as many as $85 - 90\%$ of industrial chemical processes utilize a catalyst to increase conversion efficiency and improve selectivity, examples of which include oil refining, bulk chemical synthesis, and production of pharmaceuticals [1]. Catalysis of the chemical reactions that make up these processes rely on the bonding mechanism between certain molecules and a catalyst (e.g., a metal oxide material) to lower energy barriers, allowing particular reaction pathways to proceed. Thus, a detailed understanding of the molecular structure of catalysts and how molecules bond with them is crucial for the continued improvement of a wide range of industrial chemical processes.

Perhaps one of the most widely used techniques for the determination of molecular structure

is high resolution spectroscopy of isolated molecules in the gas phase. Spectroscopic techniques have become popular in this regard due to their extraordinary sensitivity to molecular shape, which is governed by the bonding between the constituent atoms and their relative locations in three-dimensional space. Through excitation of vibrational and rotational motion of a molecule at discrete energies, it is possible to characterize molecular bonds and the spatial arrangement of the constituent atoms. In this dissertation, spectroscopy in the infrared region of the electromagnetic spectrum is utilized to investigate molecular structure, and in the following section we begin with a brief historical overview of the development of spectroscopy.

1.1 Spectroscopy

One of the first accounts of an absorption spectrum dates back to 1802 when Wollaston observed a series of dark lines interrupting the continuous spectrum of sunlight dispersed by a prism [2]. Soon after, Fraunhofer began investigating this series of dark lines from sunlight in more detail, and was able to measure the wavelength of some of the stronger lines using the first diffraction grating [3]. In addition, Fraunhofer observed light from bright stars with a telescope and found that the patterns of dark lines were different than those from the sun. It was not until 1860 that Kirchhoff proposed a theory to explain the patterns of dark lines observed by Wollaston and Fraunhofer [4]. Kirchhoff hypothesized that the dark lines in the solar spectrum were a result of gases in the sun's outer atmosphere absorbing continuum light at discrete wavelengths. These ideas gave birth to the technique of spectral analysis, which was used by Kirchoff and Bunsen to identify spectral fingerprints of a number of materials in the visible region of the electromagnetic spectrum [5, 6].

In 1881, Abney and Festing extended the methods pioneered by Kirchhoff and Bunsen in the visible to the infrared. They were able to obtain infrared absorption spectra of a wide range of compounds, and demonstrated that certain absorption bands were correlated with the presence of certain molecular groups [7]. By the early 1900's, the importance of infrared spectroscopy to chemical composition analysis was well-known, but commercial instruments did not become avail-

able until the 1940's during World War II. With the advent of commercially available instruments, the technique of infrared spectroscopy exploded in popularity due to its ability to provide a unique spectral fingerprint for many complex molecules and information regarding molecular structure. In tandem to the development of infrared spectroscopy, the theory of quantum mechanics was established, and the efforts of Born and Oppenheimer [8] laid the ground work for a quantum treatment of molecular structure. This provided the necessary link between experimentally obtained infrared spectra of a molecule and the arrangement of its constituent atoms.

1.1.1 Determination of molecular structure

The key component of the method presented by Born and Oppenheimer is to separate the molecular Hamiltonian into its electronic and nuclear components. This separation is valid in many scenarios due to the large mass difference between electrons and nuclei; therefore, the electronic component can be solved under the assumption that the nuclei are stationary (i.e., neglecting the nuclear kinetic energy) followed by solution of the nuclear motion. The former gives rise to discrete electronic energy levels, which coincide with the energy of visible photons, whereas the latter gives rise to discrete rotational and vibrational energy levels of the molecule, which coincide with the energy of infrared photons. Therefore, infrared spectroscopy effectively probes excitations of the mechanical motion of the constituent atoms in a given molecule. It is then possible to relate the excitation energy of this mechanical motion to molecular properties such as bond length, orientation, and strength.

Figure 1.1 gives a simplified representation of vibrations and rotations in a diatomic molecule, and likens these motions to the classical analogues of a simple harmonic oscillator and rigid rotor, respectively. From the figure, it is clear that by measuring the change in vibrational or rotational energy upon absorption of an infrared photon it is possible to determine the natural vibrational and rotational frequencies, ω_e and B_e, respectively. These parameters can then be related to the force constant k_v (i.e., bond strength) and the equilibrium distance between the constituent atoms r_e (i.e., bond length), which determines the molecular structure. Now, this simplistic picture

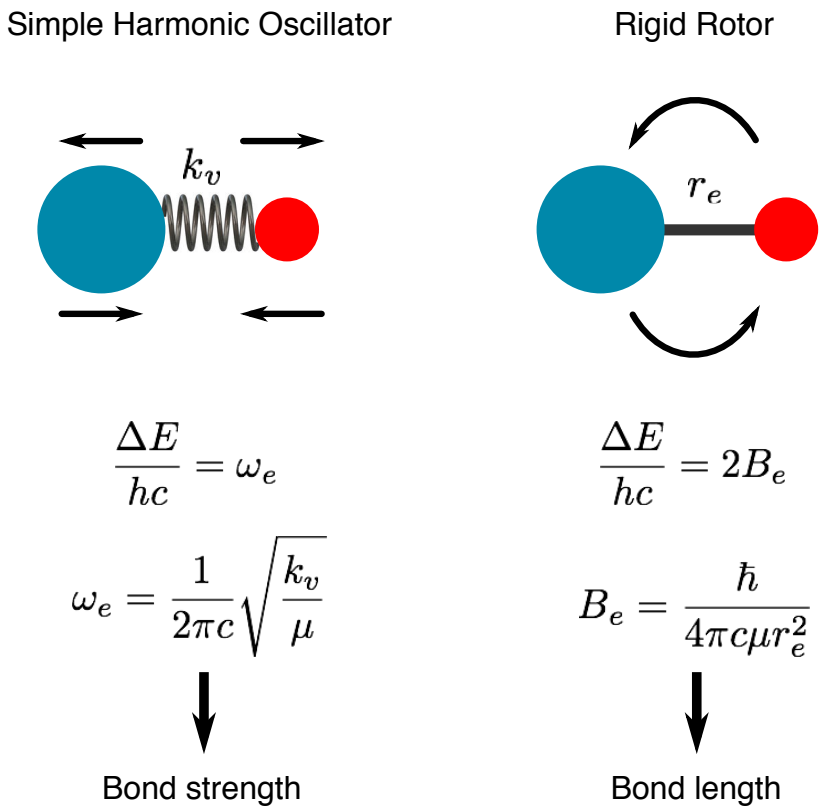

Figure 1.1: A simplified representation of vibrations and rotations in a molecule, and their relation to the classical analogues of a simple harmonic oscillator and rigid rotor, respectively. A measurement of the change in vibrational energy (proportional to ω_e) provides information about the force constant k_v (i.e., bond strength), while a measurement of the change in rotational energy (proportional to B_e) provides information about the equilibrium distance between the constituent atoms r_e (i.e., bond length). The parameters h, c, and μ are Planck's constant, the speed of light, and the reduced mass of the molecule, respectively.

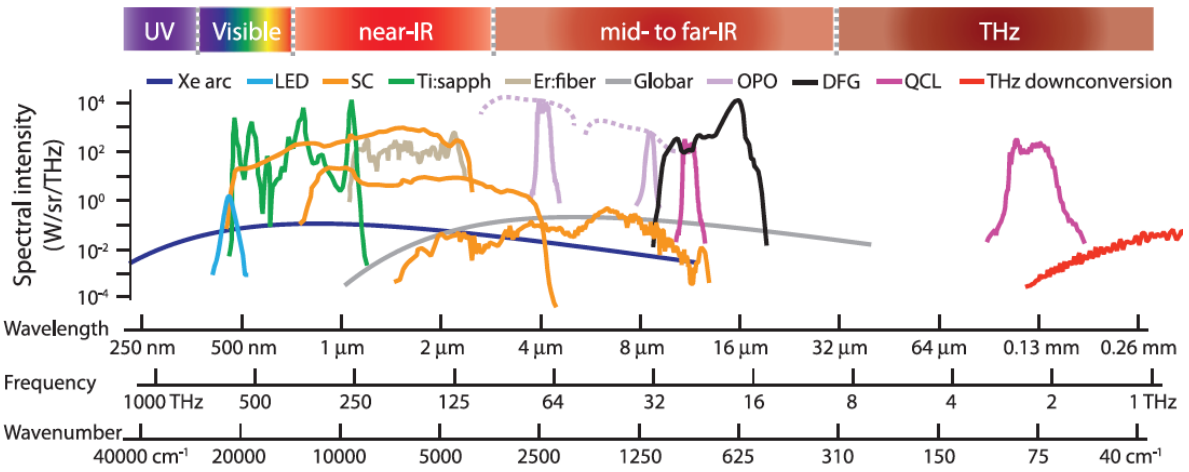

Figure 1.2: Available broadband and widely tunable sources for spectroscopy in different spectral regions. Adapted from Ref. [11].

becomes much more complicated for larger, polyatomic molecules; however, it is still possible to determine molecular structure through the measurement of infrared spectra when the technique is combined with other methods such as isotopic substitution and ab initio calculations [9, 10]. Nonetheless, these methods require the precise determination of rotational constants B_e for many different isotopologues, hence the desire for broad spectral bandwidth, high sensitivity, and high resolution spectroscopic techniques.

1.1.2 Modern techniques

There exists a very broad range of spectroscopic techniques in use today. Therefore, the present discussion will be limited to those used for high resolution absorption spectroscopy of isolated gas-phase molecules, which are most relevant to this dissertation work. Figure 1.2 provides an overview of currently available broadband and widely tunable sources used for high resolution spectroscopy. Perhaps the biggest advantage of broadband spectroscopy is the ability to simultaneously acquire high resolution spectra at many different frequencies, which greatly reduces measurement time. At the forefront of modern broadband techniques is frequency comb spectroscopy, which combines the benefits of broad spectral bandwidth, high spectral resolution, and high spectral intensity into a single technology [11, 12]. Furthermore, use of a high finesse optical cavity, such as in cavity-

enhanced direct frequency comb spectroscopy [13], provides a substantial improvement in detection sensitivity. However, frequency combs are still an emerging technology making them relatively unavailable in the infrared. In this region of the electromagnetic spectrum, a typical broadband source consists of a hot filament (e.g., globar) that acts as a blackbody; however, recent work has demonstrated promising broadband infrared sources based on supercontinuum generation in chalcogenide fiber [14], difference frequency generation in $LiGaS_2$ [15], and modelocked quantum cascade lasers [16]. Notably, broadband sources have two potential drawbacks when compared to single frequency sources used for spectroscopy – either low spectral brightness, low spectral resolution, or both. This generally limits the achievable sensitivity in an absorption spectroscopy experiment to roughly $10^{-5} - 10^{-4}$ $Hz^{-1/2}$ and the spectral resolution to a few hundred MHz or more [11]. Therefore, techniques like tunable diode laser spectroscopy offer an alternative to broadband spectroscopy that achieves both increased sensitivity and spectral resolution.

The major benefit of tunable diode laser spectroscopy is that the full output power of the laser is concentrated into a single spectral element with a bandwidth set by the laser linewidth (e.g., typically < 1 MHz for external cavity diode lasers). Thus, these techniques can achieve high sensitivity and high resolution, but require much longer acquisition times to cover even modest spectral windows on the order of a few wavenumbers. This is a major disadvantage when compared to broadband spectroscopy techniques. Nonetheless, sensitivities on the order of 10^{-13} $Hz^{-1/2}$ have been achieved with sub-MHz resolution [17, 18], which enables investigations of weak spectral features such as overtones and combination bands among other things. Furthermore, there are many perturbations to spectra (e.g., see Refs. [19, 20]) that become prominent at the high spectral resolution achievable with tunable diode laser spectroscopy.

To date, perhaps the most widely used experimental method for absorption spectroscopy of isolated gas-phase molecules utilizes a free jet source combined with a tunable laser coupled into a multipass cell or optical cavity to probe the molecules of interest. This arrangement provides a number of advantages: the free jet source provides substantial cooling of the molecular internal degrees of freedom, the multipass cell or optical cavity provides increased sensitivity, and the

tunable laser provides high spectral brightness and resolution. Indeed, this method has been used for studying a wide range of molecular systems, such as carbon clusters [21], Van der Waals complexes [22], radicals [23], large organic molecules [24], and many others. The following section will review some aspects of molecular beams, including the free jet source, before introducing the method used in this dissertation: the cryogenic buffer-gas beam source.

1.2 Molecular Beams

In molecular spectroscopy, the interest and widespread use of molecular beams stems from perhaps three very useful aspects [25]: isolation of the molecular species of interest, the ability to cool molecular internal degrees of freedom to the order of 1 K, and the ability to control or perturb the species of interest in a deterministic way. For spectroscopic purposes, the first two of these are crucial for minimizing spectral line broadening and ensuring that the molecules of interest populate only a handful of internal states – a very useful way of decongesting spectra and easing their interpretation. Furthermore, isolation of molecular species is critical to the study of highly reactive free radicals. Finally, the ability to control or perturb a beam of isolated molecules is useful for techniques like Stark and Zeeman spectroscopy, for example, which can aid in the determination of molecular dipole moments [26].

1.2.1 Traditional beam sources

Traditional molecular beam sources largely fall into two categories: effusive sources and free jet sources. In its simplest form, an effusive beam is formed by allowing a gas to leak out of a small hole in a chamber that contains the molecular species of interest at a given temperature and pressure [25]. By maintaining a low pressure inside the chamber, the conditions for molecular flow are ensured and no collisions occur between molecules as they exit the chamber to form a beam. On the other hand, a free jet source produces a molecular beam via supersonic expansion of a high pressure gas into vacuum [25]. By maintaining a large pressure differential across a small aperture, the conditions for continuum flow are ensured and many collisions occur between molecules as they

form a beam. Thus, these two beam sources give rise to very different properties, and have certain advantages and disadvantages summarized here [27]:

- Effusive sources are nearly universally applicable. In addition, beam properties are well defined and easily calculated from kinetic theory, and the molecular species has internal state populations dictated by the equilibrium state of the source. However, many species require high temperatures to create appreciable vapor pressure such that the molecular species will occupy a large number of internal states, putting an increased demand on the sensitivity of a spectroscopy system. Additionally, effusive sources have low brightness compared to free jet sources.

- Free jet sources are also nearly universally applicable when combined with techniques like laser ablation. In addition, beam properties are less well defined, and the molecular species typically has non-equilibrium internal state populations. Furthermore, optimal operating conditions tend to be empirically determined. However, the degree of translational and internal state cooling achievable with a free jet source is unprecedented, which significantly reduces the number of internal states populated. Additionally, free jet sources have substantially higher brightness than effusive sources.

In regards to molecular spectroscopy, perhaps the single most beneficial aspect of a free jet source is the degree of translational and internal state cooling that can be achieved. Not only does the degree of cooling minimize the deleterious effects of Doppler broadening on the resolution of spectral lines, it also reduces the demand on the sensitivity of a spectroscopy system by concentrating the molecular species of interest into a handful of internal states.

Given its widespread use in molecular spectroscopy, it is useful to consider the free jet source in more detail. Ideally, a free jet represents an isentropic expansion from a high pressure ($P \sim 1$ atm), high density ($n \sim 10^{19}$ cm^{-3}) gas inside a chamber through a planar aperture into vacuum ($P \sim 10^{-8}$ atm). Such a process results in a rapid decrease in temperature and density, which can be understood from the ideal gas relations $T_b = T_0 \left(P_b/P_0\right)^{2/5}$ and $n_b = n_0 \left(P_b/P_0\right)^{3/5}$, where the

subscripts indicate initial properties inside the chamber and final properties in the beam. Therefore, we see that $T_b \sim 1$ K and densities low enough to isolate molecules from collisions are readily achievable. Typically, the molecular species of interest is introduced by seeding a carrier, or buffer gas like argon or neon via laser ablation of a solid target placed immediately outside of the chamber. In this way, the molecules of interest are "captured" by the supersonically expanding carrier gas, and collisions between the molecules and carrier gas reduce the molecule temperature. An example of this style of source is depicted in Fig. 1.3. Notably, a free jet results in a molecular beam with a carrier-gas forward velocity of several hundred m/s, and collisions between the molecular species of interest and the carrier gas occur over a propagation distance of a few nozzle diameters. Therefore, the collisional cooling timescale for a traditional free jet source is on the order of 10 µs. For many molecular species, this timescale is long enough to cool molecules to the order of 1 K. However, it is difficult to cool large, strongly bound cluster molecules such as metal oxides and carbides due to the additional energy they acquire during condensation in the gas phase. Such molecules typically have binding energies of a few electron volts per bond, and this energy is deposited into the cluster every time an atom is added [28]; therefore, the molecule heats as it forms. As a result of this condensation heating, cluster molecules formed with a free jet source typically do not reach temperatures on the order of 1 K. Furthermore, clusters of different sizes generally have different temperatures as a result of larger clusters forming later in the supersonic expansion [28]. As a result of this disadvantage, it is of general interest to investigate other methods for producing molecular beams of cold cluster molecules, such as the cryogenic buffer-gas beam source [29].

1.2.2 Buffer-gas beam sources

Buffer-gas beam sources have a number of advantages over traditional free jet sources used in conjunction with laser ablation of a solid target, such as lower forward velocity, higher brightness, and a longer collisional cooling timescale [29]. Notably, the free jet source readily achieves peak carrier-gas densities $100 - 1000$ times greater than a buffer-gas beam source; however, as discussed above, molecules ablated in the vicinity of a supersonic expansion typically interact with carrier

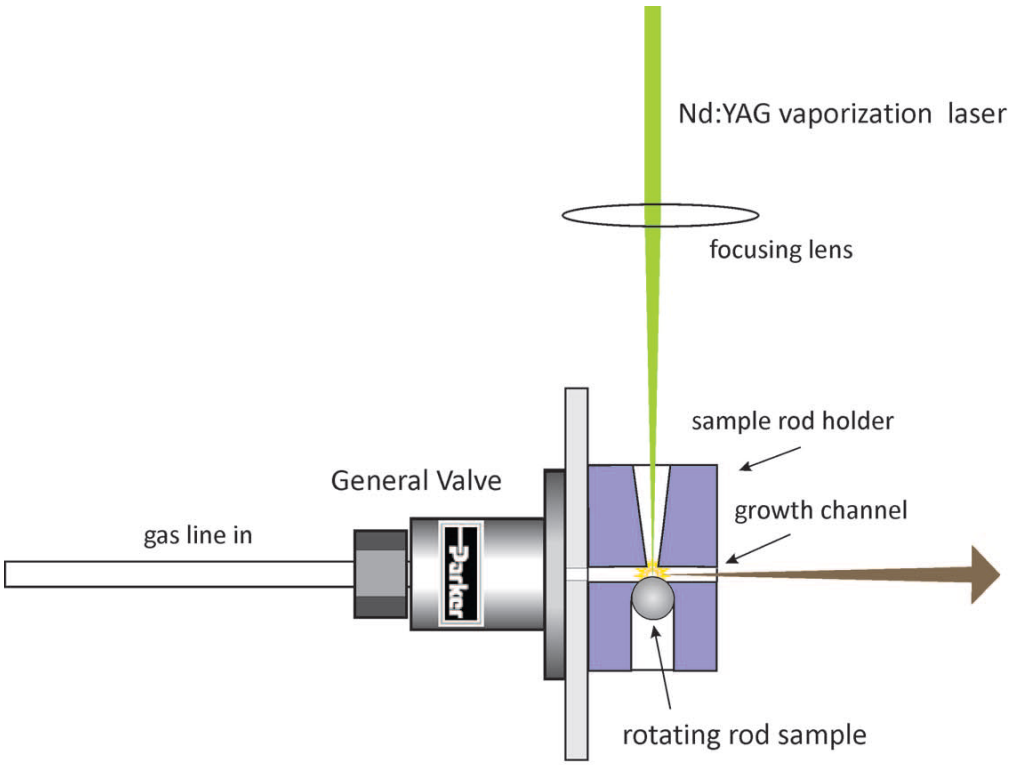

Figure 1.3: Example of a free jet source design that utilizes laser ablation of a solid target to introduce the molecular species of interest to a supersonic expansion of buffer gas. Reproduced from Ref. [28].

gas of this density for times on the order of 10 µs, whereas this timescale can be on the order of 10 ms inside a buffer-gas cell [29]. Therefore, it is likely that molecules of interest in a buffer-gas beam source experience more collisions with a high density, cold buffer gas, which could lead to lower internal state temperatures for many molecules compared to a free jet source. An additional benefit of the larger number of collisions in a buffer-gas source is the possibility of lower internal state temperatures for large, strongly bound clusters, such as carbon clusters or clusters of metal oxides and carbides. To date, many molecular species have been successfully cooled with a buffer-gas beam source, including diatomic [30–35] and polyatomic [36–41] molecules, but there are relatively few high-resolution spectroscopic studies of complex polyatomic molecules produced with a buffer-gas beam source (i.e., as in Refs. [41, 42]). Indeed, the ability to cool complex molecules to their vibrational ground state will remove much of the ambiguity associated with the spectral assignment process, and could provide validation for the large variety of theoretical techniques currently being used in conjunction with experiments to determine molecular structures.

1.3 Dissertation Outline

This dissertation consists of two very different projects; therefore, it is separated into two distinct parts. Part 1 of this dissertation consists of Chapters 1–6, and discusses an experimental project regarding high resolution spectroscopy of cold molecules in the gas phase. This project involves the characterization of a buffer-gas beam source for the production of carbon clusters and metal oxide molecules, and infrared spectroscopy of these molecules using different techniques. Part 2 of this dissertation consists of Chapters 7–11, and discusses a theoretical project regarding the dynamics of collective modes of degenerate Bose gases in spherical symmetry. This project involves the analysis of data acquired by D. S. Lobser with the JILA TOP trap experiment, and the subsequent theoretical analysis undertaken to explain the experimental observations.

Part I of this dissertation is organized as follows. Chapter 2 provides a discussion of the operating principles of buffer-gas beam sources, with a focus on collisional cooling and beam formation in different regimes of operation. A comparison between the buffer-gas beam source used for this

dissertation work and a traditional free jet source is discussed at the end of Chapter 2. Chapter 3 provides an overview of some experimental techniques for infrared absorption spectroscopy. Included is a discussion of Fourier transform infrared spectroscopy, matrix isolation spectroscopy, and laser absorption spectroscopy, as well as the techniques of wavelength modulation and balanced subtraction. Chapter 4* describes an experimental investigation of the production of carbon clusters with a buffer-gas beam source, and highlights some of the non-ideal characteristics of beam formation with such a source. Chapter 5 investigates the production and infrared rotational-vibrational spectrum of the WO molecule using a modified buffer-gas beam source and tunable diode laser absorption spectroscopy system. Chapter 6 summarizes the first part of this dissertation, and provides a future outlook. Finally, Part 2 of this dissertation begins in Chapter 7, where a separate introduction and outline can be found.

* Chapter 4 represents a publication that was a collaborative effort between the author of this dissertation, Maya I. Fabrikant, Gary E. Douberly, and Heather J. Lewandowski [43]. The author of this dissertation was the primary author of the paper, and performed the experiments and subsequent data analysis. M. I. Fabrikant constructed the majority of the experimental apparatus, G. E. Douberly and H. J. Lewandowski provided project definition, and H. J. Lewandowski provided guidance throughout the project.

Chapter 2

The Cryogenic Buffer-Gas Beam Source

Both supersonic expansion and buffer-gas beam sources rely on collisions with a dense, cold, and inert gas to cool hot molecules from > 1000 K into the few kelvin regime; however, their construction is significantly different. In its simplest form, a buffer-gas beam source consists of a cell with a constant flow of inert buffer gas (e.g., helium or neon) entering through a small aperture. The cell is held at a temperature on the order of 10 K to cool the buffer gas, into which the molecules of interest are introduced through laser ablation of a solid target located inside the cell, or via a warm capillary held in the vicinity of the entrance aperture. The molecules of interest become entrained in the flow of cold buffer gas where they rapidly cool and eventually exit the cell through a small aperture to form a bright beam of cold molecules.

In this chapter, we discuss the principles of cryogenic buffer-gas beam (CBGB) sources with a focus on collisional cooling and extraction efficiency. As noted in the Introduction, CBGB sources have a longer collisional cooling timescale compared to supersonic jet sources. Thus, it is expected that lower vibrational temperatures for complex polyatomic molecules could be achieved with a CBGB source, which could aid in the structural determination of these large molecules with high-resolution spectroscopy. Furthermore, understanding the extraction efficiency of CBGB sources is useful in maximizing the flux of cold molecules produced with such a source. By optimizing this process, beams of higher brightness can be produced and less demand placed on the detection process. The extraction efficiency of a CBGB source can be estimated in a simple fashion; however, certain non-ideal behavior is encountered where these simple estimates breakdown. Hutzler et

al. [29] have written a good introduction on the construction and performance of buffer-gas beam sources.

2.1 Buffer-Gas Cooling Cell

A schematic of the buffer-gas cooling cell used in this dissertation work is shown in Fig. 2.1. It consists of a copper box with a cylindrical bore of length $L_{\text{cell}} = 40$ mm and diameter $d_{\text{cell}} = 20$ mm. The flow of neon buffer gas into the cell is controlled by a mass flow controller (Alicat Scientific, MC-100SCCM-D), and first enters a small reservoir at the top of the cell to promote laminar flow through the main compartment of the cell. A thin aperture of diameter $d_{\text{ap}} = 5$ mm located in the bottom face of the cell allows for beam extraction. Through a weak connection to the second stage of a two-stage cryocooler (SHI Cryogenics Group, RDK-415D), the cell is held at a temperature of $T_{\text{cell}} = 25$ K to prevent neon gas from freezing to the cell walls. Note that the neon gas line is also anchored to the first stage of the cryocooler to cool the neon gas from room temperature to approximately 30 K prior to it entering the buffer-gas cell.

2.1.1 Buffer-gas flow properties

To begin, it is useful to discuss some generic properties of gas flows and the terminology used to describe different flow regimes. For simplicity, we will assume the neon buffer gas is an equilibrium monatomic ideal gas that obeys Maxwell-Boltzmann statistics.* In discussing properties of gas flows, it is useful to introduce three dimensionless quantities: the Reynolds number, the Mach number, and the Knudsen number. The Reynolds number is typically used to identify laminar and turbulent flow regimes, and is defined as [45]

$$Re = \frac{uL}{\nu}, \tag{2.1}$$

* Strictly speaking, this is not entirely justified; however, this assumption will allow us to perform simple analytic calculations and get an idea for how the buffer-gas flow is affected by different system parameters. Rigorous treatment of the buffer-gas flow at low temperatures requires complex fluid dynamics simulations and a more realistic equation of state. See Refs. [33, 44], for example.

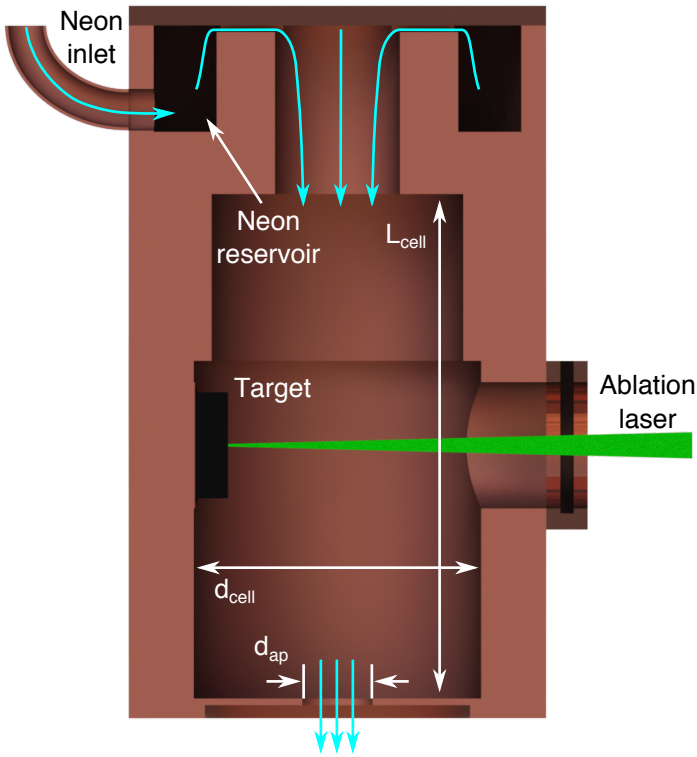

Figure 2.1: A schematic of the buffer-gas cooling cell. It consists of a copper box with a cylindrical bore ($L_{\text{cell}} = 40$ mm and $d_{\text{cell}} = 20$ mm) drilled through the center. A thin plate attached to the bottom contains an aperture of diameter $d_{\text{ap}} = 5$ mm. Neon gas (blue arrows) first enters a reservoir at the top of the cell before flowing into the main cell, and exits through the aperture at the bottom. The ablation laser enters through an uncoated window attached to the outside of the cell, and is focused onto a solid target attached to the inside of the cell.

where u is the flow velocity, L is a characteristic length scale (i.e., aperture diameter of the buffer-gas cooling cell d_{ap}), and ν is the kinematic viscosity of the gas. At low Re the flow is expected to be non-turbulent and predominantly laminar in nature. As Re increases, the onset of turbulence occurs and the properties of the flow can become very complex and even chaotic. The Mach number is typically used to identify when a flow can be treated as incompressible, and is defined as [45]

$$Ma = \frac{u}{c_s}, \tag{2.2}$$

where $c_s = \sqrt{\gamma k_B T/m}$ is the speed of sound in the gas flow, γ is the ratio of specific heats for an ideal gas ($\gamma = 5/3$ for a monatomic ideal gas like neon), k_B is Boltzmann's constant, T is the flow temperature, and m is the mass of a gas atom. For $Ma \lesssim 0.3$, real gas effects like compressibility will have minimal impact on the flow and can be neglected. However, as Ma approaches unity this approximation breaks down and more sophisticated methods are required to study the flow. Finally, the Knudsen number is typically used to determine whether or not the flow can be treated as fluid-like, and is defined as [46]

$$Kn = \frac{\lambda}{L}, \tag{2.3}$$

where $\lambda = \left(\sqrt{2} n \sigma\right)^{-1}$ is the mean free path, n is the number density of gas atoms in the flow, and σ is the elastic collision cross section between gas atoms. When Kn is much less than unity, the gas is in the hydrodynamic regime (i.e., many collisions occur over the length scale of the gas keeping it in local statistical equilibrium) and can be treated as a fluid. On the other hand, when Kn approaches unity the gas must be treated statistically in the so-called free molecular flow regime because very few collisions occur over the length scale of the gas. Finally, by introducing the relation $\nu = \lambda \bar{v}/2$ that relates the dynamic viscosity to the mean free path and mean thermal velocity $\bar{v} = \sqrt{8 k_B T/\pi m}$, we derive a relationship between Kn, Re, and Ma. The result is [46]

$$Kn = \sqrt{\frac{\pi\gamma}{2}} \frac{Ma}{Re}. \tag{2.4}$$

With the above dimensionless quantities and relations between them, we require an estimate of the equilibrium density of buffer gas inside the cooling cell to fully characterize the flow. We

find the density inside the cell by considering that all of the gas flowing into the cell must leave through the exit aperture. Here, the neon flow rate into the cell is given by $f_{i,\mathrm{Ne}}$ in units of sccm, and typically lies in the range of $1 - 100$ sccm. The flow of gas out of the cell is dictated by the conductance of the aperture, which is given by

$$C = \frac{A_{\mathrm{ap}}\bar{v}}{4}, \tag{2.5}$$

in the molecular flow regime (i.e., $Kn \gtrsim 1$), and

$$C = \frac{A_{\mathrm{ap}}\bar{v}}{2}\sqrt{\frac{\pi\gamma}{\gamma+1}}\left(\frac{2}{\gamma+1}\right)^{\frac{1}{\gamma-1}}, \tag{2.6}$$

in the continuum flow regime (i.e., $Kn \lesssim 0.01$) [47]. In arriving at the final expression for C in the continuum flow regime, we have assumed choked flow (i.e., $Ma = 1$ in the aperture), which occurs for a large pressure difference between the buffer-gas cell and the surrounding vacuum. Thus, we calculate the density of neon gas inside the cell using the relation

$$n_{\mathrm{Ne}} = 4.47796 \times 10^{17}\left(\frac{f_{i,\mathrm{Ne}}}{C}\right), \tag{2.7}$$

where the prefactor converts $f_{i,\mathrm{Ne}}$ from units of sccm to units of atoms per second.

Figure 2.2 shows the density of neon gas inside the cell as a function of flow rate, as well as the Knudsen number in the exit aperture of the cell. To calculate the Knudsen number, we use the density from Eq. (2.7) and the Ne-Ne collision cross section $\sigma = 3.02 \times 10^{-15}$ cm^2 based on a hard-sphere model with minimum potential radius from Ref. [48]. We find that both the density and Knudsen number are relatively insensitive to the assumed flow, varying by roughly a factor of two. Notably, the Knudsen number falls in the range between that for molecular and continuum flow, implying that the buffer-gas cell operates in the transitional flow regime. Nonetheless, we will focus our study on the limiting cases of molecular and continuum flow for simplicity. Finally, we use Eq. (2.4) to find the Reynolds number in the exit aperture of the cell. Here, we will consider the case of continuum flow in the aperture such that $Ma = 1$, which will result in the highest achievable Reynolds number in the aperture. Figure 2.3 shows the Reynolds number in the exit cell of the aperture as a function of flow rate. Comparing to flow through a pipe of constant diameter,

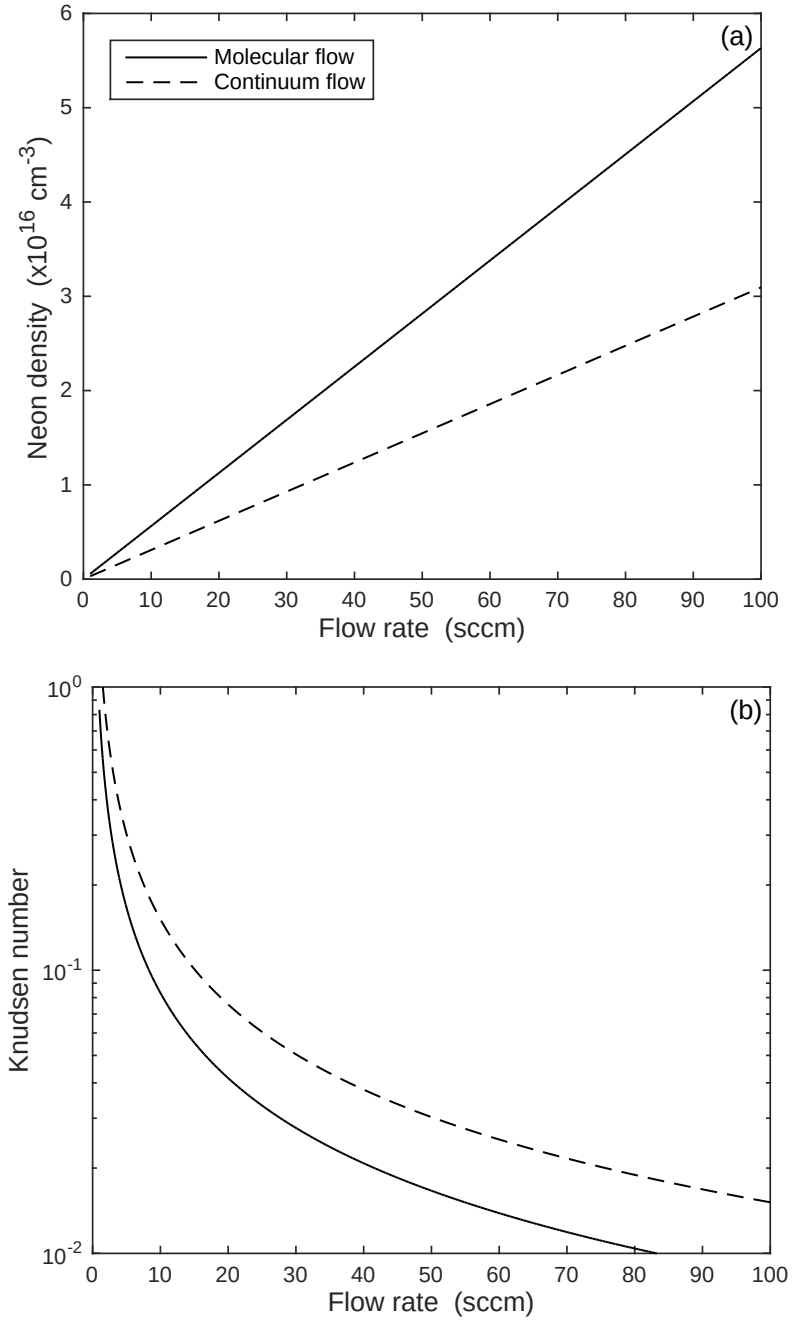

Figure 2.2: (a) Density of neon gas inside the cell and (b) Knudsen number in the exit aperture of the cell assuming molecular flow (solid) and continuum flow (dashed) through the exit aperture. The cell temperature is $T_{\text{cell}} = 25$ K and the Ne-Ne collision rate is $\sigma = 3.02 \times 10^{-15}$ cm^2. The aperture diameter is $d_{\text{ap}} = 5$ mm.

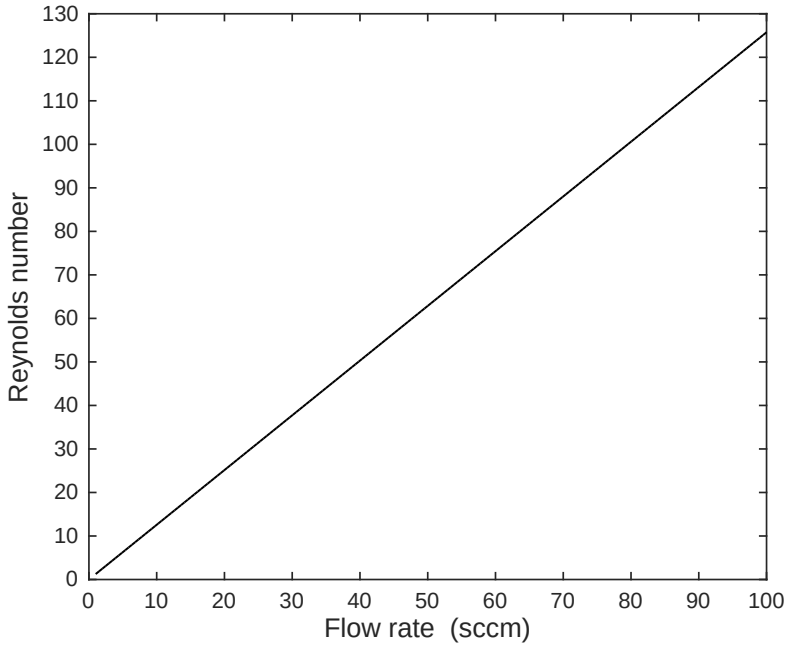

Figure 2.3: Reynolds number of the neon gas flow through the exit aperture of the cell. The cell temperature is $T_{\text{cell}} = 25$ K, the Ne-Ne collision rate is $\sigma = 3.02 \times 10^{-15}$ cm^2, and continuum flow has been assumed with $Ma = 1$. The aperture diameter is $d_{\text{ap}} = 5$ mm.

the maximum Re in the buffer-gas cooling cell is well below the transition point between laminar and turbulent flow ($Re \sim 2000$) [45]. Thus, it is expected that the flow through the cell will be predominantly laminar. However, because the cell diameter changes along its length in a step-wise manner it is possible that some large scale flow effects like eddies could form inside the cell in the vicinity of these steps, particularly near the exit aperture of the cell (e.g., as in Ref. [44]). Nonetheless, given the small value of Re, small scale turbulence and chaotic flow is not expected,[†] but an improved design might consider smoothly tapering the cell dimensions from d_{cell} to d_{ap} in an effort to minimize these eddies (e.g., as in Ref. [49]).

2.1.2 Collisional cooling – translational relaxation

During their residence time inside the cell, the molecules of interest will undergo many collisions with the buffer gas, and much of their initial energy gained from the ablation process will be dissipated. We find a rough estimate of the final temperature of the translational motion of the molecules by treating the collisions classically as elastic collisions between hard spheres (i.e., billiard balls) [29, 50]. We begin by considering a single elastic collision between a molecule of interest and a buffer gas atom with mass m_m and m_b, respectively. The initial and final velocities of the molecule and buffer-gas atom are $\mathbf{v}_m$ and $\mathbf{v}_b$, and $\mathbf{u}_m$ and $\mathbf{u}_b$, respectively. Furthermore, it is useful to define the velocity of the center of mass (COM) $\mathbf{V}$ and transform to this reference frame:

$$\mathbf{v}'_m = \mathbf{v}_m - \mathbf{V}, \tag{2.8}$$

$$\mathbf{v}'_b = \mathbf{v}_b - \mathbf{V}, \tag{2.9}$$

$$\mathbf{u}'_m = \mathbf{u}_m - \mathbf{V}, \tag{2.10}$$

$$\mathbf{u}'_b = \mathbf{u}_b - \mathbf{V}, \tag{2.11}$$

where the prime indicates velocities in the COM reference frame. From conservation of energy and momentum, we find that the center of mass velocity is unchanged in the course of the collision, so

[†] The Reynolds number indicates at which length scale dissipation of energy occurs, so small values of Re imply that large scale motion like eddies can dissipate energy directly. On the other hand, large values of Re imply that large scale motion must first cascade to smaller scales before energy dissipation can occur (i.e., turbulence).

we write

$$\mathbf{V} = \frac{m_m \mathbf{v}_m + m_b \mathbf{v}_b}{m_m + m_b} = \frac{m_m \mathbf{u}_m + m_b \mathbf{u}_b}{m_m + m_b}. \tag{2.12}$$

Furthermore, in the COM reference frame, the total momentum is equal to zero before and after the collision, a property we use to find

$$m_m \mathbf{v}'_m = -m_b \mathbf{v}'_b, \tag{2.13}$$

$$m_m \mathbf{u}'_m = -m_b \mathbf{u}'_b. \tag{2.14}$$

Finally, using this result in conjunction with conservation of energy we find

$$\left|\mathbf{v}'_m\right|^2 = \left|\mathbf{u}'_m\right|^2, \tag{2.15}$$

$$\left|\mathbf{v}'_b\right|^2 = \left|\mathbf{u}'_b\right|^2. \tag{2.16}$$

The above relations will now help us find the change in kinetic energy for a molecule undergoing a collision. In the lab frame, the final kinetic energy of the molecule is proportional to $|\mathbf{u}_m|^2$:

$$\begin{aligned} |\mathbf{u}_m|^2 &= \left|\mathbf{u}'_m + \mathbf{V}\right|^2 \\ &= \left|\mathbf{u}'_m\right|^2 + |\mathbf{V}|^2 + 2\mathbf{u}'_m \cdot \mathbf{V}, \end{aligned} \tag{2.17}$$

whereas in the COM frame, the final kinetic energy of the molecule is proportional to $|\mathbf{u}'_m|^2$:

$$\begin{aligned} \left|\mathbf{u}'_m\right|^2 = \left|\mathbf{v}'_m\right|^2 &= |\mathbf{v}_m - \mathbf{V}|^2 \\ &= |\mathbf{v}_m|^2 + |\mathbf{V}|^2 - 2\mathbf{v}_m \cdot \mathbf{V} \\ &= \left(1 - \frac{2m_m}{m_m + m_b}\right) |\mathbf{v}_m|^2 + |\mathbf{V}|^2 - \left(\frac{2m_b}{m_m + m_b}\right) \mathbf{v}_m \cdot \mathbf{v}_b. \end{aligned} \tag{2.18}$$

Combining these expressions and expanding $\mathbf{V}$ in terms of the initial velocities of the molecule and buffer-gas atom, we arrive at the following expression:

$$\begin{aligned} |\mathbf{u}_m|^2 = &\left[\frac{2m_m^2}{(m_m + m_b)^2} - \frac{2m_m}{m_m + m_b} + 1\right] |\mathbf{v}_m|^2 + \left[\frac{2m_b^2}{(m_m + m_b]^2}\right] |\mathbf{v}_b|^2 \\ &+ \left[\frac{2m_b\,(m_m - 1)}{m_m + m_b}\right] \mathbf{v}_m \cdot \mathbf{v}_b + 2\mathbf{u}'_m \cdot \mathbf{V}. \end{aligned} \tag{2.19}$$

Given the final velocity of the molecule in the lab frame for a single collision, we investigate the average change in kinetic energy for many collisions assuming the molecules and buffer-gas atoms have Maxwell-Boltzmann velocity distributions. Under this assumption, we use the equipartition theorem to equate the average initial and final kinetic energies to translational temperatures:

$$\langle |\mathbf{u}_m|^2 \rangle = \frac{3k_B T_{m,f}}{m_m}, \tag{2.20}$$

$$\langle |\mathbf{v}_m|^2 \rangle = \frac{3k_B T_{m,i}}{m_m}, \tag{2.21}$$

$$\langle |\mathbf{v}_b|^2 \rangle = \frac{3k_B T_b}{m_b}. \tag{2.22}$$

Note that we do not consider the change in kinetic energy of the buffer-gas atoms as we are working under the assumption that on average they remain at a fixed temperature due to their constant interaction with the buffer-gas cooling cell. Taking the statistical average of Eq. (2.19) and using the equipartition result, we arrive at the following expression for the final molecule temperature after a single collision:

$$T_{m,f} - T_{m,i} = -\frac{2m_m m_b}{(m_m + m_b)^2} (T_{m,i} - T_b), \tag{2.23}$$

where we have used the fact that the statistical average of the dot products in Eq. (2.19) are zero because $\langle \cos\theta \rangle = \int_{-\pi}^{\pi} d\theta \cos\theta = 0$. We then extend this result to N collisions by rewriting as a differential equation [29, 50]

$$\frac{dT_m}{dN} = -\frac{2m_m m_b}{(m_m + m_b)^2} (T_m - T_b), \tag{2.24}$$

which has the solution

$$T_m(N) = T_b + (T_{m,i} - T_b) e^{-N/\kappa}, \tag{2.25}$$

where $\kappa = (m_m + m_b)^2 / 2m_m m_b$ has been introduced. Note that κ is minimum when $m_m = m_b$ implying that molecules with a similar mass to the buffer-gas atoms will be cooled most effectively.

With a simple model for the translational cooling process in hand, it is of interest to investigate its behavior for some typical parameters. The temperature of the buffer gas is well approximated by the temperature of the cell, which is typically about 25 K for neon buffer gas. On

the other hand, the initial temperature of the molecules of interest typically lie in the range of about $10^3 - 10^4$ K for a laser ablation source; therefore, we make the approximation that $T_{m,i} - T_b \approx T_{m,i}$. Using this approximation, we then determine the number of collisions required for the molecule temperature to be within $X\%$ of the buffer gas temperature:

$$N_{X\%} \approx \kappa \ln \left[\left(\frac{100\%}{X\%} \right) \frac{T_{m,i}}{T_b} \right]. \tag{2.26}$$

It is necessary for this number of collisions to occur before the molecules either leave the cell or freeze out on the cell walls. We estimate the number of collisions that occur inside the cell by comparing the expected mean free path of molecules in the buffer gas to the average length scale of the cell. The mean free path of a molecule moving through the buffer gas is given by

$$\begin{aligned} \lambda_{m,b} &= \frac{\bar{v}_m}{n_b \ \sigma_{m,b} \ \bar{v}_{m,b}}, \\ &= \frac{1}{n_b \ \sigma_{m,b} \sqrt{1 + \frac{m_m T_b}{m_b T_m}}} \end{aligned} \tag{2.27}$$

where $\sigma_{m,b}$ is the collision cross section between a molecule and a buffer-gas atom, n_b is the density of buffer gas inside the cell, $\bar{v}_i$ is the mean thermal velocity of the molecules ($i = m$) or buffer-gas atoms ($i = b$), and $\bar{v}_{m,b} = \sqrt{\bar{v}_m^2 + \bar{v}_b^2}$ is the relative mean thermal velocity between the molecules and buffer-gas atoms. Now, T_m is a function of the number of collisions (see Eq. (2.25)), so to find the number of collisions occurring over the average length scale of the cell $\langle L \rangle$ we solve the following integral equation for $N_{\langle L \rangle}$,

$$\int_0^{N_{\langle L \rangle}} dN \lambda_{m,b}(N) = \langle L \rangle, \tag{2.28}$$

which must be done numerically.

When molecules are ablated from the target, we assume their motion through the buffer gas is primarily unidirectional because of the large initial temperature difference. Therefore, we assume the average distance travelled between collisions is proportional to $\lambda_{m,b}$ rather than its square root, as would be the case for a diffusive process (i.e., a random walk). Diffusion begins once the translational temperature of the molecules is equivalent to that of the buffer-gas atoms.

The quantities $N_{X\%}$ and $N_{\langle L \rangle}$ are plotted in Fig. 2.4 for various molecule masses and assuming neon buffer gas with $m_b = 20.18$ amu. Thus, from the figure, we expect that molecules with a mass from a few amu to a few hundred amu will achieve a translational temperature roughly equivalent to that of the buffer gas by the time they travel a distance on the order of the average length of the cell. Notably, this translational relaxation inside the cell will occur on a timescale of roughly 100 µs. Finally, once the molecules have equilibrated with the buffer-gas atoms in the cell they will begin a diffusive random walk towards the cell walls where they will freeze and be lost. During this random walk, the molecules will continue to collide with the buffer-gas atoms at a rate given by

$$R_m = n_b \, \sigma_{m,b} \, \bar{v}_{m,b}. \tag{2.29}$$

Thus, we calculate the number of additional collisions occurring over time τ using $N_D = R_m \tau$. Assuming $m_m = 100$ amu, $m_b = 20.18$ amu, $n_b = 10^{16}$ cm^{-3}, $\sigma_{m,b} = 10^{-15}$ cm^2, and $T = 25$ K we find $N_D \approx 175 - 1750$ for $\tau = 1 - 10$ ms. Here, the timescale is chosen to coincide with the expected time it takes for molecules to be extracted from the cell, which will be discussed further below. Therefore, by the time the molecules are extracted from the cell, we expect them to have undergone on the order of a few hundred to a few thousand collisions with the buffer-gas atoms depending on the buffer-gas flow rate into cell.

2.1.3 Collisional cooling – internal state relaxation

Thus far, we have been concerned with the translational temperature of the molecules, and how it relaxes through collisional interactions with the cold buffer gas. However, molecules also have internal degrees of freedom that correspond to rotational and vibrational excitations, and it is expected that many of these states will be initially populated after the laser ablation process. For example, assuming typical rotational and vibrational transitions with $\tilde{\nu} = 1$ cm^{-1} and $\tilde{\nu} = 1000$ cm^{-1}, respectively, we expect thousands of rotational states and a few vibrational states to be populated at a temperature of 5000 K. Fortunately, this excess internal energy can be transferred to the translational motion of the buffer-gas atoms. However, in order for this energy transfer to occur,

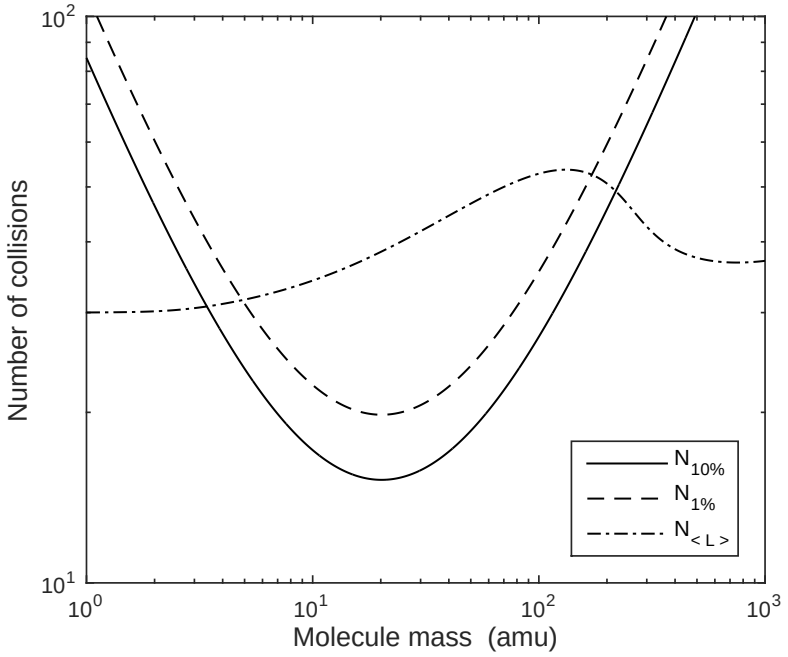

Figure 2.4: Number of collisions required for the molecule translational temperature to be within 10% (solid) and 1% (dashed) of the buffer gas temperature, and number of collisions that occur over the average length scale of the cell (dash-dot). Assumes $T_{m,i} = 5000$ K, $T_b = 25$ K, $m_m = 100$ amu, $m_b = 20.18$ amu, $n_b = 10^{16}$ cm^{-3}, $\sigma_{m,b} = 10^{-15}$ cm^2, and $\langle L \rangle = 30$ mm.

the interaction must be non-adiabatic such that the interaction time between the excited molecule and atom is short compared to the oscillation period of the molecular excited state (i.e., impulsive interactions). We investigate the adiabaticity of typical elastic collisions between molecules and buffer-gas atoms through the following adiabaticity parameter [51–53]:

$$\zeta = c\ \tau_c\ \tilde{\nu}, \tag{2.30}$$

where c is the speed of light in vacuum, τ_c is the collisional interaction timescale, and $\tilde{\nu}$ is the transition wavenumber corresponding to a rotational or vibrational state in the molecule. If $\zeta \ll 1$ the interaction is non-adiabatic and energy transfer can occur. On the other hand, if $\zeta \gg 1$ the interaction is adiabatic and energy transfer is unlikely.

We estimate the collisional interaction timescale in a hard sphere collision model as

$$\tau_c = \frac{r_0}{\bar{v}_{m,b}}, \tag{2.31}$$

where r_0 is the effective range of the potential between the molecule and a buffer-gas atom and $\bar{v}_{m,b}$ is the relative mean thermal velocity between the molecules and the buffer-gas atoms as defined above. The parameter ζ is plotted in Fig. 2.5 assuming a typical $r_0 \sim 1$ Å for interactions between neutral atoms and molecules. From the figure, we see that higher molecule temperatures lead to smaller values of ζ implying collisional energy transfer is more effective in the initial stages of cooling inside the buffer-gas cell. We find that $\zeta < 1$ for $\tilde{\nu} < 50$ cm^{-1} even at a molecule temperature of 25 K; thus, excited rotational states ($\tilde{\nu} \sim 1$ cm^{-1} for rotational transitions is typical) are likely to relax quite efficiently even once the translational motion of the molecules has equilibrated with the buffer-gas atoms. However, excited vibrational states ($\tilde{\nu} \sim 300 - 3000$ cm^{-1} for vibrational transitions is typical) are likely to not relax very efficiently at low temperatures. Nonetheless, we find $\zeta < 1$ for $\tilde{\nu} < 400$ cm^{-1} at a molecule temperature of 5000 K such that some vibrational relaxation for low frequency modes is likely to occur in the initial stages of collisional cooling inside the buffer-gas cell.

Given this simple picture of internal state relaxation via elastic collisions with cold buffer-gas atoms, it is of interest to compare our expectations with experimental results from the literature.

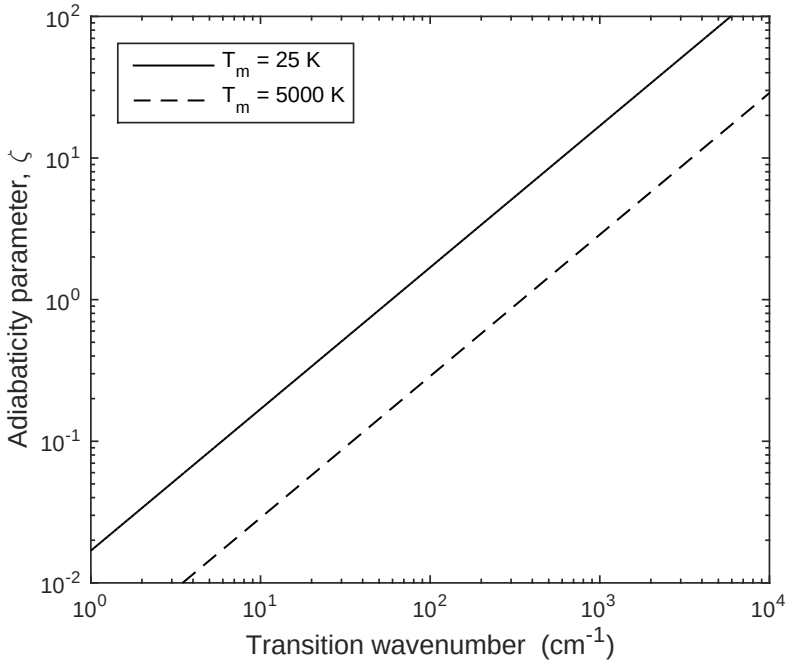

Figure 2.5: Adiabaticity parameter, ζ, for interactions between molecules and neutral atoms at a molecule temperature of $T_m = 25$ K (solid) and $T_m = 5000$ K (dashed). It is assumed that the interaction has an effective range of $r_0 = 1$ Å, the molecules have a mass of $m_m = 100$ amu, and neon buffer gas with $m_b = 20.18$ amu at a temperature of $T_b = 25$ K is used.

Many molecular species have been investigated with buffer-gas beam sources, and it is generally found that both the translational and rotational degrees of freedom exhibit temperatures equivalent to the buffer-gas temperature. For example, it has been observed that both translational and rotational temperatures equilibrate with the buffer gas for diatomic metal oxides [30, 31] and fluorides [32–35], as well as for more complex polyatomic molecules [36–41]. This is the case for both helium and neon buffer-gas sources. However, the few studies that have also investigated the vibrational degree of freedom have found it to be out of thermal equilibrium. In the case of SrF the vibrational level spacing is approximately 500 cm^{-1} [54]; therefore, approximately 10 vibrational states will be initially populated for typical ablation temperatures and some initial cooling is expected based on $\zeta \sim 1$ at 5000 K. Indeed, Barry et al. [32] observed substantial population in only the first few vibrational levels of a SrF buffer-gas beam implying that some vibrational relaxation occurred inside their buffer-gas cooling cell. Similar behavior was also observed by Bu et al. [34] for BaF, which is similar to SrF with a vibrational level spacing of approximately 450 cm^{-1} [55]. Based on the results of these studies we can conclude that our expectations for internal state relaxation based on adiabaticity arguments are reasonable, but certainly far from complete.

2.1.4 Extraction

Once the translational motion of the molecules has equilibrated with the buffer-gas atoms, the molecules will diffuse toward the cell walls and be lost unless they are extracted from the cell. Therefore, the efficiency of the extraction process can be characterized in terms of two competing timescales: the diffusion time and the time it takes to evacuate the cell through the exit aperture, or pumpout time. We define a dimensionless parameter to characterize the extraction efficiency [29],

$$\gamma_{\text{cell}} = \frac{\tau_D}{\tau_p}, \tag{2.32}$$

where τ_D is the effective diffusion time for molecules to reach the cell walls and τ_p is the pumpout time. When $\gamma_{\text{cell}} \lesssim 1$ the molecules diffuse to the cell walls faster than they are extracted from the cell, and the extraction efficiency is low. On the other hand, when $\gamma_{\text{cell}} \gtrsim 1$ the molecules are

extracted from the cell faster than they diffuse to the cell walls, and the extraction efficiency is high. We obtain an estimate for this parameter by looking at the diffusion and pumpout processes in more detail.

The rate at which buffer-gas atoms leave the cell is governed by the conductance C of the aperture; therefore, the following differential equation describes the pumpout process:

$$\dot{N}_b = \frac{C\ N_b}{V_{\text{cell}}}, \tag{2.33}$$

where $V_{\text{cell}} \approx 12.5\ \text{cm}^3$ is the volume of the buffer-gas cooling cell. Solution of this equation is a decaying exponential with a characteristic decay time given by

$$\tau_p = \frac{V_{\text{cell}}}{C}, \tag{2.34}$$

which defines the pumpout time of the cell. Assuming $T_{\text{cell}} = 25$ K, we find $\tau_p = 15.8$ ms for molecular flow and $\tau_p = 8.7$ ms for continuum flow through the exit aperture. Calculating the effective diffusion time is slightly more complicated. For a dilute, binary gas mixture, the diffusion coefficient $D_{m,b}$ for the molecules diffusing into the buffer gas is given by the Chapman-Enskog result [56]:

$$D_{m,b} = \frac{3}{16\ n_b \sigma_{m,b}} \sqrt{\frac{2\pi k_B T}{\mu_{m,b}}}, \tag{2.35}$$

where $\mu_{m,b} = m_m m_b/(m_m + m_b)$ is the reduced mass. For simplicity, we will assume the buffer-gas cooling cell is a box with an average length scale of $\langle L \rangle$; thus, the solution to the diffusion equation in Cartesian coordinates is written in terms of modes that have characteristic decay times given by [56]

$$\tau_{D,ijk} = \frac{3\langle L \rangle^2}{\pi^2 D_{m,b}} \left[(2i-1)^2 + (2j-1)^2 + (2k-1)^2 \right]^{-1}, \tag{2.36}$$

where $i, j, k \in [1, \infty)$ are positive integers representing the mode index. The lowest order diffusion mode has molecules concentrated near the center of the cell whereas molecules spread over modes of higher order will be concentrated closer to the cell walls. Notably, the diffusion time decays quadratically with larger mode indices; therefore, molecules occupying high order diffusion modes will be rapidly lost because, on average, they have a shorter distance to travel before reaching the

cell walls. Now, from the simple translational cooling model, we know that the average distance travelled by the molecules before equilibrating with the buffer gas is dependent on the mean free path $\lambda_{m,b}$, which is inversely proportional to the buffer-gas density inside the cell. Therefore, we expect the molecules to be distributed over the whole cell at low densities (i.e., low neon flow rate) and the diffusion time to be dominated by the lowest order mode $\tau_{D,000} = \langle L \rangle^2 / \pi^2 D_{m,b}$. However, as the buffer-gas density increases (i.e., higher neon flow rate), we expect the molecules to be confined closer to the ablation target at the point where they begin a diffusive random walk; thus, the molecules will be distributed over higher order diffusion modes such that the effective diffusion time is less than $\tau_{D,000}$. As this precise behavior is difficult to model, we plot γ_{cell} in Fig. 2.6 assuming the diffusion is dominated by $\tau_{D,000}$, which is a good approximation up to a certain point. We see that $\gamma_{\text{cell}} \approx 1$ at a flow rate of about 50 sccm, so we expect the extraction efficiency to not increase further with flow rate as long as $\tau_{D,000}$ is the dominant diffusion timescale.

Based on the above discussion, we expect the extraction efficiency to have a nonlinear behavior with the neon flow rate. At low flow rates (i.e., low neon density), we expect the extraction efficiency to increase approximately linearly as the diffusion time will be dominated by the lowest order mode, which has a linear dependence on buffer-gas density. Eventually, this increase will saturate around $\gamma_{\text{cell}} \approx 1$ as the diffusion and pumpout times become roughly equivalent. Finally, as the flow rate increases further (i.e., high neon density), we expect the extraction efficiency to decrease as the molecules are confined close to the cell walls and exhibit a decreased diffusion time. Indeed, this extraction behavior has been observed in a number of buffer-gas cooling experiments [31, 33, 44, 49, 57–59], and the higher order diffusion modes model described here was proposed and investigated by Skoff et al. [33] and Bulleid et al. [44]. This model is also supported by the results of Harilal et al. [60] and Farid et al. [61] who studied the expansion dynamics of laser ablation plumes at various ambient pressures and found the plume to be concentrated near the ablation target for higher background pressures. Furthermore, we observed the discussed trend with neon flow rate in our experimental study of carbon clusters with a buffer-gas cooling cell, and that data will be discussed further in Chapter 4.

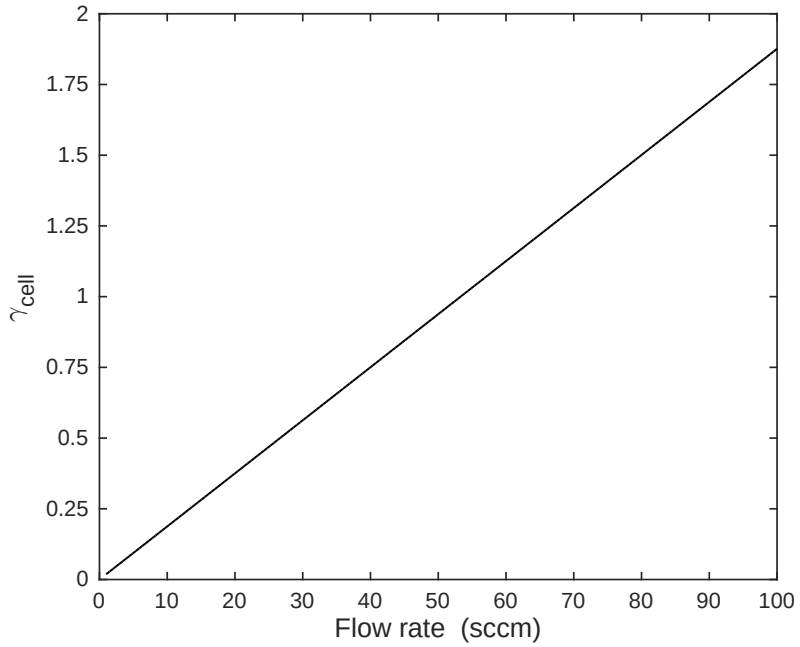

Figure 2.6: Cell extraction parameter as a function of neon flow rate into the cell. The cell temperature is $T_{\text{cell}} = 25$ K, the molecules have a mass of $m_m = 100$ amu, the collision cross section is $\sigma_{m,b} = 10^{-15}$ cm^2, and $\langle L \rangle = 30$ mm.

2.2 Molecular Beam

Up to this point, we have focused primarily on the dynamics inside the buffer-gas cooling cell, but ultimately we are interested in the properties of the molecular beam formed by extraction through the exit aperture of the cell. Given that the expected range of the Reynolds number at the exit aperture of the cell is $1 \lesssim Re \lesssim 120$ (see Fig. 2.3), it is useful to consider the formation of a molecular beam in both the effusive ($Re < 1$) and hydrodynamic ($Re > 100$) regimes, as this will cover the full range of expected beam parameters. The effusive regime is characterized by $Kn \gtrsim 1$, where there are no collisions occurring in the exit aperture. Therefore, effusive beams represent a sampling of the equilibrium velocity distribution inside the cell, and we expect a beam with low forward velocity and high divergence. On the other hand, the hydrodynamic regime is characterized by $Kn \lesssim 10^{-3}$ where there are many collisions occurring in the exit aperture. Therefore, we expect a hydrodynamic beam to have high forward velocity and low divergence as collisions near the aperture will direct the majority of atoms to leave the cell in the forward direction.

2.2.1 Effusive regime

In the effusive regime of operation, the standard kinetic theory of gases applies. We know that the fraction of buffer-gas atoms with a velocity between v and $v + dv$ at temperature T is given by the Maxwell-Boltzmann distribution in thermal equilibrium:

$$f(v)\,dv = 4\pi v^2 \left(\frac{m}{2\pi k_B T}\right)^{3/2} \exp\left(-\frac{mv^2}{2k_B T}\right) dv. \tag{2.37}$$

Furthermore, given a buffer-gas density of n_b inside the cell, we determine the number of atoms per unit time leaving the cell through an aperture to be [25, 27]

$$J(\theta, v) = n_b\ f(v)\, v \cos\theta\ dv\ dA\ \frac{d\Omega}{4\pi}, \tag{2.38}$$

where dA is the area element of the aperture, $d\Omega = \sin\theta\ d\theta\ d\phi$ is the solid angle element, and the $v\cos\theta$ term gives the flux in the forward direction with respect to the aperture normal. Integrating

this expression over all velocities we find the average flux in the forward direction to be

$$J(\theta) = n_b \ \bar{v}_b \cos\theta \ dv \ dA \ \frac{d\Omega}{4\pi}, \tag{2.39}$$

where we have used the mean thermal velocity $\bar{v}$ to simplify the expression. Far from the aperture, we make the replacement $dA \to A$ and integrate over the solid angle to find that J is equivalent to Eq. (2.5) for the conductance of a thin aperture in the molecular flow regime as expected. Given the flux through the aperture, we calculate the mean forward velocity of the beam from Eq. (2.38), where we see that the velocity distribution (normalized) of the beam is given by

$$\begin{aligned} f_J(v)\, dv &= v\sqrt{\frac{\pi m}{8k_b T}} f(v)\, dv, \\ &= \frac{v^3}{2}\left(\frac{m}{k_B T}\right)^2 \exp\left(-\frac{mv^2}{2k_B T}\right) dv, \end{aligned} \tag{2.40}$$

From this distribution, we calculate the mean forward velocity of the beam to be

$$\bar{u}_{e,f} = \int_0^\infty dv \ v f_J(v)\, dv = \left(\frac{3\pi}{8}\right)\bar{v} \approx 1.178\bar{v}, \tag{2.41}$$

where the e subscript refers to an effusive beam. Thus, we find a forward velocity slightly larger than the mean thermal velocity of the buffer-gas atoms inside the cell.

It is of interest to estimate the number of collisions we expect to occur in the beam as it propagates away from the aperture. We start from the average number density in the effusive beam exiting the cell aperture [25, 27]:

$$n_e(R,\theta) = \frac{n_b \cos\theta}{4\pi R^2} dA, \tag{2.42}$$

where R is the distance from the cell aperture and θ is the angle with respect to the aperture normal. To proceed, we assume an aperture shape and carrying out the integrations to find the density as a function of position away from the aperture. For a circular aperture with diameter d_{ap}, we write the area element in cylindrical coordinates as $dA = 2\pi r dr$ and define $z = R\cos\theta$ and

$R = \sqrt{z^2 + r^2}$ to find the density along the beam axis to be [25, 27]

$$\begin{aligned} n_e(z) &= \frac{n_b z}{2} \int_0^{d_{\mathrm{ap}}/2} \frac{r\ dr}{\left(\sqrt{z^2 + r^2}\right)^3}, \\ &= n_b \left(\frac{1}{2} - \frac{z}{\sqrt{4z^2 + d_{\mathrm{ap}}^2}} \right), \end{aligned} \tag{2.43}$$

where $z > 0$ is assumed and n_b is the density inside the buffer-gas cooling cell. Now, assuming the molecules of interest have equilibrated with the buffer gas inside the cell and are entrained in the effusive beam exiting the cell, we estimate the number of collisions that occur as the beam propagates away from the cell aperture. Here, entrained implies that the molecules and buffer-gas atoms are moving together with a velocity given by $\bar{u}_{e,f}$, and that the molecules are diffusing into the buffer gas in this moving reference frame. We know that the number of collisions occurring in the interval z to $z + dz$ is given approximately by $dz R_{m,e}(z) / \bar{v}_m$, where $R_{m,e}(z)$ is the collision rate in an effusive beam [62]:

$$R_{m,e}(z) = n_e(z)\, \sigma_{m,b} \bar{v}_{m,b} \left(\frac{7 - 4\sqrt{2}}{4} \right). \tag{2.44}$$

Here, we use $\bar{v}_m$ in the denominator for the number of collisions because this approximately corresponds to the forward velocity of an effusive beam. Recognizing the integrand as the mean free path $\lambda_{m,b}$, we integrate over distance to find the total number of collisions that will occur over some propagation distance L:

$$\begin{aligned} N_{\bar{L},e} &= 0.336 \sqrt{1 + \frac{m_m}{m_b}}\, (n_b\ \sigma_{m,b}) \int_0^L dz \left(\frac{1}{2} - \frac{z}{\sqrt{4z^2 + d_{\mathrm{ap}}^2}} \right), \\ &= 0.336 \sqrt{1 + \frac{m_m}{m_b}} \left(\frac{n_b\ \sigma_{m,b} d_{\mathrm{ap}}}{4} \right) \left(1 + 2\bar{L} - \sqrt{1 + 4\bar{L}^2} \right), \\ &\approx 0.336 \sqrt{1 + \frac{m_m}{m_b}} \left(\frac{n_b\ \sigma_{m,b} d_{\mathrm{ap}}}{4} \right), \end{aligned} \tag{2.45}$$

where $\bar{L} = L/d_{\mathrm{ap}}$ and the final expression is valid for $\bar{L} > 2 - 3$. We find that $N_{\bar{L},e}$ is of order unity far from the aperture for $m_m = 100$ amu, $m_b = 20.18$ amu, $n_b = 10^{16}$ cm^{-3}, $\sigma_{m,b} = 10^{-15}$ cm^2, and $d_{\mathrm{ap}} = 5$ mm. Therefore, in the effusive regime, we do not expect the molecules to continue to

exchange energy with the buffer-gas atoms once they have been extracted from the cell, which is precisely as expected in the molecular flow regime.

2.2.2 Hydrodynamic regime

In stark contrast to the effusive regime, the kinetic theory of gases does not apply in the hydrodynamic regime; therefore, we must adopt a fluid description of the buffer gas exiting the cell. A standard approach begins with the Bernoulli equation for isentropic flow of a compressible fluid, which is written as [52]

$$\frac{u^2}{2} + h = h_0, \tag{2.46}$$

where u is the flow velocity, h is the enthalpy of the fluid, and h_0 is the stagnation enthalpy. For an ideal gas, we have $dh = c_p\ dT$ where $c_p = \gamma/(\gamma - 1)(k_B/m)$ is the specific heat at constant pressure and $\gamma = 5/3$ for a monatomic ideal gas. Assuming c_p is constant with temperature, we integrate the Bernoulli equation to find the maximum forward velocity (i.e., terminal velocity) of the molecular beam in the hydrodynamic regime:

$$\bar{u}_{h,f} = \sqrt{\frac{2k_B}{m}\left(\frac{\gamma}{\gamma - 1}\right)(T_0 - T)}, \tag{2.47}$$

where T_0 is the stagnation temperature. If we assume $T \ll T_0$ and $\gamma = 5/3$ then we see that $\bar{u}_{h,f} \approx 1.401\bar{v}_0$, which is roughly 20% faster than an effusive beam. To proceed, we rewrite the Bernoulli equation in differential form and define stagnation parameters $u_0 = 0$, $c_{s,0}$, P_0, and n_0, for the flow velocity, sound velocity, pressure, and density, respectively. Then, substituting the above ideal gas relation for dh, we find the following relations for the properties of the flow field [25, 52]:

$$c_s = c_{s,0}\left[1 + \left(\frac{\gamma - 1}{2}\right)Ma^2\right]^{-1/2}, \tag{2.48}$$

$$T = T_0\left[1 + \left(\frac{\gamma - 1}{2}\right)Ma^2\right]^{-1}, \tag{2.49}$$

$$P = P_0\left[1 + \left(\frac{\gamma - 1}{2}\right)Ma^2\right]^{\frac{-\gamma}{\gamma-1}}, \tag{2.50}$$

$$n = n_0\left[1 + \left(\frac{\gamma - 1}{2}\right)Ma^2\right]^{\frac{-1}{\gamma-1}}, \tag{2.51}$$

where the following isentropic ideal gas relations have been used to relate the pressure and density between two points of the flow field:

$$P = P_0 \left(\frac{T}{T_0} \right)^{\frac{\gamma}{\gamma-1}}, \tag{2.52}$$

$$n = n_0 \left(\frac{T}{T_0} \right)^{\frac{1}{\gamma-1}}. \tag{2.53}$$

Here, $c_s = \sqrt{\gamma k_B T/m}$ is the speed of sound in the gas, P is the pressure, and the flow velocity can be found from the relation $u = Ma\ c_s$. The stagnation parameters refer to the gas properties inside the buffer-gas cooling cell such that $u_0 = Ma_0 = 0$ is assumed, and $n_0 \equiv n_b$ and $T_0 \equiv T_{\text{cell}}$. Thus, all relevant properties of the flow field are known as a function of Ma, which depends on the distance from the exit aperture of the cell.

Assuming a circular aperture of diameter d_{ap}, we use the results of Murphy [63] and Scoles [25] for an axisymmetric expansion of a monatomic ideal gas with $\gamma = 5/3$ to determine Ma as a function of distance z from the aperture on the beam axis:

$$Ma\,(z) = \begin{cases} 1.0 + C_1 \left(\frac{z}{d_{\text{ap}}} \right)^2 + C_2 \left(\frac{z}{d_{\text{ap}}} \right)^3 & ; \quad 0 < z < d_{\text{ap}}, \\ \left(\frac{z}{d_{\text{ap}}} \right)^{\gamma-1} \left[C_3 + C_4 \left(\frac{z}{d_{\text{ap}}} \right)^{-1} + C_5 \left(\frac{z}{d_{\text{ap}}} \right)^{-2} + C_6 \left(\frac{z}{d_{\text{ap}}} \right)^{-3} \right] & ; \quad z > d_{\text{ap}}, \end{cases} \tag{2.54}$$

where $C_1 = 3.337$, $C_2 = -1.541$, $C_3 = 3.232$, $C_4 = -0.7563$, $C_5 = 0.3937$, and $C_6 = -0.0729$ are fit constants. We now use the above expressions to find the temperature and density as a function of position away from the aperture. Unlike the effusive regime, we expect much higher densities at the cell aperture and the temperature to decrease as the beam propagates. Notably, the above treatment assumes continuum flow and does not consider the effect of a decreasing collision rate as the beam propagates, which results in the continuum flow assumption becoming invalid. This process is encapsulated by the so-called sudden freeze model [64] where the freezing, or quitting surface is defined as the point where continuum flow transitions to molecular flow. In other words, the quitting surface defines the distance from the exit aperture of the cell where collisions stop. An

approximation for this distance is given by [64]

$$z_F = z_{\text{ref}} \left(1.875\ \Xi\right)^{\frac{3}{\gamma+2}}, \tag{2.55}$$
$$\Xi = 3.189 \left(\frac{z_{\text{ref}}\ n_0\ \sigma}{T_0^{1/3}}\right) \sqrt{\frac{\gamma-1}{\gamma}},$$

where n_0 and T_0 are the stagnation density and temperature, respectively, and $z_{\text{ref}} = 0.806\ d_{\text{ap}}$ for $\gamma = 5/3$. For the typical neon buffer-gas beam source parameters of $n_0 = n_b = 10^{16}$ cm^{-3}, $T_0 = T_{\text{cell}} = 25$ K, $\sigma = 3.02 \times 10^{-15}$ cm^2, and $d_{\text{ap}} = 5$ mm we find $z_F = 7.686\ d_{\text{ap}} = 38.4$ mm. This value sets the range of validity for the continuum flow treatment; therefore, we investigate the continuum flow behavior up to $z = z_F$ by substituting the expression for $Ma\,(z)$ from Eq. (2.54) into Eqs. (2.49) and (2.51) for the temperature and density, respectively. Figure 2.7 shows the on axis temperature and density of the buffer-gas beam in the hydrodynamic regime. We see that both the temperature and density have decreased by an order of magnitude within a distance of $z = 3-5\ d_{\text{ap}}$ from the exit aperture. Note that neither quantity is equal to unity at the exit aperture as might be expected. This is an artifact of assuming $Ma\,(0) = 1$ in the aperture, and that the stagnation conditions occur far behind the aperture where the flow has zero velocity. This is not exactly correct as the buffer gas inside the cell will have a velocity component directed primarily towards the exit aperture (e.g., see the simulation results of Bulleid et al. [44]).

In a similar fashion to the effusive regime calculation, we estimate the number of collisions that occur in the beam before reaching the quitting surface by carrying out the following integration over the on axis beam density:

$$N_{z_F,h} = \sqrt{1 + \frac{m_m}{m_b}}\,(n_b\ \sigma_{m,b}) \int_0^{z_F} \frac{dz}{\left[1 + \left(\frac{\gamma-1}{2}\right) Ma\,(z)\right]^{\frac{1}{\gamma-1}}}. \tag{2.56}$$

A numerical calculation of this integral assuming $m_m = 100$ amu, $m_b = 20.18$ amu, $\sigma_{m,b} = 10^{-15}$ cm^2, $n_b = 10^{16} - 10^{17}$ cm^{-3}, $d_{\text{ap}} = 5$ mm, and z_F determined from Eq. (2.55) results in $N_{z_F,h} \approx 30 - 300$. Therefore, we expect additional collisional cooling for distances up to $z \approx 10 - 50\ d_{\text{ap}}$ from the cell aperture. Furthermore, we find that the total number of collisions between the molecules of interest and the buffer-gas atoms is on the order of a few thousand when

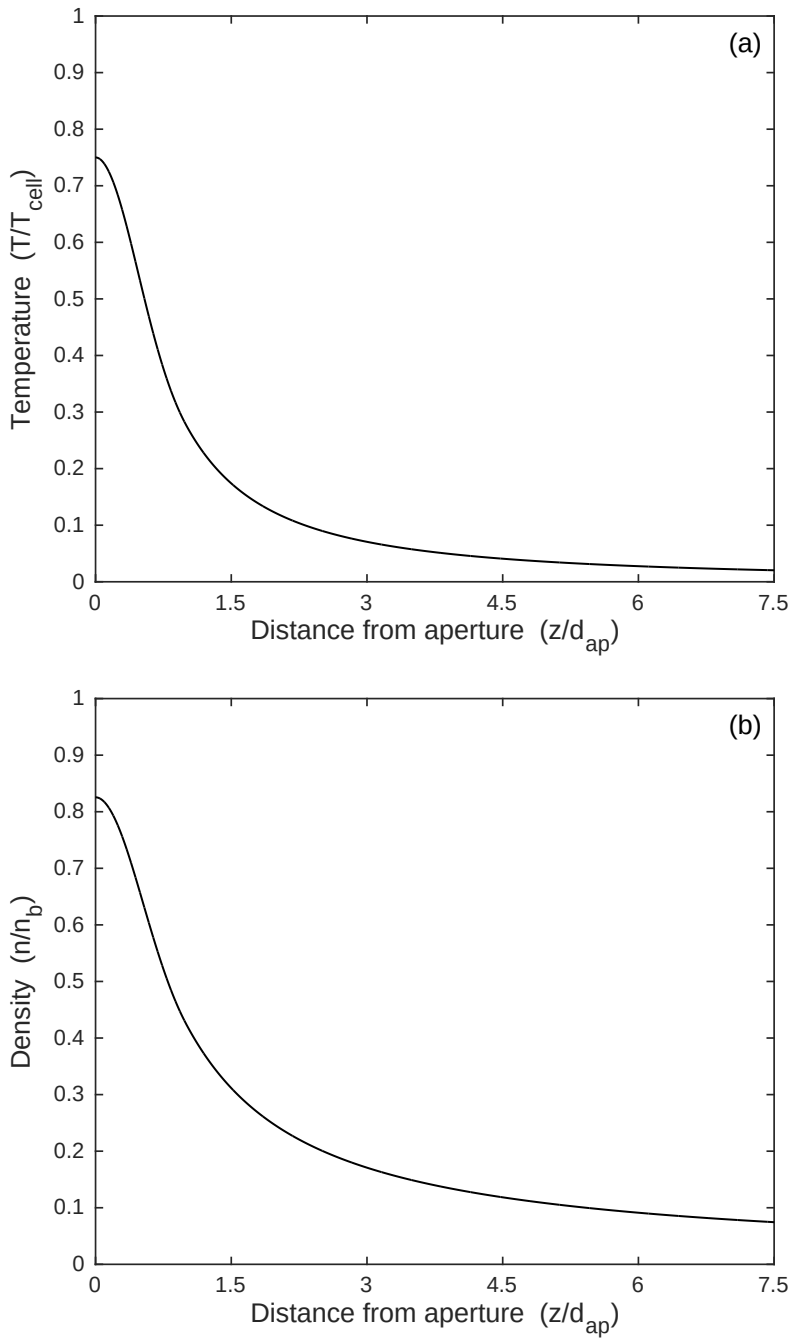

Figure 2.7: On axis (a) temperature and (b) density of a buffer-gas beam in the hydrodynamic regime. Both quantities are normalized to the initial state inside the buffer-gas cooling cell, and the distance from the exit aperture is normalized to the aperture diameter. Quantities are plotted up to the quitting surface defined by z_F in the text. Calculation assumes a monatomic ideal gas with $\gamma = 5/3$.

the buffer-gas beam source is operated in the hydrodynamic regime.

2.3 Comparison to a Traditional Free Jet Source

It is of interest to compare the expected number of collisions between molecules of interest and buffer-gas atoms in the buffer-gas beam source to that in a traditional free jet source. The closest point of comparison is the so-called "Smalley source" [65, 66], which uses laser ablation to introduce molecules of interest to the vicinity of a free jet expansion. Notably, the buffer-gas beam source will certainly have an advantage in terms of the number of molecules entrained in the expansion (i.e., beam brightness) since the molecules are introduced inside the cooling cell rather than outside near the aperture as in the Smalley source. However, the Smalley source has the advantage of much higher stagnation densities behind the exit aperture.

Typical parameters for a Smalley source are an aperture diameter of $d_{\mathrm{ap}} \sim 0.5 - 1$ mm and backing pressure of $P_0 \sim 1-5$ atm [28], which translates to densities of about $n_0 \sim 10^{19}-10^{20}$ cm^{-3} at a temperature of $T = 295$ K. Assuming that neon is used as an expansion gas, we compute the collision number using Eqs. (2.55) and (2.56) with $m_m = 100$ amu, $m_b = 20.18$ amu, and $\sigma_{m,b} = 10^{-15}$ cm^2. Note that in performing the integration, we set the lower bound to be a few millimeters rather than zero because ablated molecules are not entrained in the expanding beam at the aperture. For $d_{\mathrm{ap}} = 0.5$ mm we find that $N_{z_F,h} \sim 10^3 - 10^4$ and for $d_{\mathrm{ap}} = 1$ mm we find that $N_{z_F,h} \sim 10^4 - 10^5$. Therefore, for smaller aperture diameters it appears that the buffer-gas beam source and Smalley source have on the order of the same number of total collisions between the molecules of interest and the buffer-gas atoms. For larger aperture diameters, however, the Smalley source results in about an order of magnitude more collisions than the buffer-gas beam source described here.

It is important to realize that although the source described in this dissertation is expected to be on par with a typical Smalley source, the buffer-gas beam source provides much more design flexibility making it possible to further optimize performance. Additionally, most of the collisions in a buffer-gas beam source occur inside the cell at the buffer-gas temperature. This could be

very beneficial for studying metal cluster molecules, which experience substantial heating upon aggregation. The excess heat obtained during growth can be effectively dissipated by the cold buffer-gas before the molecules of interest are extracted from the cell, resulting in a bright beam of translationally, rotationally, and vibrationally cold molecules.

Chapter 3

Experimental Techniques for Infrared Absorption Spectroscopy

In this chapter, we outline the experimental techniques used in much of this dissertation work. We begin with a discussion of the absorption of infrared radiation and the Beer-Lambert law. We then discuss the different mechanisms that effect the absorption lineshape of a given molecular transition, and introduce the minimum detectable optical depth that can be achieved for a given measurement setup. Next, Fourier transform infrared spectroscopy is discussed, and a detailed overview of the spectrometer instrumentation and its expected performance is given. We then describe the actual performance of the spectrometer used in this dissertation work. Finally, laser absorption spectroscopy is discussed and methods to achieve shot noise limited absorption sensitivity are presented. We finish this chapter with a discussion of the actual performance of the laser spectroscopy system used in this dissertation work.

3.1 Absorption of Infrared Radiation

3.1.1 Beer-Lambert law

For absorption spectroscopy, the Beer-Lambert law relates the density of absorbers in a medium to the change in intensity of light as it propagates through the medium. In the weakly absorbing limit, and assuming scattering is negligible, the Beer-Lambert law states that the intensity of light $I(\tilde{\nu}, z)$ propagating through an absorbing medium will decrease with distance z as

$$\frac{dI(\tilde{\nu}, z)}{dz} = -\alpha(\tilde{\nu})\, I(\tilde{\nu}, z), \tag{3.1}$$

where $\alpha(\tilde{\nu})$ is the absorption coefficient of the medium (assumed to be isotropic) at wavenumber $\tilde{\nu}$. Assuming the light enters the medium at $z = 0$ and exits the medium after a distance l we solve the above differential equation to obtain

$$\frac{I(\tilde{\nu}, l)}{I(\tilde{\nu}, 0)} = e^{-\alpha(\tilde{\nu})l}. \tag{3.2}$$

From this solution we then define the optical depth $\tau(\tilde{\nu})$ as

$$\tau(\tilde{\nu}) = \ln\left[\frac{I(\tilde{\nu}, 0)}{I(\tilde{\nu}, l)}\right] = \alpha(\tilde{\nu})\, l. \tag{3.3}$$

Note that absorbance $A(\tilde{\nu})$ is commonly encountered in place of optical depth, and the two quantities are related by $A(\tilde{\nu}) = \log_{10} e\ \tau(\tilde{\nu}) \approx 0.434\ \tau(\tilde{\nu})$.

3.1.2 Absorption lineshapes

The absorption coefficient $\alpha(\tilde{\nu})$ corresponding to a particular transition in an ensemble of molecules is wavenumber dependent and has a finite extent about the transition wavenumber $\tilde{\nu}_0$. In a typical experiment, various broadening mechanisms are present that give rise to different absorption lineshapes, and they are classified as either homogeneous or inhomogeneous broadening. Homogeneous broadening mechanisms give rise to a Lorentzian lineshape such that $\alpha(\tilde{\nu})$ takes the form

$$\alpha_L(\tilde{\nu}) = \alpha(\tilde{\nu}_0)\, \frac{\Gamma_L^2}{\Gamma_L^2 + 4c^2(\tilde{\nu} - \tilde{\nu}_0)^2}, \tag{3.4}$$

where $\alpha(\tilde{\nu}_0)$ is the peak absorbance on resonance, Γ_L is the full width at half maximum (FWHM) of the homogeneously broadened transition in units of Hz, and c is the speed of light in vacuum. On the other hand, inhomogeneous broadening mechanisms give rise to a Gaussian lineshape,

$$\alpha_G(\tilde{\nu}) = \alpha(\tilde{\nu}_0) \exp\left[-4\ln 2\ c^2 \frac{(\tilde{\nu} - \tilde{\nu}_0)^2}{\Gamma_G^2}\right], \tag{3.5}$$

where Γ_G is the FWHM of the inhomogeneously broadened transition in units of Hz. If homogeneous and inhomogeneous broadening mechanisms have similar magnitudes then the absorption lineshape is a convolution of a Lorentzian and a Gaussian. This gives rise to the Voigt lineshape,

$$\alpha_V(\tilde{\nu}; \Gamma_L, \Gamma_G) = \int_{-\infty}^{\infty} d\tilde{\nu}' \alpha_L(\tilde{\nu}')\, \alpha_G(\tilde{\nu} - \tilde{\nu}'). \tag{3.6}$$

The natural linewidth of an absorption line is governed by how long a particular transition can be observed (i.e., the excited state lifetime). This can be understood via the energy-time uncertainty principle $\Delta E \Delta t \geq h/4\pi$, which sets a lower bound on how well the transition energy between a ground and excited state can be determined for a given observation time. Rearranging slightly we write the minimum FWHM of a lifetime broadened transition as $\Gamma_0 = 1/4\pi\tau$ where τ is the excited state lifetime. As the excited state naturally decays exponentially in time due to spontaneous emission, $\alpha(\tilde{\nu})$ will have a Lorentzian lineshape. The spontaneous emission rate is proportional to $\tilde{\nu}^3$ [67]; therefore, excited state lifetimes are typically much shorter (Γ_0 much larger) in the ultraviolet and visible regions of the electromagnetic spectrum compared to the infrared and microwave regions. For example, consider the natural linewidth of the ^{87}Rb cycling transition, which is roughly 10 MHz and occurs at approximately $10,000$ cm^{-1} [68]. Typical vibrational and rotational transitions occur at wavenumbers on the order of 1000 cm^{-1} and 1 cm^{-1}, respectively, resulting in natural linewidths of roughly 10 kHz and much less than 1 Hz, respectively, based on the scaling of spontaneous emission with $\tilde{\nu}^3$. Thus, Γ_0 is typically not observed in infrared absorption spectroscopy due to finite instrument linewidths, as well as the presence of other broadening mechanisms, which will now be discussed.

Given an ensemble of molecules with finite thermal energy, the FWHM of an absorption line will experience Doppler broadening due to the finite translational motion of the molecules. Assuming thermodynamic equilibrium, the ensemble of molecules will have a velocity distribution given by the Maxwell-Boltzmann distribution

$$f_v(v) = \left(\frac{m}{2\pi k_B T}\right)^{3/2} \exp\left(-\frac{mv^2}{2k_B T}\right), \tag{3.7}$$

where m is the mass of a molecule in the ensemble, k_B is Boltzmann's constant, T is the temperature of the ensemble, and v is the molecule velocity. Thus, for any given molecule, the transition wavenumber will be Doppler shifted to $\tilde{\nu}' = \tilde{\nu}_0(1 + v/c)$ and molecules in the ensemble will acquire a distribution of transition wavenumbers given by

$$f_{\tilde{\nu}'}(\tilde{\nu}') = f_v(v)\frac{dv}{d\tilde{\nu}'} = \left(\frac{c}{\tilde{\nu}_0}\right)\left(\frac{m}{2\pi k_B T}\right)^{3/2} \exp\left[-\frac{mc^2}{2k_B T}\left(\frac{\tilde{\nu}'}{\tilde{\nu}_0} - 1\right)^2\right]. \tag{3.8}$$

Therefore, the absorption coefficient will take the form of a Gaussian function

$$\alpha_D\left(\tilde{\nu}\right) = \alpha\left(\tilde{\nu}_0\right)\exp\left[-\frac{mc^2}{2k_BT\tilde{\nu}_0^2}\left(\tilde{\nu}' - \tilde{\nu}_0\right)^2\right] \tag{3.9}$$

from which we define the FWHM (in units of Hz) of a Doppler broadened transition as

$$\Gamma_D = 2\sqrt{\frac{2\ln 2k_BT}{m}}\tilde{\nu}_0. \tag{3.10}$$

Given the Gaussian form of the absorption lineshape, Doppler broadening is clearly an inhomogeneous broadening mechanism.

In addition to finite thermal energy, if the ensemble of molecules has a high density, or are entrained in a buffer gas of high density then collisional interactions cannot be neglected and the FWHM of the transition will be broadened. Unlike Doppler broadening, collisional broadening is a homogeneous mechanism and $\alpha\left(\tilde{\nu}\right)$ will maintain the form of a Lorentzian function. This is due to the fact that collisions modify the excited state lifetime of the transition and shorter lifetimes lead to larger values of Γ_{lt} as per the energy-time uncertainty principle. The magnitude of collisional broadening can be estimated using the classical collision rate determined from kinetic theory $R_c = n\sigma\bar{v}$ [69]. Here, we use the collision rate defined by Eq. (2.29) because the density of buffer-gas atoms is much larger than that of the molecules of interest. Thus, the FWHM (in units of Hz) of a transition broadened due to collisions is

$$\Gamma_c = n_b\sigma_{m,b}\bar{v}_{m,b}, \tag{3.11}$$

where n_b is the buffer-gas density, $\sigma_{m,b}$ is the collision cross section between a molecule and a buffer-gas atom, and $\bar{v}_{m,b}$ is the relative mean thermal velocity between the molecules and the buffer-gas atoms.

Finally, there is one other broadening mechanism commonly encountered in absorption spectroscopy experiments that utilize a molecular beam. In such an experiment, a beam of molecules moving with forward velocity u is intersected by a beam of light propagating orthogonal to the molecular beam. This arrangement leads to transit time broadening, which arises as a result of the finite time that the beam of light can probe the transition. Once again, this is due to the

energy-time uncertainty principle and will result in broadening if the transit time of a molecule through the beam of light is shorter than the excited state lifetime of the transition being probed. Thus, transit time broadening is a homogeneous broadening mechanism and $\alpha(\tilde{\nu})$ will maintain the form of a Lorentzian function. Assuming the light is a Gaussian beam with waist w_0, the time it takes a molecule to traverse the beam of light is given by $t = \sqrt{2\ln 2}\ w_0/u$. Thus, the FWHM (in units of Hz) of a transition broadened due to finite transit time is approximately

$$\Gamma_t = \frac{u}{\sqrt{2\ln 2}\ w_0}, \tag{3.12}$$

where u is the forward velocity of the molecular beam.

3.1.3 Minimum detectable optical depth

For absorption spectroscopy there are two main factors that contribute to the minimum optical depth that can be detected with a given instrument: optical power from the light source and detector sensitivity. Shot noise present in electromagnetic radiation sets a fundamental limit on absorption measurements because it results in fluctuations around the mean optical power incident on an absorbing sample. The noise contribution to the optical power per unit measurement bandwidth due to shot noise is given by

$$\sigma_{sn} = \sqrt{2hc\tilde{\nu}\bar{P}}, \tag{3.13}$$

where $hc\tilde{\nu}$ is the photon energy, $\bar{P}$ is the mean optical power, and σ_{sn} has units of $\mathrm{W}/\sqrt{\mathrm{Hz}}$. Notably, shot noise is independent of frequency making it a form of "white" noise. In addition to shot noise, the limited sensitivity of the detector plays an important role in determining the minimum detectable optical depth of a given instrument. Detector noise can be specified as a noise equivalent power (NEP) with units of $\mathrm{W}/\sqrt{\mathrm{Hz}}$, which defines the mean optical power that gives a signal-to-noise ratio (SNR) of unity in a 1 Hz measurement bandwidth. Although NEP is the quantity of interest in terms of noise power, it is dependent on the detector area A_d; therefore, the specific detectivity D^* is a commonly encountered metric for infrared detector performance:

$$D^* = \frac{\sqrt{A_d}}{NEP}, \tag{3.14}$$

which has units of cm$\sqrt{\text{Hz}}$/W, also known as Jones. Thus, given the detector D^* we can quantify the noise contribution due to the detector as

$$\sigma_d \equiv NEP = \frac{\sqrt{A_d}}{D^*}. \tag{3.15}$$

Thus, we define the total noise power in an absorption measurement as $\delta\bar{P} = \sqrt{\sigma_{sn}^2 + \sigma_d^2}$.

Given the total noise power, we determine the minimum detectable optical depth $\tau_{\min}$ in a given measurement bandwidth Δf by combining Eqs. (3.13) and (3.15):

$$\begin{aligned} \tau_{\min} &\approx \frac{\delta\bar{P}}{\bar{P}}\sqrt{\Delta f} \\ &= \sqrt{\frac{2hc\tilde{\nu}\Delta f}{\bar{P}} + \frac{A_d\Delta f}{\left(\bar{P}D^*\right)^2}}, \end{aligned} \tag{3.16}$$

where small optical depths have been assumed in order to expand the natural logarithm in a Taylor series to arrive at this expression. We are fortunate that infrared detectors exist with large enough D^* values to reach shot noise limited performance (i.e., the detector noise contribution falls below that of the shot noise contribution). However, to keep noise to a minimum, particularly in the $1/f$ regime, these detectors must be minimally biased. Therefore, low noise performance comes at the cost of detector linearity, which limits the incident optical power especially if detection at DC is of interest. This will be discussed more in Section 3.4.4

3.2 Fourier Transform Infrared Spectroscopy

Fourier transform infrared (FTIR) spectroscopy utilizes an interferometer-based spectrometer to simultaneously measure absorption lines over a broad range of wavenumbers. The standard FTIR spectrometer consists of a broadband source coupled to a Michelson interferometer (MI), and the output of the MI is passed through a sample region before being focused onto an infrared detector. As one of the mirrors in the MI is moved, a pathlength difference is introduced and different wavenumbers from the source experience constructive and destructive interference at the output of the MI. By monitoring the variations in intensity at the output of the MI as a function of the pathlength difference an interferogram can be recorded and subsequently Fourier transformed

to obtain the intensity of the source as a function of wavenumber. An absorbing sample placed between the output of the MI and the detector will modify the interferogram because the source intensity will be reduced at the transition wavenumbers corresponding to absorption by the sample. A simplified schematic of the Thermo Fisher Scientific Nicolet iS50 FTIR spectrometer used for this dissertation work is depicted in Fig. 3.1. This section will discuss the different aspects of the FTIR spectrometer and provide some guidelines for optimal settings that give the best quantitative results when investigating absorption features. An excellent resource for the theory and instrumentation of FTIR spectroscopy is the textbook of Griffiths and Haseth [70], which has been consulted for much of the discussion presented here.

3.2.1 Source

The source used in FTIR spectrometers is essentially a hot filament held at a temperature on the order of 1000 K; thus, its spectral energy density is modeled as a blackbody source:

$$U\left(\tilde{\nu}, T\right) = \frac{2hc^2\tilde{\nu}^3}{\exp\left(\frac{hc\tilde{\nu}}{kT}\right) - 1}. \tag{3.17}$$

Assuming a temperature of $T = 1000$ K such a source has a peak spectral energy density of approximately $570\,\mu\mathrm{W/sr\,cm^2\,cm^{-1}}$ at $\tilde{\nu} \approx 2000\ \mathrm{cm^{-1}}$. One drawback to this type of source is that it is extended with an area of approximately 1 $\mathrm{cm^2}$, which limits the extent to which the light can be collimated or focused onto a detector. However, a major advantage is that the filament source is inherently broadband, and provides light in the range of approximately $50 - 9000\ \mathrm{cm^{-1}}$ in a typical FTIR spectrometer.

3.2.2 Michelson interferometer

The operation of a FTIR spectrometer is based on that of the standard two-beam MI, which divides a beam of radiation in half with a beamsplitter and introduces a pathlength difference before recombining the beams at the output of the interferometer. By varying the pathlength difference, or optical retardation δ, a condition is created where the two beams either constructively

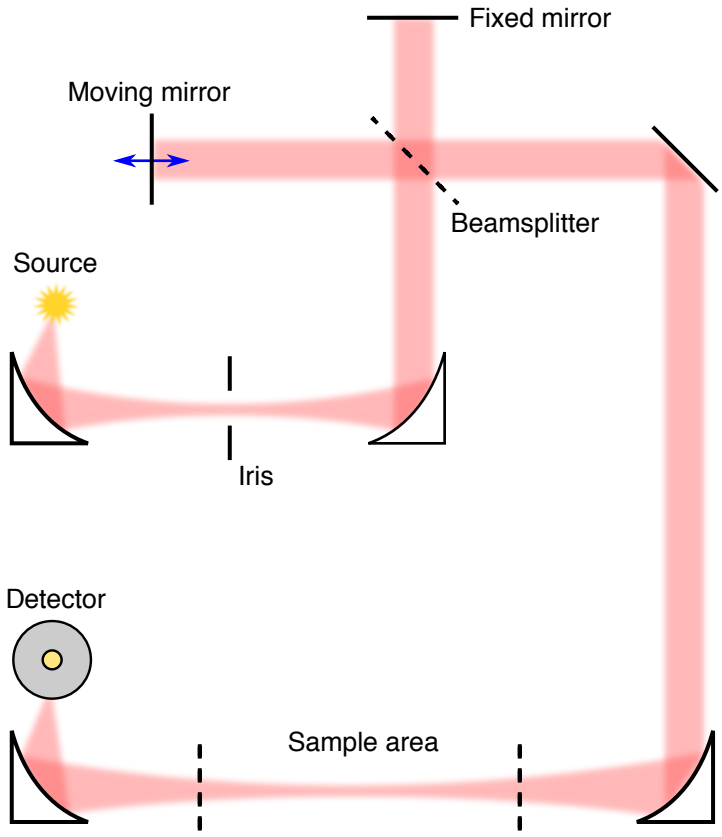

Figure 3.1: A schematic of the Nicolet iS50 FTIR spectrometer. The optics are designed to form an image of the iris in the sample region with a magnification of 1.130. The image of the iris in the sample region is then imaged onto the detector with a magnification of 0.1651.

or destructively interfere when recombined. To understand the basic operating principle of the MI, it is easiest to first consider a monochromatic source of wavenumber $\tilde{\nu}$. If $\delta = 0$ then there is no pathlength difference and the two beams will interfere constructively (i.e., all light from the source will reach the detector). However, if the moveable mirror is displaced by a quarter of a wavelength then $\delta = 1/2\tilde{\nu}$ and the two beams will interfere destructively (i.e., none of the light from the source will reach the detector). Displacing the moveable mirror by another quarter of a wavelength will result in constructive interference again; therefore, $\delta = m/\tilde{\nu}$, with m an integer, will result in constructive interference. Thus, the intensity at the detector as a function of δ is

$$I(\delta) = \frac{I(\tilde{\nu})}{2}\left[1 + \cos(2\pi\tilde{\nu}\delta)\right], \tag{3.18}$$

where $I(\tilde{\nu})$ is the source intensity. Generally, we are only interested in the cosine component such that the constant offset will be neglected in the following discussion.

Equation (3.18) is for an ideal MI and does not consider various instrument effects such as beamsplitter efficiency and detector response as a function of $\tilde{\nu}$. Therefore, it is convenient to introduce the instrument transfer function $H(\tilde{\nu})$ and the single beam spectral intensity of the source seen by the detector $B(\tilde{\nu}) = H(\tilde{\nu})\, I(\tilde{\nu})/2$. Thus, the interferogram intensity is given by

$$I(\delta) = B(\tilde{\nu}) \cos(2\pi\tilde{\nu}\delta). \tag{3.19}$$

Clearly, $I(\delta)$ and $B(\tilde{\nu})$ form a cosine Fourier transform pair, and the above formalism can be extended to a polychromatic source to obtain

$$I(\delta) = 2\int_0^\infty d\tilde{\nu} B(\tilde{\nu}) \cos(2\pi\tilde{\nu}\delta), \tag{3.20}$$

$$B(\tilde{\nu}) = 2\int_0^\infty d\delta I(\delta) \cos(2\pi\tilde{\nu}\delta), \tag{3.21}$$

In practice, $I(\delta)$ is recorded over a finite range of δ and $B(\tilde{\nu})$ is computed using a discrete transform. This results in $B(\tilde{\nu})$ having a finite resolution $\Delta\tilde{\nu}$, which is inversely proportional to the maximum retardation $\delta_{\max}$ that the FTIR spectrometer can achieve (i.e., the maximum linear travel distance of the moveable mirror). Furthermore, errors introduced in the sampling and digitization process

lead to small offsets in δ that translate into sine components being present in the interferogram. Therefore, it is typical to record a two-sided interferogram (i.e., the retardation ranges between $-\delta_{\max} < \delta < \delta_{\max}$) and compute $B(\tilde{\nu})$ using the fast Fourier transform algorithm. In addition, a phase correction procedure, such as that developed by Mertz [71], is applied to ensure a linear mapping between δ and $\tilde{\nu}$.

Given that there is a fundamental limit on the achievable resolution, it is practical to apply an apodization function $A(\delta)$ prior to transforming the interferogram. Apodization effectively truncates the interferogram at finite δ in a smooth way such that absorption features do not exhibit excess broadening or fictitious side lobes, and can suppress baseline fluctuations around weak absorption features. With the inclusion of apodization $B(\tilde{\nu})$ becomes

$$B(\tilde{\nu}) = \int_{-\infty}^{\infty} d\delta A(\delta) I(\delta) \cos(2\pi\tilde{\nu}\delta), \tag{3.22}$$

which is equivalent to convolving $B(\tilde{\nu})$ with the Fourier transform of $A(\delta)$. A variety of apodization functions have been investigated in Refs. [72–74] and their effect on Lorentzian and Gaussian absorption bands quantified in Refs. [75–77]. The conclusions of these studies imply that, in general, no single apodization function is suitable for all applications. If quantitative information on peak absorbance of an absorption line is important then a simple boxcar apodization function should be used. However, it is important to realize that this will introduce baseline fluctuations in the vicinity of weak absorption features due to the presence of large side lobes from strong absorption features that are usually present in FTIR spectra (e.g., from atmospheric H_2O and CO_2). Therefore, more aggressive apodization functions can be used to suppress sidelobes, and the simple method introduced by Jalsovszky [78] can be applied to determine true peak absorbance for weak absorption features if the actual FWHM of the absorption line is known. Particularly useful apodization functions are the Norton-Beer strong and weak functions [73], which can be used if suppression of baseline fluctuations and high resolution are critical.

In addition to the maximum retardation and choice of apodization function, the diameter of the iris located between the source and the MI (see Fig. 3.1) is a critical parameter in determining

the achievable resolution of a FTIR spectrometer. This is a result of the fact that extended sources cannot be well collimated* and the beam of light entering the MI is slightly diverging; therefore, the extent of the source imaged onto the detector must be restricted. This can be understood by considering the well-known circular fringe pattern observed at the output of a conventional MI, which consists of a central bright fringe surrounded by alternating rings of dark and bright fringes [79, 80]. As the optical retardation between the two arms of the MI increases the circular fringe pattern collapses towards the center and the central bright fringe decreases in diameter. If the extent of the source imaged onto the detector is not restricted, the average intensity on the detector will vary weakly as a function of δ due to the presence of many bright and dark fringes. Therefore, the effect of beam divergence through the MI will result in an effective decrease in the resolution of the FTIR spectrometer as a result of this self-apodization. The solution to this problem is to use an iris of variable diameter to restrict the image size of the source on the detector. In this way it is ensured that the detector only sees the central bright fringe over the full range of δ for a given resolution setting. We estimate the maximum solid angle passed by the interferometer optical system as follows. Let the beam have a divergence angle of α through the MI such that Eq. (3.20) becomes

$$I(\delta) = 2\int_0^\infty d\tilde{\nu}\ B(\tilde{\nu})\cos(2\pi\tilde{\nu}\delta\cos\alpha). \tag{3.23}$$

Assuming that the circular fringe pattern has a central bright fringe then the maximum allowed divergence angle that restricts the system to passing only this central fringe is given by the value of α at the first dark fringe:

$$2\pi\tilde{\nu}\delta - 2\pi\tilde{\nu}\delta\cos\alpha \approx 2\pi\tilde{\nu}\delta\left(\frac{\alpha^2}{2}\right) = \pi,$$
$$\alpha = \sqrt{\frac{1}{\tilde{\nu}\delta}} \tag{3.24}$$

where small α has been assumed. Now, assuming a resolution of $\Delta\tilde{\nu} = 1/\delta_{\max}$ and a maximum

* Optical elements have a finite field of view over which they can successfully convert diverging spherical wavefronts into collimated planar wavefronts. If the extent of the source falls outside this field of view then portions of the light collected from the source will continue to diverge.

wavenumber of $\tilde{\nu}_{\max}$ in the source spectrum, we find that the maximum solid angle is

$$\Omega_{\max} = 2\pi \left(1 - \cos \alpha_{\max}\right) \approx \frac{\pi \Delta \tilde{\nu}}{\tilde{\nu}_{\max}}. \tag{3.25}$$

Therefore, we see that higher resolution (i.e., smaller $\Delta\tilde{\nu}$) and broader optical bandwidth (i.e., larger $\tilde{\nu}_{\max}$) requires a smaller iris diameter to restrict Ω, which will reduce the amount of light passed to the detector. Given that the spectral energy density of broadband, blackbody-like sources is already quite low, further restricting the throughput of the optical system increases the demand on detector sensitivity.

3.2.3 Detectors

The Nicolet iS50 FTIR spectrometer is equipped with two infrared detectors: a pyroelectric bolometer with a deuterated, L-alanine doped triglycine sulfate (DLaTGS) element and a quantum detector with a mercury cadmium telluride (MCT) element. The optical bandwidth of both detectors is similar, about $350 - 12,500$ cm^{-1} for the DLaTGS and about $600 - 11,700$ cm^{-1} for the MCT; however, the sensitivity of the DLaTGS detector is approximately two orders of magnitude lower than that of the MCT detector. Nonetheless, the DLaTGS detector is useful in applications that involve static sample environments and high incident flux because the detector responds on thermal timescales and remains linear over a wide range of incident flux conditions. On the other hand, MCT detectors excel in all FTIR spectroscopy applications as long as the incident flux is kept low because the detector response saturates and becomes nonlinear under even moderate incident flux conditions.

An important aspect of MCT detectors used in FTIR spectrometers is that they are typically photoconductive (PC) type detectors, which exhibit large $1/f$ noise due to the necessity of biasing the detector element to a linear operating point. This results in low sensitivity at frequencies below a few kHz; thus, the light incident on the detector must be modulated to achieve high sensitivity. Fortunately, modern FTIR spectrometers make use of a rapid scan technique where the moveable mirror is translated at constant velocity v from $-\delta_{\max}$ to $\delta_{\max}$ such that $\delta \rightarrow \delta(t) = 2vt$. This

results in modulation of the spectral components in the source occurring at frequencies $f_{\tilde{\nu}} = 2v\tilde{\nu}$. Considering maximum and minimum wavenumbers of 7000 cm^{-1} (limited by the KBr beamsplitter) and 600 cm^{-1}, respectively, incident on the detector, and a typical mirror velocity of about 3.2 cm/s we find that $f_{600} = 3.8$ kHz and $f_{7000} = 44.8$ kHz. Given that the optimal frequency response of a PC MCT detector lies in the range of approximately 1 kHz to 1 MHz we find that all wavenumbers in the source spectrum will be detected at high sensitivity. Notably, because DLaTGS detectors have a slow response time, the mirror velocity must be much slower (typically $v < 1$ cm/s), which results in substantially longer interferogram acquisition times compared to MCT detectors. This highlights yet another advantage of using MCT detectors for FTIR spectroscopy.

3.2.4 Detection limit

In order to determine the achievable detection limit of a given FTIR spectrometer measurement, the optical power reaching the detector must be determined. The spectral energy density emitted by the source is given by Eq. (3.17), but we must determine the maximum throughput, or etendue G of the FTIR spectrometer optical system to determine the optical power at the detector. Etendue is the product of beam area and its solid angle at any focus; thus, the MI has a maximum etendue G_M dictated by the area of the mirrors A_M and the solid angle defined by Eq. (3.25):

$$G_M = \frac{\pi A_M \Delta\tilde{\nu}}{\tilde{\nu}_{\max}}. \tag{3.26}$$

Additionally, the optical system that focuses light onto the detector has a maximum etendue $G_d = A_d\Omega_d$. Therefore, the limiting etendue of the optical system can be either G_M or G_d depending on the choice of parameters. Typically, G_d is the limiting factor for low resolution ($\Delta\tilde{\nu} > 1$ cm^{-1}) measurements due to the small size of MCT detector elements, whereas G_M will limit the optical throughput at high resolutions as a result of the restricted solid angle given by Eq. (3.25). The total signal power contributing to a measurement is then

$$\bar{P}_{\text{FTIR}} = \eta\, U\left(\tilde{\nu}, T\right) G\Delta\tilde{\nu}, \tag{3.27}$$

where G is chosen as the smaller of G_M and G_d, and η is the efficiency of the spectrometer optical system that incorporates losses due to beamsplitter efficiency, reflectivity of mirrors, optical misalignment, and detector quantum efficiency.

Given the total optical power reaching the detector, we define the detection limit of a single beam spectrum acquired with a FTIR spectrometer using Eq. (3.16)

$$\tau_{\mathrm{min,FTIR}} = \sqrt{\frac{2hc\tilde{\nu}\Delta f}{\eta\, U\left(\tilde{\nu},T\right) G\Delta\tilde{\nu}} + \frac{A_d\Delta f}{\left(\eta\, U\left(\tilde{\nu},T\right) G\Delta\tilde{\nu}D^*\right)^2}}. \tag{3.28}$$

Equation (3.28) provides a good approximation to the minimum detectable optical depth in FTIR spectroscopy, and provides insight into the effect of different parameters on the sensitivity. For a given source and detector, the sensitivity of a measurement is largely determined by the choice of resolution and measurement time. Depending on whether G_M or G_d limits the etendue of the system, the resolution can have a large effect on sensitivity. For example, if G_M is the limiting etendue, then doubling the resolution will decrease the sensitivity by a factor of 4. In order to compensate for this loss in sensitivity, the measurement time must increase by a factor of 16. Thus, we see that the choice of resolution and desired sensitivity strongly dictates how long a given measurement will take. The following subsection provides details of the performance of the Nicolet iS50 FTIR spectrometer over a range of settings and compares these experimental results with the predictions outlined so far.

3.2.5 Performance of the Nicolet iS50 FTIR spectrometer

Based on the choice of resolution and maximum wavenumber, the Nicolet iS50 FTIR spectrometer automatically adjusts the diameter of the iris located between the source and interferometer to set Ω_{max} based on Eq. (3.25). This sets the value of G_M, which can be calculated based on the iris diameter and $f/\#$ of the source collimation optics. The value of G_d is fixed by the detector area and the $f/\#$ of the detector focusing optics. In regards to the optical system, the iS50 documentation specifies that the source collimation optics and detector focusing optics have $f/\# \approx 2.9$ and $f/\# \approx 0.7$, respectively, which corresponds to solid angles of approximately $\Omega_M = 0.1$ sr and $\Omega_d = 2$ sr,

Table 3.1: Aperture diameter and etendue of Nicolet iS50 spectrometer as a function of resolution for a maximum wavenumber of $\tilde{\nu}_{\max} = 4000\ \mathrm{cm}^{-1}$ and a MCT detector with area $A_d = 0.1 \times 0.1\ \mathrm{cm}^2$.

Resolution $\left(\mathrm{cm}^{-1}\right)$	Aperture Diameter (mm)	G_M $\left(\mathrm{cm}^2\ \mathrm{sr}\right)$	G_d $\left(\mathrm{cm}^2\ \mathrm{sr}\right)$	$\tau_{\mathrm{min,FTIR}}$ $\left(\mathrm{Hz}^{-1/2}\right)$
4	10.6	0.088	0.022	2.0×10^{-6}
2	6.52	0.033	0.022	4.0×10^{-6}
1	4.58	0.017	0.022	1.0×10^{-5}
0.5	3.20	0.008	0.022	4.4×10^{-5}
0.25	2.21	0.004	0.022	1.8×10^{-4}
0.125	1.56	0.002	0.022	7.0×10^{-4}

respectively. Furthermore, the MCT detector element has an area $A_d = 0.1 \times 0.1\ \mathrm{cm}^2$ resulting in $G_d \approx 0.022\ \mathrm{cm}^2\ \mathrm{sr}$ for the detector-limited etendue. Table 3.1 provides information on the iris diameter as a function of resolution assuming a maximum wavenumber of $\tilde{\nu}_{\max} = 4000\ \mathrm{cm}^{-1}$ chosen because we are interested in the mid to far infrared region of the electromagnetic spectrum. We see from Table 3.1 that the Nicolet iS50 has a detector-limited etendue for resolutions $\Delta\tilde{\nu} > 1\ \mathrm{cm}^{-1}$, and an interferometer-limited etendue for $\Delta\tilde{\nu} \leq 1\ \mathrm{cm}^{-1}$. It is instructive at this stage to calculate the detection limit of a typical single beam FTIR spectrum at different resolutions. The following is a list of typical parameter values used to evaluate the detection limit:

- Peak spectral energy density of $U\left(\tilde{\nu}, T\right) \approx 570\,\mu\mathrm{W/sr\,cm^2\,cm^{-1}}$ at $\tilde{\nu} = 2000\ \mathrm{cm}^{-1}$ and $T = 1000\ \mathrm{K}$.
- Optical system efficiency of $\eta = 0.1$ as a conservative estimate.
- Specific detectivity of $D^* = 10^{10}\ \mathrm{cm}\sqrt{\mathrm{Hz}}/\mathrm{W}$ as a lower bound for a typical MCT detector.

The result of this calculation is displayed in the final column of Table 3.1. Clearly, if weak spectral features are of interest, then it is advantageous to take measurements at as low a resolution as possible. However, if high resolution is necessary then multiple interferograms can be averaged to increase the sensitivity as $\sqrt{N}$, where N is the number of interferograms averaged.

In the final portion of this section, we present measurements of the iS50 detection sensitivity for a range of parameters. All of the measurements are performed with a maximum wavenumber

of $\tilde{\nu}_{\max} = 4000$ cm^{-1} and an interferometer mirror velocity of $v = 3.1647$ cm/s. Figure 3.2 shows a typical single beam spectrum acquired by averaging 100 scans at a resolution of $\Delta\tilde{\nu} = 1$ cm^{-1}. There are a number of absorption features present in this spectrum that correspond to atmospheric H_2O between about $3500 - 3900$ cm^{-1} and $1300 - 2100$ cm^{-1}, and atmospheric CO_2 around 2350 cm^{-1}. Additionally, there is a feature between approximately $2850 - 3000$ cm^{-1} that corresponds to hydrocarbons in an epoxy used to mount the vacuum window on the MCT detector. The spectrum peaks around 2200 cm^{-1} and looks like the spectrum of a blackbody for larger wavenumbers. However, the low wavenumber region of the spectrum is cutoff as a result of the increasing absorption of the KBr beamsplitter and the drop off in responsivity of the MCT detector. This results in a low wavenumber cutoff of approximately 650 cm^{-1}.

In order to estimate $\tau_{\min}$ from a single beam spectrum, we take $\delta\bar{P}$ and $\bar{P}$ as the standard deviation and mean, respectively, of the signal amplitude in a small wavenumber range near the peak of the spectrum, but away from any absorption features. This is particularly important for boxcar apodization as the sidelobes introduced by the H_2O absorption lines will seriously degrade $\tau_{\min}$. We then estimate the measurement bandwidth based on the scan time and calculate $\tau_{\min}$ in units of Hz$^{-1/2}$. Figure 3.3 shows a plot of $\tau_{\min}$ as a function of the number of scans averaged as well as the expected $N^{-1/2}$ behavior. These data were acquired at a resolution of $\Delta\tilde{\nu} = 1$ cm^{-1} with boxcar apodization and an energy screen with 10% transmission in place to prevent the MCT detector from saturating. We see that for an average of $10 - 100$ scans that $\tau_{\min}$ follows the expected behavior, but tends towards a minimum value of approximately 5×10^{-5} Hz$^{-1/2}$ after averaging about $N > 1000$ scans. This indicates that other noise sources and system instabilities are present that dominate at larger values of N. Thus, regardless of resolution the system sensitivity appears to be limited to this level, and averaging a larger number of scans is not beneficial. In addition to the ultimate sensitivity, it is important to point out that the sensitivity of roughly 10^{-3} Hz$^{-1/2}$ for $N = 1$ is 100 times larger than the estimated value in Table 3.1. However, the estimated value does not incorporate the energy screen, which reduces the amount of light reaching the detector by a factor of 10, so the difference in sensitivity is really a factor of 10. This discrepancy is most

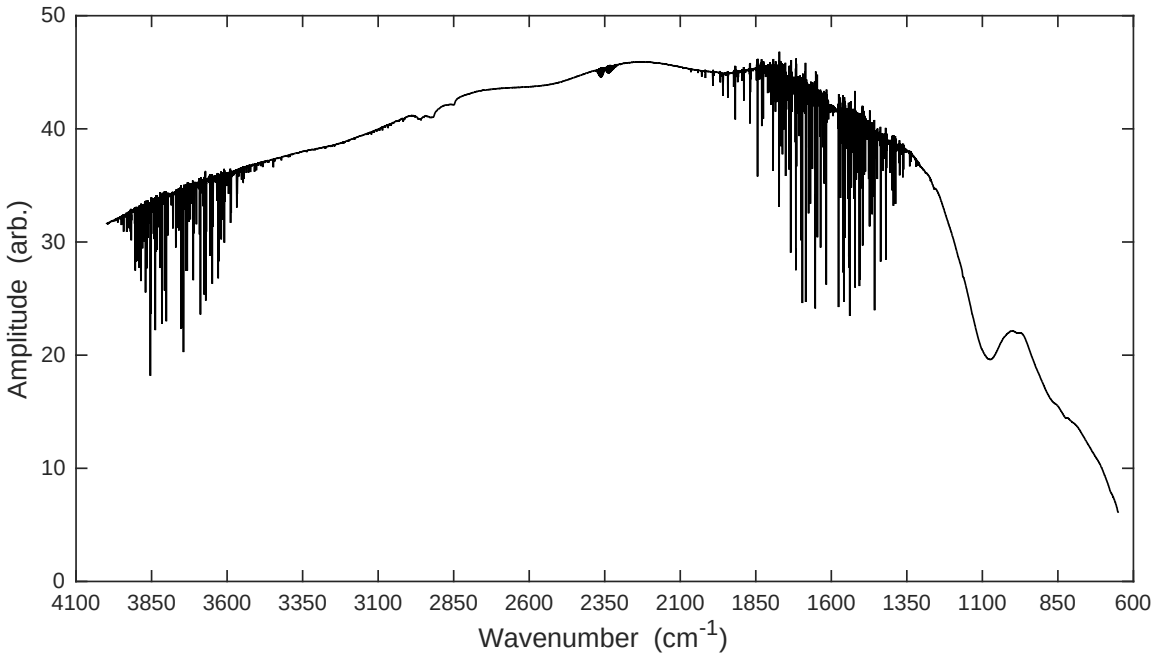

Figure 3.2: Nicolet iS50 single beam spectrum acquired by averaging 100 scans at a resolution of $\Delta\tilde{\nu} = 1$ cm^{-1}. A 10% transmission energy screen was used to prevent the MCT detector from saturating, and boxcar apodization was chosen. Note the absorption features due to atmospheric H_2O between about $3500 - 3900$ cm^{-1} and $1300 - 2100$ cm^{-1}, and atmospheric CO_2 around 2350 cm^{-1}.

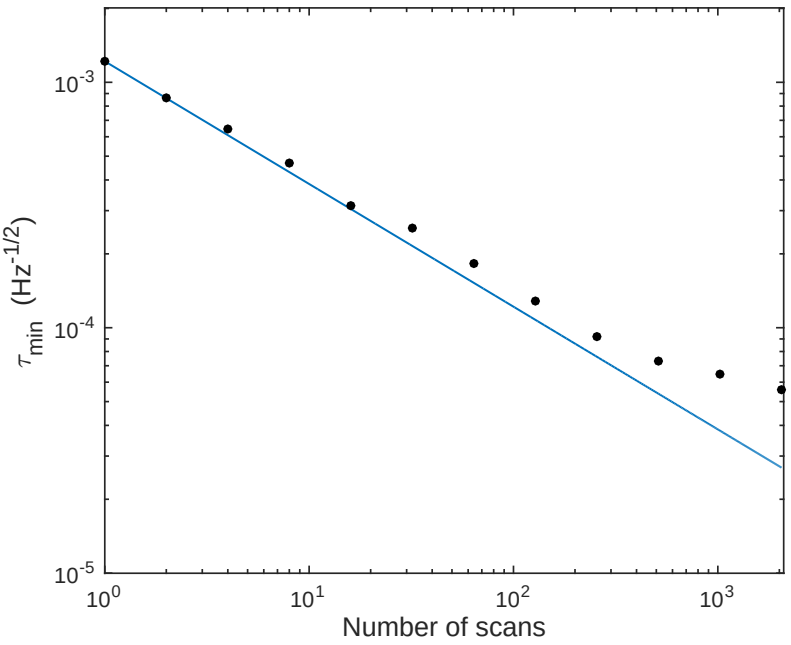

Figure 3.3: Nicolet iS50 FTIR spectrometer sensitivity as a function of the number of scans averaged (black points). The expected behavior is a $N^{-1/2}$ trend plotted as the blue line. The spectrometer resolution was $\Delta\tilde{\nu} = 1$ cm^{-1}, boxcar apodization was used, and an energy screen with 10% transmission was in place to prevent the MCT detector from saturating. The noise floor appears to occur at a sensitivity of approximately 5×10^{-5} Hz$^{-1/2}$ after averaging a few thousand scans.

Table 3.2: Single beam sensitivity of the iS50 spectrometer with boxcar apodization. For $\Delta\tilde{\nu} = 1$ cm^{-1} a 10% transmission energy screen is used to prevent saturation of the MCT detector. All other resolution settings use a 30% transmission energy screen.

Resolution $\left(\text{cm}^{-1}\right)$	$\tau_{\min}$ $\left(\text{Hz}^{-1/2}\right)$ $N = 1$	$\tau_{\min}$ $\left(\text{Hz}^{-1/2}\right)$ $N = 100$
1	1.26×10^{-3}	1.12×10^{-4}
0.5	3.03×10^{-3}	3.06×10^{-4}
0.25	1.23×10^{-2}	1.21×10^{-3}
0.125	3.00×10^{-2}	2.93×10^{-3}

likely due to other factors such as noise from the detector amplifier and quantization noise from the digitization process, which are not included in the simple noise model presented here. Additionally, the choice of boxcar apodization can degrade the noise floor due to the presence of many strong absorption features in the single beam scan. This will be discussed more below.

It is also of interest to investigate the effect of other parameters on the sensitivity of the spectrometer. Table 3.2 gives the sensitivity as a function of the spectrometer resolution setting for an average of $N = 1$ and $N = 100$ scans. The sensitivity of the spectrometer clearly decreases as the resolution increases, where doubling the resolution causes the sensitivity to decrease by a factor of $2 - 4$ as expected from Eq. (3.28). Additionally, averaging $N = 100$ scans improves the sensitivity by about a factor of 10 for all resolutions demonstrating the expected scaling with small N. Another important spectrometer parameter that can affect the sensitivity is the choice of apodization function. Table 3.3 gives the sensitivity as a function of the apodization function for a single scan ($N = 1$). As expected, boxcar apodization gives the worst sensitivity performance in the presence of strong absorption features in the spectrum (e.g., those resulting from atmospheric H_2O), and the Norton-Beer strong function gives the best sensitivity performance. This is a result of the poor sidelobe suppression of boxcar apodization compared to the other functions. However, the Norton-Beer strong function suppresses the peak optical depth of absorption features compared to boxcar apodization as evidenced by the data shown in the third column of Table 3.3. Other apodization functions provide similar tradeoffs between peak optical depth suppression and sensitivity enhancement. Notably, the Happ-Genzel and Norton-Beer strong functions provide the most

Table 3.3: Single beam sensitivity of the iS50 spectrometer, and the peak optical depth and FWHM linewidth of a strong H_2O absorption line at about 1617 cm^{-1} for different apodization functions. The resolution is $\Delta\tilde{\nu} = 1$ cm^{-1} and a 10% transmission energy screen is used to prevent saturation of the MCT detector.

Apodization Function	$\tau_{\min}$ $\left(Hz^{-1/2}\right)$	Peak OD	Linewidth $\left(cm^{-1}\right)$
Boxcar	1.28×10^{-3}	0.608	0.620
Triangular	6.89×10^{-4}	0.283	0.965
Cosine	9.14×10^{-4}	0.371	0.868
Blackman-Harris	6.84×10^{-4}	0.215	1.41
Happ-Genzel	7.61×10^{-4}	0.319	1.01
Norton-Beer Weak	9.11×10^{-4}	0.404	0.810
Norton-Beer Medium	8.16×10^{-4}	0.338	0.946
Norton-Beer Strong	6.38×10^{-4}	0.288	1.06

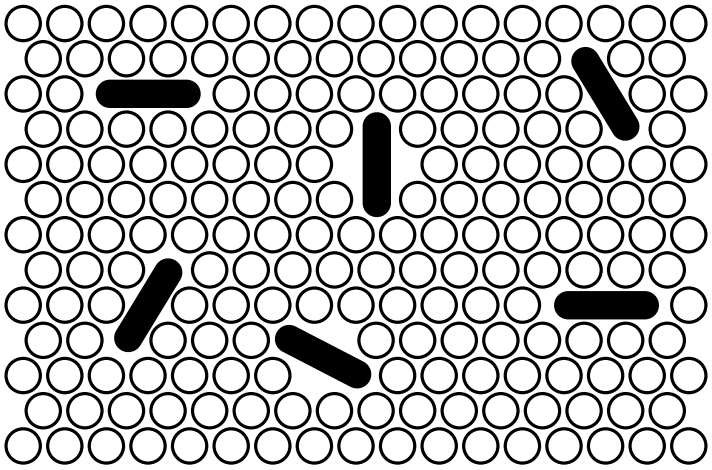

Figure 3.4: A schematic representation of the matrix isolation technique adopted from [82]. The inert gas host (open circles) confines molecules of interest (solid black objects) to vacancies in the crystal lattice. Note that different types of vacancies are possible, which leads to different local environments for the trapped molecules.

accurate representation of the spectrometer resolution setting, good sensitivity, and only moderate peak optical depth suppression. Therefore, they are the recommended apodization functions for most studies.

3.3 Matrix Isolation Spectroscopy

The principle of matrix isolation spectroscopy is to trap molecules of interest inside a solid matrix of an inert host material, and then use a desired spectroscopic technique to probe the trapped molecules. In this way, the trapped molecules cannot diffuse and are prevented from reacting with one another. Perhaps the most common method of matrix isolation is to co-deposit the molecules of interest with an inert gas (e.g., neon) onto an infrared transparent window held at a temperature well below the melting point of the host gas. In fact, the temperature of the window should be held at a temperature well below the point at which diffusion of trapped molecules inside the host matrix becomes appreciable, which is approximately 10 K for neon gas [81]. Figure 3.4 provides a simple depiction of the matrix isolation technique.

As depicted in Fig. 3.4, molecules become trapped in substitutional sites of the host matrix where individual atoms of the host material are replaced by the molecules of interest. These substi-

tutional sites can differ in shape and size, and may even occur near matrix dislocation boundaries resulting in different local environments for the trapped molecules. These environmental perturbations will lead to small frequency shifts of the molecular transitions, and can result in the observation of multiple absorption features for a single transition. In addition to these frequency shifts, the majority of molecules will be rigidly held within the host matrix such that rotational transitions cannot occur.[†] Therefore, one typically observes pure vibrational transitions with matrix isolation spectroscopy, where absorption linewidths of < 1 cm^{-1} are readily observed.

In conjunction with a FTIR spectrometer, matrix isolation is a useful method for obtaining a broadband survey spectrum of a molecular source, and is a simple addition to an apparatus that already employs a cold beam source. In this dissertation work, we use the technique of matrix isolation spectroscopy to characterize the performance of our buffer-gas beam source as well as to optimize the production of a given molecule of interest. This is done by situating a CaF_2 or KBr window below the buffer-gas cooling cell at a 45° angle such that it intersects the molecular beam. By connecting this window to the second stage of the cryocooler, matrix temperatures of about 5 K are readily achieved. A major drawback of matrix isolation spectroscopy is the lack of rotational spectra for most molecules; thus, it is of interest to study molecules in the gas phase after their production has been optimized using FTIR spectroscopy.

3.4 Infrared Laser Absorption Spectroscopy

A key advantage to FTIR spectroscopy is the broadband source and multiplexed acquisition, which makes it possible to simultaneously obtain molecular absorption spectra over thousands of wavenumbers in a few seconds. However, major disadvantages are the low resolution of the spectrometer and low spectral energy density of the source. In the case of the Nicolet iS50 FTIR, the resolution is limited to $\Delta\tilde{\nu} = 0.125$ cm^{-1} or about 3.75 GHz — this is many orders of magnitude larger than the natural linewidth of vibrational and rotational transitions in the infrared, and can

[†] There are certain small molecules which exhibit rotational transitions in matrix isolation spectroscopy, e.g., HCl [83].

make it difficult to fully resolve the rotation-vibration spectrum of many molecules. In addition, the peak spectral energy density of broadband sources used in FTIR spectroscopy is so low that only a few microwatts of power per spectral element can be used to probe molecular transitions. This is in stark contrast to infrared laser sources, which have very high spectral energy density and narrow linewidths on the order of 10 MHz. In addition, tunable infrared laser sources exist that can cover broad spectral windows on the order of $100\,\mathrm{cm}^{-1}$; however, acquisition is not multiplexed such that it can take many hours to cover this spectral window at high resolution.

As an example to compare with the Nicolet iS50 FTIR spectrometer, consider an infrared diode laser operating at $\tilde{\nu} = 2000\ \mathrm{cm}^{-1}$ with 1 mW of output power and a linewidth of 30 MHz or about $0.001\,\mathrm{cm}^{-1}$. Assuming the output of this laser can be focused to a diffraction limited spot size, we find that the spectral energy density is roughly $1\,\mathrm{MW/sr\,cm^2\,cm^{-1}}$, which is roughly ten orders of magnitude larger than the blackbody source used in the FTIR spectrometer. Note, however, that high sensitivity, low-noise detectors used in infrared spectroscopy typically saturate with incident powers of less than 100 µW, and this greatly limits the advantage gained from using a source with extremely high spectral energy density like a laser. Nonetheless, the narrow linewidth, wide tunability, and excellent spectral selectivity of diode laser sources offer substantial benefits for high-resolution spectroscopy. In addition, commercial diode lasers are practically turn-key systems with a relatively low degree of complexity making them very straightforward to operate. Before proceeding, it is worth mentioning here that frequency comb sources offer the best of both worlds as they are broadband, and have high spectral energy density and narrow linewidth [11, 13]. However, frequency combs are still a developing technology and are not commercially available for the infrared region of the spectrum that we are currently interested in.

3.4.1 Quantum cascade lasers

Standard diode lasers rely on carrier recombination across a bandgap (i.e., interband transitions) inside a semiconductor active region where the bandgap energy dictates the wavelength of laser operation. This principle works exceptionally well in the visible to near-infrared region of the

electromagnetic spectrum, but becomes problematic when applied in the mid- to far-infrared. As the photon energy decreases the bandgap of the active region also decreases and laser operation becomes prohibitively sensitive to temperature fluctuations. Additionally, it becomes difficult to fabricate high quality (i.e., free of defects) semiconductor devices with small bandgaps resulting in poor reliability [84]. These problems eventually led to the development of quantum cascade lasers (QCLs) at Bell Labs in 1994 [85].

QCLs rely on a completely different mechanism of operation that involves electrons transitioning between discrete energy levels in a quantum well (i.e., intersubband transitions) where the energy level spacing dictates the wavelength of laser operation. This is in contrast to interband transitions in a semiconductor material because electrons transitioning to a lower energy level in a quantum well through release of a photon remain in the conduction band allowing the electrons to tunnel into subsequent quantum well regions and emit more photons. This results in a cascade effect, which makes larger quantum efficiencies possible compared to traditional semiconductor laser diodes. Thus, by patterning many quantum wells on a single device, laser operation at larger output powers than semiconductor laser diodes can be achieved. Furthermore, by patterning quantum wells with different energy level spacings, a single device can be created that provides gain over a spectral range of hundreds of wavenumbers. High spectral selectivity and mode-hop free tunability can then be achieved through standard diode laser methods such as distributed feedback or an external cavity in conjunction with temperature and injection current tuning. Good reviews on QCL technology and their applications to spectroscopy can be found in Refs. [84, 86, 87].

The QCL used in this dissertation work is a Daylight Solutions CW-MHF system (model 21095) that provides about 100 mW of continuous wave power and continuous, mode-hop free tuning from $1020 - 1115$ cm^{-1}. The MHF series of QCLs are external cavity lasers with grating feedback in a modified Littrow configuration that prevents beam pointing deviation as the laser is tuned. The specified linewidth is less than 30 MHz, and tuning can be achieved by changing the laser temperature, rotating the grating via a PZT element (DC $-$ 100 Hz bandwidth), or changing the laser injection current (10 kHz $-$ 2 MHz bandwidth). This QCL is used for studying cold beams

of molecules in the gas phase, and its narrow linewidth and broad tuning range allow for high resolution ro-vibrational spectroscopy in the mid-infrared region of the electromagnetic spectrum.

As discussed in section 3.1.3, shot noise sets a fundamental limit on the minimum detectable optical depth in an absorption spectroscopy experiment. However, laser sources are plagued by excess intensity noise due to spontaneous emission, thermal fluctuations, acoustic vibrations, and current noise from the injection current source. Therefore, special techniques must be employed to achieve shot noise limited measurements, and, in principle, there are three common methods to minimize excess intensity noise: (1) active noise reduction through feedback stabilization of the laser intensity, (2) use of a modulation scheme to encode the absorption signal of interest onto a frequency band where the intensity noise is negligible, and (3) direct cancellation of the laser intensity noise via balanced subtraction of a signal and reference beam derived from the same laser. The first of these methods is impractical in the mid- to far-infrared region of the electromagnetic spectrum due to the lack, or huge expense of available devices like acousto- and electro-optic modulators. The other two methods, however, are of interest and will be discussed further below.

3.4.2 Wavelength modulation

The simplest and perhaps most commonly used modulation technique for diode lasers is direct modulation of the injection current, which results in a frequency modulation of the laser output. The subsequent interaction of the frequency modulated laser light with an absorbing species results in modulation of the laser intensity at the modulation frequency and its harmonics, from which absorption data can be retrieved via a detector and lock-in amplifier. In regards to spectroscopy, this technique is broadly classified into two categories depending on whether the modulation frequency is much greater or much less than the spectral width of the absorption feature being probed. The former is the case of frequency modulation spectroscopy (FMS) [88], which is typically implemented with modulation frequencies of 100 MHz to 1 GHz. The latter is the case of wavelength modulation spectroscopy (WMS), which is typically implemented with modulation frequencies of 100 kHz or less. Notably, QCLs can be effectively modulated via their injection current up to frequencies of only

about 1 MHz as a result of thermal effects being the dominant frequency modulation mechanism [89]. Therefore, the FMS technique is not applicable and only the WMS technique will be discussed here.

Application of a sinusoidal modulation to the QCL injection current results in modulation of the laser wavenumber according to

$$\tilde{\nu}\left(t\right) = \tilde{\nu}_c + \tilde{\nu}_a \cos\left(2\pi f_m t\right), \tag{3.29}$$

where $\tilde{\nu}_c$ is the center laser wavenumber, $\tilde{\nu}_a$ is the modulation amplitude, and f_m is the modulation frequency. In addition to this frequency modulation, the output intensity of the QCL will be modulated as a consequence of modulating the injection current. This effect is known as residual amplitude modulation (RAM), and results in spurious signals at the modulation frequency and its harmonics even in the absence of an absorbing species. This is a well documented effect in WMS, and limits the ultimate sensitivity of the technique. We write the modulated laser intensity as follows:

$$I_0\left(\tilde{\nu}_c, \tilde{\nu}_a, t\right) = \bar{I}_0\left(\tilde{\nu}_c\right)\left[1 + \sum_{n=1}^{\infty} \kappa_n\left(\tilde{\nu}\right)\tilde{\nu}_a^n \cos\left(2\pi n f_m t + \phi_n\right)\right], \tag{3.30}$$

where $\bar{I}_0\left(\tilde{\nu}_c\right)$ is the average laser intensity at the center wavenumber, the $\kappa_n\left(\tilde{\nu}\right)$ represent the wavenumber dependent intensity modulation coefficients, and the ϕ_n represent phase shifts between the frequency and intensity modulations. Depending on the modulation depth, terms up to $n = 4$ may need to be included to accurately describe RAM for QCLs [90]. Furthermore, QCLs exhibit significantly larger linear and nonlinear RAM signals compared to diode lasers used in the near-infrared [90, 91].

Given that both the modulated laser wavenumber and intensity are periodic signals in time, the detected signal will also be periodic in time. Thus, Fourier decomposition is a useful method for mathematically representing the generation and detection of the harmonic components of the absorption and background signals in an absorption spectroscopy experiment. Both Kluczynski and Axner [92] and Schilt et al. [93] have developed rigorous theoretical descriptions of the wavelength modulation process, so we only give the highlights here. Following the method of Kluczynski and

Axner [92], we define the detected signal $S(\tilde{\nu})$ in terms of background and absorption signals as

$$S_{\mathrm{BG}} = \beta T(\tilde{\nu}) I_0(\tilde{\nu}) = \beta I(\tilde{\nu}), \tag{3.31}$$

$$S_{\mathrm{A}} = -\beta \alpha_0 \chi(\tilde{\nu}) T(\tilde{\nu}) I_0(\tilde{\nu}) = -\beta \alpha_0 \chi(\tilde{\nu}) I(\tilde{\nu}), \tag{3.32}$$

where β is a detector gain factor, $T(\tilde{\nu})$ represents the wavenumber dependent transmission of the optical system, $I_0(\tilde{\nu})$ is the output intensity of the laser, $I(\tilde{\nu})$ is the intensity seen by the detector in the absence of an absorbing species, α_0 is the peak absorbance, and $\chi(\tilde{\nu})$ is a peak-normalized absorption lineshape function. Using a lock-in amplifier, the kth harmonic of the detector signal can be extracted, which is written in terms of even and odd Fourier components of the lineshape function and detected intensity as

$$S^e_{\mathrm{BG},k}(\tilde{\nu}_c, \tilde{\nu}_a) = \beta I^e_k(\tilde{\nu}_c, \tilde{\nu}_a), \tag{3.33}$$

$$S^o_{\mathrm{BG},k}(\tilde{\nu}_c, \tilde{\nu}_a) = \beta I^o_k(\tilde{\nu}_c, \tilde{\nu}_a), \tag{3.34}$$

$$\begin{aligned} S^e_{\mathrm{A},k}(\tilde{\nu}_c, \tilde{\nu}_a) = -\beta\alpha_0 \Bigg[& \frac{1+\delta_{k,0}}{2} \sum_{m=0}^{k} \chi^e_{k-m}(\tilde{\nu}_c, \tilde{\nu}_a) I^e_m(\tilde{\nu}_c, \tilde{\nu}_a) \\ & + \frac{2-\delta_{k,0}}{4} \sum_{m=0}^{\infty} \chi^e_{k+m}(\tilde{\nu}_c, \tilde{\nu}_a) I^e_m(\tilde{\nu}_c, \tilde{\nu}_a) \\ & + \frac{2-\delta_{k,0}}{4} \sum_{m=0}^{\infty} \chi^e_m(\tilde{\nu}_c, \tilde{\nu}_a) I^e_{k+m}(\tilde{\nu}_c, \tilde{\nu}_a) \Bigg], \end{aligned} \tag{3.35}$$

$$\begin{aligned} S^o_{\mathrm{A},k}(\tilde{\nu}_c, \tilde{\nu}_a) = -\beta\alpha_0 \Bigg[& \frac{1}{2} \sum_{m=0}^{k} \chi^e_{k-m}(\tilde{\nu}_c, \tilde{\nu}_a) I^o_m(\tilde{\nu}_c, \tilde{\nu}_a) \\ & - \frac{1}{2} \sum_{m=0}^{\infty} \chi^e_{k+m}(\tilde{\nu}_c, \tilde{\nu}_a) I^o_m(\tilde{\nu}_c, \tilde{\nu}_a) \\ & + \frac{1}{2} \sum_{m=0}^{\infty} \chi^e_m(\tilde{\nu}_c, \tilde{\nu}_a) I^e_{k+m}(\tilde{\nu}_c, \tilde{\nu}_a) \Bigg]. \end{aligned} \tag{3.36}$$

In the above equations, the superscripts represent the even (e) and odd (o) Fourier components of the various quantities and the subscripts correspond to the different harmonics, and $\delta_{k,0}$ is the Kronecker delta function. Because the detected intensity passes through an optical system with a

wavenumber dependent transmission function, we express the Fourier components of $I\left(\tilde{\nu}_c, \tilde{\nu}_a\right)$ in terms of the output intensity of the laser as

$$I_k^e\left(\tilde{\nu}_c, \tilde{\nu}_a\right) = -\beta\alpha_0 \left[\frac{1+\delta_{k,0}}{2} \sum_{m=0}^{k} T_{k-m}^e\left(\tilde{\nu}_c, \tilde{\nu}_a\right) I_{0,m}^e\left(\tilde{\nu}_c, \tilde{\nu}_a\right) + \frac{2-\delta_{k,0}}{4} \sum_{m=0}^{\infty} T_{k+m}^e\left(\tilde{\nu}_c, \tilde{\nu}_a\right) I_{0,m}^e\left(\tilde{\nu}_c, \tilde{\nu}_a\right) + \frac{2-\delta_{k,0}}{4} \sum_{m=0}^{\infty} T_{m}^e\left(\tilde{\nu}_c, \tilde{\nu}_a\right) I_{0,k+m}^e\left(\tilde{\nu}_c, \tilde{\nu}_a\right) \right], \tag{3.37}$$

$$I_k^o\left(\tilde{\nu}_c, \tilde{\nu}_a\right) = -\beta\alpha_0 \left[\frac{1}{2} \sum_{m=0}^{k} T_{k-m}^e\left(\tilde{\nu}_c, \tilde{\nu}_a\right) I_{0,m}^o\left(\tilde{\nu}_c, \tilde{\nu}_a\right) - \frac{1}{2} \sum_{m=0}^{\infty} T_{k+m}^e\left(\tilde{\nu}_c, \tilde{\nu}_a\right) I_{0,m}^o\left(\tilde{\nu}_c, \tilde{\nu}_a\right) + \frac{1}{2} \sum_{m=0}^{\infty} T_{m}^e\left(\tilde{\nu}_c, \tilde{\nu}_a\right) I_{0,k+m}^e\left(\tilde{\nu}_c, \tilde{\nu}_a\right) \right]. \tag{3.38}$$

Notably, only the even Fourier components of $\chi\left(\tilde{\nu}_c, \tilde{\nu}_a\right)$ and $T\left(\tilde{\nu}_c, \tilde{\nu}_a\right)$ are considered because the values of these functions follow the modulation with no phase delay (i.e., only the cosine components are non-zero). Thus, once we define a mathematical form for the $\chi\left(\tilde{\nu}_c, \tilde{\nu}_a\right)$ and $T\left(\tilde{\nu}_c, \tilde{\nu}_a\right)$, and substitute the Fourier components of Eq. (3.30) for $I_0\left(\tilde{\nu}_c, \tilde{\nu}_a\right)$, we have a closed form description of the WMS method. Assuming a Lorentzian absorption lineshape, we can the result derived by Arndt [94] to define the Fourier components of $\chi\left(\tilde{\nu}_c, \tilde{\nu}_a\right)$. Additionally, if we wish to investigate the effects of unwanted etalons in the optical system (i.e., as a result of reflections from uncoated optical surfaces) we treat $T\left(\tilde{\nu}_c, \tilde{\nu}_a\right)$ as a low finesse Fabry-Perot cavity; otherwise, we can set $T_0^e = 1$ and $T_n^e = 0$ for all $n > 0$.

With a theoretical description of WMS in hand, it is advantageous to investigate the expected absorption signals in the presence of RAM and unwanted etalons in the optical system. For this analysis, we will consider both $1f$ and $2f$ detection corresponding to the first and second harmonic, respectively, of the detector signal. Furthermore, we will assume that the absorption lineshape is a Lorentzian with a width limited by the laser linewidth at $\Gamma_L = 30$ MHz. Finally, the modulation index, defined as the ratio of modulation amplitude to the half-width at half-maximum absorption

linewidth, is chosen to be 2.0 for $1f$ detection and 2.2 for $2f$ detection, which corresponds to the maximum achievable signal in each case [95]. Figure 3.5 shows the expected signals at the output of a lock-in amplifier for a peak absorbance of $\alpha_0 = 10^{-6}$ and the assumption of pure frequency modulation. In the absence of RAM and etalon effects, we observe signals that resemble the first and second derivative of the absorption lineshape for $1f$ and $2f$ detection, respectively. Notably, the signal amplitude is reduced compared to the expected value of 10^{-6} for direct absorption. This is a result of the signal power not being completely concentrated in the sidebands of interest, but instead spread over many sidebands. Thus, the signal amplitude will be largest for $1f$ detection and decrease monotonically for schemes that detect higher harmonics of the modulation frequency. However, higher harmonics are less sensitive to RAM and etalon effects such that $2f$ detection is the most common scheme used for WMS. This is apparent in Fig. 3.6, which shows the effect of RAM on the signals of Fig. 3.5. Here, we use the results of Ref. [90] to include the effects of non-zero $\kappa_n(\tilde{\nu})$. Clearly, the $1f$ signal becomes completely obscured by the large RAM background showing the total loss of absorption sensitivity. The $2f$ signal also resides on a non-zero RAM background, but due to the substantially smaller value of κ_2 compared to κ_1 the effect is less detrimental. Nonetheless, $2f$ detection also experiences a loss of sensitivity. Finally, we look at the effect of unwanted etalons in the optical system. We model the etalon as a Fabry-Perot cavity formed by two uncoated, plane-parallel KBr windows (i.e., vacuum chamber windows), which result in a finesse of approximately 0.17. Figure 3.7 shows the expected signals at the output of a lock-in amplifier when frequency modulation, RAM, and etalon effects are all included. With the addition of etalon effects, the $1f$ signal remains completely obscured while the $2f$ signal experiences further degradation. Although the $2f$ signal is still discernible, it has lost much of its second derivative character making it difficult to recognize.

In principle, detecting at higher harmonics of the modulation frequency will minimize the deleterious effects of RAM and etalons. However, the signal strength also decreases for higher harmonics such that the overall sensitivity of an absorption measurement goes down. Therefore, it is useful to consider other methods of dealing with excess laser intensity noise when attempting to

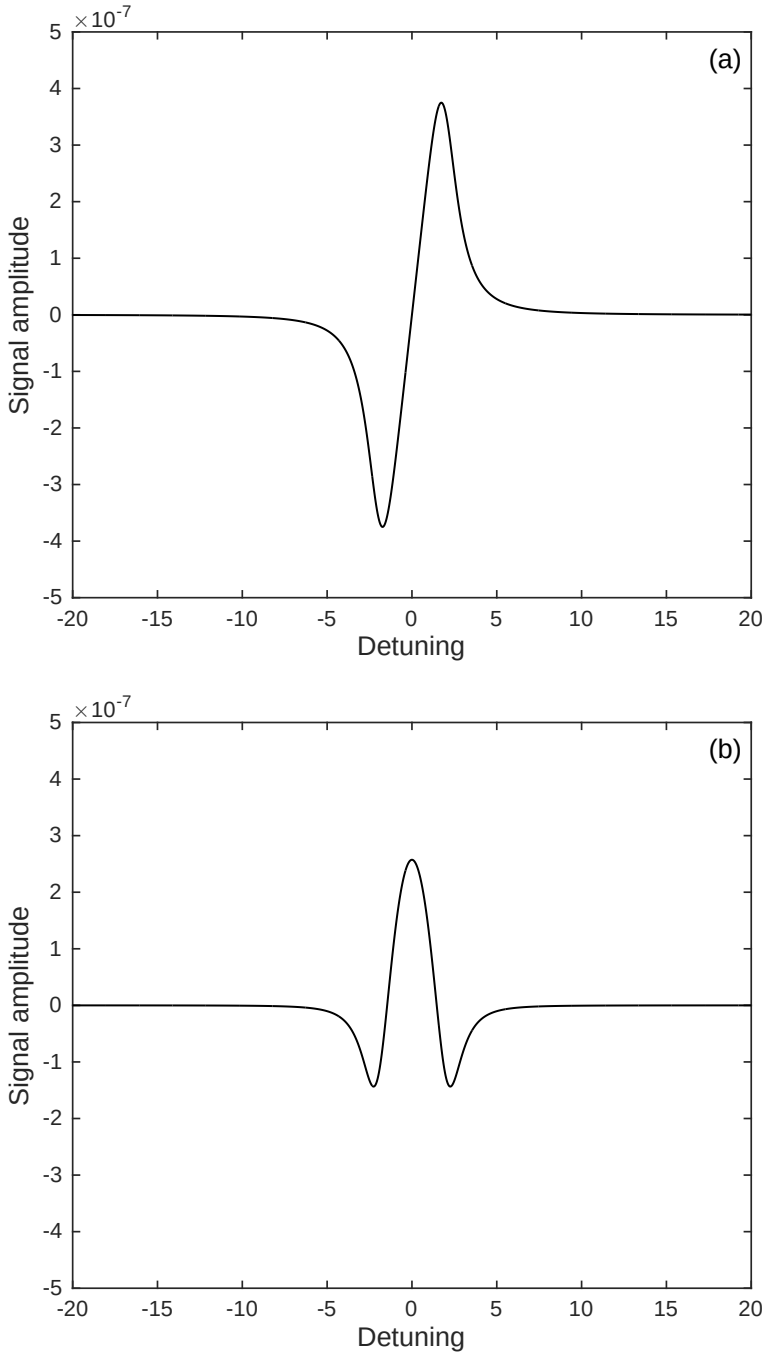

Figure 3.5: (a) $1f$ and (b) $2f$ detection of WMS signals from a Lorentzian absorption line with $\alpha_0 = 10^{-6}$. These signals represent the case of pure frequency modulation such that $\kappa_n(\tilde{\nu}) = 0$ for all n. Additionally, it is assumed that there are no unwanted etalons in the optical system such that $T_0^e = 1$ and $T_n^e = 0$ for all $n > 0$.

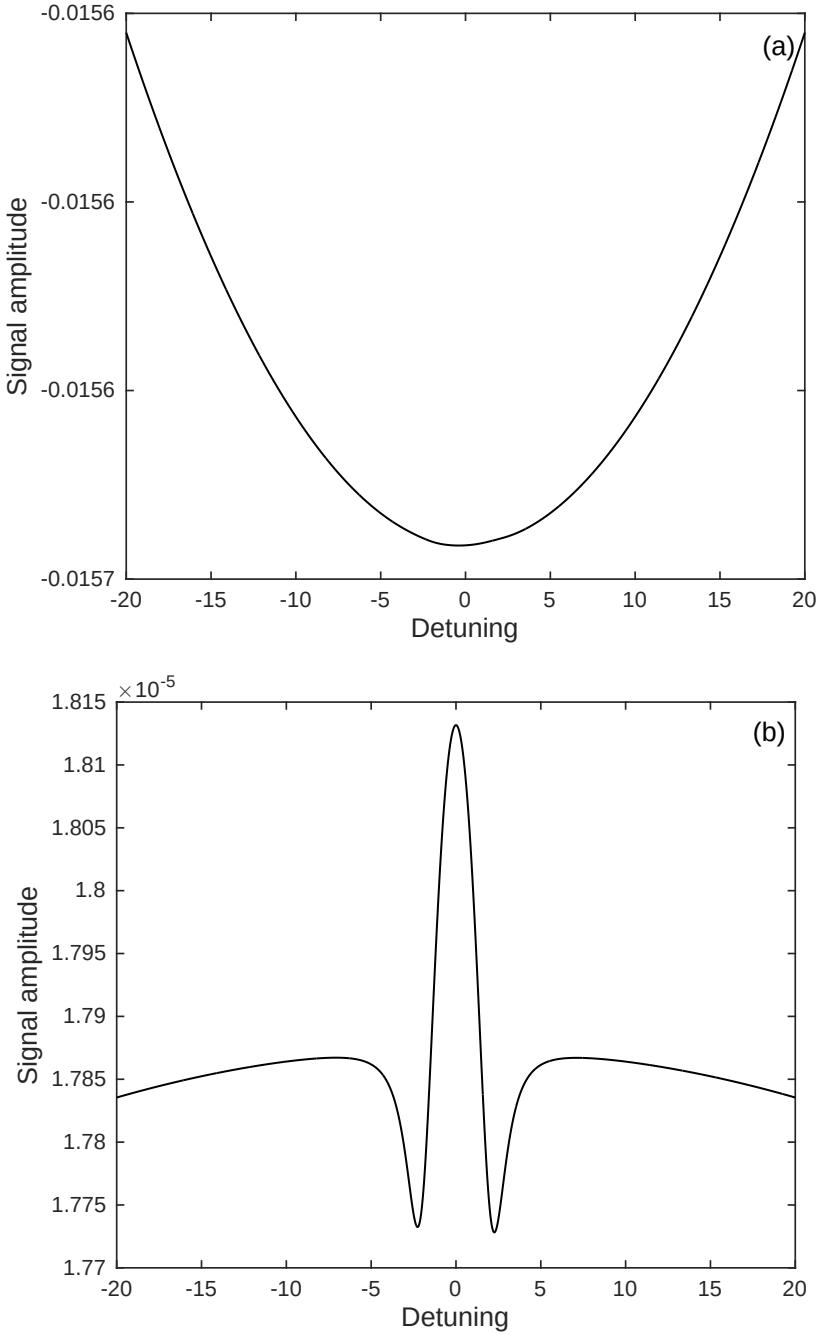

Figure 3.6: (a) $1f$ and (b) $2f$ detection of WMS signals from a Lorentzian absorption line with $\alpha_0 = 10^{-6}$. These signals represent the case of frequency modulation in the presence of RAM, where we have used average values of $\kappa_1 = 1.8 \times 10^{-10}$ Hz^{-1}, $\kappa_2 = 1.1 \times 10^{-20}$ Hz^{-2}, $\phi_1 = 1.08\pi$, and $\phi_2 = 1.58\pi$ based on data from Ref. [90]. Additionally, it is assumed that there are no unwanted etalons in the optical system such that $T_0^e = 1$ and $T_n^e = 0$ for all $n > 0$.

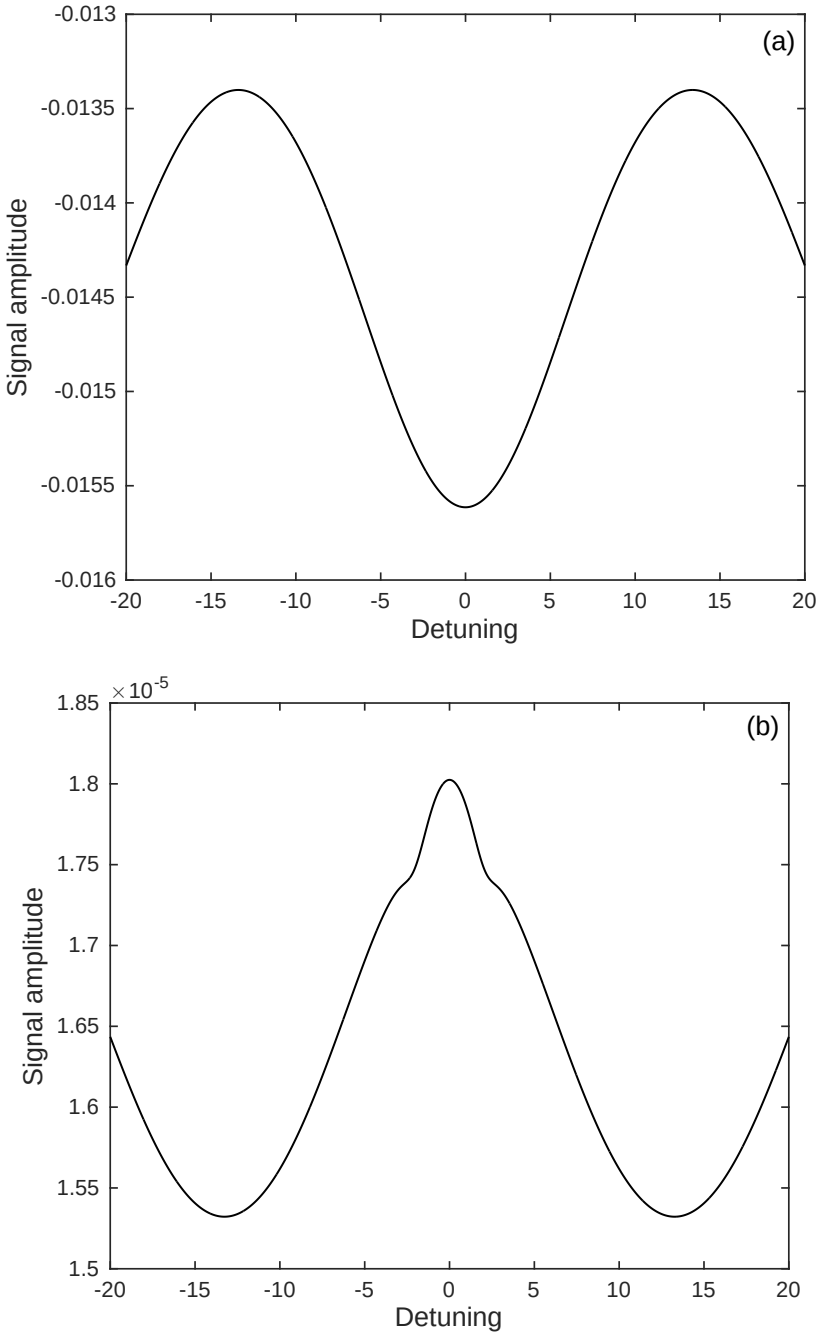

Figure 3.7: (a) $1f$ and (b) $2f$ detection of WMS signals from a Lorentzian absorption line with $\alpha_0 = 10^{-6}$. These signals represent the case of frequency modulation in the presence of RAM, where we have used average values of $\kappa_1 = 1.8 \times 10^{-10}$ Hz^{-1}, $\kappa_2 = 1.1 \times 10^{-20}$ Hz^{-2}, $\phi_1 = 1.08\pi$, and $\phi_2 = 1.58\pi$ based on data from Ref. [90]. Additionally, a Fabry-Perot etalon with finesse of about 0.17 is included to model the effect of uncoated, plane-parallel KBr windows on the vacuum chamber.

achieve shot-noise limited performance in an absorption spectroscopy experiment.

3.4.3 Balanced subtraction

The balanced subtraction technique is the principle used in differential absorption spectroscopy, where the output of the laser is split into a signal and reference beam. The signal beam interacts with the absorbing species of interest before being passed to a detector while the reference beam is passed directly to a separate detector. By subtracting the resulting detector signals it is possible to completely eliminate any correlated excess noise present in the measurement. However, to achieve shot-noise limited sensitivity, the two signals must be balanced to a high degree of precision prior to subtraction. For example, to achieve 40 dB of noise subtraction over the full measurement bandwidth the two signals must be balanced to a part in 10^2, or 1% over that same bandwidth. This is challenging to do optically, but straightforward to do electronically.

In the early 1990's, Philip Hobbs at the IBM Thomas J. Watson Research Center developed a novel electronic noise cancellation circuit for differential absorption spectroscopy measurements [96, 97]. The basic principle of the circuit is to employ negative feedback to automatically adjust the reference detector signal to achieve near perfect subtraction of the signal and reference detector signals at DC. As long as the intensity noise in the signal and reference beams remains correlated, subtraction at DC effectively cancels the excess intensity noise at all frequencies because this noise is directly proportional to the average, or DC intensity. A monograph by Hobbs [98] provides a detailed discussion of this circuit along with its limitations and some variations that are useful for different measurement setups. Notably, use of this circuit can readily achieve shot-noise limited absorption sensitivity.

In this dissertation work, we employ an auto-balanced subtractor circuit based on the principle developed by Hobbs. This circuit was developed by Terry Brown from the JILA electronics shop, and was designed for use with infrared detectors. Figure 3.8 provides the schematic for this circuit. The input stages allow for adjustable gain and offset trimming of both the signal and reference channels, and the feedback bandwidth can be adjusted based on the integrator time constant.

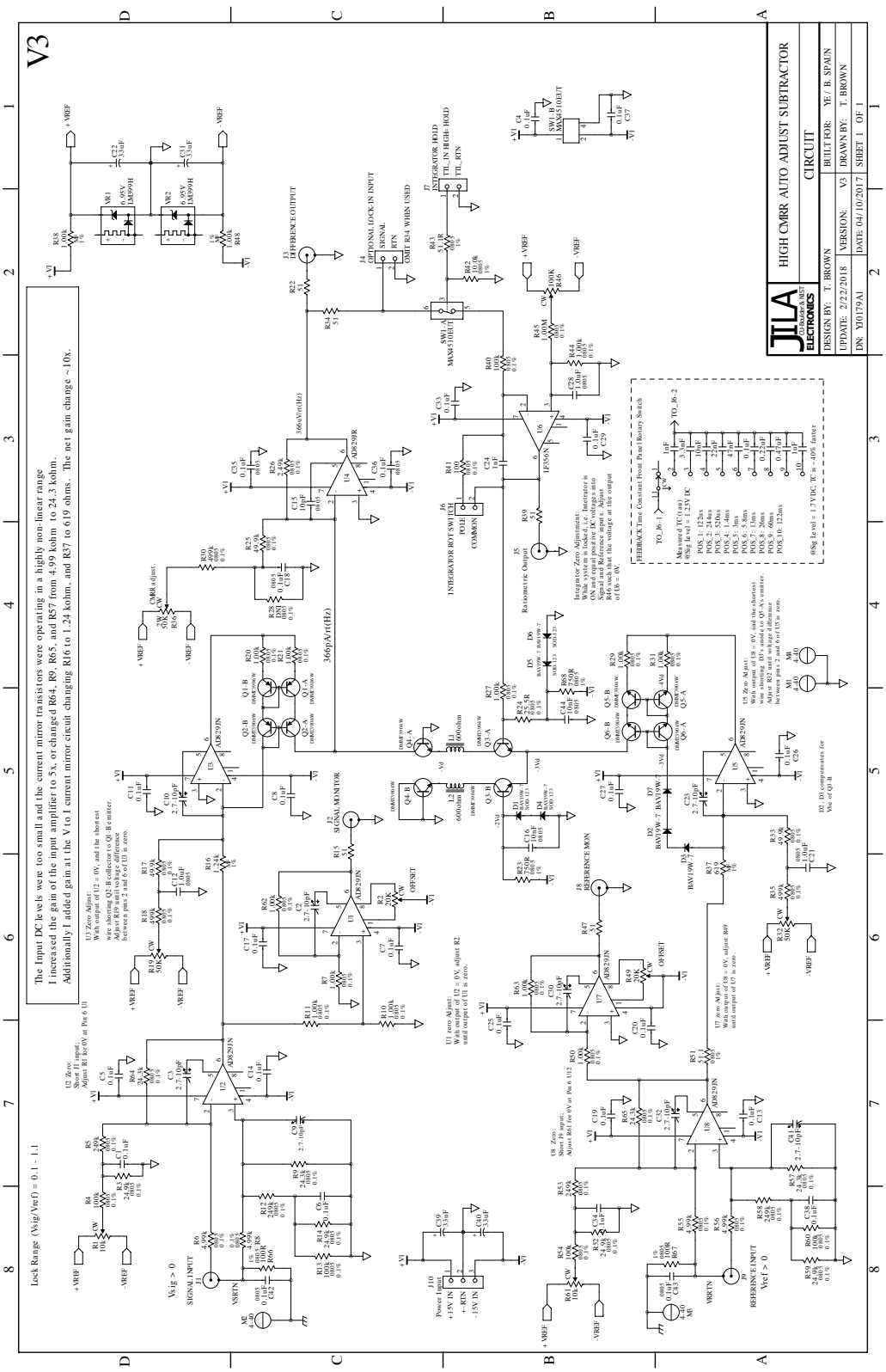

Figure 3.8: Schematic of the high CMRR auto-balanced subtractor circuit.

Additionally, either the subtracted output or the ratiometric output can be used. The former is a high-pass filtered version of the balanced difference between the signal and reference channels while the latter is a low-pass filtered version of the balanced difference divided by the signal channel. The corner frequency of these filters are set by the integrator. Bench tests of the circuit demonstrate greater than 60 dB of common-mode rejection at frequencies in excess of 100 kHz. The circuit is setup in such a way that it can be used for either direct absorption spectroscopy measurements at DC or for WMS measurements using a lock-in detection scheme. For the direct absorption spectroscopy case, it is crucial to eliminate DC offsets on the signal and reference detectors as well as to prevent any unwanted intensity modulation on either beam, which can result from poor focusing of the beams onto the detector elements or beam clipping elsewhere in the optical setup. For WMS measurements these factors are less crucial as long as the unwanted intensity modulation is not at the modulation frequency or its harmonics.

3.4.4 Detectors

In order for the balanced subtraction technique to work for direct absorption spectroscopy, the detectors used must have low noise down to DC. This precludes the use of PC detectors because they exhibit large $1/f$ noise characteristics. Instead, photovoltaic (PV) detectors are preferred, and PV MCT detectors from Kolmar Technologies are some of the best on the market with a characteristic D^* on the order of 10^{11} Jones at 50 kHz and extremely low noise transimpedance amplifiers. We use two such detectors from Kolmar (model KLD-0.5-J1/DC/10) with a detector area of $A_d = 0.05 \times 0.05$ cm^2, bandwidth of DC-1 MHz, responsivity of greater than 5×10^5 V/W,[‡] a cutoff wavlength above 10 µm or 1000 cm^{-1}, and field of view of 15°. Figure 3.9 shows the dark noise spectrum for both of these detectors, where the vertical axis has been converted into current noise density using the specified transimpedance of the detector amplifier. Given the white noise floor of approximately 3 pA/Hz$^{-1/2}$ above 10 kHz, these detectors exhibit a NEP of about

[‡] The responsivity of the MCT element is in the range of $4 - 6$ A/W, and the transimpedance amplifier has a gain of 10^5 V/A.

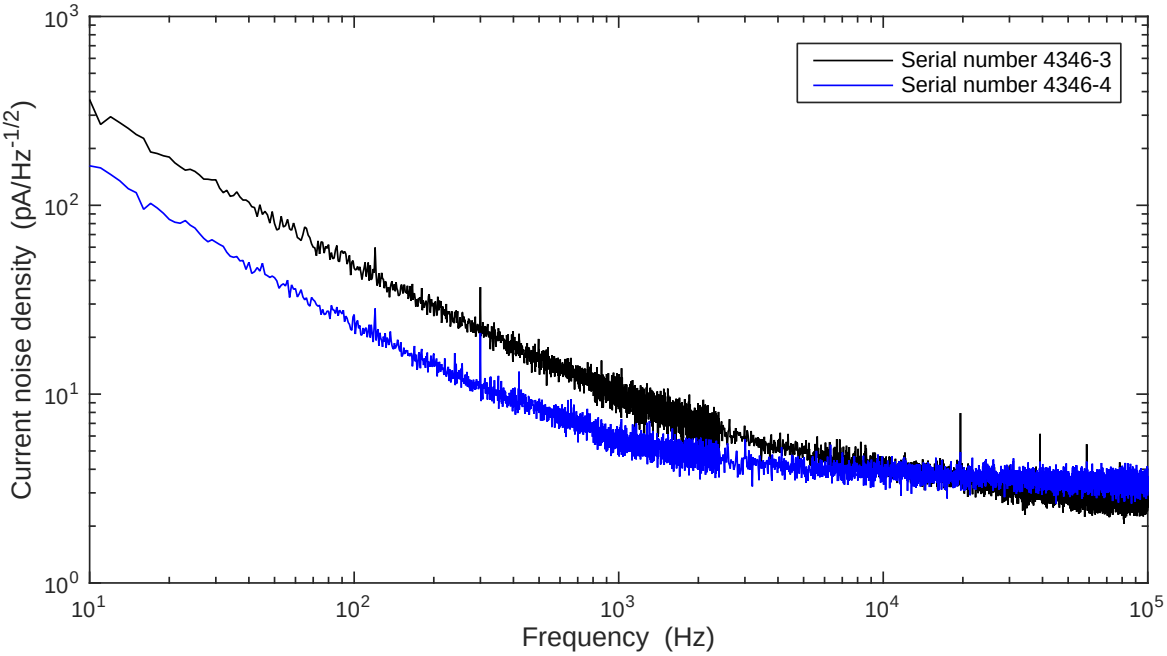

Figure 3.9: Current noise density of the PV MCT detectors from Kolmar Technologies measured with an SR780 FFT spectrum analyzer. The white noise floor above 10 kHz is equivalent to a NEP of about 0.6 pW/Hz$^{-1/2}$ or $D^* \sim 10^{11}$ Jones assuming a responsivity of 5 A/W.

$0.6\,\mathrm{pW/Hz^{-1/2}}$ or $D^* \sim 10^{11}$ Jones assuming a responsivity of 5 A/W. Plugging the detector parameters into Eq. (3.16), we find a detection limit of approximately 10^{-7} $\mathrm{Hz^{-1/2}}$ for an incident power of about 10 µW. Notably, this noise floor occurs at frequencies above 10 kHz such that a combination of WMS and balanced subtraction will be required to reach the ultimate detection sensitivity. Unfortunately, the $1/f$ noise appears to be less than optimal on these detectors, which could be a result of the high transimpedance gain or detector degradation.[§]

The MCT detectors used here likely have far too large of a transimpedance gain (10^5 V/A), which greatly limits the amount of optical power that can be used – at 5×10^5 V/W the transimpedance amplifier will saturate at about 20 µW (about 10 V amplifier output for ±12 V rails). Furthermore, considering the typical series resistance of the MCT element at liquid nitrogen temperature to be $5 - 10\ \Omega$, and a typical bias voltage to be 100 mV, we expect linear operation for incident powers greater than 1 mW. Therefore, a more reasonable transimpedance would be $< 10^4$ V/A, which would greatly improve our shot-noise limited sensitivity. However, it may be better to work with a lower bias voltage to minimize $1/f$ noise if DC balanced detection is the method of choice.

An important note about the MCT detectors is their sensitivity to room temperature blackbody radiation. From Wien's displacement law ($\lambda_p \approx 3000$ µm K), we find that the room temperature ($T \sim 300$ K) blackbody spectrum peaks at a wavelength of approximately 10 µm, which is precisely where the responsivity of the MCT detectors peak. Therefore, small changes in the temperature of the area surrounding the detectors can cause large DC offsets, which are detrimental to the functionality of the auto-balanced subtraction circuit. It is necessary to shield the spectroscopy setup from background blackbody radiation (e.g., warm bodies moving around the room) and frequently check the DC offsets on each detector to ensure that the local environment has not changed.

[§] We have borrowed these detectors from the Nesbitt group in JILA, and they were manufactured in 2011.

3.4.5 Performance of the laser absorption spectroscopy system

Here, we discuss the performance of the laser absorption spectroscopy system, and investigate both the balanced subtraction and wavelength modulation techniques to maximize the absorption sensitivity of the setup. Due to the low optical powers required to avoid saturating the detectors, we use crossed wire grid polarizers with an extinction ratio of $> 10^4$ at 1060 cm^{-1} or 9.4 µm. Furthermore, we focus the laser onto the detectors using anti-reflection coated, ZnSe plano-convex lenses with a focal length of 20 mm. Figure 3.10 shows the excess noise present on the QCL used in this dissertation work. As can be seen in the figure, the noise is dominated by the detector up to about 100 Hz, at which point the QCL noise begins to dominate. The broad feature around $200 - 250$ Hz is due to a mechanical resonance of the QCL laser cavity, which is most likely related to mounting of the feedback grating. The majority of the other noise spikes up to a few kHz appear to be feedthrough of power line harmonics (e.g., harmonics of 60 Hz), and the large spike near 30 kHz is likely from a switching power supply used in the QCL laser controller. At the time of this measurement, a function generator and PZT driver were connected to the modulation inputs on the QCL laser head; therefore, it is possible that the power line noise is a result of ground loops. Besides the noise spikes, the noise floor from about $0.5 - 5$ kHz is about $2 - 3$ times larger than the detector noise floor. This is far too low for the auto-balanced subtraction circuit to be useful, because, at best, it can achieve a noise floor that is the quadrature sum of the detector noise floors. Looking at Fig. 3.9, we see that this quadrature sum will be larger than the low frequency noise of the laser itself. Indeed, attempts to use the auto-balanced subtractor resulted in a higher noise floor than without it, and the circuit appeared to do very little for the many spikes present in the noise spectrum. Therefore, we conclude that auto-balanced subtraction is not beneficial for direct absorption spectroscopy measurements with the current setup.

It is of interest, then, to investigate the sensitivity we can achieve with a single detector. For the measurements presented here we use approximately 15 µW of laser power, which corresponds to a DC output voltage of 8 V from the detector. Furthermore, we connect a 10 kHz low pass

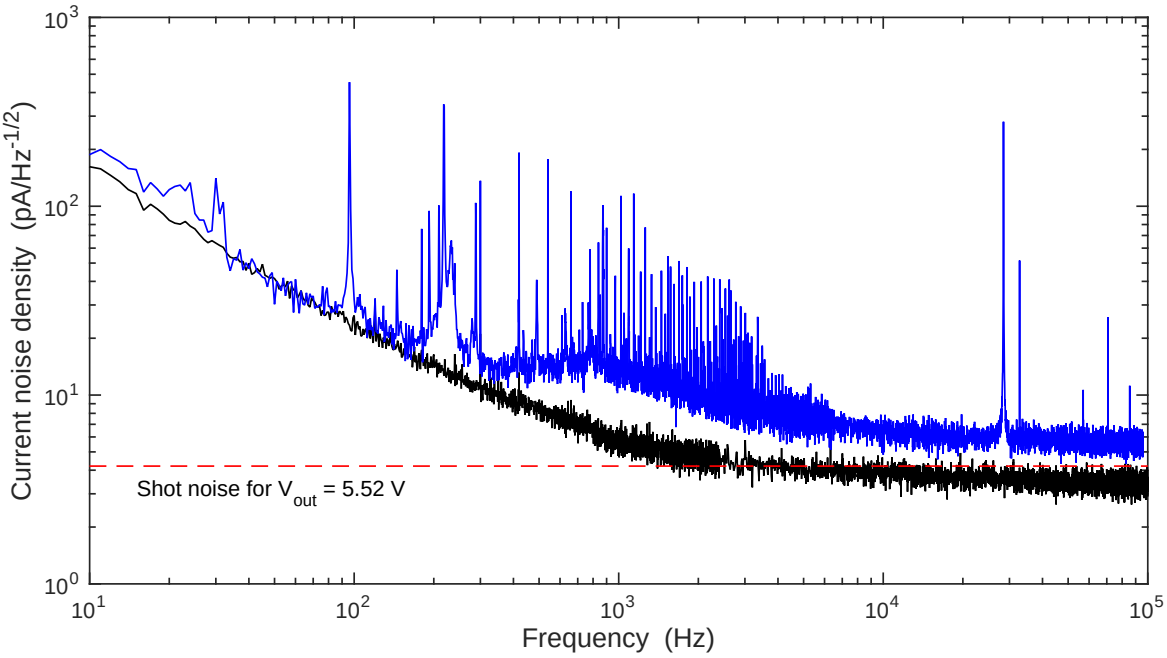

Figure 3.10: Excess noise of the Daylight Solutions QCL for approximately 10 µW power incident on detector 4346-4, which corresponds to a DC output voltage of 5.52 V. The red, dashed line is the shot noise photocurrent density of 4.2 pA/Hz$^{-1/2}$ corresponding to 5.52 V output voltage. Also shown is the dark noise floor of detector 4346-4.

filter between the detector output and oscilloscope input, and AC couple the signal with a 10 Hz high pass filter. To simulate an actual experiment, we trigger the oscilloscope at the ablation laser repetition rate of 10 Hz, and acquire 40 ms of data at a rate of 1 MS/s. Note that we expect the molecule signal to consist of a pulse with a rise time of a few hundred microseconds and a fall time of a few milliseconds, which corresponds to the time it takes after a pulse of the ablation laser for molecules to be entrained in the buffer-gas flow and extracted from the cell. Figure 3.11 shows the results of this measurement for a single acquisition and an average of 16 acquisitions. From the figure, we find that the standard deviation of the laser noise is about 2×10^{-4} V and 4×10^{-5} V for a single acquisition and an average of 16 acquisitions, respectively. In a 10 kHz bandwidth these values correspond to approximately 20 pA/Hz$^{-1/2}$ and 4 pA/Hz$^{-1/2}$ equivalent photocurrent noise densities, respectively, which are roughly 4 times larger than the shot noise photocurrent density at a DC output voltage of 8 V from the detector. In terms of minimum detectable optical depth, the laser noise corresponds to about 2.5×10^{-7}/Hz$^{-1/2}$ and 5×10^{-8}/Hz$^{-1/2}$ for a single acquisition and an average of 16 acquisitions, respectively. Notably, the detector noise is about $2 - 3$ times larger than shot noise. Therefore, it appears that we are very close to the detector limited noise floor, which is also very close to the shot noise limited noise floor. Notably, this likely represents the best we can achieve with this setup at DC, and the performance will likely get worse once the laser is aligned through the vacuum chamber and all of the vacuum pumps are running.

Although we have not utilized any specialized techniques to achieve the above noise floor, it is important to mention that it was crucial to vibration isolate the optical system as much as possible. Thus, the optical breadboard is mounted on sorbothane and the QCL is mounted to a second optical breadboard that is isolated from the main breadboard through more sorbothane. Additionally, care must be taken with filling the MCT detector liquid nitrogen dewar. Once the detector has cooled down a ball driver is inserted into the dewar to "quiet" the liquid nitrogen inside, otherwise bubbling can vibrate the detector. This shows up as noise around 120 Hz, which can easily be mistaken for power line noise. Furthermore, all electronics are connected through power line filters in an effort to isolate the system from the main building power as much as possible. Finally,

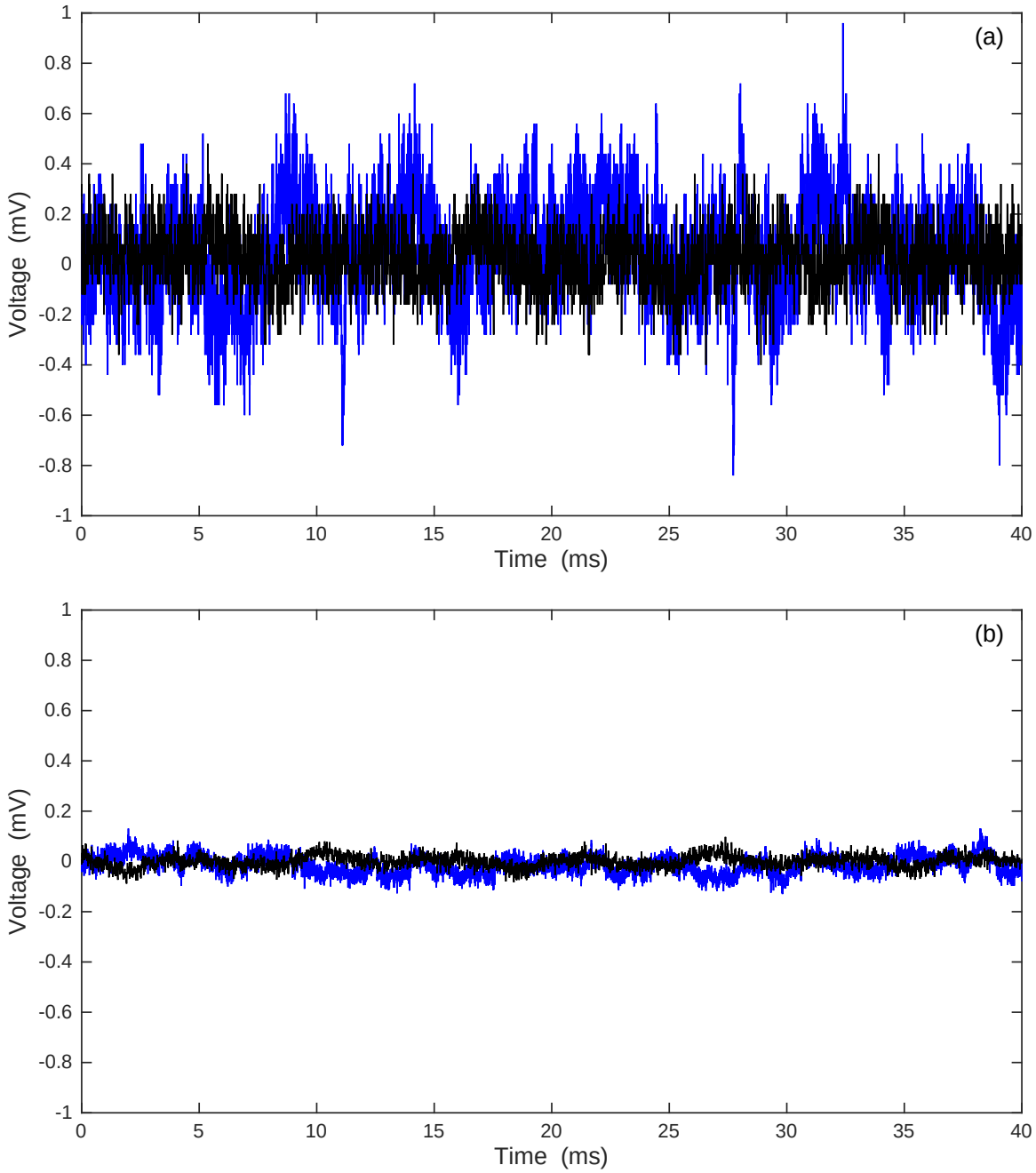

Figure 3.11: Single detector noise floor of the QCL absorption spectroscopy system for (a) a single acquisition and (b) an average of 16 acquisitions. The black curve is the dark noise with the detector (4346-4) blocked, and the blue curve is with the laser incident on the detector. A 10 Hz high pass filter and 10 kHz low pass filter are used to set the measurement bandwidth, and data is acquired at a rate of 1 MS/s. The DC output voltage from the detector is 8 V, which corresponds to approximately 15 µW of laser power.

the current limitation is likely that the optical setup is not on a proper floating optical table, but instead a normal table with a wood top. Therefore, low frequency vibrations around 30 Hz and below get transmitted to the optical system because the sorbothane does not provide isolation from these frequencies. Fortunately, the period of these vibrations are long compared to our expected signal duration, so we do not expect this to have a substantial impact on measurements.

Although the single detector performance appears to be quite good at DC, it is worth investigating wavelength modulation as a method to improve measurement sensitivity and experiment robustness (i.e., insensitivity to vibration noise). For this measurement, we current modulate the laser with a 0.1 V_{pp} sinusoid at 42.345 kHz, and investigate the RAM with a spectrum analyzer. Figure 3.12 shows the RAM at the fundamental of the modulation frequency. From the figure, we see that the RAM peak corresponds to an equivalent current noise density of about 40 nA/Hz$^{-1/2}$, which is well above the detector and shot noise floors. The two sets of sidebands correspond to modulation at about 30 Hz and 220 Hz, which correspond to low frequency vibrations transmitted to the optical system and a mechanical resonance of the QCL cavity, respectively. Notably, the noise floor away from the RAM peak and the modulation sidebands is equivalent to about 5 pA/Hz$^{-1/2}$, which is very close to the shot noise floor of about 4 pA/Hz$^{-1/2}$ for a DC output voltage of 5.52 V from the detector. Therefore, if we use a high pass filter to eliminate frequencies below about 30 Hz and do not introduce any additional RAM in the optical system, we will be able to make shot noise limited measurements with wavelength modulation spectroscopy. However, a detailed characterization of the QCL is necessary to find the optimal modulation depth for a given absorption lineshape, which adds complexity to a given measurement.

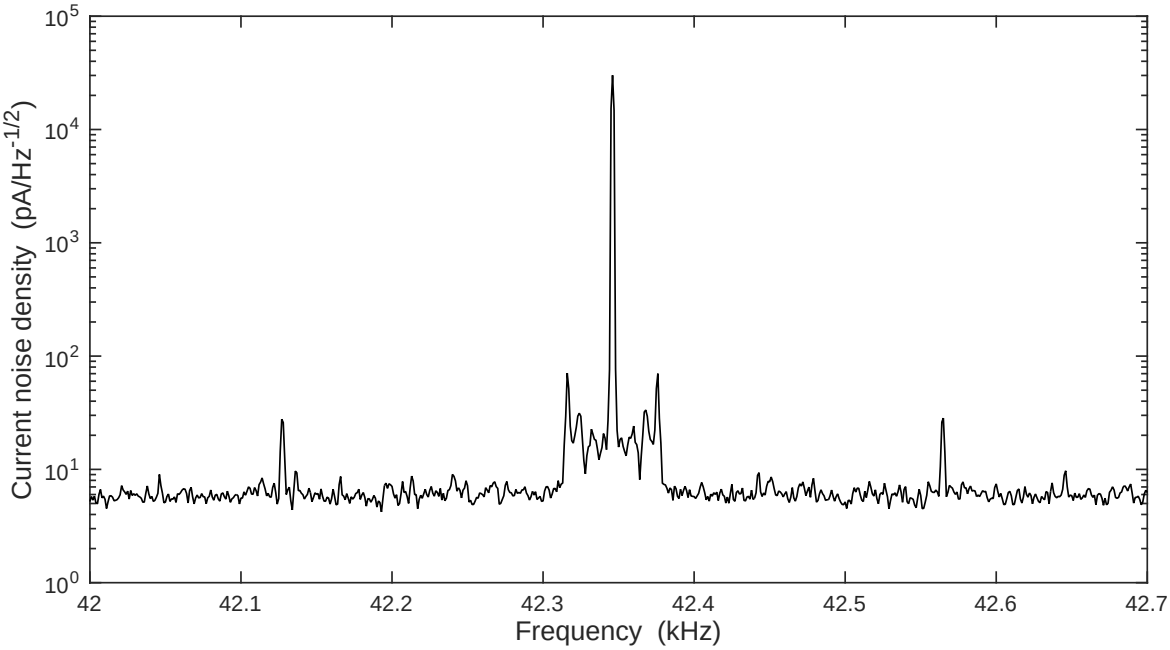

Figure 3.12: Residual amplitude modulation on the Daylight Solutions QCL for current modulation with a 0.1 V_{pp} sinusoid at 42.345 kHz, and a DC output voltage of 5.52 V from the detector.

Chapter 4

Production of carbon clusters with a cryogenic buffer-gas beam source*

In this work, we investigate the production of carbon clusters with a neon buffer-gas beam source, which is in contrast to previous studies of small carbon clusters [99] that primarily utilized supersonic expansion sources. Using matrix isolation spectroscopy, we observe clusters ranging in size from C_3 to C_{12}, and estimate the number of each cluster produced. Clusters in this size range have been previously produced using a supersonic expansion source with a small growth channel [100–102]. This chapter is organized as follows. Section 4.1 provides an overview of the apparatus and the experimental procedure used to characterize the buffer-gas beam source. Section 4.2 investigates the production of carbon clusters as a function of various system parameters, and describes a method for quantifying the number of each cluster produced. Section 4.3 concludes and provides a future outlook.

4.1 Experimental Methods

Carbon clusters are produced inside the buffer-gas cell (see Fig. 2.1) by laser ablation of a graphite target located at the edge of the cylindrical bore halfway along the length of the cell. To ablate graphite, the output of a Nd:YAG laser (Spectra Physics, Quanta-Ray Lab-150, 532 nm) is focused onto the target to a spot roughly 30 µm in diameter using a biconvex lens with a 400 mm focal length. To prevent the ablation laser from drilling a hole into the target [28], the beam is constantly scanned in two dimensions using a motorized mirror mount. Without scanning, we observe rapid

* A version of this chapter has been published in Ref. [43].

degradation in the number of molecules produced per laser pulse.

Following ablation, the carbon clusters undergo collisions with the cold neon buffer gas for a few milliseconds before becoming entrained in the molecular beam extracted from the cell. The properties of this buffer-gas beam are determined by the cell geometry, the aperture diameter, and the flow rate of neon gas into the cell [29]. The first two variables are fixed in this experiment, whereas the neon flow rate can be varied in the range $0 - 100$ sccm using the mass flow controller. Notably, both cluster formation and collisional cooling of the ablation products occur during the interaction time inside the cell.

To measure the number and composition of carbon clusters produced inside the neon buffer-gas cell, we use a matrix isolation spectroscopy setup [82]. The buffer-gas beam exiting the cell is frozen onto a CaF_2 window ($T \sim 5$ K) located approximately 2 cm from the cell aperture. Infrared absorption spectra of matrix isolated carbon clusters are acquired in the range $4000 - 1000$ cm^{-1} at 1 cm^{-1} resolution using a Fourier-transform infrared spectrometer (Thermo Fisher Scientific, Nicolet iS50). We average 36 scans for each acquired spectrum resulting in a dynamic range of approximately 70 dB. This leads to a signal-to-noise ratio of about $925 : 1$ for the ν_6 mode of C_9 as depicted in the spectrum of Fig. 4.1(a), which is acquired after 30 minutes of deposition.

For a given set of system parameters, which include the neon flow rate Q_{Ne}, laser pulse energy E_p, and laser repetition rate f_r, we ablate continuously for two minutes then acquire a spectrum. During the acquisition of each spectrum, the neon flow is turned off and the ablation laser is physically blocked by a mechanical shutter. This process is repeated 15 times for a total deposition time of 30 minutes to determine the rate of increase in optical depth (i.e., absorbance) for each observed peak. Given this change in optical depth, we quantify the performance of our buffer-gas beam source by estimating the number of each carbon cluster produced per pulse of the ablation laser. The following section discusses the results of this experiment as a function of Q_{Ne}, E_p, and f_r, and describes our method for estimating molecule production per pulse from the rate of increase in optical depth.

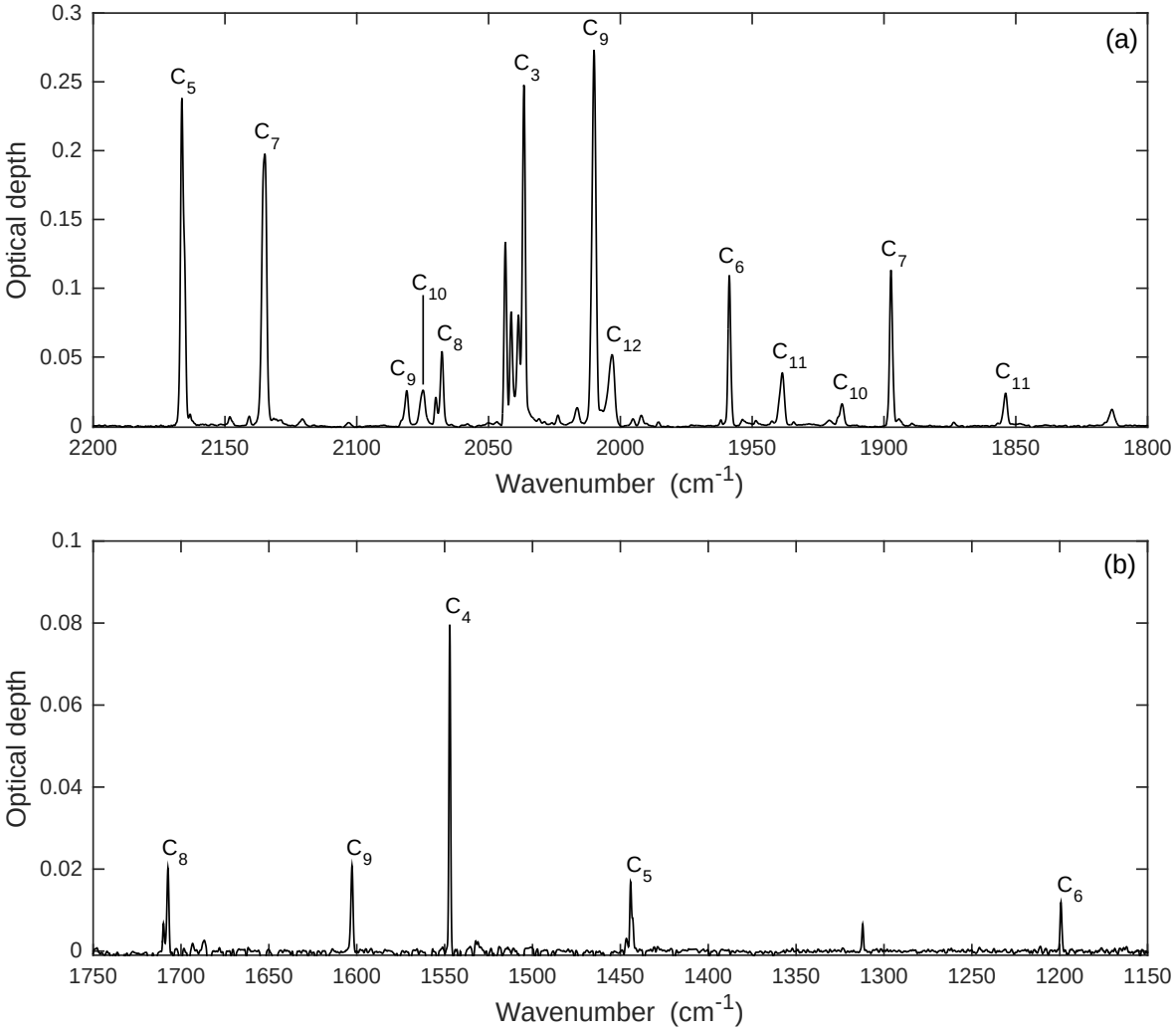

Figure 4.1: Infrared absorption spectrum of carbon clusters isolated in a neon matrix at 5 K. The system parameters were $Q_{\mathrm{Ne}} = 40$ sccm, $E_p = 2$ mJ, and $f_r = 7.5$ Hz. Note the difference in the vertical scale for the spectral range (a) $2200 - 1800$ cm^{-1} and (b) $1750 - 1150$ cm^{-1}. Reproduced from Ref. [43].

4.2 Results and Discussion

A typical infrared spectrum of carbon clusters isolated in a neon matrix, acquired using the apparatus described above, is shown in Fig. 4.1. We observe vibrational modes of linear carbon chains ranging in size from C_3 up to C_{12}, where peak assignments are based on previous matrix isolation spectroscopy results [103–114]. Notably, we have not observed signatures of C_{60} or carbon cluster ions isolated in the matrix based on the absence of known vibrational transitions in these molecules [115, 116]. As a consistency check, we have calculated correlation coefficients for all clusters with multiple absorption lines (C_5 to C_{11}) using data over a wide range of system parameters, and find $r > 0.995$ in all cases. This indicates that our peak assignment based on previous work is valid. A summary of the data depicted in Fig. 4.1 is given in the first three columns of Table 4.1. Note that the spectrum in Fig. 4.1 is acquired after 30 minutes of deposition onto the matrix window held at a temperature of about 5 K. Because 5 K is below the neon matrix annealing temperature of about 10 K, we conclude that the larger clusters observed spectroscopically are formed within the buffer-gas cell. This is in contrast to other matrix isolation studies of carbon clusters [103–105, 107, 110], where an additional annealing step was necessary to promote diffusive aggregation of smaller clusters into larger clusters [118, 119].

To quantify the number of each cluster present in a given spectrum, we start from Beer's law:

$$\tau(\nu) = \ln\left[\frac{I_0(\nu)}{I(\nu)}\right], \tag{4.1}$$

where $I_0(\nu)$ and $I(\nu)$ are the incident and transmitted intensity, respectively, and $\tau(\nu)$ is the frequency-dependent optical depth of the sample (absorbance is related to optical depth by $A \approx 0.434\tau$). From Beer's law, we define the integrated molar absorption coefficient, or infrared intensity S as [67]

$$S = \frac{1}{nl}\int d\nu\ \tau(\nu), \tag{4.2}$$

where n is the molar concentration of the absorbing species, l is the absorption length, and the integration is over the entire absorption line. Assuming that we probe an area of uniform density,

Table 4.1: Representative data for $Q_{\mathrm{Ne}} = 40$ sccm, $E_p = 2$ mJ, and $f_r = 7.5$ Hz. The center frequency of each absorption line, ν_0, is given along with theoretical infrared intensities, S, peak optical depth per ablation pulse, $\Delta\tau_{pp}$, and the number of each carbon cluster produced per ablation pulse, N_{pp}. Quoted uncertainties are statistical.

Molecule	Mode	ν_0 $(\mathrm{cm}^{-1})^*$	S $(\mathrm{km/mol})^\dagger$	$\Delta\tau_{pp}$ (10^{-6})	N_{pp} (10^{11})
C_3	ν_3	2036.59(1)	612.0	21.6(4)	10.8(2)
C_4	ν_3	1547.07(1)	321.0	6.44(8)	6.12(8)
C_5	ν_3	2166.36(3)	1648.8	20.4(3)	3.78(6)
	ν_4	1444.24(3)	97.3	1.38(6)	4.3(2)
C_6	ν_4	1958.65(1)	800.8	8.7(1)	3.33(4)
	ν_5	1199.29(2)	60.3	0.91(7)	4.6(4)
C_7	ν_4	2135.08(2)	2695	16.4(2)	1.86(2)
	ν_5	1897.31(1)	677.4	9.16(6)	4.13(3)
C_8	ν_5	2067.69(1)	1366.3	4.20(4)	0.937(9)
	ν_6	1707.47(5)	984.8	1.61(8)	0.50(3)
C_9	ν_5	2081.13(3)	2324	1.99(4)	0.261(5)
	ν_6	2010.02(1)	3030	22.1(2)	2.22(2)
	ν_7	1602.74(1)	376.5	1.68(5)	1.36(4)
C_{10}	–	2075.01(3)	–	1.97(4)	–
	–	1915.85(5)	–	1.24(9)	–
C_{11}	ν_7	1938.72(3)	–	2.88(6)	–
	ν_8	1853.86(5)	–	1.75(5)	–
$C_{12}{}^\ddagger$	ν_8	2003.47(8)	–	4.08(6)	–

* Line centers are determined from a Gaussian fit to each peak, and uncertainties represent 95% confidence bounds on the fit.

† Infrared intensities from Ref. [117].

‡ Tentative assignment based on Ref. [112].

we estimate the number of molecules in the matrix as

$$N \approx \left(\frac{N_A A_p}{S} \right) \Delta\nu \ \tau_p, \tag{4.3}$$

where N_A is Avogadro's constant, A_p is the approximate area of the buffer-gas beam at the matrix window, and the integral has been approximated as the product between the width of the absorption line, $\Delta\nu$, and the peak optical depth, τ_p. For the calculations here, we use $A_p \sim 5$ cm^2, and assume $\Delta\nu \sim 1$ cm^{-1} as a typical value for matrix isolated species [120].

Given Eq. (4.3), we calculate the number of molecules produced per ablation pulse in the following way. We first extract τ_p for each observed peak in the spectrum after every two-minute deposition cycle, then use linear regression to calculate the time rate of change of τ_p for each peak. Finally, we convert this time rate of change to a change in peak optical depth per ablation pulse, $\Delta\tau_{pp}$, using the repetition rate of the laser. Thus, we arrive at the following expression for the number of molecules produced per ablation pulse:

$$N_{pp} \approx 3 \times 10^{19} \left(\frac{\Delta\tau_{pp}}{S} \right), \tag{4.4}$$

where S is in units of km/mol, and we have substituted A_p and $\Delta\nu$ for the values given above. Table 4.1 shows the results of this analysis for a representative data set with $Q_{\mathrm{Ne}} = 40$ sccm, $E_p = 2$ mJ, and $f_r = 7.5$ Hz. Note that this calculation depends on knowledge of the infrared intensity for a given molecular transition. As this parameter is difficult to measure directly, we rely on results from density functional theory calculations for linear C_3 to C_9 [117]. We neglect C_{10} to C_{12} in our analysis as we have been unable to find consistent theoretical values of S for the observed absorption lines. For C_5 to C_8, we find reasonable agreement (i.e., same order of magnitude) for the value of N_{pp} calculated from different absorption lines of the same molecule, which implies good relative accuracy of the theoretical infrared intensities. However, for C_9, the value of N_{pp} calculated for the ν_5 mode is off by an order of magnitude from the corresponding values for the ν_6 and ν_7 modes. This inconsistency likely stems from a neglect of electrical anharmonicity in the theoretical method used to determine S.

We now apply the analysis described above to investigate carbon cluster production in the buffer-gas cell as a function of the system parameters. For clusters that have multiple absorption lines, we use the line with the largest infrared intensity (corresponding to largest peak optical depth) to calculate N_{pp}. In Fig. 4.2, the number of each carbon cluster produced per pulse is plotted versus the flow rate of neon buffer gas. For all detected clusters, we observe a linear increase in production with flow rate up to about $Q_{\mathrm{Ne}} = 40$ sccm. This increase then saturates and begins to decrease for higher flow rates, an effect that has been observed in a number of other buffer gas experiments [31, 33, 44, 57, 58].

The effect of neon flow rate on the number of each cluster detected in the matrix can be understood by considering the two relevant timescales that characterize the buffer-gas cell dynamics: the molecule diffusion time to the cell walls, t_d, and the cell pumpout time, t_p. If $t_d \ll t_p$ then molecules produced by ablation diffuse to the cell walls and are lost before they are extracted from the cell. On the other hand, if $t_d \gg t_p$, we expect that the molecules are extracted from the cell before being lost to the cell walls resulting in a larger number of molecules detected inside the matrix. The cell pumpout time is governed by the conductance of the cell aperture, and is therefore purely geometrical. The diffusion time, however, depends on the density of neon buffer gas inside the cell, which is linearly proportional to the flow rate. Thus, we characterize the extraction behavior using the dimensionless quantity [29] $\gamma_{\mathrm{cell}} \equiv t_d/t_p$. It is typically assumed that t_d is dominated by the lowest order diffusion mode in the cell (a good approximation at low buffer-gas density [33]), and increases linearly with the neon density in the cell [56]. For our system parameters, we find $\gamma_{\mathrm{cell}} \approx 1$ for $Q_{\mathrm{Ne}} \approx 25$ sccm, which corresponds to $t_d = t_p \approx 8$ ms. This correlates well with the observed linear increase in molecules per pulse up to about $Q_{\mathrm{Ne}} = 30 - 40$ sccm shown in Fig. 4.2. As γ_{cell} becomes much larger than unity, we would expect the number of detected clusters to saturate as all molecules should be extracted from the cell before diffusing to the cell walls. However, at high buffer-gas densities (i.e., high flow rate) the diffusion process is no longer dominated by the lowest order mode [33]. Since higher-order diffusion modes have smaller time constants [56], the result is an effective decrease in γ_{cell}, and therefore in the extraction efficiency. Additionally, it is possible

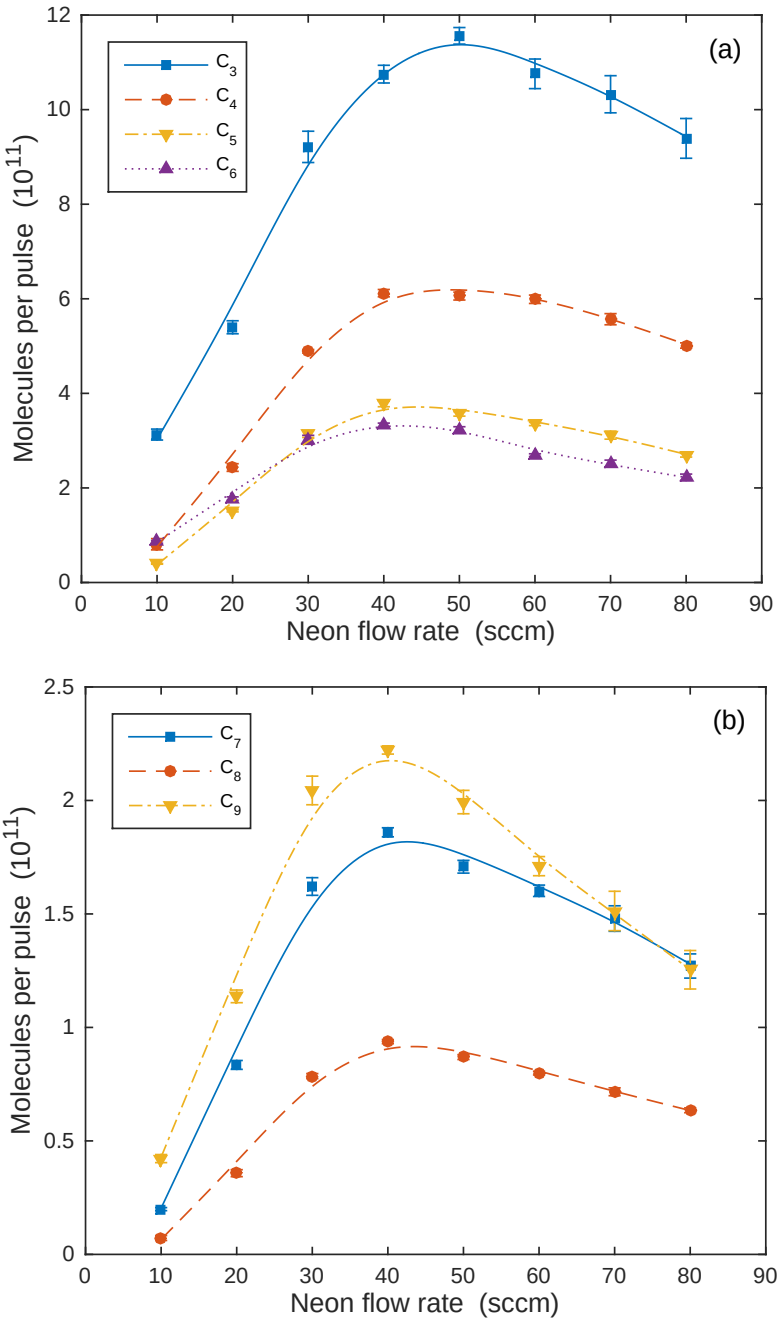

Figure 4.2: Number of each carbon cluster produced per pulse for (a) C_3 to C_6 and (b) C_7 to C_9 as a function of neon flow rate for $E_p = 2$ mJ and $f_r = 7.5$ Hz. Error bars represent statistical uncertainty propagated from the determination of $\Delta\tau_{pp}$. Lines are guides for the eye. Reproduced from Ref. [43].

that the neon flow becomes turbulent [44], and negatively impacts the extraction efficiency in a similar way. We observe these effects as a reduction in the number of each carbon cluster detected in the matrix at neon flow rates in excess of about $40 - 50$ sccm.

In addition to flow rate, carbon cluster production as a function of the ablation laser pulse energy and repetition rate is investigated, the former of which is plotted in Fig. 4.3. We observe a linear increase in the production of all carbon clusters with increasing ablation pulse energy up to $E_p = 4$ mJ, at which point a substantial amount of carbon dust was present in the vacuum chamber. Therefore, we did not explore higher pulse energies. We observed no variation in cluster production rate for laser repetition rates of $f_r = 3,\ 5,$ and 7.5 Hz, implying local heating of the substrate does not effect cluster production at these low repetition rates.

4.3 Summary

We have produced carbon clusters C_3 to C_{12} using a cryogenic buffer-gas beam source. For each of the C_3 to C_9 molecules, we estimate a production rate on the order of $10^{11} - 10^{12}$ molecules per pulse of the ablation laser based on infrared intensities determined from density functional theory calculations. Similar to other buffer-gas beam experiments, we observe an initial linear increase in molecule production with neon flow rate followed by a decrease at high flow rates (i.e., high neon density in the cell). We attribute this decrease at high flow rates to a reduction in the diffusion time for molecules to be lost to the cell walls.

Based on the direct observation of large numbers of carbon clusters containing more than a few atoms, the buffer-gas beam source may be a viable method for the production of more exotic cluster systems such as metal oxides and carbides. Furthermore, given the increased number of collisions in comparison to a supersonic expansion source, we anticipate the buffer-gas beam to be a useful source for the production of vibrationally cold cluster systems and other complex polyatomic molecules. Used as the source in a high-resolution infrared spectroscopy system, it could then be possible to determine molecular structures to a high degree of precision.

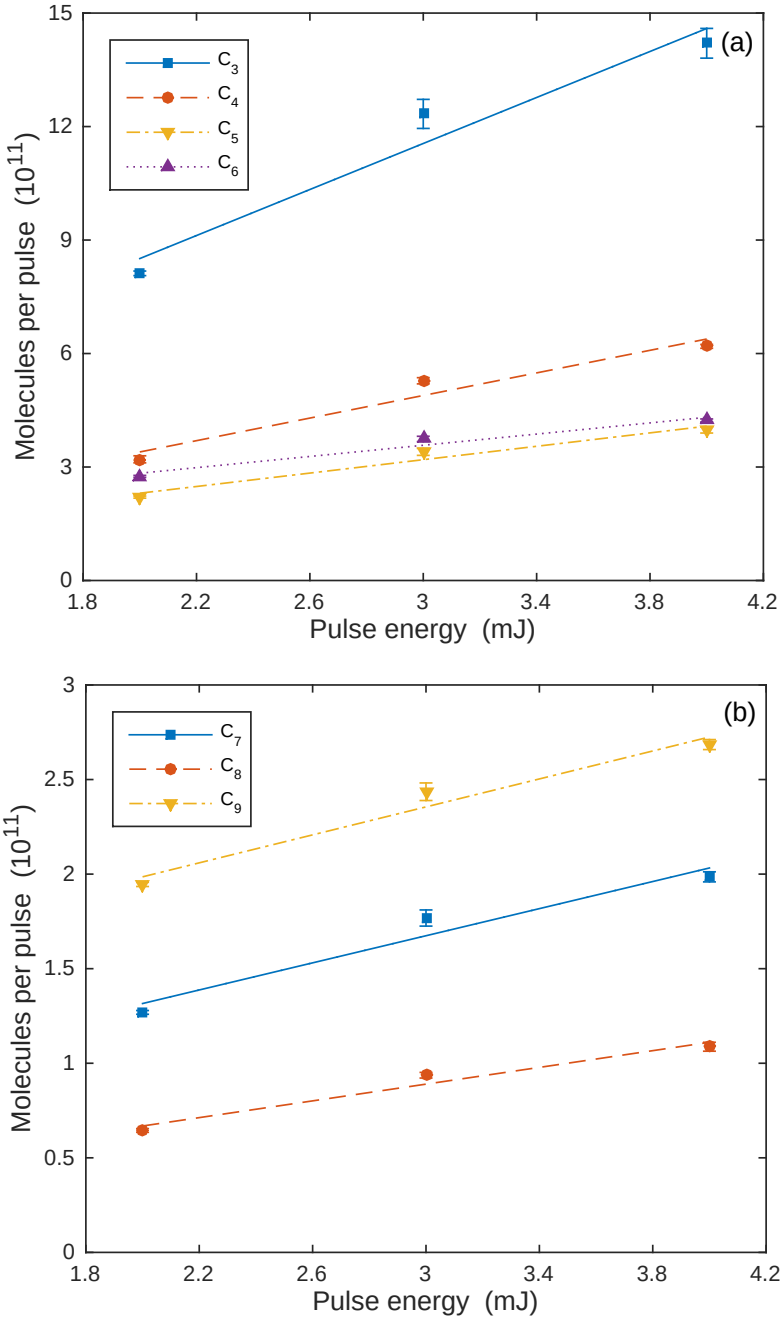

Figure 4.3: Number of each carbon cluster produced per pulse for (a) C_3 to C_6 and (b) C_7 to C_9 as a function of ablation pulse energy for $Q_{\mathrm{Ne}} = 40$ sccm and $f_r = 7.5$ Hz. Error bars represent statistical uncertainty propagated from the determination of $\Delta\tau_{pp}$. Lines are guides for the eye. Reproduced from Ref. [43].

Chapter 5

Infrared Spectroscopy of the WO Molecule

A detailed understanding of the bonding and electronic structure in transition metal containing molecules is of interest to a variety of fields including catalysis [121], semiconductor science [122], and astrophysics [123, 124]. Typically, such an understanding comes from laboratory-based spectroscopic studies, where analysis of high-resolution spectra is used to deduce the geometrical arrangement of the individual atoms in a molecule, as well as the strength of bonds between those atoms. Notably, transition metal containing molecules typically possess rich spectra due to their complicated electronic structure and multitude of low-lying, interacting states, which serve to perturb and further complicate the interpretation of spectra. In fact, WO is an excellent example of this complexity. Until the work of Ram et al. [125] in 2001, the electronic structure of WO was not well characterized and even its ground state was not known with certainty. Starting from the initial observation of WO bands by Gatterer and Krishnamurty [126], through the experimental work of Weltner and McLeod [127], Green and Ervin [128], Samoilova et al. [129], and Lorenz and Bondybey [130], as well as the theoretical work by Nelin and Bauschlicher [131], there was much debate about whether WO possessed a $^3\Sigma^-$ or $^5\Pi$ ground state. Through extensive electronic spectroscopy and complex ab initio calculations, Ram et al. provided a detailed analysis of the ^{184}WO molecule [125, 132]. We make use of the results of Ram et al. in this chapter to predict the infrared rotational-vibrational spectrum of the WO molecule for all four naturally occurring isotopes of tungsten. Following this, we develop a method for reliably producing WO molecules in the gas phase and optimize WO production using FTIR matrix isolation spectroscopy.

5.1 Expected WO Rotational-Vibrational Spectrum

5.1.1 Energy levels

Ram et al. [125, 132] carried out extensive characterization of the electronic structure of ^{184}WO, and computed rotational and vibrational constants with anharmonic and centrifugal distortion corrections for a variety of electronic states. We are interested in the ground electronic state of WO, which is a $^3\Sigma^-$ state with the lowest energy belonging to the $\Omega = 0$ spin component. Here, $\Omega = \Lambda + \Sigma$ and represents the projection of the electronic orbital and spin angular momentum along the internuclear axis [67]. Thus, we have a minimum total angular momentum of $J = 0$, and the rotational energy levels follow the standard expression for a diatomic rigid rotor with centrifugal distortion [67, 133]:

$$F_v(J) = B_v J(J+1) - D_v J^2 (J+1)^2, \tag{5.1}$$

where the v subscript indicates the vibrational level, B_v is the rotational constant, and D_v is the centrifugal distortion constant. In general, the above polynomial expansion can be continued to higher-order corrections; however, these are not necessary to describe rotational-vibrational transitions in the electronic ground state of WO. Note that the rotational and centrifugal distortion constants are dependent on the vibrational energy level because as v increases so does the average internuclear separation of the atoms in the molecule (i.e., the bond length increases with v). The lowest vibrational level corresponds to $v = 0$, and the vibrational energy levels follow the standard expression for an anharmonic oscillator [67, 133]:

$$G(v) = \omega_e \left(v + \frac{1}{2}\right) - \omega_e x_e \left(v + \frac{1}{2}\right)^2 + \omega_e y_e \left(v + \frac{1}{2}\right)^3, \tag{5.2}$$

where ω_e is harmonic oscillation frequency, and $\omega_e x_e$ and $\omega_e y_e$ are constants that represent quadratic and cubic corrections to the harmonic oscillator result. In general, and similar to the rotational energy levels, the above polynomial expansion for vibrational energy levels can be continued to higher-order corrections, but it is not necessary here. We find the total energy of a given molecular

state to be

$$T(v, J) = F_v(J) + G(v). \tag{5.3}$$

Note that ω_e is proportional to the force constant k_v through the following relation:

$$\omega_e = \frac{1}{2\pi c}\sqrt{\frac{k_v}{\mu}}, \tag{5.4}$$

where μ is the reduced mass of the WO molecule; therefore, measurement of vibrational spectra provides information on the strength of the molecular bond. Now, given an expression for the vibrational energy levels, we write the rotational and centrifugal distortion constants as [67, 133]

$$B_v = B_e - \alpha_e\left(v + \frac{1}{2}\right), \tag{5.5}$$

$$D_v = D_e + \beta_e\left(v + \frac{1}{2}\right), \tag{5.6}$$

where B_e is the equilibrium rotational constant, and α_e represents a correction due to vibrational excitation. Here, B_e is proportional to the moment of inertia I_r through the relation

$$B_e = \frac{\hbar}{4\pi c I_r}, \tag{5.7}$$

where $I_r = \mu r_e^2$ for a diatomic molecule, and r_e is the equilibrium separation between the atoms. Therefore, measurement of rotational spectra provides information on the length of the molecular bond. In addition to ω_e and its corrections, the equilibrium rotational constant and its corrections are quantities found through measurement of infrared rotational-vibrational spectra. On the other hand, the equilibrium centrifugal distortion constant D_e and its correction β_e are derived quantities based on the following expressions [133]

$$D_e = \frac{4B_e^3}{\omega_e^2}, \tag{5.8}$$

$$\beta_e = D_e\left(\frac{8\omega_e x_e}{\omega_e} - \frac{5\alpha_e}{B_e} - \frac{\alpha_e^2\omega_e}{24B_e^3}\right). \tag{5.9}$$

Table 5.1 provides equilibrium constants for the $\Omega = 0$ component of the $^3\Sigma^-$ ground state of ^{184}WO as reported by Ram et al. [132]. From these values, we expect the fundamental vibrational transition from $v = 0$ to $v = 1$ for the $\Omega = 0$ component to occur at approximately $\tilde{\nu}_0 = 1057.57$ cm^{-1}.

Table 5.1: Equilibrium constants (in units of cm^{-1}) for the $\Omega = 0$ component of the $^3\Sigma^-$ ground state of ^{184}WO. Data reproduced from Ref. [132].

ω_e	$\omega_e x_e$	$\omega_e y_e$	B_e	α_e
1065.5951(71)	4.0103(40)	-0.00268(60)	0.4165548(60)	0.0020237(23)

An interesting feature of the $^3\Sigma^-$ ground state is the additional spin component $\Omega = 1$, which represents a doublet separated from the $\Omega = 0$ spin component by an amount of $2\lambda \approx 414 - 1898$ cm^{-1} [132], where λ is the spin-spin coupling constant. The lower bound on λ is from experimental observations, while the upper bound is from ab initio calculations; however, Ram et al. note that their estimate from experimental observations makes the assumption of an isolated $^3\Sigma^-$ ground state, which is likely incorrect. Furthermore, ab initio calculations on a system such as WO are challenging, so the precise value of λ is practically unknown. Thus, it is of interest to investigate the expected rotational-vibrational spectrum of the $\Omega = 1$ spin component of the $^3\Sigma^-$ ground state, as it is possible that we will have some population of WO molecules in this state. Since $\Omega = 1$ represents a doublet, excitation of rotational transitions in the molecule will lift the degeneracy through spin-orbit interactions. Therefore, we modify the rotational energy level expression to include a J-dependent splitting [132]:

$$F_v(J) = B_v J(J+1) - D_v J^2 (J+1)^2 \pm q_v J(J+1), \tag{5.10}$$

where q_v is a lambda-doubling constant that in general depends on the vibrational energy level. Note that this expression is valid only for $\Omega = 1$ component, and the vibrational energy levels follow Eq. (5.2). Table 5.2 provides equilibrium constants for the $\Omega = 1$ component of the $^3\Sigma^-$ ground state of ^{184}WO as reported by Ram et al. [132]. From these values, we expect the fundamental vibrational transition from $v = 0$ to $v = 1$ for the $\Omega = 1$ component to occur at approximately $\tilde{\nu}_0 = 1059.93$ cm^{-1}, which is about 2 cm^{-1} higher than that of the $\Omega = 0$ component.

Table 5.2: Equilibrium constants (in units of cm^{-1}) for the $\Omega = 1$ component of the $^3\Sigma^-$ ground state of ^{184}WO. Values of q_v (in units of cm^{-1}) for the $v = 0$ and $v = 1$ vibrational states are also included. Data reproduced from Ref. [132].

ω_e	$\omega_e x_e$	$\omega_e y_e$	B_e	α_e	$q_0\ (\times 10^4)$	$q_1\ (\times 10^4)$
1067.9939(34)	4.0314(6)	-	0.4172526(31)	0.002022(15)	1.6254(56)	1.6228(36)

5.1.2 Transition wavenumbers

With expressions for the rotational and vibrational energy levels in hand, we now investigate the observable transitions between these energy levels. Selection rules for diatomic molecules dictate that allowed transitions have $\Delta v = \pm 1$ and $\Delta J = \pm 1$ [67]; therefore, we are primarily interested in transitions from $v = 0$ to $v = 1$ with $\Delta J = \pm 1$. Since $\Delta J = 0$ is forbidden, we do not expect to see the Q-branch in the spectrum. However, both the R- and P-branches will be observable, which correspond to $\Delta J = +1$ and $\Delta J = -1$, respectively. To find the wavenumber corresponding to a transition between J in the $v = 0$ state and J' in the $v = 1$ state, we use Eq. (5.3):

$$\begin{aligned}
\tilde{\nu}_{J-J'} &= T\left(1, J'\right) - T\left(0, J\right), \\
&= \left(B_e - \frac{3\alpha_e}{2}\right) J'\left(J'+1\right) - \left(D_e + \frac{3\beta_e}{2}\right) J'^2\left(J'+1\right)^2 \pm q_1 J'\left(J'+1\right) \\
&\quad - \left(B_e - \frac{\alpha_e}{2}\right) J\left(J+1\right) - \left(D_e + \frac{\beta_e}{2}\right) J^2\left(J+1\right)^2 \mp q_0 J\left(J+1\right) \\
&\quad + \omega_e - 2\omega_e x_e + \frac{13}{4}\omega_e y_e. \qquad (5.11)
\end{aligned}$$

Now, for the R-branch we have $J' = J + 1$ and for the P-branch we have $J' = J - 1$, which leads to the following expressions for the transition wavenumbers:

$$\begin{aligned}\tilde{\nu}_R(J) &= 2B_e(J+1) - \alpha_e(J+1)(J+3) \\ &\quad - 4D_e(J+1)^3 + \beta_e\left(J^4 + 8J^3 + 19J^2 + 18J + 6\right) \\ &\quad \pm q_1(J+1)(J+2) \mp q_0 J(J+1) \\ &\quad + \omega_e - 2\omega_e x_e + \frac{13}{4}\omega_e y_e, \end{aligned} \tag{5.12}$$

$$\begin{aligned}\tilde{\nu}_P(J) &= -2B_e J - \alpha_e J(J-2) \\ &\quad + 4D_e J^3 + \beta_e J^2\left(J^2 - 4J + 1\right) \\ &\quad \pm q_1 J(J-1) \mp q_0 J(J+1) \\ &\quad + \omega_e - 2\omega_e x_e + \frac{13}{4}\omega_e y_e, \end{aligned} \tag{5.13}$$

where the J value corresponds to the $v = 0$ state, and the minimum value is $J = 0$ and $J = 1$ for the R- and P-branch, respectively. For the $\Omega = 0$ component, we set $q_0 = q_1 = 0$ in the above expression. As previously mentioned, the W atom has four naturally occurring isotopes — ^{182}W (26.50%), ^{183}W (14.31%), ^{184}W (30.64%), and ^{186}W (28.43%), where the values in parentheses indicate the natural abundance. Therefore, each rotational-vibrational transition observed will consist of a quartet for the $\Omega = 0$ component and an octet for the $\Omega = 1$ component. Using ω_e and B_e for the ^{184}WO molecule from Tables 5.1 and 5.2, and Eqs. (5.4) and (5.7), we estimate isotopic splittings on the order of roughly $0.2 - 0.5$ cm^{-1} or $6 - 15$ GHz, which is resolvable with our apparatus.

5.1.3 Population of rotational states

Assuming all of the molecules are initially in the ground electronic and vibrational states, then the relative intensity of the transitions in the R- and P-branches depends on the ground state population of the rotational states. We calculate the fractional population of WO molecules in each J state

using classical Boltzmann statistics and the fact that each state has a $2J+1$ degeneracy:

$$\frac{N_J}{N} = \frac{(2J+1)\exp\left\{-\left(\frac{hc}{k_B T_r}\right)\left[\left(B_e - \frac{\alpha_e}{2}\right)J(J+1) - \left(D_e + \frac{\beta_e}{2}\right)J^2(J+1)^2\right]\right\}}{\sum_{J=0}^{\infty}(2J+1)\exp\left\{-\left(\frac{hc}{k_B T_r}\right)\left[\left(B_e - \frac{\alpha_e}{2}\right)J(J+1) - \left(D_e + \frac{\beta_e}{2}\right)J^2(J+1)^2\right]\right\}}, \tag{5.14}$$

where the denominator is the rotational partition function. We now have all of the necessary expressions to calculate the expected infrared rotational-vibrational spectrum of WO. Figure 5.1 shows a representative spectrum for the $\Omega = 0$ component of ^{184}WO molecules with a rotational temperature of 10 K. From the figure, we see that the strongest transitions (i.e., highest fractional population) occur for $J = 2 - 3$ in the R- and P-branches at this temperature. At higher temperatures, the peak will shift to larger values of J and the relative intensity of each transition will decrease as the molecules are spread over more states. The opposite will occur at lower temperatures. Finally, Fig. 5.2 shows a representative spectrum for the $\Omega = 1$ component of ^{184}WO molecules with a rotational temperature of 10 K. Other than the slight shift to higher wavenumbers, the spectrum appears identical to that of the $\Omega = 0$ component. However, for $\Omega = 1$ each line is in fact a doublet (see inset of Fig. 5.2), hence the reduced intensity of each transition by a factor of two. The splitting of the doublet depends on the value of the doubling constant q_v, and is approximately 0.002 cm^{-1} or 60 MHz for ^{184}WO, which is resolvable with our apparatus.

5.2 Survey of WO Production with FTIR Spectroscopy

In this section, we outline two different techniques that were investigated to produce WO in the gas phase. The first method involves pressing WO_3 powder* into a small pellet, and ablating at a few mJ of pulse energy. The second technique involves ablating pure W metal† in the presence of O_2 gas. In each case, characteristic matrix isolation spectra are presented to highlight the key differences between the two methods. Note that for this work, we replaced the CaF_2 matrix isolation window and vacuum chamber windows with KBr to increase the spectral range from approximately 1000 cm^{-1} to 650 cm^{-1}, which is limited by the Nicolet iS50 FTIR spectrometer. This is necessary

* Sigma-Aldrich, part number 95410-100G, 99.9% purity

† A piece of a thermal evaporation boat from R. D. Mathis, part number S1-.010W, 99.95% purity

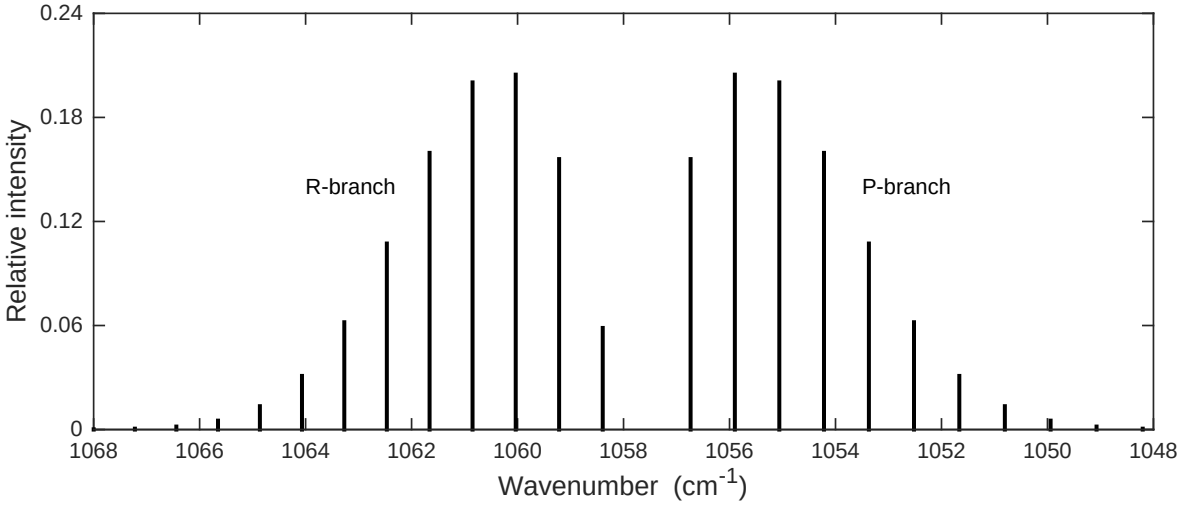

Figure 5.1: Calculated infrared rotational-vibrational spectrum of the $\Omega = 0$ spin component of the ground state of ^{184}WO assuming a rotational temperature of $T_r = 10$ K.

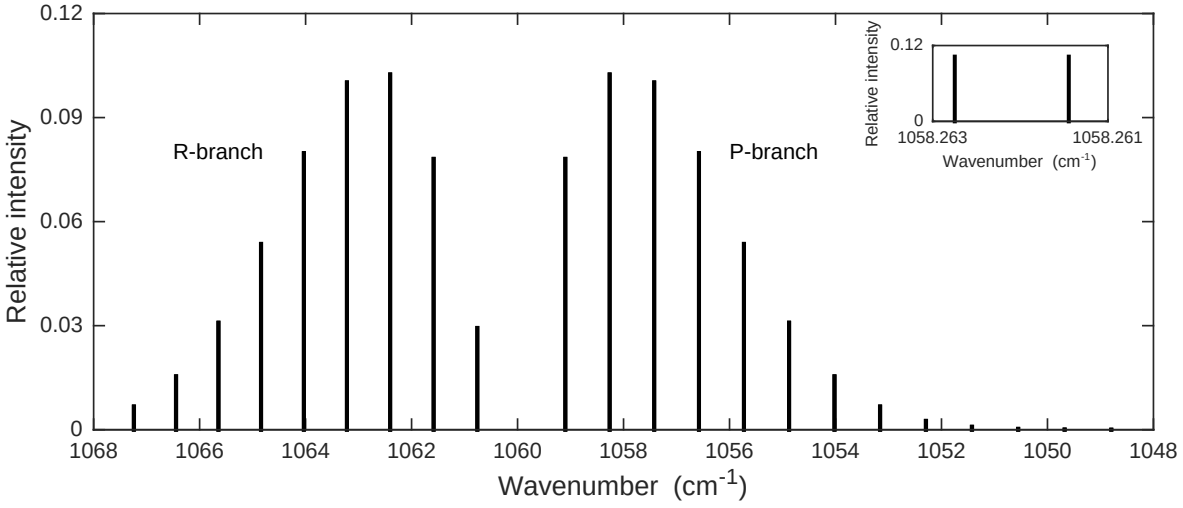

Figure 5.2: Calculated infrared rotational-vibrational spectrum of the $\Omega = 1$ spin component of the ground state of ^{184}WO assuming a rotational temperature of $T_r = 10$ K. The inset shows the doublet corresponding to the $J = 2$ transition of the P-branch.

for investigating metal oxide compounds because many of the characteristic vibrational modes lie below 1000 cm^{-1}. In addition, we reduced the temperature of the buffer-gas cooling cell to $T_{cell} =$ 16 K, which is approximately the lowest temperature that neon gas maintains an appreciable vapor pressure. This was motivated by our desire to achieve the lowest possible molecule temperature for rotational-vibrational spectroscopy, and did not affect the absolute production of WO as determined by matrix isolation spectroscopy.

5.2.1 Laser ablation of WO_3

One approach to producing WO molecules in the gas phase involves laser ablation of hydrostatically pressed WO_3 powder. Due to the bright yellow color of WO_3, we mix approximately one part of pure W metal shavings with three parts of the WO_3 powder (i.e., 1:3 mixing ratio) prior to pressing. This leads to slightly more consistent results, and higher yield of WO, which we believe is a result of the increased absorptivity of the material (the W metal shavings darken the appearance of the target). Once the two components are well mixed, we place a small amount of the powder mixture in a homemade die setup and apply a force of approximately 10,000 psi for about 5 minutes. The die consists of a stainless steel cylinder with a central bore 0.375 inches in diameter, which was made to be a snug fit for two hardened steel dowel pins. The powder to be pressed is then placed between the dowel pins inside the stainless steel cylinder, and the whole assembly is placed in a hydraulic press. The resulting targets are typically quite brittle, but hold together well enough to be epoxied to the target holder[‡] and installed inside the buffer-gas cooling cell.

To study the production of WO from a pressed target, we ablate the target at 532 nm with pulse energies between $E_p = 2 - 8$ mJ and a repetition rate of $f_r = 10$ Hz. As in the case of graphite ablation, we focus the beam to a spot size of roughly 30 µm using a biconvex lens with a focal length of 400 mm. Furthermore, we constantly scan the ablation beam in two dimensions across the target to prevent localized target degradation. Figure 5.3 shows a typical FTIR spectrum acquired as described in Section 4.1 with 5 mJ ablation pulse energy. In addition to unidentified

[‡] We use Armstrong A-12 epoxy, which works well under vacuum and at cryogenic temperatures.

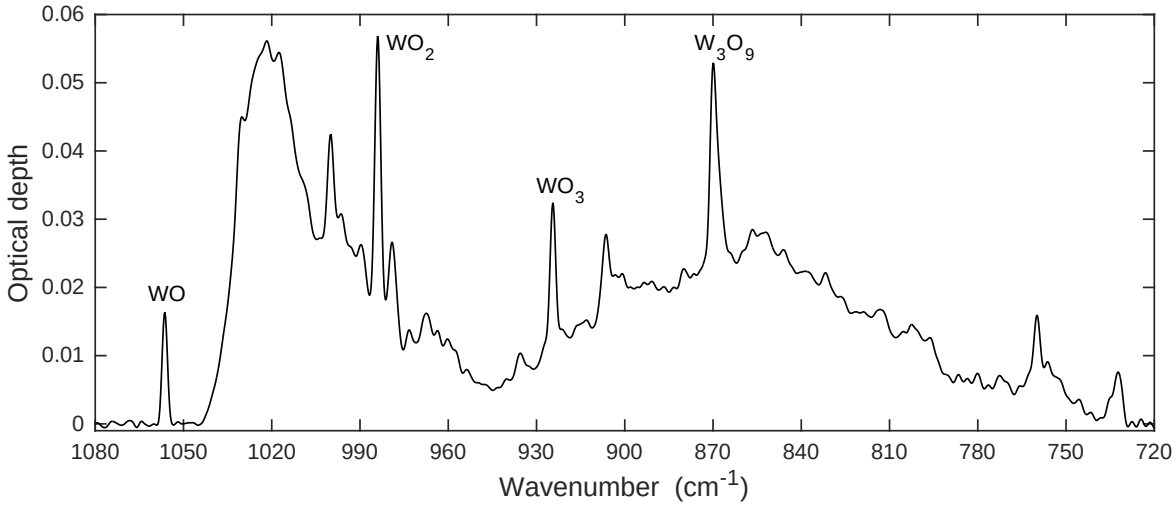

Figure 5.3: Infrared absorption spectrum of WO_3 ablation products isolated in a neon matrix at 5 K. The system parameters are $Q_{\mathrm{Ne}} = 40$ sccm, $E_p = 5$ mJ, and $f_r = 10$ Hz.

peaks, we observe vibrational modes of WO, WO_2, WO_3, and W_3O_9, where peak assignments are based on previous matrix isolation spectroscopy results [127, 128, 130, 134, 135]. Note that the spectrum in Fig. 5.3 is acquired after 7.5 minutes of deposition onto the matrix window held at a temperature of about 5 K. An interesting feature of the spectrum of WO_3 ablation products are the two broad transitions centered at about 850 cm^{-1} and 1020 cm^{-1}. It is thought that these spectral features represent a practically solid film of a tungsten oxide compound that results from the dusty nature of the ablation target. Indeed, upon visual inspection of the neon matrix after deposition, there is a clear signature of a localized dark spot corresponding to the expected location that the buffer-gas beam hits the matrix window. Additionally, this dark spot sometimes sticks to the matrix window as a deposited film that can only be removed by gently brushing it off. Furthermore, large amounts of dust are found inside the buffer-gas cooling cell after a few runs of ablating a pressed target. Therefore, we believe these broad spectral features are a result of the dust produced during the ablation process. It would be interesting to investigate the ablation products entrained in the buffer-gas beam using a mass spectrometer as it is likely that the dust being produced is made up of metal oxide cluster molecules of various sizes. Notably, we observe very similar characteristics and spectral features from laser ablation of a V_2O_5 sputtering target; thus, these seemingly messy targets could be an excellent source of more complex metal oxide cluster molecules.

Notably, our goal with the current study is not to identify signatures of new molecules, but to find system parameters that maximize the production of the WO molecule. To this end, we repeated the above study for a range of flow rates and pulse energies, and found that a neon flow rate of about $40 - 60$ sccm and a pulse energy of $E_p = 8$ mJ gave the best results. Increasing the pulse energy further leads to rapid target degradation, which is thought to be due to the brittle nature of the pressed targets. With optimum parameters, we found that we could produce a peak change in optical depth per ablation pulse of approximately $\Delta\tau_{pp} \sim 3 \times 10^{-6}$ for WO. However, we found the WO production from ablation of pressed powder targets to be very inconsistent between experimental runs, and we found it difficult to produce "good" targets in a consistent fashion — in fact, some targets resulted in no WO being observed in the matrix. This motivated us to develop

a more consistent method for producing WO.

5.2.2 Laser ablation of W with O_2 gas

In order to improve the consistency of WO production, we switched from ablating pressed powder targets to ablating pure W metal in the presence of O_2 gas. This is not trivial at cryogenic temperatures because O_2 freezes at a temperature of about 54 K, which is well above the typical temperature of the buffer-gas cooling cell. Therefore, we cannot simply mix O_2 gas with the neon buffer gas. Instead, we installed a secondary gas line that injects O_2 into the vicinity of the ablation target, and thermally insulated the gas line from the buffer-gas cell using a piece of Vespel.[§] With such a spacer material, the additional gas line is held at a temperature of approximately 100 K. Notably, this configuration is not restricted to O_2, and can be used for a wide variety of reactive gases. The addition of nichrome wire wrapped around the gas line allows heating as necessary. Figure 5.4 depicts the upgraded buffer-gas cooling cell. The cell is identical to that depicted in Fig. 2.1 except for the addition of the Vespel plug and stainless steel gas line with a 0.125 inch outer diameter. The plug is machined to sit nearly flush with the inner wall of the buffer-gas cooling cell, and the gas line is fixed with a teflon set screw such that it also sits nearly flush with inner wall of the cell. The flow of O_2 gas into the cell is controlled by a mass flow controller (Alicat Scientific, MC-0.5SCCM-D), and is arranged such that it intersects the ablation plume.

To study the production of WO in this configuration, we ablate W metal at 532 nm with pulse energies up to $E_p = 20$ mJ and a repetition rate of $f_r = 10$ Hz while flowing $Q_{O_2} = 0.1 - 0.2$ sccm of O_2 gas. As in other experiments, we focus the beam to a spot size of roughly 30 µm using a biconvex lens with a focal length of 400 mm. Furthermore, we constantly scan the ablation beam in two dimensions across the target to prevent localized target degradation. Figure 5.5 shows a typical FTIR spectrum acquired as described in Section 4.1 with 20 mJ ablation pulse energy. Here, we observe vibrational modes of WO, WO_2, and WO_3 in addition to O_3, where peak assignments

[§] Vespel is a polyimide material that has one of the lowest thermal conductivities at cryogenic temperatures among readily available materials.

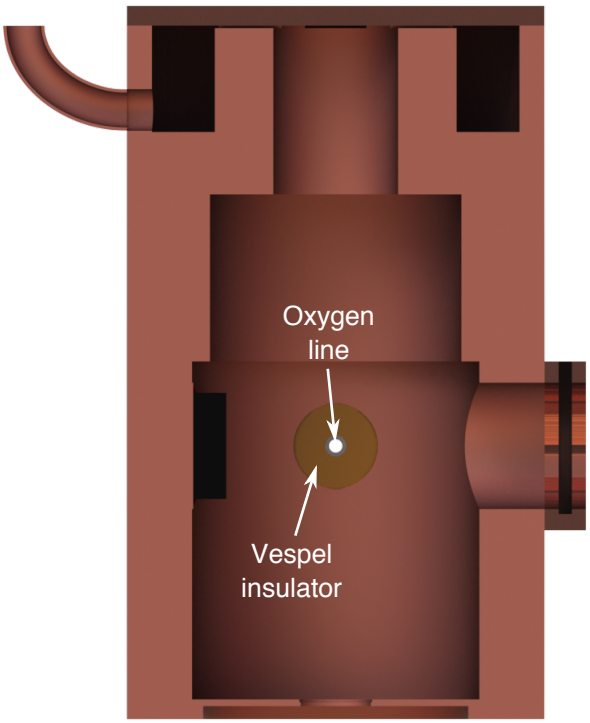

Figure 5.4: A schematic of the buffer-gas cooling cell with a secondary gas line for in-cell reactions. The cell is identical to that depicted in Fig. 2.1 except for the addition of a thermally insulated gas line for flowing oxygen gas into the vicinity of the ablation plume. A piece of Vespel acts to isolate the gas line from the cold cell.

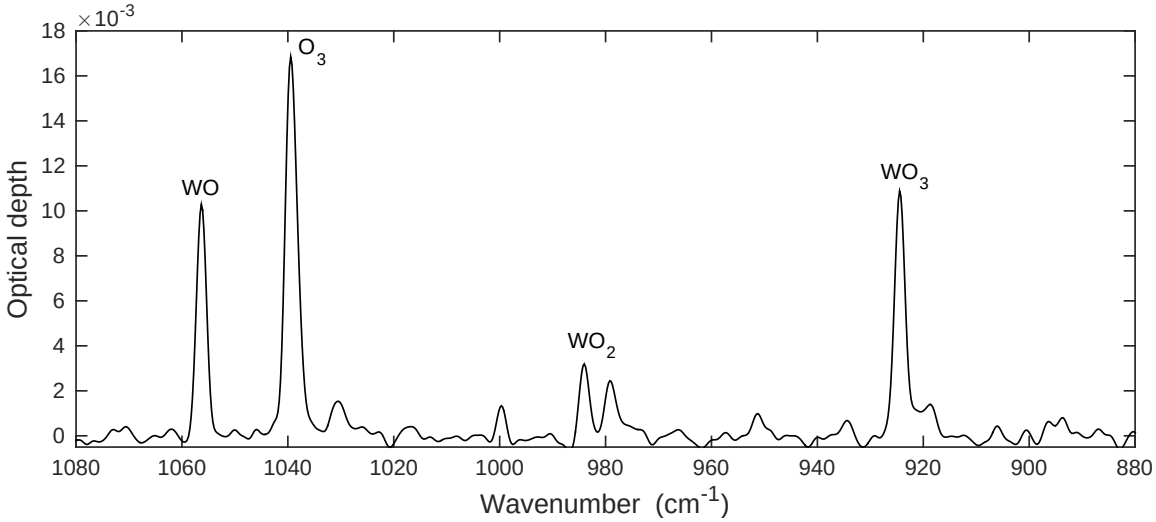

Figure 5.5: Infrared absorption spectrum of W plus O_2 gas ablation products isolated in a neon matrix at 5 K. The system parameters are $Q_{\mathrm{Ne}} = 40$ sccm, $Q_{\mathrm{O_2}} = 0.15$ sccm, $E_p = 20$ mJ, and $f_r = 10$ Hz.

are based on previous matrix isolation spectroscopy results [127, 128, 130, 134–136]. Note that the spectrum in Fig. 5.5 is acquired after 5 minutes of deposition onto the matrix window held at a temperature of about 5 K. Clearly, the broad spectral features present in the ablation of pressed WO_3 powder targets are completely absent. In addition, upon visual inspection of the neon matrix after deposition, there is no signature of a dark spot, and no dust is found inside the buffer-gas cooling cell after a few runs of ablating pure W metal. Thus, we find that ablating W metal in the presence of O_2 gas is a much cleaner method of producing WO.

We repeated the above study for a range of flow rates and pulse energies, and found that a neon flow rate of about $40 - 60$ sccm and a pulse energy of $E_p = 20$ mJ gave the best results. Increasing the pulse energy further leads to burning of either the vacuum chamber window or the buffer-gas cooling cell window, or both. To circumvent this issue, a substantially longer tube is required to move the buffer-gas cooling cell window far from the cell and very close to the vacuum chamber window. This modification would likely allow pulse energies up to 50 mJ or more to be used, which could be very advantageous for ablating a high melting point material like W. Regardless, with optimum parameters, we found that we could produce a peak change in optical depth per ablation pulse of approximately $\Delta\tau_{pp} \sim 3 - 4 \times 10^{-6}$ for WO, which is similar yield to the pressed WO_3 target. However, we found the WO production to be substantially more consistent between experimental runs, and that a piece of W metal about $1 - 2$ mm thick lasts many months.

Before proceeding to a discussion of the expected gas phase spectrum of WO, it is of interest to investigate the FTIR matrix isolation spectra of W plus O_2 gas ablation products at higher resolution to see if we can identify the isotopic splitting due to the four naturally ocurring isotopes of W. Here, we increase the FTIR spectrometer resolution to its maximum value of 0.125 cm^{-1} and acquire a single beam spectrum of the matrix isolated ablation products. Figure 5.6 shows a high resolution FTIR spectrum in a narrow band around the WO and O_3 transitions. We clearly observe the isotopic splitting of the WO vibrational transition, as well as the matrix site shift of the antisymmetric stretch vibrational mode of the O_3 molecule [136]. Note that the spectrum in Fig. 5.6 is acquired after 20 minutes of deposition onto the matrix window held at a temperature of

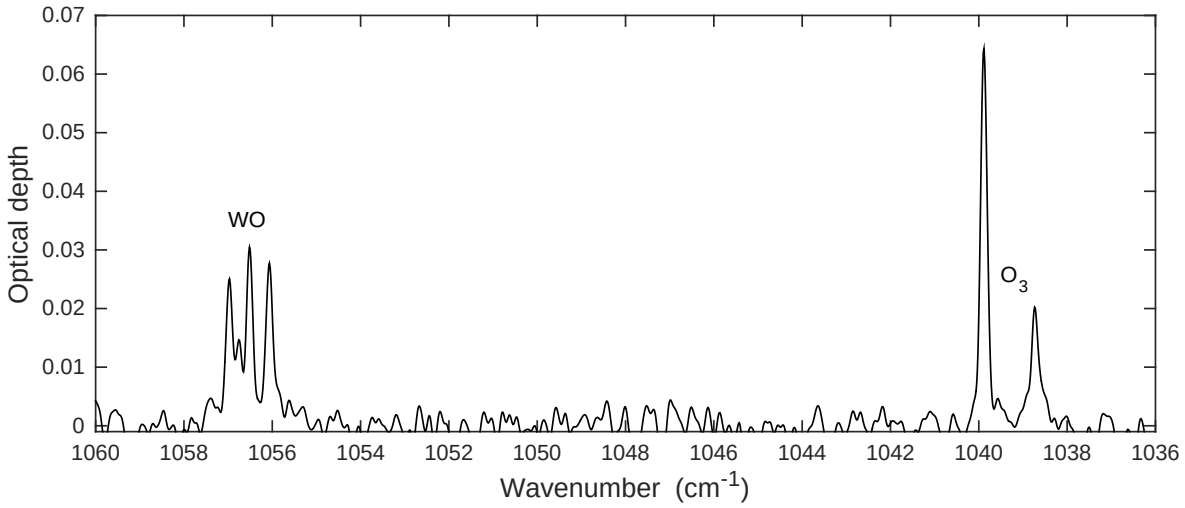

Figure 5.6: High resolution infrared absorption spectrum of W plus O_2 gas ablation products isolated in a neon matrix at 5 K. The system parameters are $Q_{\mathrm{Ne}} = 40$ sccm, $Q_{\mathrm{O_2}} = 0.1$ sccm, $E_p = 10$ mJ, and $f_r = 10$ Hz.

about 5 K. Based on the center frequency of the vibrational transition for each WO isotopologue, which is determined from a Gaussian fit of each peak, we use Eq. (5.4) to obtain $k_v = 9.6 \pm 0.5$ mdyne/Å from the slope of a linear fit. This value is in good agreement with previous work by Lorenz and Bondybey [130]; thus, we conclude that our identification of matrix isolated WO is valid and consistent with previous work.

5.3 Expected Gas Phase Absorption Signal

Given the matrix isolation spectroscopy results, we now aim to estimate the change in peak optical depth per pulse of the ablation laser for WO molecules in the gas phase. The first step is to estimate the FWHM absorption linewidth of a WO transition by calculating the contributions of the various broadening mechanisms discussed in Section 3.1.2. Here, we will assume that the molecular beam is probed very close to the exit aperture of the buffer-gas cooling cell, and that the molecules and buffer-gas atoms have equal translational temperatures. The following properties will be assumed to estimate the gas phase absorption linewidth:

- Molecule mass of $m_m = 200$ amu and neon buffer gas with $m_b = 20.18$ amu.
- Transition wavenumber of $\tilde{\nu}_0 = 1057.57$ cm^{-1}.
- Buffer-gas density of $n_b = 10^{16}$ cm^{-3} and collision cross section of $\sigma_{m,b} = 10^{-15}$ cm^2.
- Transverse temperature of $T = 25$ K and forward velocity of $u = 200$ m/s for the molecular beam.
- Probe laser beam waist of $w_0 = 100\,\mu$m.

Using these values, we find that Doppler broadening, collisional broadening, and transit time broadening result in linewidths of $\Gamma_D \sim 8$ MHz, $\Gamma_c \sim 150$ kHz, and $\Gamma_t \sim 2$ MHz, respectively. Therefore, we expect that the finite QCL linewidth on the order of $10-30$ MHz over our estimated integration time of about 5 ms will be the dominant broadening mechanism for laser absorption spectroscopy of gas phase WO.

The second step is to convert the matrix isolation spectroscopy result of $\Delta\tau_{pp} \sim 3 - 4 \times 10^{-6}$ into an equivalent value for gas phase spectroscopy. We can estimate this value in the gas phase by considering Eq. (4.2) for the infrared intensity, which is a conserved quantity. If we approximate the integral as $\int d\tilde{\nu}\ \tau(\tilde{\nu}) \approx \Delta\tilde{\nu}\ \tau_p$, and assume that the number of molecules probed in the matrix is equivalent to that in the gas phase then we obtain the following expression:

$$\tau_{pp,\mathrm{GP}} = \left(\frac{A_{\mathrm{MI}}}{A_{\mathrm{GP}}}\right)\left(\frac{\Delta\tilde{\nu}_{\mathrm{MI}}}{\Delta\tilde{\nu}_{\mathrm{GP}}}\right)\tau_{pp,\mathrm{MI}}, \tag{5.15}$$

where A_{MI} and A_{GP} are the areas probed in matrix isolation and gas phase spectroscopy, respectively, and $\Delta\tilde{\nu}_{\mathrm{MI}}$ and $\Delta\tilde{\nu}_{\mathrm{GP}}$ are the absorption linewidths in matrix isolation and gas phase spectroscopy, respectively. For matrix isolation, we assume that the molecules are uniformly distributed over the cold window of area $A_{\mathrm{MI}} \sim 5$ cm^2 and that the absorption linewidth is that of the FTIR spectrometer $\Delta\tilde{\nu}_{\mathrm{MI}} = 1$ cm^{-1} or 30 GHz. For gas phase, we assume a beam velocity of 200 m/s, a beam diameter of 5 mm, and a molecule pulse length of 5 ms, which corresponds to an effective area of $A_{\mathrm{GP}} = 50$ cm^2. Furthermore, we assume a QCL linewidth of $\Delta\tilde{\nu}_{\mathrm{GP}} = 30$ MHz, which leads to a peak change in optical depth per pulse of the ablation laser of $\Delta\tau_{pp,\mathrm{GP}} \sim 3 - 4 \times 10^{-4}$ for gas phase spectroscopy.

Finally, the distribution of WO molecules among rotational and vibrational states must be considered. This distribution is strongly dependent on the temperature of the molecules entrained in the buffer-gas beam. Assuming the molecules are in the ground electronic state with $\Omega = 0$, we write the rotational and vibrational partition functions in a simplified form as [27]

$$Z_r \approx \left(\frac{k_B T_r}{hcB_e}\right)\exp\left(\frac{hcB_e}{3k_B T_r}\right), \tag{5.16}$$

$$Z_v = \frac{1}{2\sinh\left(\frac{hc\omega_e}{2k_B T_v}\right)}, \tag{5.17}$$

respectively, where the centrifugal distortion and anharmonic correction terms have been neglected for simplicity. Here, we have defined separate rotational and vibrational temperatures, denoted by T_r and T_v, respectively, because the rotational degree of freedom is typically in equilibrium with the buffer gas while the vibrational degree of freedom is not (see discussion in Section 2.1.3).

Therefore, it is difficult to precisely estimate the number of populated vibrational states. Using the spectroscopic constants for ^{184}WO from Ref. [132] we find $Z_r \sim 40$ for $T_r = 25$ K, and $Z_v \sim 5$ for the worst case scenario of $T_v = 5000$ K (i.e., no vibrational relaxation occurs after ablation). Furthermore, the molecule population will be spread over the four naturally occurring isotopes of W; thus, in the worst case situation, we could have molecules spread over approximately 800 states. However, in a more likely scenario we will have $Z_v \sim 1$ and $Z_r \sim 10$ due to additional collisional cooling in the molecular beam, and the molecule population will be spread over approximately 40 states. Thus, we expect a change in peak optical depth per pulse of the ablation laser in the range of $\Delta\tau_{pp,\mathrm{GP}} = 10^{-6} - 10^{-5}$. Notably, this is on the order of $2 - 20$ times larger than the minimum detectable optical depth of $\tau_{\mathrm{min}} \approx 5 \times 10^{-7}$ for 20 µW incident on the detectors and a 5 ms integration time, as determined by Eq. (3.16).

5.4 Summary

We have investigated the production of WO using a cryogenic buffer-gas beam source, and found that ablating pure W metal in the presence of O_2 gas is a reliable and consistent source of WO molecules. Using matrix isolation spectroscopy, we identified a number of different molecules present in the buffer-gas beam including WO_2, WO_3, and larger polyatomic tungsten oxides, as well as an appreciable amount of O_3. To date, we have been unsuccessful in observing rotational-vibrational spectra of WO in the gas phase using the tunable diode laser absorption spectroscopy system described in Section 3.4.5. We attribute this to a lack of sensitivity; thus, it is necessary to both increase the production of WO by increasing the ablation laser pulse energy, and decrease the noise floor of the spectroscopy system through incorporation detectors with lower $1/f$ noise or a modulation scheme.

Chapter 6

Conclusion to Part 1

6.1 Summary

This first part of this dissertation has investigated the application of a buffer-gas beam source to the production of large polyatomic molecules, including carbon clusters and metal oxide molecules. The original motivation for this work was based on the longer collisional cooling timescale available with buffer-gas beam sources compared to traditional free jet sources. Indeed, the possibility of achieving lower internal state temperatures for large, strongly bound clusters is of general interest, and would aid in determining the structure of these complex molecules. Used in conjunction with a high resolution infrared spectroscopy system, such a source would help to remove much of the ambiguity associated with the spectral assignment process, and provide validation for the large variety of theoretical techniques currently being used in conjunction with experiments to determine molecular structures.

In Chapter 2 and 3, we outlined the major experimental techniques used in this dissertation work. Chapter 2 provided a detailed background on collisional cooling and beam formation in cryogenic buffer-gas beam sources, and compared the source used in this dissertation to a traditional free jet source. It was found that the number of collisions between buffer gas atoms and the molecules of interest is likely lower in our buffer-gas beam source compared to a traditional free jet source; however, the buffer-gas beam source has much more design flexibility such that improvements can be made. Chapter 3 provided a detailed background on infrared absorption spectroscopy, including the techniques of Fourier transform infrared spectroscopy, matrix isolation spectroscopy,

wavelength modulation spectroscopy, and direct absorption spectroscopy with a tunable diode laser system. The performance of various aspects of the experimental apparatus was also presented in Chapter 3.

In Chapter 4, we discussed production of carbon clusters C_3 to C_{12} using a cryogenic buffer-gas beam source. For each of the C_3 to C_9 molecules, we estimated a production rate on the order of $10^{11} - 10^{12}$ molecules per pulse of the ablation laser based on infrared intensities determined from density functional theory calculations. Similar to other buffer-gas beam experiments, we observed an initial linear increase in molecule production with neon flow rate followed by a decrease at high flow rates (i.e., high neon density in the cell). We attribute this decrease at high flow rates to a reduction in the diffusion time for molecules to be lost to the cell walls. Notably, the results presented in Chapter 4 highlight an interesting aspect of the buffer-gas beam source – it performs very similarly for a wide range of molecule masses from 36 amu to 144 amu.

In Chapter 5, we investigated the production of WO using a cryogenic buffer-gas beam source, and found that ablating pure W metal in the presence of O_2 gas is a reliable and consistent source of WO molecules. Using matrix isolation spectroscopy, we identified a number of different molecules present in the buffer-gas beam, including WO_2, WO_3, and larger polyatomic tungsten oxides, as well as an appreciable amount of O_3. To date, we have been unsuccessful in observing rotational-vibrational spectra of WO in the gas phase using the tunable diode laser absorption spectroscopy system described in Section 3.4.5. We attribute this to a lack of sensitivity; thus, it is crucial to both increase the production of WO by increasing the ablation laser pulse energy, and decrease the noise floor of the spectroscopy system either through incorporation of detectors with lower $1/f$ noise or developing a modulation scheme free from residual amplitude modulation effects.

6.2 Future Outlook

In moving forward on this project, there are a number of apparatus upgrades that could be made to improve system performance. Firstly, the buffer-gas cooling cell geometry can be optimized to increase the number of collisions as well as extraction from the cell and beam formation. For

example, increasing the inner cell dimensions would allow more collisions to occur inside the cell before molecules are extracted. Additionally, tapering the cell at the exit aperture would promote laminar flow and prevent eddies from forming, which can trap molecules and force them towards the cell walls. Secondly, the signal-to-noise ratio of the tunable diode laser absorption spectroscopy system could be improved dramatically by locking the laser to a tunable cavity. This could largely eliminate much of the low frequency noise that plagues the Daylight Solutions QCL, and ultimately limits the detection sensitivity. Furthermore, this could reduce the laser linewidth to the sub-MHz regime, which is generally advantageous for spectroscopy. Additionally, MCT detectors with a lower transimpedance gain would be beneficial as more laser power could be used to probe molecular transitions, which effectively reduces the shot noise limited detection sensitivity. The limiting factor in this regard is the linear operating regime of the MCT detector – balanced subtraction does not work if the signal and reference beams are not linearly proportional. Finally, incorporation of a better multipass cell would increase the signal by a factor of $10 - 100$.

In regards to science, there is a plethora of interesting molecular systems that can be studied with the apparatus described in this dissertation. For example, it would be very interesting to optimize the buffer-gas beam source to produce larger metal oxide molecules such as V_4O_{10}, which has a vibrational transition around 1030 cm^{-1}; thus, in principle rotational-vibrational transitions could be probed in the gas phase with the QCL system. Notably, such a study would provide unprecedented resolution for the infrared spectra of large metal oxide cluster molecules, the investigation of which has been largely confined to action spectroscopy techniques [137]. In addition, other molecules, like metal carbides and hydrides, for example, could be produced by flowing reactive gases into the buffer-gas cell via the secondary gas line installed to produce WO.

Another interesting research avenue would be to investigate the production of free radicals with the buffer-gas beam source. Coupled with the matrix isolation spectroscopy technique, chemical reactions involving free radicals could be investigated, and undetermined reaction intermediates could be isolated and probed with the Fourier transform spectrometer. For example, CH could be produced via ablation of graphite in the presence of hydrogen gas, and trapped in a neon matrix

with excess oxygen to study intermediates of the reaction $CH + O_2$, which has a number of different product channels [138]. Such reactions have widespread applicability, particularly to the chemistry of the interstellar medium where many reactions occur at low temperature.

Part 2: Dynamics of Bose Gases in Spherical Symmetry

Chapter 7

Introduction to Part 2*

In strongly interacting systems, the study of collective modes of a quantum many-body problem provides revealing information about the nature of the underlying Hamiltonian. In ultracold atomic gases, due to the fact that binary interactions between particles at low energy are well understood, the experimental measurement of collective modes provides a means of evaluating many-body theoretical methods used to describe these systems. Experiments probing the collective modes of ultracold gases were carried out shortly after the demonstration of Bose-Einstein condensation in a dilute atomic vapor [140, 141]. In early experiments at JILA [142] and MIT [143], the low-lying quadrupole modes of a nearly pure Bose-Einstein condensate (BEC) were excited, and the observed oscillation frequencies showed good agreement with the Bogoliubov spectrum [144, 145]. Experiments were then conducted over a range of temperatures below the critical point, and temperature-dependent shifts in the oscillation frequencies and damping rates were observed [146, 147]. At the time, existing theoretical models were unable to reproduce the experimental observations.

The observation of these unexplained temperature-dependent shifts motivated further exploration of collective-mode behavior at finite temperature, where experiments probed the interaction between the condensate and thermal component of the gas (i.e., noncondensate). Experiments on the scissors modes [148] provided an alternative means of measurement of temperature-dependent shifts of the mode frequencies and damping rates through observation of the angle oscillations of the condensate and noncondensate, and reasonable agreement with existing theories was found. Fur-

* A version of this chapter has been published in Ref. [139].

thermore, a study of the transverse breathing mode in an elongated harmonic trap [149] found uncharacteristically small damping rates and observed that the mode frequency was quasi-independent of temperature.

In order to address the unexpected behavior of the experiments, models were initially developed to explain the anomalous temperature dependence of the quadrupole mode found in Ref. [146]. Early efforts assuming a static noncondensate were unable to reproduce the experimental results; however, inclusion of the dynamics of the noncondensate lead to a consistent framework that matched the experiment. Using a semi-classical coupled-modes model, Stoof, Bijlsma, and Al Khawaja [150, 151] described the coupled dynamics of the condensate and noncondensate in terms of in-phase and out-of-phase eigenmodes, which are collisionless analogs of first and second sound hydrodynamic modes [152–154]. They concluded that the anomalous behavior found in Ref. [146] was the result of simultaneous excitation of both eigenmodes of the system. Numerical simulation of the Zaremba-Nikuni-Griffin (ZNG) equations by Jackson and Zaremba [155–157] confirmed this picture, and Morgan, Rusch, Hutchinson, and Burnett provided additional analysis in an extension of their previous work [158–162]. These efforts highlighted the important role of the noncondensate dynamics in the behavior of collective modes at finite temperature.

Experiments to date have operated with anisotropic trapping geometries, which lead to an increased degree of complexity in the collective-mode spectrum. An isotropic harmonic trap simplifies the mode spectrum due to its spherical symmetry, and allows for a detailed comparison between experimental measurements and existing theoretical models. Furthermore, a spherical trapping geometry eases the computational burden of sophisticated numerical studies such as the simulation of the ZNG equations. However, experiments in this regime face the technological hurdle of minimizing asphericities in the trapping potential, which, previous to the work described here, has prevented the study of collective modes in such a simplified geometry. Thus, fundamental comparisons between theoretical predictions for the collective-mode spectrum of condensates, as well as their frequency shifts and damping rates at finite temperature, had not been made.

Prior to the work presented here, Lobser et al. [163] investigated the monopole mode of a

classical gas of ^{87}Rb atoms confined in an isotropic harmonic trap in an effort to test a prediction from Boltzmann that the monopole mode does not damp in time. Lobser et al. found that the monopole mode was practically undamped, with a small residual damping rate due to minor imperfections in the trap geometry. A detailed theoretical analysis of the experiment found that the residual damping rate of the monopole mode was caused primarily by anharmonicity along one axis of the trap, and identified a range of collision rates that minimized the residual damping [164]. Given the success of the experiment and theoretical analysis for a classical gas, we were motivated to investigate the behavior of the monopole mode in an isotropic harmonic trap below the Bose-Einstein condensation transition temperature. In this regime, it is expected that the interplay between the condensed and non-condensed portions of the gas will give rise to dynamics not observed above the transition temperature. Indeed, the results of D. S. Lobser's experiment below the transition temperature showed interesting behavior — the oscillation amplitude of the monopole mode exhibited damping and a characteristic modulation in time [165]. Thus, the work presented here describes our methods, analysis, and interpretation of the experimental results.

The second part of this dissertation begins by outlining the theoretical basis of the ZNG method. Following this background material, a detailed description of a code developed to numerically solve the ZNG equations in an isotropic harmonic trap is given. Given the spherical symmetry of such a problem, the dimensionality of the ZNG equations can be reduced, resulting in a fast and accurate code for investigating the unique problem of the monopole mode of a finite temperature Bose gas confined in an isotropic harmonic trap. Thus, the final chapter in the second part of this dissertation provides a detailed analysis of this problem including both experimental data and numerical results from the developed spherically symmetric ZNG code.[†]

[†] The final chapter of this dissertation represents a publication that was a collaborative effort between the author of this dissertation, Victor E. Colussi, Matthew J. Davis, Dan S. Lobser, Murray J. Holland, Dana Z. Anderson, Heather J. Lewandowski, and Eric A. Cornell [139]. The author of this dissertation was the primary author of the paper, and performed numerical simulations using the ZNG method and analyzed the experimental data. V. E. Colussi performed a theoretical analysis of the monopole mode problem in the collisionless regime, M. J. Davis performed numerical simulations using classical field methods, and D. S. Lobser conducted the experiments. M. J. Holland, H. J. Lewandowski, and E. A. Cornell provided project definition and guidance throughout. All authors contributed to interpretation of the results.

Chapter 8

Background for the ZNG Method

This chapter provides an outline of the theoretical basis for the ZNG equations. It begins with a brief discussion of the phenomenon of Bose-Einstein condensation in an isotropic harmonic trap, given in the context of an ideal gas of non-interacting particles. To move beyond this simple treatment, the system Hamiltonian for a gas of weakly interacting particles is introduced and an equation of motion for the condensate at zero temperature is derived. In order to move beyond the zero temperature limit, fluctuations about the condensed state are introduced perturbatively and an equation of motion that governs their evolution is given. Thus, the end result is a closed system of self-consistent equations that describe the dynamical evolution of a degenerate Bose gas at finite temperature.

8.1 Bose-Einstein Condensation in an Isotropic Harmonic Trap

At room temperature, a gas of identical particles behave classically, and are well described by a Boltzmann distribution function. In this limit, the thermal de Broglie wavelength Λ is small compared to the interparticle spacing ($\propto n^{-1/3}$, where n is the density) and quantum effects can be ignored. As the temperature decreases, however, quantum effects become relevant and the nature of the individual particles becomes important. For bosons, there exists a critical temperature T_c at which point Λ becomes comparable to the interparticle spacing and a phase transition known as Bose-Einstein condensation can occur. In contrast to the room temperature case, where individual energy states of the system have a mean occupation much less than unity, in the presence of Bose-

Einstein condensation there exists a macroscopic occupation of the lowest energy state of the system (i.e., the condensate).

The temperature at which Bose-Einstein condensation occurs can be calculated for an isotropic harmonic trap via the equilibrium Bose-Einstein distribution function

$$f_0\left(\epsilon_i\right) = \frac{1}{e^{\beta(\epsilon_i - \mu)} - 1}, \tag{8.1}$$

where $\beta = 1/k_B T$ with k_B Boltzmann's constant and T the temperature of the gas, ϵ_i is the energy of state i in the system, and μ is the equilibrium chemical potential. At room temperature, the chemical potential is small and negative such that $\mu \ll \epsilon_0$, where ϵ_0 is the lowest energy state of the system. In this regime, the Bose-Einstein distribution is approximately equal to the classical Boltzmann distribution. As the temperature is lowered, the chemical potential increases to the point where $\mu = \epsilon_0$ and the mean occupation of the lowest energy state diverges. This is precisely the point at which Bose-Einstein condensation occurs; thus, we can define T_c as the temperature at which $\mu = \epsilon_0$ and all particles in the gas occupy excited states such that

$$N = \int_0^\infty \frac{d\epsilon g\left(\epsilon\right)}{e^{\beta\epsilon} - 1}, \tag{8.2}$$

where N is the number of particles in excited states, and $g\left(\epsilon\right) = \epsilon^2/2\left(\hbar\omega\right)^3$ is the density of states for an isotropic harmonic trap with frequency ω [166]. Assuming N is large, the zero point energy of the harmonic trap is neglected and $\mu = \epsilon_0 \approx 0$ is used in the above equation. Evaluating the integral and equating $T_c \equiv T$ gives the critical temperature for a Bose gas confined in an isotropic harmonic trap:

$$k_B T_c = \hbar\omega \left(\frac{N}{\zeta\left(3\right)}\right)^{1/3}, \tag{8.3}$$

where $\zeta\left(s\right)$ is the Riemann zeta function. We can then use this result to define the number of atoms in the condensate, N_c, below the critical temperature to be

$$N_c = N\left[1 - \left(\frac{T}{T_c}\right)^3\right]. \tag{8.4}$$

Clearly, unless $T = 0$ some of the atoms remain in higher energy states of the system (i.e., the noncondensate). Thus, to obtain a full description of the system at finite temperature it is necessary

to include the dynamics of both the condensate and noncondensate, as well as the interactions between them. To accomplish this task, we must go beyond the above analysis, which assumes an ideal, non-interacting gas of identical particles. The following sections outline a theory for finite temperature Bose gases in the weakly interacting limit.

8.2 Many-Body System Hamiltonian

In the dilute, weakly interacting limit of Bose gases only binary collisions (i.e., two-body interactions) are relevant, and the Hamiltonian for a system of N interacting particles is written in second quantization as [167]

$$\begin{aligned} \hat{H} &= \int d^3\mathbf{r}\ \hat{\Psi}^\dagger(\mathbf{r},t)\,\hat{H}_0\hat{\Psi}(\mathbf{r},t) \\ &+ \frac{1}{2}\int\int d^3\mathbf{r}\ d^3\mathbf{r}'\hat{\Psi}^\dagger(\mathbf{r},t)\,\hat{\Psi}^\dagger\left(\mathbf{r}',t\right)V\left(\mathbf{r}-\mathbf{r}'\right)\hat{\Psi}\left(\mathbf{r}',t\right)\hat{\Psi}(\mathbf{r},t), \end{aligned} \tag{8.5}$$

where $\hat{H}_0 = \hbar^2\nabla^2/(2m) + V_{\text{ext}}(\mathbf{r},t)$ is the Hamiltonian for a single particle of mass m confined in an external potential $V_{\text{ext}}(\mathbf{r},t)$ and $V(\mathbf{r}-\mathbf{r}')$ represents the two-body interaction potential. Here, $\hat{\Psi}^\dagger(\mathbf{r},t)$ and $\hat{\Psi}(\mathbf{r},t)$ are Bose field operators that represent the addition (creation) or removal (annihilation), respectively, of a particle at position $\mathbf{r}$ and time t. Such field operators can be constructed from a linear combination of suitable basis states

$$\hat{\Psi}(\mathbf{r},t) = \sum_i \hat{a}_i(t)\,\phi_i(\mathbf{r},t), \tag{8.6}$$

$$\hat{\Psi}^\dagger(\mathbf{r},t) = \sum_i \hat{a}_i^\dagger(t)\,\phi_i^*(\mathbf{r},t), \tag{8.7}$$

where the summation is carried over a complete set of single-particle basis states $\phi_i(\mathbf{r},t)$, and $\hat{a}_i^\dagger(t)$ and $\hat{a}_i(t)$ are creation and annihilation operators, respectively, for state i. For bosons, these operators satisfy the usual commutation relations:

$$\left[a_i, a_j^\dagger\right] = \delta_{ij}, \tag{8.8}$$

$$\left[\hat{\Psi}(\mathbf{r},t), \hat{\Psi}^\dagger\left(\mathbf{r}',t\right)\right] = \delta\left(\mathbf{r}-\mathbf{r}'\right), \tag{8.9}$$

$$\left[a_i^\dagger, a_j^\dagger\right] = [a_i, a_j] = 0, \tag{8.10}$$

$$\left[\hat{\Psi}^\dagger(\mathbf{r},t), \hat{\Psi}^\dagger\left(\mathbf{r}',t\right)\right] = \left[\hat{\Psi}(\mathbf{r},t), \hat{\Psi}\left(\mathbf{r}',t\right)\right] = 0. \tag{8.11}$$

In this dissertation, we are concerned with dilute gases at low temperature such that binary collisions can be treated approximately as localized, perfectly elastic collisions like those between billiard balls. In this so-called s-wave scattering regime, the two-body interaction potential is approximated by [166]

$$V\left(\mathbf{r}-\mathbf{r}'\right) \approx g\ \delta\left(\mathbf{r}-\mathbf{r}'\right), \tag{8.12}$$

where $g = 4\pi\hbar^2 a_s/m$ characterizes the interaction strength, and a_s is the s-wave scattering length for a given atomic species. Making this substitution in the many-body Hamiltonian of Eq. (8.5) results in:

$$\begin{aligned} \hat{H} &= \int d^3\mathbf{r}\ \hat{\Psi}^\dagger(\mathbf{r},t)\,\hat{H}_0\hat{\Psi}(\mathbf{r},t) \\ &+ \frac{g}{2}\int d^3\mathbf{r}\ \hat{\Psi}^\dagger(\mathbf{r},t)\,\hat{\Psi}^\dagger(\mathbf{r},t)\,\hat{\Psi}(\mathbf{r},t)\,\hat{\Psi}(\mathbf{r},t). \end{aligned} \tag{8.13}$$

This Hamiltonian represents the starting point for the subsequent discussion of the dynamical evolution of the Bose field operator $\hat{\Psi}(\mathbf{r},t)$.

8.3 Equations of Motion

In the Heisenberg picture, we can derive an equation of motion for $\hat{\Psi}(\mathbf{r},t)$ as follows:

$$\begin{aligned} i\hbar\frac{\partial\hat{\Psi}(\mathbf{r},t)}{\partial t} &= \left[\hat{\Psi}(\mathbf{r},t),\ \hat{H}\right] \\ &= \hat{H}_0\hat{\Psi}(\mathbf{r},t) + g\hat{\Psi}^\dagger(\mathbf{r},t)\,\hat{\Psi}(\mathbf{r},t)\,\hat{\Psi}(\mathbf{r},t). \end{aligned} \tag{8.14}$$

To proceed in the presence of Bose-Einstein condensation, it is convenient to separate the condensate contribution from the remainder of $\hat{\Psi}(\mathbf{r},t)$. Assuming a single state of the system is macroscopically occupied with $N_0 \gg 1$ atoms (i.e., the condensate) the Bose field operator is split into two parts,

$$\hat{\Psi}(\mathbf{r},t) = \hat{\phi}(\mathbf{r},t) + \hat{\delta}(\mathbf{r},t), \tag{8.15}$$

where $\hat{\phi}(\mathbf{r},t)$ is a field operator for the atoms in the state occupied by the condensate and $\hat{\delta}(\mathbf{r},t)$ represents atoms occupying all other states of the system (i.e., the noncondensate). Once again,

these new field operators can be represented in a suitable basis as

$$\hat{\phi}\left(\mathbf{r},t\right) = \hat{a}_0\left(t\right)\phi_0\left(\mathbf{r},t\right), \tag{8.16}$$

$$\hat{\delta}\left(\mathbf{r},t\right) = \sum_{i\neq 0}\hat{a}_i\left(t\right)\phi_i\left(\mathbf{r},t\right), \tag{8.17}$$

where it is assumed that the condensate occupies the lowest state ($i = 0$) of the system and the noncondensate occupies all other states ($i \neq 0$). Since we are assuming that state $i = 0$ is macroscopically occupied and $N_0 \gg 1$, we can make a simplification based on the following argument. Let state $i = 0$ be represented by $|N_0\rangle$ in the occupation number representation such that

$$\hat{a}_0^{\dagger}|N_0\rangle = \sqrt{N_0+1}\,|N_0+1\rangle \approx \sqrt{N_0}\,|N_0\rangle\,,$$
$$\hat{a}_0|N_0\rangle = \sqrt{N_0}\,|N_0-1\rangle \approx \sqrt{N_0}\,|N_0\rangle\,,$$

where $N_0 \pm 1 \approx N_0$ holds true as long as $N_0 \gg 1$. Under this assumption $\hat{a}_0^{\dagger}$ and $\hat{a}_0$ approximately commute, and we can make the replacement $\hat{a}_0^{\dagger} \approx \hat{a}_0 \approx \sqrt{N_0}$, which is commonly referred to as the Bogoliubov approximation [168]. Thus, the field operator $\hat{\Psi}\left(\mathbf{r},t\right)$ can be decomposed as

$$\hat{\Psi}\left(\mathbf{r},t\right) \approx \phi\left(\mathbf{r},t\right) + \hat{\delta}\left(\mathbf{r},t\right), \tag{8.18}$$

where the condensate wavefunction is given by the complex number $\phi\left(\mathbf{r},t\right) = \sqrt{N_0}\ \phi_0\left(\mathbf{r},t\right)$ and all operator dependence is contained in $\hat{\delta}\left(\mathbf{r},t\right)$. Thus, $\hat{\delta}\left(\mathbf{r},t\right)$ represents fluctuations of the system about the condensed state. Note that the Bogoliubov approximation does not conserve particle number since we have explicitly assumed that adding or removing an atom from the condensate does not change the state of the system.

In what follows, equations of motion for both the condensed and non-condensed portions of the Bose gas will be derived. To aid with readability, the following variables and notation will be used to describe properties of the system: $n\left(\mathbf{r},t\right)$ and N represent the total density and number of atoms, respectively, in the system; $n_c\left(\mathbf{r},t\right)$ and N_c represent the density and number of atoms, respectively, in the condensate; $\tilde{n}\left(\mathbf{r},t\right)$ and $\tilde{N}$ represent the density and number of atoms,

respectively, in the noncondensate (therefore, $n(\mathbf{r},t) = n_c(\mathbf{r},t) + \tilde{n}(\mathbf{r},t)$ and $N = N_c + \tilde{N}$); the subscript "c" will be used to denote condensate quantities; a tilde ($\sim$) over symbols will be used to represent non-condensate quantities; and the subscript "0" will be used to denote equilibrium quantities. Given this notation, and working within the Bogoliubov approximation, the densities and number of particles in the condensed and non-condensed portions of the system are given by

$$n_c(\mathbf{r},t) = |\phi(\mathbf{r},t)|^2, \tag{8.19}$$

$$\tilde{n}(\mathbf{r},t) = \langle \hat{\delta}^\dagger(\mathbf{r},t)\,\hat{\delta}(\mathbf{r},t)\rangle, \tag{8.20}$$

where the total number of particles in the system is $N = \int d^3\mathbf{r}\,[n_c(\mathbf{r},t) + \tilde{n}(\mathbf{r},t)] = N_c + \tilde{N}$.

8.3.1 Zero-temperature limit

In the limit that $T = 0$, all atoms in the Bose gas occupy the condensate such that $\hat{\delta}(\mathbf{r},t) = \hat{\delta}^\dagger(\mathbf{r},t) = 0$. Taking an ensemble average of Eq. (8.14) in this limit, and using the fact that $\langle\hat{\Psi}(\mathbf{r},t)\rangle = \phi(\mathbf{r},t)$, results in the Gross-Pitaevskii equation (GPE) [166],

$$i\hbar\frac{\partial\phi(\mathbf{r},t)}{\partial t} = \left[-\frac{\hbar^2}{2m}\nabla^2 + V_{\text{ext}}(\mathbf{r},t) + g\,|\phi(\mathbf{r},t)|^2\right]\phi(\mathbf{r},t), \tag{8.21}$$

where $\phi(\mathbf{r},t)$ is normalized to the total number of atoms in the condensate – $\int d^3\mathbf{r}\,|\phi(\mathbf{r},t)|^2 = N_c$. The GPE is a nonlinear Schrödinger equation that describes the dynamical evolution of the condensate wavefunction. The potential acting on the atoms in the condensate is the sum of the external potential and a nonlinear term that represents the mean-field potential produced by two-body interactions between all atoms in the condensate.

Stationary states of the GPE can be found by minimizing the energy of the system:

$$\begin{aligned} E_c(\phi) &= \langle\phi^*(\mathbf{r})|\,\hat{H}\,|\phi(\mathbf{r})\rangle \\ &= \int d^3\mathbf{r}\left[\frac{\hbar^2}{2m}|\nabla\phi(\mathbf{r})|^2 + V_{\text{ext}}(\mathbf{r})\,|\phi(\mathbf{r})|^2 + \frac{g}{2}|\phi(\mathbf{r})|^4\right]. \end{aligned} \tag{8.22}$$

However, care must be taken as a result of the Bogoliubov approximation, which violates particle number conservation. The energy minimization must occur subject to the constraint that the

number of particles in the condensate remains constant. Therefore, the energy of the system is minimized in the grand-canonical ensemble, $E_c - \mu_{c,0} N_c$, where $\mu_{c,0}$ is the equilibrium chemical potential. The minimal energy state is found by setting the functional derivative $\delta E_c - \mu_{c,0} \delta N_c = 0$. This procedure results in the time-independent GPE:

$$\mu_{c,0} \phi_0 (\mathbf{r}) = \left[-\frac{\hbar^2}{2m} \nabla^2 + V_{\text{ext}} (\mathbf{r}) + g \left| \phi_0 (\mathbf{r}) \right|^2 \right] \phi_0 (\mathbf{r}) , \tag{8.23}$$

where the chemical potential $\mu_{c,0}$ represents the eigenvalue of the condensate rather than the energy per particle as in the case of the standard Schrödinger equation; these two quantities are equivalent only in the limit of non-interacting particles.

Before proceeding to a discussion of the finite temperature ZNG theory, it is advantageous to introduce an alternative system of equations that describe the dynamical evolution of the condensate in terms of its density and the gradient of its phase. This leads to two equations of motion akin to the hydrodynamic equations for a classical fluid, and provides a description of local quantities of the condensate that arise in the ZNG theory. To proceed, we can write the condensate wavefunction in terms of its density and phase,

$$\phi (\mathbf{r}, t) = \sqrt{n_c (\mathbf{r}, t)} \, e^{i \theta (\mathbf{r}, t)}, \tag{8.24}$$

where $n_c (\mathbf{r}, t) = \left| \phi (\mathbf{r}, t) \right|^2$ as defined above and $\theta (\mathbf{r}, t) = \arg [\phi (\mathbf{r}, t)] = \arctan [\phi^* (\mathbf{r}, t) / \phi (\mathbf{r}, t)]$. Making this substitution in Eq. (8.21) and equating real and imaginary parts results in the following two coupled equations [166]:

$$\frac{\partial n_c (\mathbf{r}, t)}{\partial t} + \nabla \cdot [n_c (\mathbf{r}, t) \, \mathbf{v}_c (\mathbf{r}, t)] = 0, \tag{8.25}$$

$$\frac{\partial \mathbf{p}_c (\mathbf{r}, t)}{\partial t} - \nabla \epsilon_c (\mathbf{r}, t) = 0, \tag{8.26}$$

where the following local properties of the condensate have been introduced:

$$\mu_c (\mathbf{r}, t) = -\frac{\hbar^2}{2m \sqrt{n_c (\mathbf{r}, t)}} \nabla^2 \sqrt{n_c (\mathbf{r}, t)} + V_{\text{ext}} (\mathbf{r}, t) + g n_c (\mathbf{r}, t) , \tag{8.27}$$

$$\mathbf{p}_c (\mathbf{r}, t) = \hbar \nabla \theta (\mathbf{r}, t) , \tag{8.28}$$

$$\epsilon_c (\mathbf{r}, t) = \mu_c (\mathbf{r}, t) + \frac{1}{2m} \left| \mathbf{p}_c (\mathbf{r}, t) \right|^2 . \tag{8.29}$$

Here, $\mu_c(\mathbf{r},t)$ is the local chemical potential (i.e., potential energy) of the condensate, $\mathbf{p}_c(\mathbf{r},t)$ is the local superfluid momentum (i.e., kinetic energy) of the condensate, and $\epsilon_c(\mathbf{r},t)$ represents the total energy of an atom in the condensate as the sum of the local potential and kinetic energies. These localized quantities are a necessary component of the ZNG theory, which is described in the next section.

8.3.2 Finite temperature – the ZNG method

When $T > 0$ we can no longer neglect the fluctuations of the system described by the operator $\hat{\delta}(\mathbf{r},t)$. Taking an ensemble average of Eq. (8.14) and using the fact that $\langle\hat{\Psi}(\mathbf{r},t)\rangle = \phi(\mathbf{r},t)$ once again results in an equation of motion for the condensate wavefunction:

$$i\hbar\frac{\partial\phi(\mathbf{r},t)}{\partial t} = \left[-\frac{\hbar^2}{2m}\nabla^2 + V_{\text{ext}}(\mathbf{r},t)\right]\phi(\mathbf{r},t) + g\langle\hat{\Psi}^\dagger(\mathbf{r},t)\,\hat{\Psi}(\mathbf{r},t)\,\hat{\Psi}(\mathbf{r},t)\rangle, \tag{8.30}$$

where the operator triplet represents the effects of two-body interactions with contributions from both the condensate and non-condensate. The operator triplet on the right-hand side of the above equation can be expanded and simplified by first utilizing the Bogoliubov approximation of Eq. (8.18),

$$\hat{\Psi}^\dagger\hat{\Psi}\hat{\Psi} = |\phi|^2\phi + \phi^*\hat{\delta}\hat{\delta} + 2|\phi|^2\hat{\delta} + \phi^2\hat{\delta}^\dagger + 2\phi\hat{\delta}^\dagger\hat{\delta} + \hat{\delta}^\dagger\hat{\delta}\hat{\delta}, \tag{8.31}$$

and then taking an ensemble average of the resulting expression:

$$\langle\hat{\Psi}^\dagger\hat{\Psi}\hat{\Psi}\rangle = n_c\phi + \tilde{m}\phi^* + 2\tilde{n}\phi + \langle\hat{\delta}^\dagger\hat{\delta}\hat{\delta}\rangle, \tag{8.32}$$

where the space and time dependence has been omitted for clarity, n_c and $\tilde{n}$ are given by Eqs. (8.19) and (8.20), respectively, and the property $\langle\hat{\delta}\rangle = \langle\hat{\delta}^\dagger\rangle = 0$ has been used to arrive at the final expression. Equation (8.32) includes contributions from the anomalous density $\tilde{m} = \langle\hat{\delta}\hat{\delta}\rangle$ and a three-field correlation function of the non-condensate $\langle\hat{\delta}^\dagger\hat{\delta}\hat{\delta}\rangle$. The standard ZNG approach makes the Popov approximation ($\tilde{m}(\mathbf{r},t) = 0$) to avoid complexity associated with the anomalous density term. This approximation is typically valid in the case of repulsive two-body interactions and isotropic trapping potentials since $\tilde{m}(\mathbf{r},t)$ is negligible in this regime [168]. However, the three-field correlation function is kept to first-order in the interaction strength g, and it will be shown

that this leads to a term describing particle exchange between the condensate and noncondensate. Thus, we have the following equation of motion for the condensate wavefunction – the generalized GPE (GGPE):

$$\begin{aligned} i\hbar\frac{\partial\phi\left(\mathbf{r},t\right)}{\partial t} &= \left[-\frac{\hbar^2}{2m}\nabla^2+V_{\mathrm{ext}}\left(\mathbf{r},t\right)+gn_c\left(\mathbf{r},t\right)+2g\tilde{n}\left(\mathbf{r},t\right)\right]\phi\left(\mathbf{r},t\right) \\ &+ g\langle\hat{\delta}^{\dagger}\left(\mathbf{r},t\right)\hat{\delta}\left(\mathbf{r},t\right)\hat{\delta}\left(\mathbf{r},t\right)\rangle. \end{aligned} \tag{8.33}$$

Notably, compared to the zero temperature GPE, the GGPE contains an additional mean-field contribution due to the density of atoms in the noncondensate.

In order to evaluate the three-field correlation function of the noncondensate, it is necessary to find an equation of motion that describes the evolution of the noncondensate field operator $\hat{\delta}\left(\mathbf{r},t\right)$. In the case of the ZNG method, this is a lengthy and involved procedure that has been covered in detail previously (e.g., see Refs. [169–171]). Therefore, only the main points will be given here. The noncondensate can be represented by the Wigner operator

$$\hat{f}\left(\mathbf{r},\mathbf{p},t\right)=\int d\mathbf{r}'e^{i\mathbf{p}\cdot\mathbf{r}'}\delta^{\dagger}\left(\mathbf{r}+\frac{\mathbf{r}'}{2},t\right)\delta\left(\mathbf{r}-\frac{\mathbf{r}'}{2},t\right), \tag{8.34}$$

where $\mathbf{r}$ and $\mathbf{r}'$ are the center-of-mass and relative coordinates, respectively, and $\mathbf{p}$ is the momentum. Taking the expectation value of the Wigner operator yields the Wigner distribution function, $f\left(\mathbf{r},\mathbf{p},t\right)$, the evolution of which is governed by a QBE [169–171]

$$\begin{aligned} &\frac{\partial f\left(\mathbf{r},\mathbf{p},t\right)}{\partial t}+\frac{\mathbf{p}}{m}\cdot\nabla_{\mathbf{r}}f\left(\mathbf{r},\mathbf{p},t\right)-\nabla_{\mathbf{r}}\tilde{U}\left(\mathbf{r},t\right)\cdot\nabla_{\mathbf{p}}f\left(\mathbf{r},\mathbf{p},t\right) \\ &\quad=C_{12}\left[f\left(\mathbf{r},\mathbf{p},t\right),\phi\left(\mathbf{r},t\right)\right]+C_{22}\left[f\left(\mathbf{r},\mathbf{p},t\right)\right], \end{aligned} \tag{8.35}$$

where $\tilde{U}\left(\mathbf{r},t\right)=V_{\mathrm{ext}}\left(\mathbf{r},t\right)+2gn_c\left(\mathbf{r},t\right)+2g\tilde{n}\left(\mathbf{r},t\right)$ is the effective potential for the noncondensate in the Hartree-Fock approximation. The left-hand side of Eq. (8.35) describes the free evolution of the distribution function in phase space as a result of Liouville's theorem while the right-hand side describes the modification of the distribution function as a result of interatomic collisions. Note

that in this formalism the density and number of atoms in the noncondensate are defined as

$$\tilde{n}\left(\mathbf{r},t\right)=\int\frac{d\mathbf{p}}{\left(2\pi\hbar\right)^{3}}f\left(\mathbf{r},\mathbf{p},t\right), \tag{8.36}$$

$$\tilde{N}=\int d\mathbf{r}\ \tilde{n}\left(\mathbf{r},t\right), \tag{8.37}$$

respectively. The two collision processes in Eq. (8.35) represent a collision between a condensed atom and a non-condensed atom (C_{12}) and two non-condensed atoms (C_{22}). The former process is related to the three-field correlation function by [171]

$$\langle\hat{\delta}^{\dagger}\left(\mathbf{r},t\right)\hat{\delta}\left(\mathbf{r},t\right)\hat{\delta}\left(\mathbf{r},t\right)\rangle\approx-\frac{i\hbar}{2g\phi^{*}\left(\mathbf{r},t\right)}\int\frac{d\mathbf{p}}{\left(2\pi\hbar\right)^{3}}C_{12}\left[f\left(\mathbf{r},\mathbf{p},t\right),\phi\left(\mathbf{r},t\right)\right], \tag{8.38}$$

where only the first-order in g has been kept. Notably, this quantity is purely imaginary and will contribute a non-Hermitian source term to the GGPE of Eq. (8.33). Therefore, the C_{12} collision process leads to the addition or removal of particles from the condensate, and causes the normalization of $\phi\left(\mathbf{r},t\right)$ to change in time. In terms of the noncondensate distribution function and the local condensate properties of Eqs. (8.27)–(8.29), the C_{12} collision process is described by [171]

$$\begin{aligned}C_{12}\left[f,\phi\right]=\frac{\sigma\left|\phi\right|^{2}}{\pi m^{2}}\int d\mathbf{p}_{2}d\mathbf{p}_{3}d\mathbf{p}_{4}\delta\left(\mathbf{p}_{c}+\mathbf{p}_{2}-\mathbf{p}_{3}-\mathbf{p}_{4}\right)\delta\left(\epsilon_{c}+\tilde{\epsilon}_{2}-\tilde{\epsilon}_{3}-\tilde{\epsilon}_{4}\right)\\ \times\left[\delta\left(\mathbf{p}-\mathbf{p}_{2}\right)-\delta\left(\mathbf{p}-\mathbf{p}_{3}\right)-\delta\left(\mathbf{p}-\mathbf{p}_{4}\right)\right]\left[\left(1+f_{2}\right)f_{3}f_{4}-f_{2}\left(1+f_{3}\right)\left(1+f_{4}\right)\right],\end{aligned} \tag{8.39}$$

where the space and time dependence has been omitted for clarity, $\sigma=8\pi a_{s}^{2}$ is the Bose-enhanced scattering cross-section, and $\tilde{\epsilon}\equiv\left|\mathbf{p}\right|^{2}/2m+\tilde{U}\left(\mathbf{r},t\right)$ is the energy of a non-condensed particle within the Hartree-Fock approximation. In a similar fashion, the C_{22} collision process is described by [171]

$$\begin{aligned}C_{22}\left[f\right]=\frac{\sigma}{\pi h^{3}m^{2}}\int d\mathbf{p}_{2}d\mathbf{p}_{3}d\mathbf{p}_{4}\delta\left(\mathbf{p}+\mathbf{p}_{2}-\mathbf{p}_{3}-\mathbf{p}_{4}\right)\delta\left(\tilde{\epsilon}+\tilde{\epsilon}_{2}-\tilde{\epsilon}_{3}-\tilde{\epsilon}_{4}\right)\\ \times\left[\left(1+f\right)\left(1+f_{2}\right)f_{3}f_{4}-ff_{2}\left(1+f_{3}\right)\left(1+f_{4}\right)\right].\end{aligned} \tag{8.40}$$

In Eqs. (8.39) and (8.40) the delta functions ensure conservation of energy and momentum in a collision, and f_i represents the value of $f\left(\mathbf{r},\mathbf{p},t\right)$ at the phase-space coordinates $\left(\mathbf{r}_{i},\mathbf{p}_{i}\right)$. The $(1+f_i)$ terms represent Bose enhancement of the scattering process (i.e. particles have a higher probability of scattering into occupied states).

8.3.2.1 Thermodynamic equilibrium

In thermodynamic equilibrium, both the condensate and noncondensate are stationary in time, and no net particle exchange occurs between the two components of the gas. Therefore, the C_{12} and C_{22} collision integrals vanish and the distribution function for the non-condensate takes the form of a stationary Bose-Einstein distribution:

$$f_0(\mathbf{r},\mathbf{p}) = \frac{1}{e^{\beta_0(\tilde{\epsilon}_0-\tilde{\mu}_0)}-1}, \tag{8.41}$$

where $\beta_0 = 1/k_B T_0$ is the equilibrium inverse temperature and $\tilde{\mu}_0$ is the equilibrium chemical potential of the noncondensate. Noting that $\tilde{\epsilon}_0 = |\mathbf{p}|^2/2m + \tilde{U}_0(\mathbf{r})$, we can use Eq. (8.36) to find the equilibrium noncondensate density:

$$\tilde{n}_0(\mathbf{r}) = \frac{1}{\Lambda^3} g_{3/2}[z_0(\mathbf{r})], \tag{8.42}$$

where $\Lambda = \sqrt{2\pi\hbar^2/k_B T_0 m}$ is the thermal de Broglie wavelength, $z_0(\mathbf{r}) = e^{-\beta_0[\tilde{U}_0(\mathbf{r})-\tilde{\mu}_0]}$ is the local fugacity, and $g_{3/2}[z]$ is the polylogarithm function of order $s = 3/2$ defined by the series (see Ref. [69], for example)

$$g_s[z] = \sum_{n=1}^{\infty} \frac{z^n}{n^s}, \tag{8.43}$$

which is convergent if and only if $|z| < 1$. For $z = 1$, $g_s[1] = \zeta(s)$, where $\zeta(s)$ is the Riemann zeta function. Note that the equilibrium state of the noncondensate depends on that of the condensate through the mean-field interaction term contained in the definition of the noncondensate potential energy $\tilde{U}_0(\mathbf{r}) = V_{\text{ext}}(\mathbf{r}) + 2g n_{c,0}(\mathbf{r}) + 2g\tilde{n}_0(\mathbf{r})$. Thus, the two components of the gas remain coupled in the absence of the C_{12} collision process.

In equilibrium, the GGPE takes on a time-independent form similar to that of Eq. (8.23), but modified by the mean-field of the non-condensate:

$$\mu_{c,0}\phi_0(\mathbf{r}) = \left[-\frac{\hbar^2}{2m}\nabla^2 + V_{\text{ext}}(\mathbf{r}) + g n_{c,0}(\mathbf{r}) + 2g\tilde{n}_0(\mathbf{r})\right]\phi_0(\mathbf{r}), \tag{8.44}$$

where the term related to the three-field correlation function vanishes in thermal equilibrium. For the two components of the gas to remain in diffusive equilibrium (i.e., no net particle exchange) they

must have the same chemical potential; therefore, we have the condition $\tilde{\mu}_0 = \mu_{c,0}$ in equilibrium. Thus, equilibrium solutions to the ZNG equations can be found by solving Eqs. (8.42) and (8.44) self-consistently subject to the conditions that $\tilde{\mu}_0 = \mu_{c,0}$ and the temperature T_0 and total number of atoms in the gas N remain fixed.

8.4 Validity of the ZNG Method

In the ZNG approach, the fluctuations about the condensed state are represented semiclassically with a phase-space distribution function. Physically, this implies that atoms in the noncondensate behave like billiard balls that interact via elastic collisions, and move around in an effective Hartree-Fock potential that consists of the external trapping potential and contributions from both the condensate and noncondensate mean-field potentials. Such a treatment completely neglects any quantum fluctuations of the condensed state such as Bogoliubov quasi-particle excitations; therefore, the ZNG method is valid only in certain regimes. The use of a semiclassical approximation for the noncondensate is valid as long as the condensate appears locally homogeneous on the scale of variation in the noncondensate distribution function. This is typically the case at higher temperatures close to T_c and as long as the external trapping potential is not highly anisotropic. Furthermore, use of the Hartree-Fock excitation spectrum to described the fluctuations about the condensed state as opposed to the Bogoliubov spectrum is generally valid for trapped Bose gases as the dominant fluctuations are well described in the Hartree-Fock limit down to very low temperatures [172]. Therefore, the ZNG approach should provide an accurate representation of the problem studied in this dissertation, which involves a finite temperature Bose gas close to T_c confined in a highly isotropic harmonic trap.

Chapter 9

Numerical Solution of the ZNG Equations in Spherical Symmetry

The ZNG equations consist of a nonlinear Schrödinger equation (the GGPE of Eq. (8.33)) coupled to a collisional Boltzmann equation (the QBE of Eq. (8.35)). These styles of equations have been widely investigated; thus, there exists a variety of numerical methods for treating the dynamical evolution of such equations independently. However, coupling them in a self-consistent fashion is challenging as the numerical methods used to solve each equation differ significantly. A numerical solution to the full ZNG equations is presented by Jackson and Zaremba in Ref. [173], and this chapter focuses on the adaptation of their technique to problems with spherical symmetry.

The goal of this chapter is to outline the specific numerical methods used to propagate an initial state of the system forward in time through subsequent time steps denoted by Δt. The numerical methods presented are second-order accurate in time (i.e., the leading error term is $\mathcal{O}\left(\Delta t^3\right)$), which provides a good balance between accuracy and algorithm complexity. Furthermore, the focus will be on spherically symmetric problems such that the number of degrees of freedom needed to accurately describe the system is greatly reduced. The problem investigated in this dissertation involves an isotropic harmonic trap; thus, the problem can be reduced from six dimensions to three – a radial displacement $r \equiv |\mathbf{r}|^2$, a momentum magnitude $p \equiv |\mathbf{p}|^2$, and an angular variable $\cos\theta$ that describes the orientation of p with respect to r. This choice of variables reduces the GGPE to an equation in one variable and greatly simplifies the implementation of the numerical method for solving the QBE, as only three variables need be considered in the Monte Carlo sampling routines rather than the usual six. This can lead to significant speedup of the

numerical solution to the ZNG equations. Of course, a caveat to this is that only problems with spherical symmetry can be investigated.

This chapter begins by outlining the numerical method used to propagate an initial state of the GGPE forward in time. A very popular class of numerical methods for nonlinear Schrödinger equations are split operator pseudospectral methods, where the potential and kinetic energy portions of the Hamiltonian operator are separated and applied to a given wavefunction in succession. This allows the potential energy operator to be applied as a simple point-wise multiplication whereas the kinetic energy operator can be applied in momentum space using the fast Fourier transform (FFT) [174], or in position space using the method of finite differences (e.g., the Crank-Nicolson method [175]).

Following a discussion of the GGPE, a numerical method for solving the QBE with spherical symmetry is given. Compared to a nonlinear Schrödinger equation, the collisional Boltzmann equation is significantly more complex and nearly impossible to solve directly due to its high dimensionality. A method applicable to a wide range of problems that has found widespread use is the direct simulation Monte Carlo (DSMC) method [176]. The key aspect of the DSMC method is to represent the phase space distribution function $f(\mathbf{r}, \mathbf{p}, t)$ as a swarm of point-like test particles that evolve in time based on Liouville's theorem and sample the available phase space. Monte Carlo techniques are then utilized to incorporate the effect of collisions on the test particles, and the approximate evolution of the distribution function is obtained by averaging over the motion of all test particles. The main advantage to this method is that it avoids having to store and update a six-dimensional quantity on a discrete grid – a nearly impossible task even for modern computers.

The final section of this chapter will discuss the full dynamical simulation of the ZNG equations. The first step of this process is to generate an equilibrium state of the system that is dictated by the temperature of the gas and the total number of atoms it contains. This is done in a self-consistent fashion such that equilibrium densities for both the condensate and noncondensate are obtained. As the noncondensate is represented by a distribution of test particles in a dynamical simulation, an initial position and momentum must be calculated for each test particle based on the

equilibrium properties of the gas. The simulation then proceeds based on the update schemes that will be outlined below. Finally, to test the numerical method developed for spherical symmetry, a quench simulation is performed and directly compared to previous results in the field.

Throughout this chapter, some examples of the numerical methods developed will be given. An example problem with an equilibrium temperature of $T_0 = 200$ nK, total atom number of $N = 50,000$ ^{87}Rb atoms, and a harmonic trap frequency of $\omega = 2\pi \times 187$ rad/s will be used for these numerical examples. The mass and scattering length used are $m = 1.44 \times 10^{-25}$ kg and $a_s = 5.29$ nm, respectively, which correspond to ^{87}Rb atoms. Regarding the numerical simulations, it is advantageous to identify characteristic properties of a given problem that can be used to convert a system of equations to an equivalent, dimensionless form. This avoids limitations of computer arithmetic that give rise to overflow and underflow errors, which arise through the addition, subtraction, multiplication, and/or division of very small and/or very large numbers (e.g., Planck's constant $h = 6.626 \times 10^{-34}$ m^{2}kg/s, or it's inverse). For a degenerate Bose gas confined by a harmonic trap with oscillator frequency ω, the following characteristic properties are used:

$$a_{ho} = \sqrt{\frac{\hbar}{m\omega}}, \tag{9.1}$$

$$p_{ho} = \sqrt{\hbar m\omega}, \tag{9.2}$$

$$\epsilon_{ho} = \frac{\hbar\omega}{2}, \tag{9.3}$$

which correspond to the harmonic oscillator length, momentum, and ground state energy, respectively. The results of numerical examples will be given in these dimensionless units.

9.1 Solution of the GGPE

This section will outline the numerical method for propagating the solution of the GGPE forward in time. The GGPE takes the following form in spherical symmetry:

$$i\hbar\frac{\partial\phi(r,t)}{\partial t} = \left[-\left(\frac{\hbar^2}{2m}\right)\frac{1}{r^2}\frac{\partial}{\partial r}\left(r^2\frac{\partial}{\partial r}\right) + V_{\text{ext}}(r,t) + gn_c(r,t) + 2g\tilde{n}(r,t) - iR(r,t)\right]\phi(r,t), \tag{9.4}$$

where the function $R(r,t)$ has been introduced to represent the effect of the three-field correlation function on the condensate wavefunction:

$$R(r,t) = \frac{\hbar}{2n_c(r,t)} \int \frac{d\mathbf{p}}{(2\pi\hbar)^3} C_{12}[f,\phi]. \tag{9.5}$$

In an isotropic harmonic trap of frequency ω, the external potential is given by $V_{\text{ext}}(r,t) \equiv \frac{1}{2}m\omega^2 r^2$ and the GGPE can be cast in an alternative form with the substitution $\phi(r,t) \to \varphi(r,t)/r$,

$$i\hbar\frac{\partial\varphi(r,t)}{\partial t} = \left[-\left(\frac{\hbar^2}{2m}\right)\frac{\partial^2}{\partial r^2} + \frac{1}{2}m\omega^2 r^2 + gn_c(r,t) + 2g\tilde{n}(r,t) - iR(r,t)\right]\varphi(r,t). \tag{9.6}$$

The advantages of this substitution are the simplification of the Laplacian term to a single second derivative and a simplification of the boundary conditions since $\varphi(r,t) \to 0$ as $r \to 0,\infty$. This comes at the expense of a slightly more complicated nonlinear term as $n_c(r,t) \equiv |\varphi(r,t)|^2/r^2$; however, the advantages outweigh this minor inconvenience. This is the form of the GGPE that is assumed for application of the numerical methods outlined below.

9.1.1 Derivation of the time evolution operator

To proceed with a derivation of the numerical method, it is convenient to write the GGPE in the following form:

$$i\hbar\frac{\partial\varphi(r,t)}{\partial t} = \hat{H}(t)\varphi(r,t), \tag{9.7}$$

where $\hat{H}(t) \equiv \hat{T} + \hat{V}(t)$ is the time-dependent Hamiltonian operator with the kinetic and potential energy operators defined as

$$\hat{T} \equiv -\left(\frac{\hbar^2}{2m}\right)\frac{\partial^2}{\partial r^2}, \tag{9.8}$$

$$\hat{V}(t) \equiv \frac{1}{2}m\omega^2 r^2 + gn_c(r,t) + 2g\tilde{n}(r,t) - iR(r,t), \tag{9.9}$$

respectively. A formal solution to this equation is given by application of the time evolution operator $\hat{U}(t;t_0)$ to some initial state $\varphi(r,t_0)$

$$\varphi(r,t) = \hat{U}(t;t_0)\varphi(r,t_0), \tag{9.10}$$

where $t \equiv t_0 + \Delta t$ and application of $\hat{U}(t;t_0)$ evolves the wavefunction over the interval Δt. In general, the time evolution operator takes the following form for a time-dependent Hamiltonian [177]:

$$\hat{U}(t;t_0) = 1 + \sum_{n=1}^{\infty} \left(\frac{1}{i\hbar}\right)^n \int_{t_0}^{t} dt_1 \int_{t_0}^{t_2} dt_2 \; \cdots \int_{t_0}^{t_{n-1}} dt_n \hat{H}(t_1)\hat{H}(t_2)\cdots\hat{H}(t_n). \tag{9.11}$$

As this expression represents an infinite sum of terms, the present task is to find a closed form expression that has a leading error term of $\mathcal{O}\left(\Delta t^3\right)$. With this in mind, we proceed by expanding the $\hat{H}(t_n)$ terms of Eq. (9.11) in a Taylor series:

$$\begin{aligned}\hat{H}(t_n) &= \hat{H}(t) + \frac{\partial \hat{H}(t)}{\partial t}(t_n - t) + \frac{1}{2}\frac{\partial^2 \hat{H}(t)}{\partial t^2}(t_n - t)^2 + \ldots \\ &\equiv \alpha_0 + \alpha_1(t_n - t) + \frac{\alpha_2}{2}(t_n - t)^2 + \ldots,\end{aligned} \tag{9.12}$$

where the shorthand form $\alpha_n = \partial^n \hat{H}(t)/\partial t^n$ has been introduced. Expanding the first two terms of the sum in Eq. (9.11) and substituting the Taylor series expansion for $\hat{H}(t_n)$ results in

$$\begin{aligned}\hat{U}(t;t_0) = 1 &+ \frac{1}{i\hbar}\int_{t_0}^{t} dt_1 \left[\alpha_0 + \alpha_1(t_1 - t) + \frac{\alpha_2}{2}(t_1 - t)^2 + \ldots\right] \\ &+ \left(\frac{1}{i\hbar}\right)^2 \int_{t_0}^{t} dt_1 \int_{t_0}^{t_1} dt_2 \left[\alpha_0 + \alpha_1(t_1 - t) + \frac{\alpha_2}{2}(t_1 - t)^2 + \ldots\right] \\ &\times \left[\alpha_0 + \alpha_1(t_2 - t) + \frac{\alpha_2}{2}(t_2 - t)^2 + \ldots\right] + \ldots.\end{aligned} \tag{9.13}$$

Carrying out the integration, making the substitution $\Delta t \equiv t - t_0$, and keeping only terms up to Δt^2 then gives

$$\begin{aligned}\hat{U}(t;t_0) &= 1 + \frac{1}{i\hbar}\left(\alpha_0 \Delta t - \frac{\alpha_1}{2}\Delta t^2\right) + \left(\frac{1}{i\hbar}\right)^2 \frac{\alpha_0^2}{2}\Delta t^2 + \ldots \\ &\approx \exp\left[-\frac{i}{\hbar}\left(\alpha_0 + \frac{\alpha_1}{2}\Delta t\right)\Delta t\right] + \mathcal{O}\left(\Delta t^3\right),\end{aligned} \tag{9.14}$$

Finally, using the Taylor series expansion for $\hat{H}(t_n)$ an expression for α_1 can be found by a backward finite-difference approximation:

$$\alpha_1 \equiv \frac{\partial \hat{H}(t)}{\partial t} \approx \frac{\hat{H}(t) - \hat{H}(t - \Delta t)}{\Delta t} + \mathcal{O}(\Delta t). \tag{9.15}$$

Therefore, the exponent in the time evolution operator can be written as

$$\begin{aligned}\tilde{H}(t) &\equiv \alpha_0 + \frac{\alpha_1}{2}\Delta t \\ &= \frac{3\hat{H}(t) - \hat{H}(t - \Delta t)}{2},\end{aligned} \tag{9.16}$$

and the second-order accurate time evolution operator is

$$\hat{U}\left(t;t_0\right) \approx e^{-i\tilde{H}(t)\Delta t/\hbar} + \mathcal{O}\left(\Delta t^3\right). \tag{9.17}$$

Note that the backward finite-difference approximation for α_1 has a leading error term proportional to Δt, which would appear to spoil the second-order accuracy of this method. However, α_1 is multiplied by Δt^2 in the exponent of the time evolution operator; therefore, the approximation for $\hat{U}\left(t;t_0\right)$ maintains second-order accuracy.

9.1.2 Application of the time evolution operator

Given the form of $\hat{U}\left(t;t_0\right)$, a numerical method for applying the exponential operator of Eq. (9.17) to a given wavefunction is required. A standard approach that maintains second-order accuracy makes use of the symmetric operator splitting first introduced by Strang [178]:

$$\hat{U}\left(t;t_0\right) \approx e^{-i\tilde{H}(t)\Delta t/\hbar} + \mathcal{O}\left(\Delta t^3\right) \approx e^{-i\hat{T}\Delta t/2\hbar} e^{-i\tilde{V}(t)\Delta t/\hbar} e^{-i\hat{T}\Delta t/2\hbar} + \mathcal{O}\left(\Delta t^3\right), \tag{9.18}$$

where $\tilde{V}\left(t\right) = \left[3\hat{V}\left(t\right) - \hat{V}\left(t-\Delta t\right)\right]/2$ is the potential energy operator evaluated at the midpoint of a full time step, $t = \Delta t/2$. To apply the time evolution operator to a given wavefunction each exponential term is applied in succession, which is mathematically equivalent to solving three partial differential equations consecutively:

$$i\hbar\frac{\partial\varphi\left(r,t\right)}{\partial t} = \hat{T}\varphi\left(r,t\right), \qquad \left(t_0 \rightarrow t_0 + \frac{\Delta t}{2}\right),$$

$$\downarrow$$

$$i\hbar\frac{\partial\varphi\left(r,t\right)}{\partial t} = \tilde{V}\left(t\right)\varphi\left(r,t\right), \qquad \left(t_0 \rightarrow t_0 + \Delta t\right),$$

$$\downarrow$$

$$i\hbar\frac{\partial\varphi\left(r,t\right)}{\partial t} = \hat{T}\varphi\left(r,t\right), \qquad \left(t_0 + \frac{\Delta t}{2} \rightarrow t_0 + \Delta t\right),$$

where t_0 is the initial time point, $t_0 + \Delta t$ is the final time point for both operators, and it is understood that the solution of the first equation is used in the second equation and the solution of the second equation is used in the third equation.

To implement this numerical method on the computer, all functions of space are represented on a discrete grid of points spaced uniformly by Δr and extending from $r = 0$ to $r = r_{\max}$, where $r_{\max}$ is chosen large enough that the boundary condition $\varphi(\infty, t) = 0$ is accurately represented. Therefore, the equation involving the potential energy operator is straightforward to solve and the exponential operator can be applied directly to the wavefunction as a point-wise multiplication. However, the equations involving the kinetic energy operator include a derivative such that a more complex approach is needed. Due to the spherical symmetry of the problem standard FFT pseudospectral methods are not applicable, so the Crank-Nicolson finite-difference method is chosen instead.

The Crank-Nicolson method is an implicit finite-difference numerical scheme that is unconditionally stable and second-order accurate in both space and time. In order to use the Crank-Nicolson method to apply an exponential operator to a given wavefunction, Cayley's form [175] is used to obtain a finite-difference representation of the kinetic energy portion of the GGPE:

$$\left(1 + \frac{i\Delta t}{4\hbar}\hat{T}\right)\varphi_j^{n+1/2} = \left(1 - \frac{i\Delta t}{4\hbar}\hat{T}\right)\varphi_j^n, \tag{9.19}$$

where the space and time dependence of φ is represented by j, a discrete spatial point, and n, a discrete point in time, respectively. Expanding $\hat{T}$ and using a second-order accurate finite-difference approximation for the second derivative results in

$$\begin{aligned}\left[\varphi_j^{n+1/2} - \left(\frac{i\hbar\Delta t}{8m\Delta r^2}\right)\left(\varphi_{j+1}^{n+1/2} - 2\varphi_j^{n+1/2} + \varphi_{j-1}^{n+1/2}\right)\right] = \\ \left[\varphi_j^n + \left(\frac{i\hbar\Delta t}{8m\Delta r^2}\right)\left(\varphi_{j+1}^n - 2\varphi_j^n + \varphi_{j-1}^n\right)\right],\end{aligned} \tag{9.20}$$

which is a system of linear equations that represents a tridiagonal problem. A solution for φ_j^{n+1} at all j can be obtained efficiently using the well known Thomas algorithm [175] in conjunction with the boundary conditions $\varphi_0^n = \varphi_{j_{\max}}^n = 0$ for all n.

9.2 Solution of the QBE

This section will outline the numerical method for propagating the solution of the QBE forward in time. The premise of the DSMC method is to sample the distribution function $f(\mathbf{r},\mathbf{p},t)$ over a large number of points in phase space, and then evolve each of these points forward in time. These phase space points are referred to here as test particles, and their relation to the distribution function is given by

$$f(\mathbf{r},\mathbf{p},t) \approx \gamma (2\pi\hbar)^3 \sum_i \delta[\mathbf{r}-\mathbf{r}_i(t)]\,\delta[\mathbf{p}-\mathbf{p}_i(t)], \tag{9.21}$$

where $\mathbf{r}_i(t)$ and $\mathbf{p}_i(t)$ are the position and momentum, respectively, of test particle i, and the delta functions imply that the distribution function is represented only at the discrete phase space points of each test particle. The weighting factor $\gamma = \tilde{N}/N_{\mathrm{tp}}$ describes the relationship between the number of physical particles in the non-condensate $\tilde{N}$ and the number of test particles N_{tp} used to represent them. Thus, a solution to the QBE is found by evolving the distribution of test particles forward in time and using their properties to obtain a local estimate of $f(\mathbf{r},\mathbf{p},t)$ and the effect of collisions. To begin, it is convenient to separate the collisionless evolution of the test particle distribution from the effects of collisions. This separation is accurate as long as the position and momentum of the test particles change over a time that is less than the average collisional timescales.

9.2.1 Collisionless evolution of the test particle distribution

Similar to the approach used to derive a numerical method for the GGPE, it is convenient to write the collisionless QBE in the following form:

$$\frac{\partial z}{\partial t} = -i\mathcal{L}(t)\,z, \tag{9.22}$$

where $z \equiv (r,p)$ is a phase space coordinate and $\mathcal{L}$ is the Liouville operator [179] defined as

$$i\mathcal{L}(t) \equiv \{\ \cdot\ , H(t)\} = \left(\frac{\partial H(t)}{\partial p}\right)\frac{\partial}{\partial r} - \left(\frac{\partial H(t)}{\partial r}\right)\frac{\partial}{\partial p}, \tag{9.23}$$

where $\{ \cdot \}$ denotes a Poisson bracket, and $H(t)$ is the classical Hamiltonian. Note that only a single pair of canonically conjugate coordinates, (r, p), are considered here given the assumption of spherical symmetry. Thus, the usual summation over all coordinates is neglected in the definition of $\mathcal{L}(t)$. In a completely analogous fashion to the approach used for the GGPE, a second-order accurate update scheme consists of finding a closed form expression for the time evolution operator, which takes the familiar form

$$U(t; t_0) \approx e^{-i\tilde{\mathcal{L}}(t)\Delta t} + \mathcal{O}\left(\Delta t^3\right), \tag{9.24}$$

where $\tilde{\mathcal{L}}(t) = \left[3\mathcal{L}(t) - \mathcal{L}(t - \Delta t)\right]/2$. To apply this operator to a given initial state the Strang splitting approach is again used to obtain

$$U(t; t_0) \approx e^{-i\tilde{\mathcal{L}}(t)\Delta t} + \mathcal{O}\left(\Delta t^3\right) \approx e^{-i\mathcal{L}_T \Delta t/2} e^{-i\tilde{\mathcal{L}}_V(t)\Delta t} e^{-i\mathcal{L}_T \Delta t/2} + \mathcal{O}\left(\Delta t^3\right), \tag{9.25}$$

where the classical kinetic and potential energy operators are defined as

$$\mathcal{L}_T \equiv \frac{p}{m}\frac{\partial}{\partial r}, \tag{9.26}$$

$$\tilde{\mathcal{L}}_V(t) \equiv -\frac{\partial \tilde{V}(t)}{\partial r}\frac{\partial}{\partial p}, \tag{9.27}$$

respectively, and $\tilde{V}(t) = \left[3V(t) - V(t - \Delta t)\right]/2$ is the potential energy operator defined at the midpoint of a full time step, $t = \Delta t/2$. To apply the time evolution operator to a given state of the system, each exponential term is applied in succession, which is mathematically equivalent to solving three partial differential equations consecutively:

$$\frac{\partial r(t)}{\partial t} = \frac{p(t)}{m}, \qquad \left(t_0 \to t_0 + \frac{\Delta t}{2}\right),$$

$$\downarrow$$

$$\frac{\partial p(t)}{\partial t} = -\frac{\partial \tilde{V}(t)}{\partial r}, \qquad \left(t_0 \to t_0 + \Delta t\right),$$

$$\downarrow$$

$$\frac{\partial r(t)}{\partial t} = \frac{p(t)}{m}, \qquad \left(t_0 + \frac{\Delta t}{2} \to t_0 + \Delta t\right),$$

where t_0 is the initial time point, $t_0 + \Delta t$ is the final time point for both operators, and it is understood that the solution of the first equation is used in the second equation and the solution of the second equation is used in the third equation. These equations are found by expanding the phase space coordinate z and writing equations of motion for r and p separately. Notably, $\mathcal{L}_T$ operates only on the position of the test particles while $\mathcal{L}_V$ operates only on the momentum of the test particles.

To implement this numerical method on the computer, each test particle is represented by a discrete phase space coordinate $z_i \equiv (r_i, p_{i,x}, p_{i,y}, p_{i,z})$ and finite difference approximations are used to estimate the derivatives in the above equations. To update the position of each test particle in spherical symmetry, the method outlined by Bird [176] is used, and only the radial position of each test particle is stored. However, the complete motion of each particle in 3D space must be tracked such that three momentum components are stored for each particle. At the beginning of each time step the spherical symmetry of the problem is utilized to arbitrarily align the position vector of each particle with the x-axis. The action of momentum components directed along the y- and z-axes is to then push the particle away from the x-axis. It is straightforward to calculate the new radial position of the particle; however, the off-axis motion causes a rotation of the particle trajectory and the momentum components must be rotated accordingly. The new particle position on the x-axis after a half time step of $\Delta t/2$ is

$$x = r_i^n + \frac{p_{i,x}^n}{2m}\Delta t, \tag{9.28}$$

where n represents a discrete time point, r_i^n is the initial radial position of particle i, and $p_{i,x}^n$ it's momentum along the x-axis. The action of the off-axis momentum components moves the particle by a distance

$$d = \sqrt{\left(\frac{p_{i,y}^n}{2m}\Delta t\right)^2 + \left(\frac{p_{i,z}^n}{2m}\Delta t\right)^2}, \tag{9.29}$$

such that the new radial position of particle i is

$$r_i^{n+1/2} = \sqrt{x^2 + d^2}. \tag{9.30}$$

The rotation of the particle trajectory is defined by

$$\sin\vartheta = d/r_i^{n+1/2}, \tag{9.31}$$

$$\cos\vartheta = x/r_i^{n+1/2}, \tag{9.32}$$

and an azimuthal angle chosen at random such that $\varphi \in [0, 2\pi]$. Thus, the rotated momentum components are given by

$$p_{i,x}^{n+1/2} = p_{i,x}^{n}\cos\vartheta + \sqrt{\left(p_{i,y}^{n}\right)^2 + \left(p_{i,z}^{n}\right)^2}\sin\vartheta, \tag{9.33}$$

$$p_{i,y}^{n+1/2} = p_{i,c}^{n+1/2}\sin\varphi, \tag{9.34}$$

$$p_{i,z}^{n+1/2} = p_{i,c}^{n+1/2}\cos\varphi, \tag{9.35}$$

where the circumferential momentum component is $p_{i,c}^{n+1/2} = -p_{i,x}^{n}\sin\vartheta + \sqrt{\left(p_{i,y}^{n}\right)^2 + \left(p_{i,z}^{n}\right)^2}\cos\vartheta$. This completes a single update of the particle position. Note that although three momentum components are stored for each particle in addition to the radial position, the algorithm is effectively three-dimensional since the azimuthal angle φ is randomized at each time step. Thus, the only unique momentum coordinates are $p_{i,x}$ and the angle ϑ.

Following a single update of the position for each test particle, the momentum along the x-axis is updated based on the effect of the potential energy operator. The x component is updated since this is the axis that is chosen to coincide with the position of the test particle at the beginning of each time step. The update scheme for each test particle is then

$$p_{i,x}^{n+1} = p_{i,x}^{n+1/2} - \Delta t\left[\frac{\partial\tilde{V}(t)}{\partial r}\right]_{r=r_i}^{n+1/2}, \tag{9.36}$$

where the derivative term is calculated at the recently updated position of test particle i. In practice, $\tilde{V}_j^n$ is represented on the same discrete grid as the condensate wavefunction, φ_j^n. Therefore, the spatial derivative of $\tilde{V}_j^n$ is approximated using a fourth-order finite difference approximation,

$$\frac{\partial\tilde{V}(t)}{\partial r} \approx \frac{\tilde{V}_{j-2}^n - 8\tilde{V}_{j-1}^n + 8\tilde{V}_{j+1}^n - \tilde{V}_{j+2}^n}{12\Delta r}, \tag{9.37}$$

and linear interpolation is used to obtain an estimate at the position of the test particle. Finally,

a second update of each test particle's position over a half time step $\Delta t/2$ is performed, and his completes the update scheme for the test particle ensemble at each time step.

Before proceeding to a discussion of collision effects it is important to mention a complication that arises with the above numerical update scheme when estimating the spatial derivative of $\tilde{V}(t)$. As shown in Chapter 8, the noncondensate – and therefore the test particle distribution – evolves in an effective Hartree-Fock potential given by

$$V(t) \equiv \frac{1}{2}m\omega^2 r^2 + 2gn_c(r,t) + 2g\tilde{n}(r,t). \tag{9.38}$$

This potential includes a term proportional to the noncondensate density, which must be estimated from the test particle distribution at each time step. This is challenging because a smooth, differentiable function must be constructed from a set of discrete points in phase space to employ Eq. (9.37), and this function must be represented on the same discrete grid as the condensate wavefunction. The following section outlines a method for accomplishing this task in a spherically symmetric geometry.

9.2.1.1 Estimation of $\tilde{n}(r,t)$ from the test particle distribution

Given the positions of each test particle in the distribution, a method for numerically generating a smooth and differentiable form of $\tilde{n}(r,t)$ at each time step is required. This is typically accomplished with a cloud-in-cell scheme [180], which is commonly used in particle-in-cell simulations of plasmas. In a 1D simulation, application of the cloud-in-cell scheme consists of assigning each particle to its two nearest grid points with a linear weight factor given by the distance of the particle to each grid point. However, such a linear weighting scheme introduces errors in a spherical coordinate system, particularly near the boundaries of the discrete grid [181]. To avoid these errors a volume weighting scheme is employed where the test particle weight factors are given by the volume of space between the particle and a given grid point [182, 183] rather than the linear distance.

The first step in estimating $\tilde{n}(r,t)$ is to break up the spatial domain into a series of bins, where each bin extends over a small portion of the computational domain. The edges of these bins

then make up a discrete grid that $\tilde{n}(r,t)$ can be represented on. Not only is this necessary for obtaining an estimate of $\tilde{n}(r,t)$, it is also required to estimate the effects of collisions, which will be discussed further in the next section. Due to the spherical symmetry of the problem and the choice of a volume weighting scheme, the test particles are binned into radial shells of constant volume. Given the size of the simulation domain, $r_{\max}$, and the total number of desired bins, N_b, the radial position of the start of each bin is given by

$$r_{b,k} = r_{\max}\left(\frac{k}{N_b}\right)^{1/3}, \tag{9.39}$$

where $k \in [0, N_b]$ is an integer representing the bin index. For a given time step, the two nearest bin edges, denoted by l and $l+1$, are computed for each test particle by inverting Eq. (9.39) and solving for k. Each test particle is then weighted to the grid positions r_l and r_{l+1} using the following volume weighting scheme

$$\tilde{n}_l = \tilde{n}_l + \left(\frac{1}{V_b}\right)\left(\frac{r_{l+1}^3 - r_i^3}{r_{l+1}^3 - r_l^3}\right), \tag{9.40}$$

$$\tilde{n}_{l+1} = \tilde{n}_{l+1} + \left(\frac{1}{V_b}\right)\left(\frac{r_i^3 - r_l^3}{r_{l+1}^3 - r_l^3}\right), \tag{9.41}$$

where $\tilde{n}_l$ is the noncondensate density at the bin edges, V_b is the volume of each bin, and r_i is the radial position of test particle i. This procedure is applied to all test particles and an initial estimate of $\tilde{n}(r,t)$ is obtained. In order to find $\tilde{n}(r,t)$ on the same discrete grid used to represent the condensate wavefunction, a standard 1D linear interpolation routine is used to compute the discrete function $\tilde{n}_j$.

The initial estimate of $\tilde{n}_j$ based on the cloud-in-cell scheme with volume weighting is generally not smooth and differentiable. Therefore, it is necessary to smooth $\tilde{n}_j$ using a Gaussian low-pass filter, which is accomplished by convolving $\tilde{n}_j$ with a finite extent Gaussian function $S_j = e^{-r_j^2/\eta^2}$. This procedure is accomplished by Fourier transforming $\tilde{n}_j$ using a FFT routine, multiplying the result by the Fourier transform of S_j, and inverse Fourier transforming to obtain the smoothed version of $\tilde{n}_j$. The simulation results are not strongly dependent on the choice of smoothing parameter, η, which is chosen empirically to provide just enough smoothing to make $\tilde{n}_j$ differentiable.

Furthermore, for a given grid spacing Δr the smoothing parameter remains fixed throughout a simulation.

Figure 9.1 provides an example of the procedure outlined above for generating $\tilde{n}_j$ from the test particle distribution at each time step. The initial cloud-in-cell estimate accurately captures the overall shape of $\tilde{n}_j$, but the discrete nature of the particle distribution contributes substantial fluctuations. Application of the Gaussian low-pass filter effectively eliminates these fluctuations and results in a $\tilde{n}_j$ that closely resembles the theoretical density distribution. The next section describes the numerical implementation of the C_{12} and C_{22} collision processes.

9.2.2 Collisional evolution of the test particle distribution

Collisionless evolution of the distribution function is a conservative process in that the number of particles contained in the infinitesimal phase space volume element $d\mathbf{r}d\mathbf{p}/(2\pi\hbar)^3$ does not change in time. The collision integrals of Eqs. (8.39) and (8.40) represent the number of particles entering or leaving $d\mathbf{r}d\mathbf{p}/(2\pi\hbar)^3$ per unit time, and therefore result in a change of $f(\mathbf{r}, \mathbf{p}, t)$. If the typical collision timescale is much larger than the time step for collisionless evolution, Δt, then the effect of collisions can be treated separately at the end of a given time step. In this limit, the probability of a test particle undergoing a collision in time Δt is much less than unity, and an accurate representation of the collision integrals can be obtained via Monte Carlo sampling. The present task is then to calculate the rate of each collision process and define a collision probability for each test particle in the distribution. We begin by considering the C_{22} collision integral (Eq. (8.40)), which corresponds to the scattering of two atoms in the noncondensate.

9.2.2.1 Probability of the C_{22} collision process

Since the quantity $\int d\mathbf{r}d\mathbf{p}/(2\pi\hbar)^3 C_{22}[f]$ represents the total number of particles entering or leaving the volume $d\mathbf{r}d\mathbf{p}/(2\pi\hbar)^3$ per unit time, we can define the mean collision rate at point r by integrating

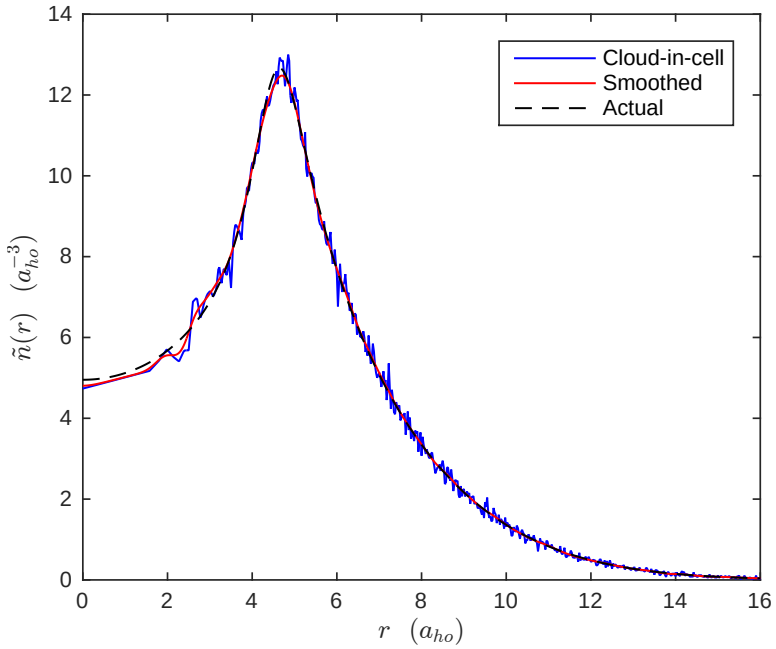

Figure 9.1: Example of generating $\tilde{n}_j$ using the procedure described in the main text. The cloud-in-cell profile (blue, solid) is constructed from $N_{tp} = 100,000$ test particles. The smoothed profile (red, solid) is an accurate representation of the actual equilibrium density profile obtained with the method outlined in Section 9.3.1 (black, dashed), and does not exhibit the fluctuations present in the cloud-in-cell profile. The actual noncondensate density is the equilibrium solution $\tilde{n}_0(r)$ for temperature $T_0 = 200$ nK, total atom number $N = 50,000$, trap frequency $\omega = 2\pi \times 187$ rad/s, and ^{87}Rb atoms with a scattering length $a_s = 5.29$ nm.

$C_{22}[f]$ over momentum:

$$\Gamma_{22}^{\text{out}}(r,t) = \frac{\sigma}{\pi h^6 m^2}\int d\mathbf{p}d\mathbf{p}_2 d\mathbf{p}_3 d\mathbf{p}_4 \delta(\mathbf{p}_1+\mathbf{p}_2-\mathbf{p}_3-\mathbf{p}_4)\,\delta(\tilde{\epsilon}+\tilde{\epsilon}_2-\tilde{\epsilon}_3-\tilde{\epsilon}_4) \times f_1 f_2 (1+f_3)(1+f_4), \tag{9.42}$$

where the 1 and 2 subscripts represent the incoming (i.e., pre-collision) momenta of the two atoms and the 3 and 4 subscripts represent the outgoing (i.e., post-collision) momenta of the two atoms. In the above equation, only the half of the collision integral that corresponds to particles leaving the volume $d\mathbf{r}d\mathbf{p}/(2\pi\hbar)^3$ is considered, hence the usage of the "out" superscript. This is valid because the "in" process is symmetric and will lead to the same value for the mean collision rate at point r, which we only need in order to define a probability that a given test particle undergoes a collision at each time step. Furthermore, the C_{22} collision process conserves the total number of atoms in the noncondensate.

To simplify the expression for $\Gamma_{22}^{\text{out}}(r,t)$ it is convenient to transform the momentum coordinates to the center of mass frame by defining

$$\mathbf{p}_{\text{cm}} \equiv \frac{\mathbf{p}_1+\mathbf{p}_2}{\sqrt{2}}, \tag{9.43}$$

$$\mathbf{p}_{\text{rel}} \equiv \frac{\mathbf{p}_1-\mathbf{p}_2}{\sqrt{2}}, \tag{9.44}$$

$$\mathbf{p}'_{\text{cm}} \equiv \frac{\mathbf{p}_3+\mathbf{p}_4}{\sqrt{2}}, \tag{9.45}$$

$$\mathbf{p}'_{\text{rel}} \equiv \frac{\mathbf{p}_3-\mathbf{p}_4}{\sqrt{2}}. \tag{9.46}$$

The expression can then be simplified using conservation of energy and momentum in an elastic collision (i.e., $\mathbf{p}'_{\text{cm}} = \mathbf{p}_{\text{cm}}$ and $|\mathbf{p}'_{\text{rel}}| = |\mathbf{p}_{\text{rel}}|$) and properties of the delta function. The end result is

$$\Gamma_{22}^{\text{out}}(r,t) = \frac{\sigma}{m}\int \frac{d\mathbf{p}_1}{(2\pi\hbar)^3} f_1 \int \frac{d\mathbf{p}_2}{(2\pi\hbar)^3} f_2 \int \frac{d\Omega}{4\pi} |\mathbf{p}_1-\mathbf{p}_2|(1+f_3)(1+f_4). \tag{9.47}$$

Thus, calculation of this rate involves integrals over all possible incoming momenta and all possible scattering angles defined by the solid angle Ω. In the center of mass frame, the outgoing momenta

are given in terms of the incoming momenta by

$$\mathbf{p}_3 = \frac{\mathbf{p}_{\rm cm} + |\mathbf{p}_{\rm rel}|\,\hat{\mathbf{u}}\,(\Omega)}{\sqrt{2}}, \tag{9.48}$$

$$\mathbf{p}_4 = \frac{\mathbf{p}_{\rm cm} - |\mathbf{p}_{\rm rel}|\,\hat{\mathbf{u}}\,(\Omega)}{\sqrt{2}}, \tag{9.49}$$

where $\hat{\mathbf{u}}\,(\Omega)$ is a unit vector in the direction determined by the solid angle Ω.

To determine the probability that a given test particle in the distribution undergoes a C_{22} type collision, the Monte Carlo sampling technique [175] can be utilized to estimate the integrals in Eq. (9.47). Notably, the random phase space points necessary for Monte Carlo sampling are conveniently provided by the test particle distribution. As discussed in section 9.2.1.1, at each time step the test particle distribution is binned in position space using radial shells of equal volume. The particles within each bin are then paired at random, and a probability for a pair of particles to undergo a collision for the time step Δt is [173]

$$P_{ij}^{22} = \frac{\sigma \tilde{n}_{ij}}{m} \left|\mathbf{p}_i - \mathbf{p}_j\right| \int \frac{d\Omega}{4\pi} \left(1 + f_3\right)\left(1 + f_4\right) \Delta t, \tag{9.50}$$

where i and j represent a pair of particles and $\tilde{n}_{ij}$ represents the local noncondensate density. The integration over Ω is estimated by randomly generating the unit vector $\hat{\mathbf{u}}\,(\Omega)$ such that $\cos\vartheta \in [-1, 1]$ and $\varphi \in [0, 2\pi]$. This results in a random scattering angle Ω_R and the following collision probability:

$$P_{ij}^{22} = \frac{\sigma \tilde{n}_{ij}}{m} \left|\mathbf{p}_i - \mathbf{p}_j\right| \left(1 + f_3^{\Omega_R}\right)\left(1 + f_4^{\Omega_R}\right) \Delta t, \tag{9.51}$$

which depends on the value of the distribution function evaluated at the outgoing momenta $f_3^{\Omega_R}$ and $f_4^{\Omega_R}$. As the collision probability depends on a local estimate of the distribution function at specific momenta, the test particle distribution within each spatial bin must also be binned in momentum space. This procedure will be discussed in detail below after the probabilities associated with the C_{12} collision process are introduced.

9.2.2.2 Probability of the C_{12} collision process

In an analogous fashion to the C_{22} process, mean collision rates at point r can be found by integrating $C_{12}[f,\phi]$ over momentum to obtain the corresponding "out" and "in" rates:

$$\Gamma_{12}^{\text{out}}(r,t) = \frac{\sigma n_c}{\pi h^3 m^2}\int d\mathbf{p}_2 d\mathbf{p}_3 d\mathbf{p}_4 \delta(\mathbf{p}_c+\mathbf{p}_2-\mathbf{p}_3-\mathbf{p}_4)\,\delta(\epsilon_c+\tilde{\epsilon}_2-\tilde{\epsilon}_3-\tilde{\epsilon}_4) \times f_2(1+f_3+f_4), \tag{9.52}$$

$$\Gamma_{12}^{\text{in}}(r,t) = \frac{\sigma n_c}{\pi h^3 m^2}\int d\mathbf{p}_2 d\mathbf{p}_3 d\mathbf{p}_4 \delta(\mathbf{p}_c+\mathbf{p}_2-\mathbf{p}_3-\mathbf{p}_4)\,\delta(\epsilon_c+\tilde{\epsilon}_2-\tilde{\epsilon}_3-\tilde{\epsilon}_4) \times f_2 f_4, \tag{9.53}$$

where the cubic terms $f_2 f_3 f_4$ formally cancel and have therefore been dropped from the expressions for each rate. The "out" process represents an atom from the noncondensate scattering off of the condensate to produce two non-condensed atoms (i.e., an atom is removed from the condensate and added to the noncondensate). On the other hand, the "in" process represents the scattering of two atoms in the noncondensate to produce one atom in the noncondensate and one atom in the condensate (i.e, a particle is removed from the noncondensate and added to the condensate). These two processes must be considered independently because neither conserves the number of atoms in the condensate or noncondensate alone.

To simplify the expression for the "out" rate, we once again transform to the center of mass frame, and utilize conservation of energy and momentum in an elastic collision and properties of the delta function to obtain

$$\Gamma_{12}^{\text{out}}(r,t) = \frac{\sigma n_c}{m}\int \frac{d\mathbf{p}_2}{(2\pi\hbar)^3} f_2 \int \frac{d\Omega}{4\pi}\left|\mathbf{p}_{\text{rel}}^{\text{out}}\right|(1+f_3+f_4), \tag{9.54}$$

where $\left|\mathbf{p}_{\text{rel}}^{\text{out}}\right| = \sqrt{|\mathbf{p}_c-\mathbf{p}_2|^2 - 4gmn_c}$ is the relative momentum of the incoming atoms corrected for the additional local mean-field energy of the noncondensate. Similar to the C_{22} process, the outgoing momenta are given in terms of the incoming momenta by

$$\mathbf{p}_3 = \frac{\mathbf{p}_{\text{cm}}^{\text{out}} + \left|\mathbf{p}_{\text{rel}}^{\text{out}}\right|\hat{\mathbf{u}}(\Omega)}{\sqrt{2}}, \tag{9.55}$$

$$\mathbf{p}_4 = \frac{\mathbf{p}_{\text{cm}}^{\text{out}} - \left|\mathbf{p}_{\text{rel}}^{\text{out}}\right|\hat{\mathbf{u}}(\Omega)}{\sqrt{2}}, \tag{9.56}$$

where $\mathbf{p}_{\rm cm}^{\rm out} = (\mathbf{p}_c + \mathbf{p}_2)/\sqrt{2}$. In Eq. (9.54), it is understood that the integration over $\mathbf{p}_2$ is restricted by the condition that $\left|\mathbf{p}_{\rm rel}^{\rm out}\right|$ is a real, positive number. This leads to the constraint $|\mathbf{p}_c - \mathbf{p}_2|^2 > 4gmn_c$, which implies that only noncondensate atoms satisfying this constraint can undergo an "out" collision. The physical meaning behind this constraint can be understood from the difference in potential energy between a condensed and non-condensed atom, which differ by a factor of gn_c. Therefore, to conserve energy, the atom in the noncondensate with momentum $\mathbf{p}_2$ must have excess kinetic energy to compensate for the potential energy gained by an atom leaving the condensate and entering the noncondensate.

The probability that a test particle located in a given spatial bin undergoes an "out" collision for the time step Δt is [173]

$$P_i^{\rm out} = \frac{\sigma n_{c,i}}{m}\left|\mathbf{p}_{\rm rel}^{\rm out}\right|\left(1 + f_3^{\Omega_R} + f_4^{\Omega_R}\right) \tag{9.57}$$

where $n_{c,i}$ is the condensate density at the position of particle i, and Ω_R represents a random scattering angle once again determined by randomly generating the unit vector $\hat{\mathbf{u}}(\Omega)$ such that $\cos\vartheta \in [-1,1]$ and $\varphi \in [0, 2\pi]$. Similar to the C_{22} process, $P_i^{\rm out}$ depends on the value of the distribution function evaluated at the outgoing momenta.

Unlike the collision processes already discussed, the momenta of the incoming non-condensate atoms are restricted for "in" collisions. Conservation of energy and momentum requires that $(\mathbf{p}_c - \mathbf{p}_2)\cdot(\mathbf{p}_c - \mathbf{p}_4) = mgn_c$, where 2 and 4 label the incoming atoms. To simplify the expression for the "in" rate, we once again transform to the center of mass frame, and utilize conservation of energy and momentum in an elastic collision and properties of the delta function to obtain

$$\Gamma_{12}^{\rm in}(r,t) = \frac{\sigma n_c}{\pi m}\int \frac{d\mathbf{p}_2}{(2\pi\hbar)^3} f_2 \int d\mathbf{p}_\perp \frac{f_4}{\left|\mathbf{p}_{\rm rel}^{\rm in}\right|}, \tag{9.58}$$

where $\left|\mathbf{p}_{\rm rel}^{\rm in}\right| = |\mathbf{p}_2 - \mathbf{p}_c|$ and the second integral is a 2D integral over a momentum vector $\mathbf{p}_\perp$ that lies in a plane normal to $\mathbf{p}_{\rm rel}^{\rm in}$. The constraint mentioned above leads to the requirement that the second incoming noncondensate atom, labelled 4, has a momentum

$$\mathbf{p}_4 = \mathbf{p}_\perp + \mathbf{p}_c + \frac{gn_c}{\left|\mathbf{p}_{\rm rel}^{\rm in}\right|}\hat{\mathbf{p}}_{\rm rel}^{\rm in}, \tag{9.59}$$

where $\hat{\mathbf{p}}_{\rm rel}^{\rm in}$ is a unit vector in the direction of $\mathbf{p}_{\rm rel}^{\rm in}$. The momentum of the outgoing non-condensate atom is then

$$\begin{aligned}\mathbf{p}_3 &= \mathbf{p}_\perp + \mathbf{p}_2 + \frac{gn_c}{\left|\mathbf{p}_{\rm rel}^{\rm in}\right|}\hat{\mathbf{p}}_{\rm rel}^{\rm in} \\ &= \mathbf{p}_4 + \mathbf{p}_2 - \mathbf{p}_c,\end{aligned} \tag{9.60}$$

as required by momentum conservation. Finally, the probability that a test particle in a given spatial bin undergoes an "in" collision for the time step Δt is [173]

$$P_i^{\rm in} = \frac{\sigma n_{c,i} A_p}{\pi m \left|\mathbf{p}\right|_{\rm rel}^{\rm in}} f_4^{\mathbf{p}_\perp^R} \Delta t, \tag{9.61}$$

where $\mathbf{p}_\perp^R$ is a randomly generated vector that lies within a momentum plane of area A_p. Note that although the choice of A_p is arbitrary, its exact value has little effect on the total mean collision rate as long as A_p is large enough to completely sample the region of occupied phase space. In practice, $A_p = \pi p_{\rm max}^2$, where $p_{\rm max}$ is the maximum momentum magnitude found in the test particle distribution being sampled. This will be discussed in more detail in section 9.2.2.3.

As discussed in section 9.1, the dissipative term in the GGPE is governed by the C_{12} collision integral (see Eq. (9.5)) and can be rewritten in terms of the mean collision rates:

$$R\left(r,t\right) = \frac{\hbar}{2n_c\left(r,t\right)}\left[\Gamma_{12}^{\rm out}\left(r,t\right) - \Gamma_{12}^{\rm in}\left(r,t\right)\right]. \tag{9.62}$$

In a simulation, $R\left(r,t\right)$ is represented on the same discrete grid as the condensate such that an estimate of R_j is required at each time step. The discrete function R_j is constructed from the test particle distribution in a similar fashion as the function $\tilde{n}_j$, and is calculated based on the value of R_i for each test particle:

$$R_i = \frac{\gamma\hbar}{2n_{c,i}V_b\Delta t}\left(P_i^{\rm out} - P_i^{\rm in}\right), \tag{9.63}$$

where γ gives the scaling between test particles and real noncondensate atoms, $n_{c,i}$ is evaluated at the location of particle i, and V_b is the volume of the spatial bin which contains particle i. Generation of this quantity at each time step will be discussed in more detail in section 9.2.2.3.

9.2.2.3 Implementation of the collision processes

The collision processes are implemented at the end of a time step after the test particle positions and momenta are updated. In order to sample the collision processes, the local test particle distribution in each spatial bin is considered independently in succession. The following procedure outlines the steps for **each** spatial bin:

(1) A 2D momentum grid is defined with the momentum magnitude $p \in [0, p_{\max}]$ along one dimension and $\cos\theta \in [-1, 1]$ along the other dimension. Here, $p_{\max}$ is the maximum momentum magnitude found in the local test particle distribution. With the momentum grid set, a local estimate of the distribution function at the current time step is found using the cloud-in-cell scheme to weight each test particle to the momentum grid. Similar to the scheme used to compute $\tilde{n}$, a 2D volume weighting scheme is used to construct the distribution function on the $(p, \cos\theta)$ grid points. Here, $p_i \equiv |\mathbf{p}_i|$ and $\cos\theta_i \equiv p_{i,x}/|\mathbf{p}_i|$ for particle i. This results in a discrete representation of $f(r, p, \cos\theta)$ in the current spatial bin.

(2) With a local estimate of $f(r, p, \cos\theta)$ we proceed by calculating the probabilities for the C_{12} collision process for the test particles in the local distribution. Therefore, the following sequence is repeated for **each** test particle in the current spatial bin:

   (a) First, the local condensate momentum and density are calculated at the position of the test particle using linear interpolation. Next, the outgoing momenta for the "out" process are generated by randomly choosing two numbers* such that $X_1 \in [-1, 1] \equiv \cos\vartheta$ and $X_2 \in [0, 2\pi] \equiv \varphi$. The unit vector describing the random scattering angle is then given by $\hat{\mathbf{u}}(\Omega_R) = \left(-X_1, \sqrt{1-X_1^2}\sin X_2, \sqrt{1-X_1^2}\cos X_2\right)$ and the outgoing momenta $\mathbf{p}_3$ and $\mathbf{p}_4$ are calculated using Eqs. (9.55) and (9.56), respectively. Note that the unit vector is defined in such a way as to make the x component

* Random numbers are denoted by the subscripted variable X, and they are generated using the MT19937 routine. Each time a unique random number is introduced the subscript is incremented. In practice, a generated random number is never used more than once.

align with the radial position of the particle. Given the outgoing momenta, values of $f_3^{\Omega_R}$ and $f_4^{\Omega_R}$ are found at the momentum coordinates $(|\mathbf{p}_3|, \cos\theta_3 = p_{3,x}/|\mathbf{p}_3|)$ and $(|\mathbf{p}_4|, \cos\theta_4 = p_{4,x}/|\mathbf{p}_4|)$ by interpolating from the function $f(r, p, \cos\theta)$ using bilinear interpolation. Finally, the probability P_i^{out} is calculated for the current test particle using Eq. (9.57).

(b) The next step is to generate the incoming momentum $\mathbf{p}_4$ for the "in" process, which depends on the value of a randomly generated momentum vector $\mathbf{p}_\perp^R$ that lies in a plane orthogonal to $\hat{\mathbf{p}}_{\text{rel}}^{\text{in}}$. This vector is constructed by randomly choosing two numbers such that $X_3 \in \left[0, p_{\max}^2\right]$ and $X_4 \in [0, 2\pi] \equiv \varphi$. Note that the range of X_3 is chosen to ensure that $\mathbf{p}_\perp$ samples the full area A_p defined in Eq. (9.61); otherwise, the "in" collision rate will not be properly reproduced. Thus, the random number X_3 defines the vector magnitude as $\left|\mathbf{p}_\perp^R\right| = \sqrt{X_3}$, and the components of $\mathbf{p}_\perp^R$ are given by

$$p_{\perp,x}^R = -\sqrt{X_3}\cos X_4 \sin\theta_2, \tag{9.64}$$

$$p_{\perp,y}^R = \sqrt{X_3}\left(\cos X_4 \cos\theta_2 \sin\phi + \sin X_4 \cos\phi\right), \tag{9.65}$$

$$p_{\perp,z}^R = \sqrt{X_3}\left(\cos X_4 \cos\theta_2 \cos\phi - \sin X_4 \sin\phi\right), \tag{9.66}$$

where $\cos\theta_2 = \hat{p}_{\text{rel},x}^{\text{in}}$ and $\sin\theta_2 = \sqrt{1 - \cos\theta_2{}^2}$, and

$$\cos\phi = \begin{cases} \frac{\hat{p}_{\text{rel},z}}{\sin\theta_2}, & \text{if } \sin\theta_2 > 0 \\ 1, & \text{otherwise} \end{cases} \tag{9.67}$$

$$\sin\phi = \begin{cases} \frac{\hat{p}_{\text{rel},y}}{\sin\theta_2}, & \text{if } \sin\theta_2 > 0 \\ 0, & \text{otherwise} \end{cases} \tag{9.68}$$

Note that $\cos\theta_2$ is chosen to lie along the x component of the relative momentum unit vector to coincide with the routine for updating the test particle positions, where the x component of the particle momentum is chosen to align with the radial position of the particle. This is correct since the condensate momentum only has a component in

the radial direction due to spherical symmetry, and therefore the relative momentum unit vector must point in the radial direction. Given $\mathbf{p}_{\perp}^{R}$ the incoming momentum $\mathbf{p}_4$ is calculated using Eq. (9.59) and the value of $f_4^{\mathbf{p}_{\perp}^{R}}$ is found at the momentum coordinate $(|\mathbf{p}_4|, \cos\theta_4 = p_{4,x}/|\mathbf{p}_4|)$ by interpolating from the function $f(r, p, \cos\theta)$ using bilinear interpolation. Finally, the probability P_i^{in} is calculated for the current test particle using Eq. (9.61).

(c) Given P_i^{out} and P_i^{in} for the current test particle, the dissipative term of the GGPE is calculated using Eq. (9.63). This is done in the same way as described in section 9.2.1.1 where the cloud-in-cell scheme with volume weighting is used followed by linear interpolation and smoothing with a Gaussian low-pass filter. This procedure results in an estimate of the discrete function R_j for the current time step.

(d) Finally, the type of collision that the current test particle undergoes, if any, is determined by comparing the calculated probabilities to a random number $X_5 \in [0, 1]$. One of three outcomes is possible:

(i) If $X_5 < P_i^{\text{out}}$ then an "out" collision occurs. The current test particle's momentum is updated to $\mathbf{p}_3$ (Eq. (9.55)) and a new test particle is created at the same position as the current test particle, but with momentum $\mathbf{p}_4$ (Eq. (9.56)). The current test particle is flagged as having undergone a collision, and the new test particle data is temporarily stored such that it can be added to the distribution after all current test particles have been considered for collisions. The routine then advances to the next test particle.

(ii) If $P_i^{\text{out}} < X_5 < P_i^{\text{out}} + P_i^{\text{in}}$ then an "in" collision occurs. A test particle in the current spatial bin with momentum $\mathbf{p}_4$ (Eq. (9.59)) that has not already undergone a collision must be located and eliminated from the test particle distribution. If no test particles matching this criteria exist in the momentum bin that contains $\mathbf{p}_4$ then no collision occurs and the routine advances to the next test particle.

Otherwise, the current test particle's momentum is updated to $\mathbf{p}_3$ (Eq. (9.60)) based on the momentum of the actual test particle found (not the ideal value of $\mathbf{p}_4$ calculated with Eq. (9.59), which would not conserve momentum). Then, the current test particle is flagged as having undergone a collision, and the test particle to be eliminated is temporarily stored such that it can be eliminated from the distribution after all current test particles have been considered for collisions.

(iii) If $P_i^{\text{out}} + P_i^{\text{in}} < X_5$ then no collision occurs and the routine advances to the next test particle.

(3) Once each test particle in the local distribution has been considered for a C_{12} collision, a list of randomly paired test particles is generated to calculate the probability for the C_{22} collision process. Therefore, the following sequence is repeated for **each pair** of test particles in the current spatial bin:

(a) First, the local noncondensate density is estimated as $\tilde{n}_{ij} \approx \gamma N_{tp,k}/V_b$, where γ gives the scaling between test particles and real noncondensate atoms, $N_{tp,k}$ is the total number of test particles in the current spatial bin, and V_b is the bin volume. Next, the outgoing momenta are generated by randomly choosing two numbers such that $X_6 \in [-1,1] \equiv \cos\vartheta$ and $X_7 \in [0,2\pi] \equiv \varphi$. The unit vector describing the random scattering angle is then given by $\hat{\mathbf{u}}(\Omega_R) = \left(-X_6, \sqrt{1-X_6^2}\sin X_7, \sqrt{1-X_6^2}\cos X_7\right)$ and the outgoing momenta $\mathbf{p}_3$ and $\mathbf{p}_4$ are calculated using Eqs. (9.48) and (9.49), respectively. Given the outgoing momenta, values of $f_3^{\Omega_R}$ and $f_4^{\Omega_R}$ are found at the momentum coordinates $(|\mathbf{p}_3|, \cos\theta_3 = p_{3,x}/|\mathbf{p}_3|)$ and $(|\mathbf{p}_4|, \cos\theta_4 = p_{4,x}/|\mathbf{p}_4|)$ by interpolating from the function $f(r,p,\cos\theta)$ using bilinear interpolation. Finally, the probability P_{ij}^{22} is calculated for the current test particle pair using Eq. (9.51).

(b) It is determined if the current test particle pair undergoes a collision by comparing the calculated probability to a random number $X_8 \in [0,1]$. One of two outcomes is possible:

(i) If $X_8 < P_{ij}^{22}$ then a collision occurs. The current test particle pair's momenta are updated to $\mathbf{p}_3$ (Eq. (9.48)) and $\mathbf{p}_4$ (Eq. (9.49)). The routine then advances to the next test particle pair.

(ii) $P_{ij}^{22} < X_8$ then no collision occurs and the routine advances to the next test particle pair.

After each spatial bin has been considered the test particle distribution must be updated based on the temporarily stored data of particles to be added and eliminated based on the C_{12} collision process. This procedure changes the total number of test particles in the simulation, and therefore the total number of real noncondensate atoms because γ remains fixed for a given simulation. However, the total number of atoms in the simulation is conserved because the normalization of the condensate wavefunction changes due to $R(r,t)$, which is also a result of the C_{12} collision process. In practice, the total atom number is conserved only to within statistical fluctuations $\propto \sqrt{N}$ because the noncondensate atom number changes in discrete jumps while the condensate atom number changes continuously.

We have now outlined the numerical procedures used to propagate both the GGPE and QBE forward in time. The next section provides a detailed description of how to initialize and perform a full dynamical simulation that evolves a computed equilibrium state forward in time. Simulation results are then given that directly compare the presented numerical implementation of the ZNG equations with previous work in the field.

9.3 Full Dynamical Evolution of the ZNG Equations

A full dynamical simulation begins by computing an equilibrium solution to the ZNG equations given a temperature and total atom number. Given an equilibrium state, the test particle distribution is generated by randomly choosing positions and momenta for each test particle that accurately reproduce the equilibrium phase-space distribution function. This equilibrium state is then propagated forward in time using the routines developed in sections 9.1 and 9.2. As an exam-

ple, results of a quench simulation are presented that demonstrate growth of the condensate, decay of the noncondensate, and conservation of total atom number. These results are directly compared to previous work in the field and provide a validation for the numerical implementation of the ZNG equations described in this dissertation.

9.3.1 Calculation of equilibrium solutions to the ZNG equations

As discussed in section 8.3.2.1, an equilibrium state of the system can be found by solving Eqs. (8.42) and (8.44) self-consistently subject to the conditions that $\tilde{\mu}_0 = \mu_{c,0}$ and the temperature T_0 and total number of atom in the gas N remain fixed. Therefore, the starting point for any simulation is to set T_0 and N to the desired values, set the isotropic harmonic trap frequency ω to the desired value, set $\tilde{n}_0(r) = 0$, and then make an educated guess of the functional form of the condensate wavefunction. A standard approach is to neglect the kinetic energy term in Eq. (8.44) and use the so-called Thomas-Fermi solution for the condensate wavefunction [166]. However, this approach can lead to numerical instabilities due to the discontinuity present at the edge of the condensate. Therefore, it is preferable to use the non-interacting ground state wavefunction with Gaussian widths broadened by the effect of interatomic interactions.[†] The condensate wavefunction $\varphi_0(r)$ is then normalized to the number of atoms in the condensate $N_{c,0}$, which is initially estimated using the critical temperature and ideal gas relations of Eqs. (8.3) and (8.4), respectively. Finally, an initial estimate of the chemical potential is obtained by integrating Eq. (8.44) over all space:

$$\mu_{c,0} \approx \frac{4\pi}{N_{c,0}} \int_0^\infty dr r^2 \left[\frac{1}{2} m\omega^2 r^2 + g n_{c,0}(r) \right] |\varphi_0(r)|^2 \tag{9.69}$$

Note that the kinetic energy portion of the Hamiltonian has been neglected to coincide with the method used to obtain a variational estimate of the condensate wavefunction.

With an initial estimate for the ground state of the time-independent GGPE, the numerical routine for calculating an equilibrium state of the system proceeds as follows:

(1) Calculate the effective potential for the noncondensate using $\tilde{U}_0(r) = \frac{1}{2} m\omega^2 r^2 + 2g n_{c,0}(r) +$

[†] See Ref. [166], section 6.2.1 for a variational estimate of this wavefunction

$2g\tilde{n}_0(r)$.

(2) Calculate the noncondensate density $\tilde{n}_0(r)$ using Eq. (8.42), and calculate the number of atoms in the noncondensate $\tilde{N}_0$ by integrating over all space.

(3) Calculate the number of atoms in the condensate using $N_{c,0} = N - \tilde{N}_0$, and renormalize the condensate wavefunction to this value.

(4) Calculate the effective potential for the condensate using $U_{c,0}(r) = \frac{1}{2}m\omega^2 r^2 + gn_{c,0}(r) + 2g\tilde{n}_0(r)$

(5) Propagate the GGPE in imaginary time using the Crank-Nicolson method (see section 9.1.2), renormalize $\varphi_0(r)$ to $N_{c,0}$, and calculate a new value for the chemical potential.

(6) Compare the updated chemical potential and noncondensate atom number to the previous values and proceed as follows:

   (a) If the change in $\mu_{c,0}$ and $\tilde{N}_0$ is less than some predefined tolerance then stop the calculation because the equilibrium state has been found.

   (b) Otherwise, return to step (1).

There are a few subtleties with the above method that must be addressed. First, if the chemical potential exceeds the minimum value of $\tilde{U}_0(r)$ then it must be artificially set equal to this minimum value. Otherwise, the fugacity $z_0(r) > 1$ and the polylogarithm function becomes divergent. This anomaly is typically encountered when temperatures close to T_c are studied, and currently limits the application of the above procedure. Second, the numerical evaluation of the polylogarithm function with double precision is not straightforward. To address this issue, a Chebyshev expansion method introduced by MacLeod [184] is employed. Finally, it is useful to explain the reason for propagating the GGPE in imaginary time. Let the condensate wavefunction be expanded in an orthonormal basis of eigenstates $\chi_{n,0}(r)$:

$$\varphi_0(r) = \sum_{n=0}^{\infty} c_n e^{-iE_n t/h} \chi_{n,0}(r), \tag{9.70}$$

where it is assumed that E_0 corresponds to the ground state and $E_n < E_{n+1}$ for all n. If the substitution $t \to -i\tau$ is made then clearly the above expansion becomes a summation over decaying exponential terms. Therefore, if an initial estimate for $\varphi_0(r)$ is propagated over many imaginary time steps, and renormalized at every step, eventually only the ground state contribution to the above summation will remain. This is a result of the fact that the decay time for each state decreases as n increases.

An example equilibrium solution for the characteristic problem described at the beginning of this chapter is shown in Fig. 9.2. The computed state contains $N_{c,0} = 26,324$ atoms in the condensate and $\tilde{N}_0 = 23,676$ atoms in the noncondensate, which is significantly different than the initial estimate from the ideal gas relation. This difference arises due to the mean-field repulsion terms present in the expressions for the effective potentials felt by the condensate and noncondensate, the effect of which is particularly evident in the density distributions of each component depicted in Fig. 9.2(a). The noncondensate experiences a repulsive force at $r = 0$ due to the large density of the condensate at this location, and $\tilde{n}_0(r)$ obtains a maximum value near the edge of the condensate where $n_{c,0}(r)$ approaches zero. The condensate, on the other hand, experiences only a weak repulsive force near its edge where the two components have a similar density, resulting in a slight narrowing of the condensate density distribution. These effects are clear when examining the effective potentials plotted in Fig. 9.2(b), where $\tilde{U}_0(r)$ is peaked at $r = 0$ while $U_{c,0}(r)$ is effectively flat in this region, and $\tilde{U}_0(r)$ is minimal at the edge of the condensate.

9.3.2 Initialization of the test particle distribution

With an equilibrium state computed it is necessary to find initial positions and momenta for the test particle distribution such that the test particles accurately represent the equilibrium distribution function of the noncondensate. Furthermore, the positions and momenta of the test particles must be chosen at random such that they sample all of the available phase space. A simple, generally applicable algorithm that generates random deviates which follow a given distribution is the acceptance-rejection method [175], and it is used here to initialize the test particle distribution.

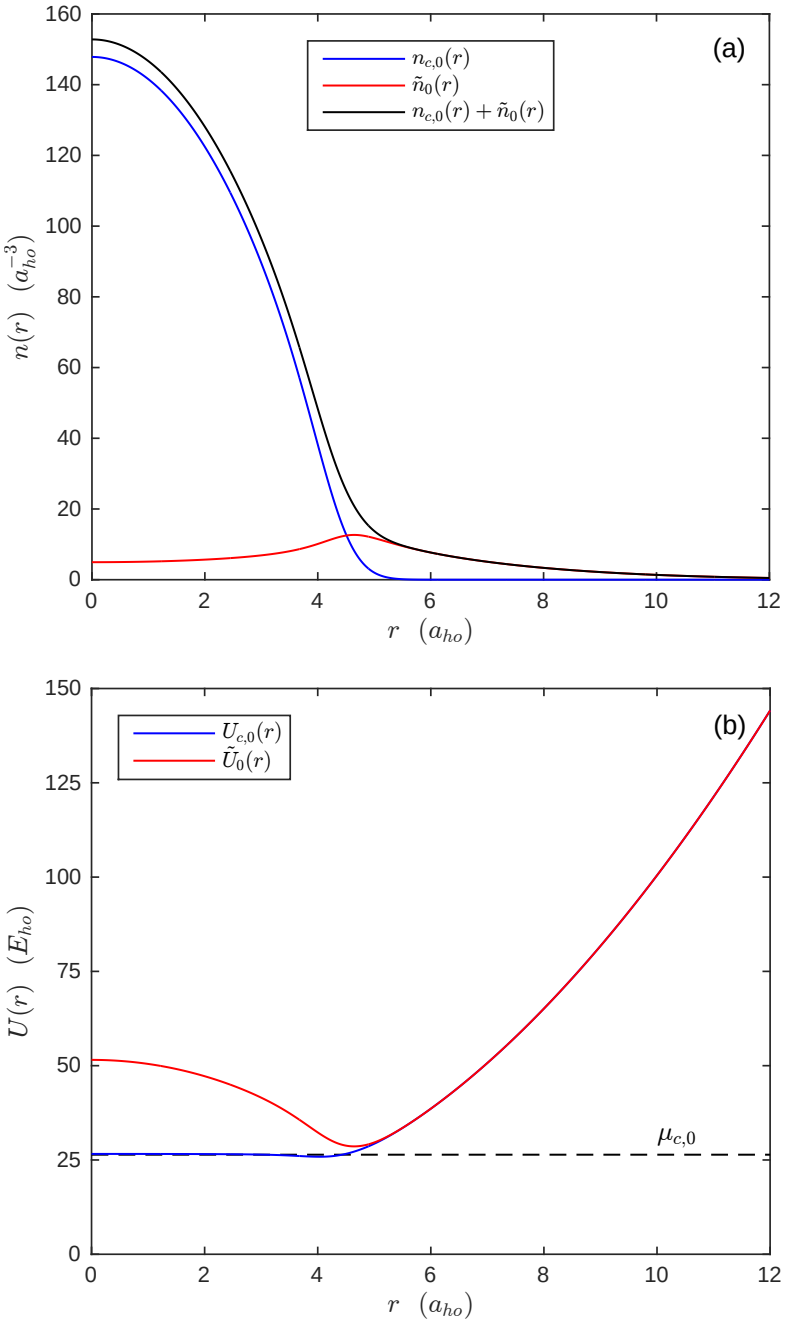

Figure 9.2: (a) Equilibrium density distributions for the condensate (blue), non-condensate (red), and total system (black). (b) Equilibrium effective potentials felt by the condensate (blue) and non-condensate (red). The black dashed line indicates the equilibrium chemical potential, which lies below the minimum value of the noncondensate effective potential. The temperature is $T_0 = 200$ nK, the total atom number is $N = 50,000$, the trap frequency is $\omega = 2\pi \times 187$ rad/s, and ^{87}Rb atoms are assumed with a scattering length $a_s = 5.29$ nm.

The algorithm employed here first finds a suitable position for a test particle based on the equilibrium noncondensate density $\tilde{n}_0(r)$. Once a position has been determined the equilibrium fugacity is calculated and a suitable momentum magnitude for the test particle is found based on the equilibrium Bose-Einstein distribution. This process is repeated until the desired number of test particles have been initialized. The following procedure outlines the steps for **each** test particle:

(1) Generate two random numbers such that $X_9 \in [0, r_{\max}]$ and $X_{10} \in \left[0, r^2\tilde{n}_0(r)\big|_{\max}\right]$, where the "max" subscript indicates the maximum value of the function $r^2\tilde{n}_0(r)$.

(2) Compare X_{10} to $X_9^2\ \tilde{n}_0(X_9)$:

   (a) If $X_{10} < X_9^2\ \tilde{n}_0(X_9)$ then assign $r_i = X_9$ as the position of the test particle and proceed to find it's momentum

   (b) Otherwise, return to step (1).

(3) Calculate the equilibrium fugacity at the position of the test particle $z_0(r_i)$.

(4) Generate two random numbers such that $X_{11} \in [0, p_{\max}]$ and $X_{12} \in \left[0, p^2 f_0(r_i, p)\big|_{\max}\right]$, where the "max" subscript indicates the maximum value of the function

$$p^2 f_0(r_i, p) = \frac{p^2 z_0(r_i)}{e^{\beta_0 p^2/2m} - z_0(r_i)}. \tag{9.71}$$

(5) Compare X_{12} to $X_{11}^2\ f_0(r_i, X_{11})$:

   (a) If $X_{12} < X_{11}^2\ f_0(r_i, X_{11})$ then assign $|p_i| = X_{11}$ as the momentum magnitude of the test particle and proceed to find the momentum components.

   (b) Otherwise, return to step (4).

(6) Generate two random numbers such that $X_{13} \in [-1, 1] \equiv \cos\vartheta$ and $X_{14} \in [0, 2\pi] \equiv \varphi$ and

calculate the momentum components as

$$p_{i,x} = -X_{11}X_{13}. \tag{9.72}$$

$$p_{i,y} = X_{11}\sqrt{1 - X_{13}^2}\sin X_{14}, \tag{9.73}$$

$$p_{i,z} = X_{11}\sqrt{1 - X_{13}^2}\cos X_{14}. \tag{9.74}$$

Note that in the above procedure, values of functions (e.g., $\tilde{n}_0(r)$) at arbitrary r and p are found using standard 1D linear interpolation. Once each test particle has been assigned a position and momentum it is necessary to subtract the average momentum of the entire test particle distribution along each axis from each individual test particle's momentum components. This ensures that there is no net momentum of the distribution function at equilibrium, and is necessary because of numerical errors introduced by the acceptance-rejection method.

9.3.3 Procedure for a full dynamical simulation

Finally, we have all of the necessary components to perform a full dynamical simulation of the ZNG equations in spherical symmetry. The following procedure outlines the necessary steps to evolve the ZNG equations over a single time step Δt:

(1) Set T_0, N, and ω, and calculate the equilibrium state (see section 9.3.1).

(2) Initialize the test particle distribution (see section 9.3.2).

(3) Update the test particle positions by $\Delta t/2$ (see section 9.2.1).

(4) Construct $\tilde{n}_j^n$ (see section 9.2.1.1) and $\tilde{V} = \left(3\tilde{U}_j^n - \tilde{U}_j^{n-1}\right)/2$ where

$$\tilde{U}_j^n = \frac{1}{2}m\omega^2 r_j^2 + 2gn_{c,j}^n + 2g\tilde{n}_j^n. \tag{9.75}$$

(5) Update the test particle momenta by Δt (see section 9.2.1).

(6) Update the test particle positions by $\Delta t/2$ (see section 9.2.1).

(7) Check for C_{12} collisions and construct R_j^n (see section 9.2.2.3).

(8) Check for C_{22} collisions (see section 9.2.2.3).

(9) Update the number of test particles in the simulation (see section 9.2.2.3).

(10) Construct $\tilde{V}_c = \left(3U_{c,j}^n - U_{c,j}^{n-1}\right)/2$ where

$$U_{c,j}^n = \frac{1}{2}m\omega^2 r_j^2 + g n_{c,j}^n + 2g\tilde{n}_j^n - iR_j^n. \tag{9.76}$$

(11) Update the condensate wavefunction by Δt (see section 9.1.2).

(12) Return to step (3).

An example of this procedure applied to the characteristic problem described at the beginning of this chapter is shown in Fig. 9.3. This simulation represents the propagation of an equilibrium state forward in time, which should remain unchanged. We observe no readjustment of the number of atoms in the condensate and noncondensate, which indicates the equilibrium state is accurate and the update procedure outlined above is functioning correctly. Note that due to the difference in how the number of condensate and noncondensate atoms change in a dynamical simulation there are some noticeable fluctuations in these quantities. Nonetheless, the total atom number is conserved to within $\sqrt{N}$ as depicted by the shaded area in Fig. 9.3. The next section will investigate the non-equilibrium performance of the spherically symmetric ZNG code by comparing results of a quench simulation to previous work.

9.3.4 Results of a quench simulation

In order to better characterize the spherically symmetric ZNG code, it is important to perform a non-equilibrium simulation to ensure the mean field interaction between the condensate and noncondensate, in addition to the collision processes, drive the system towards equilibrium. A simple non-equilibrium test case is realized by taking an equilibrium state and suddenly reducing the temperature by a factor of two. This method has been used previously to test the original ZNG code developed by Jackson and Zaremba [156], as well as a parallelized ZNG code developed by

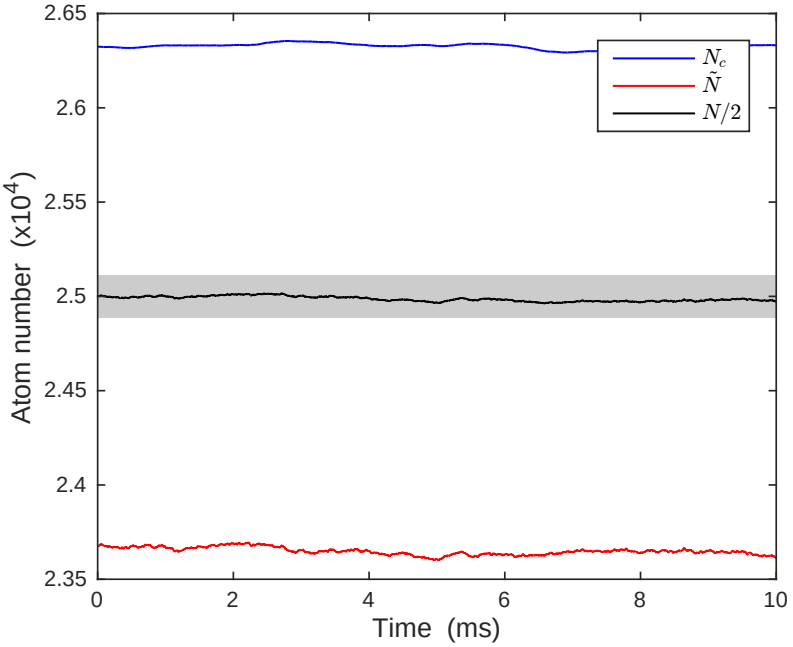

Figure 9.3: Condensate (blue), noncondensate (red), and total (black) atom numbers as a function of time for a full dynamical simulation of an equilibrium state. The gray shaded area represents the expected region of total atom number conservation given by $N/2 \pm \sqrt{N}/2$. The temperature is $T_0 = 200$ nK, the total atom number is $N = 50,000$, the trap frequency is $\omega = 2\pi \times 187$ rad/s, and ^{87}Rb atoms are assumed with a scattering length $a_s = 5.29$ nm. The simulation uses $200,000$ test particles, 8000 bins in position space, 20 bins for the momentum magnitude, 10 bins for the angular variable, and a time step of 10^{-3}. Parameters were found empirically.

Märkle [185]. By directly comparing the results of this quench simulation to previous work, we can ensure the spherically symmetric ZNG code is consistent with codes developed by others.

The quench simulation begins with the equilibrium state of the characteristic problem described at the beginning of this chapter (see section 9.3.1). Following the procedure outlined in section 9.3.2, the quench is performed by initializing the test particle distribution to a distribution function with the substitution $\beta_0 \rightarrow 2\beta_0$:

$$p^2 f_0\left(r_i, p\right) = \frac{p^2 z_0\left(r_i\right)}{e^{2\beta_0 p^2/2m} - z_0\left(r_i\right)}. \tag{9.77}$$

This results in a test particle distribution with half the temperature of the equilibrium state; therefore, the test particles momenta are too low to remain in equilibrium and substantial particle transfer from the noncondensate to the condensate should occur. Furthermore, the noncondensate will collapse towards the center of the trap before being repelled by the large mean field potential of the condensate. This will lead to small oscillations of both the condensate and noncondensate, the effect of which is evident in the evolution of the number of atoms in each component of the gas. This behavior is depicted in Fig. 9.4, which shows the growth of the condensate, decay of the noncondensate, and conservation of total atom number as the system evolves forward in time. Notably, the results of the spherically symmetric ZNG code exhibit slightly more atoms transferred from the noncondensate to the condensate; however, the total particle number experiences less fluctuations and appears to be slightly more stable. The small, periodic oscillations in the condensate and noncondensate atom numbers show good agreement between all three codes demonstrating that the mean field potentials are accurately reproduced. Given the consistency of the results for a quench simulation, we conclude that the developed spherically symmetric ZNG code is consistent with previous work.

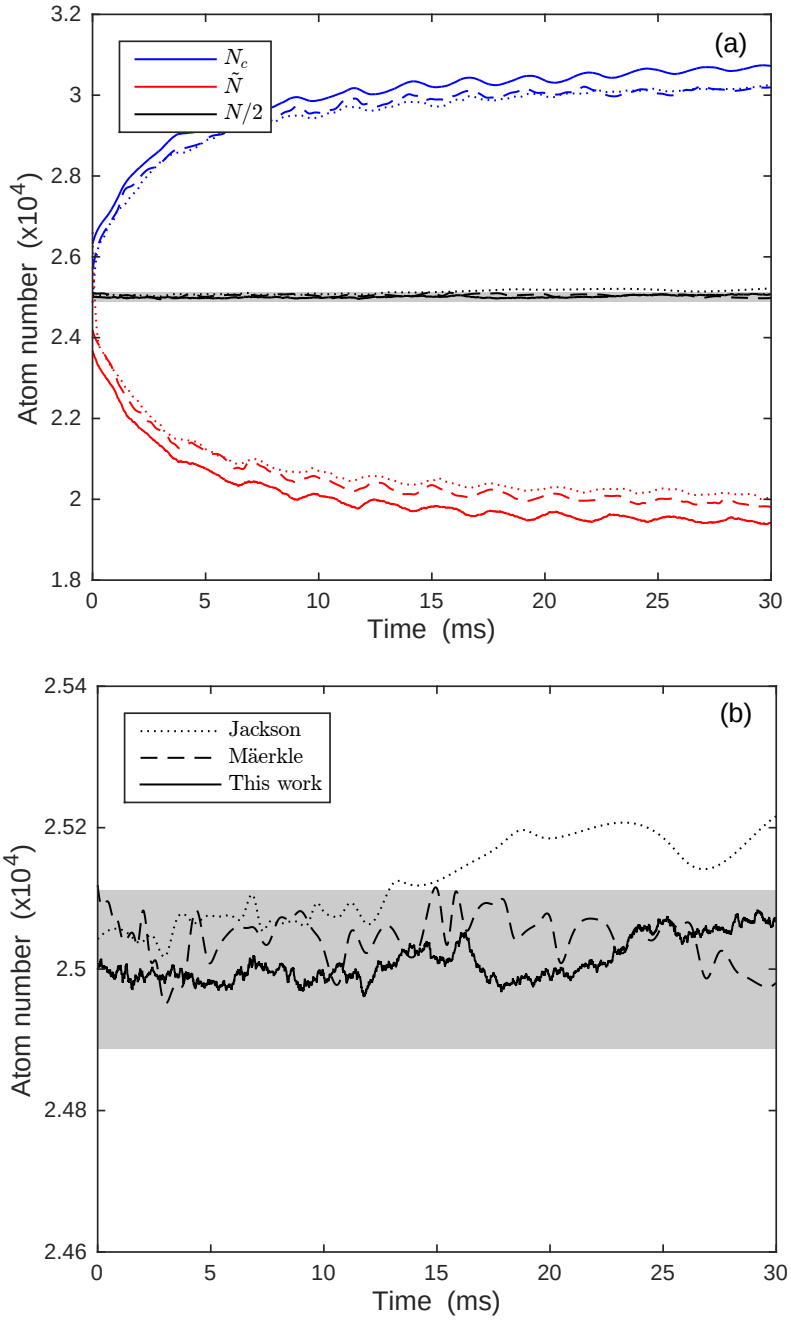

Figure 9.4: (a) Time evolution of the condensate (blue), noncondensate (red), and total atom number (black) after a sudden quench of the system temperature. (b) Comparison of total atom number conservation for ZNG codes developed by Jackson and Zaremba [156] (dotted) and Märkle [185] (dashed), and the spherically symmetric code developed here (solid). The gray shaded area represents the expected region of total atom number conservation given by $N/2 \pm \sqrt{N}/2$. The temperature of the initial state (before the quench) is $T_0 = 200$ nK, the total atom number is $N = 50,000$, the trap frequency is $\omega = 2\pi \times 187$ rad/s, and ^{87}Rb atoms are assumed with a scattering length $a_s = 5.29$ nm. The simulation uses $200,000$ test particles, 8000 bins in position space, 20 bins for the momentum magnitude, 10 bins for the angular variable, and a time step of 10^{-3}. Parameters were found empirically.

Chapter 10

Collapse and revival of the monopole mode of a degenerate Bose gas in an isotropic harmonic trap*

In this chapter, we present experimental measurements and analysis of the monopole mode of a finite temperature BEC confined in an isotropic harmonic trap. We observe a collapse and partial revival of the condensate oscillation, and compare these results to the predictions of finite temperature BEC models. We set the scene in Sec. 10.1 by providing an overview of the limiting cases for the collective modes of a BEC and ideal gas in an isotropic harmonic trap. This is followed by a theoretical analysis of the spectrum of coupled modes of the condensate and noncondensate at finite temperatures in Sec. 10.1.2. This provides a framework for understanding the collapse and revival time scales observed in the experiment. In Sec. 10.2 we provide a description of the experimental procedure and the main results of this chapter. In Sec. 10.3 we investigate the damping observed experimentally through numerical simulations within the ZNG formalism. After discussing the results of the numerical simulations, we summarize in Sec. 10.4.

10.1 Collisionless Dynamics

Here, we provide an overview of the collisionless dynamics of a trapped Bose gas, beginning with a discussion of the limiting cases for collective modes in an isotropic trap. We then discuss the monopole mode of a finite temperature BEC through application of the semiclassical collisionless model from Ref. [150, 151] to a spherically symmetric trapping geometry, and show how the

* A version of this chapter has been published in Ref. [139].

monopole mode response can be cast in terms of two eigenmodes of the system. This analysis provides a framework for understanding the collapse and revival behavior of the condensate oscillation observed in the experimental results.

10.1.1 Collective modes in an isotropic harmonic trap

In an isotropic harmonic trap, the collective modes of a Bose gas are well understood in two limits. In the Thomas-Fermi (TF) limit at zero temperature, the ratio of the kinetic to interaction energy is small when the number of atoms in the BEC is large; thus, the kinetic energy can be neglected. The collective mode frequencies of a BEC in a three-dimensional isotropic harmonic trap in this limit can be estimated using a hydrodynamic approach [145]. The mode frequencies depend on the principle quantum number n and angular quantum number l according to

$$\omega^2 = \omega_0^2 \left(l + 3n + 2nl + 2n^2 \right), \tag{10.1}$$

where ω_0 is the harmonic trap frequency and ω is the frequency of the collective mode. For the spherically symmetric monopole, or breathing mode ($n = 1, l = 0$), the mean-square radius of the condensate oscillates at $\omega = \sqrt{5}\omega_0$, and the motion is undamped. Above the BEC critical temperature, T_c, mean-field effects can be neglected and the gas can be described by a classical Boltzmann equation. In this case, the mode oscillates at $\omega = 2\omega_0$ in both the collisionless and hydrodynamic regimes [186], and the motion is undamped. In the collisionless regime individual atoms may undergo many oscillations before experiencing a collision while the hydrodynamic regime implies the gas is in local statistical equilibrium.

10.1.2 Coupled-modes analysis[†]

To obtain insight into the behavior of the monopole mode at finite temperature in an isotropic trap, we apply a model previously developed by Bijlsma and Stoof [150]. This methodology introduces a dynamical scaling ansatz for the condensate and noncondensate that successfully reproduces the

[†] The analysis presented in this section was done by V. E. Colussi under the supervision of M. J. Holland. The author of this dissertation made use of the results as part of the work published in Ref. [139].

limiting cases of the monopole mode behavior described in the previous section. The condensate and noncondensate are described by a Gross-Pitaevskii equation (GPE) and a collisionless quantum Boltzmann equation (QBE), respectively, which are coupled by their mean-field interaction. The analysis here assumes a small amplitude perturbation of the system, and a linear response such that the effects of damping are absent.

In the following calculation, a scaling ansatz is made for the time evolution of the condensate density,

$$n_c(\mathbf{r},t) = \frac{1}{\lambda^3} n_c^0\left(\frac{\mathbf{r}}{\lambda}\right), \tag{10.2}$$

and the Wigner distribution function of the noncondensate,

$$f(\mathbf{r},\mathbf{p},t) = \frac{1}{\bar{\alpha}^6} f^0\left(\frac{\mathbf{r}}{\alpha\bar{\alpha}}, \frac{\alpha}{\bar{\alpha}}\left[\mathbf{p} - \frac{m\dot{\alpha}}{\alpha}\right]\right), \tag{10.3}$$

which are written in terms of a Gaussian density profile n_c^0 for the condensate and a saturated Bose-Einstein distribution f^0 for the noncondensate:

$$\begin{aligned} n_c^0(\mathbf{r}) &= N_c\left(\frac{m\omega_0}{\pi\hbar}\right)^{1/2} e^{-\frac{m\omega_0}{\hbar}r^2}, \\ f^0(\mathbf{r},\mathbf{p}) &= \tilde{N}\left(\frac{\hbar\omega_0}{k_B T\zeta(3)}\right) \\ &\times \left[e^{\left(\frac{p^2}{2m}+\frac{1}{2}m\omega_0^2 r^2\right)/k_B T} - 1\right]^{-1}. \end{aligned} \tag{10.4}$$

The number of atoms in the condensate and noncondensate are denoted by N_c and $\tilde{N}$, respectively, and $\zeta(s)$ is the Riemann zeta function. The scaling parameters, $\lambda(t)$ and $\alpha(t)$, capture the oscillation of the widths of the two components, and the bar denotes the equilibrium value. Inserting the scaling ansatz into the GPE and QBE results in a set of coupled equations of motion for the condensate and noncondensate characteristic widths:

$$\ddot{\mathbf{u}} + \omega_0^2 \mathbf{u} = \mathbf{v}(\mathbf{u}), \tag{10.5}$$

where the vector $\mathbf{u}$ contains the scaling parameters

$$\mathbf{u} = \begin{pmatrix} \lambda \\ \\ \alpha \end{pmatrix}, \tag{10.6}$$

and $\mathbf{v}(\mathbf{u})$ is a nonlinear vector function describing the spreading of the cloud due to kinetic energy and the effects of nonlinear interactions (see Ref. [150] for details).

In the limit of a small amplitude oscillation, the total density of the system can be written as

$$n(\mathbf{r},t) = \bar{n}(\mathbf{r}) + \delta n(\mathrm{r}) e^{i\omega t}, \tag{10.7}$$

where the perturbation is generated by modulating the trap frequency with amplitude ϵ:

$$\omega_0(t) = \left(1 + \epsilon e^{i\omega t}\right)\omega_0. \tag{10.8}$$

In this limit Eq. (10.5) can be linearized:

$$-\omega^2 \delta\mathbf{u} + \omega_0^2 \delta\mathbf{u} = \left[\nabla_{\mathbf{u}}\mathbf{v}\right]\big|_{\bar{\mathbf{u}}} \cdot \delta\mathbf{u} - 2\epsilon\omega_0^2 \bar{\mathbf{u}}, \tag{10.9}$$

and the eigenfrequencies ω_n and eigenmodes $\mathbf{u}^{(n)}$ of the homogeneous part of Eq. (10.9) can be extracted with a solution of the form

$$\delta\mathbf{u} = 2\epsilon\omega_0^2 \sum_n \frac{\mathbf{u}^{(n)} \cdot \bar{\mathbf{u}}}{\omega^2 - \omega_n^2} \mathbf{u}^{(n)}. \tag{10.10}$$

From this solution, we find two eigenmodes that we refer to as the in-phase and out-of-phase modes of the system. The in-phase mode corresponds to the condensate and noncondensate monopole modes oscillating together with a phase difference of $\phi = 0$, and the out-of-phase mode corresponds to a phase difference of $\phi = \pi$. In Fig. 10.1, the frequencies of the in-phase and out-of-phase modes as a function of temperature are shown.

Given the eigenmodes of the system, the time-averaged work done by a perturbation of the trap frequency can be used to characterize the response of the system:

$$W = \sum_n \frac{b_n}{\omega^2 - \omega_n^2}, \tag{10.11}$$

where the b_n are a measure of the magnitude that each eigenmode responds with when the system is perturbed. Figure 10.2 shows the b_n as a function of temperature for the two modes discussed above. For temperatures $T > 0.2\ T_c$ both modes of the system will be excited by a perturbation of

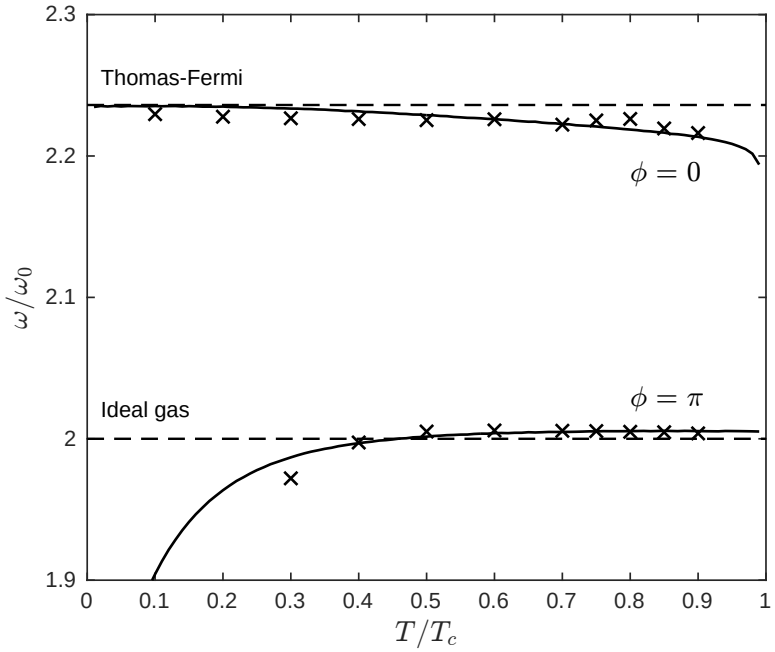

Figure 10.1: Oscillation frequency of the in-phase ($\phi = 0$) and out-of-phase ($\phi = \pi$) modes as a function of temperature from the coupled-modes analysis (solid lines) and ZNG simulations (crosses). The dashed lines represent the TF limit ($\sqrt{5}\omega_0$) and ideal gas limit ($2\omega_0$) for the monopole mode frequency of the condensate and noncondensate, respectively. Assumptions made regarding the form of excitations become invalid for $T \lesssim 0.2\ T_c$. Reproduced from Ref. [139].

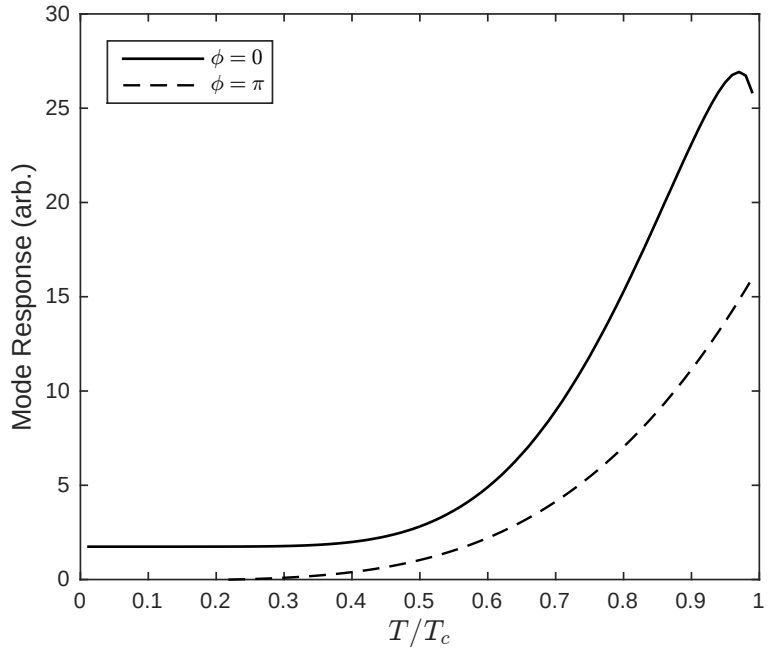

Figure 10.2: Magnitude of the response of the in-phase ($\phi = 0$) and out-of-phase ($\phi = \pi$) modes to a trap frequency perturbation as a function of temperature. The amplitude of the trap frequency modulation is $\epsilon = 0.01$. Reproduced from Ref. [139].

the trap frequency.

The coupled-modes analysis suggests that the oscillation of a single component of the gas (e.g., condensate) is described by a superposition of two eigenmodes oscillating at slightly different frequencies. Therefore, we expect measurements of the condensate width as a function of time for temperatures $T > 0.2\ T_c$ to beat at a frequency corresponding to the frequency difference between the two eigenmodes, $\Delta\omega/\omega_0 \sim 0.2$–$0.25$ (see Fig. 10.1). Given this result, we present experimental observations of the monopole mode in an isotropic trap in the next section.

10.2 Experiment[‡]

The experimental system is a Bose gas of ^{87}Rb atoms cooled to quantum degeneracy via forced radio-frequency evaporation in a time-averaged, orbiting potential (TOP) trap [187]. A standard TOP trap configuration results in an oblate harmonic trap with an aspect ratio of $\omega_z/\omega_r = \sqrt{8}$, where ω_z (ω_r) is the axial (radial) trapping frequency. Here, the overall harmonic confinement of the trap is reduced and the trap minimum is allowed to sag under the force of gravity. This causes the curvature of the magnetic field along the z axis to decrease, which effectively decreases the ratio ω_z/ω_r. The end result is an isotropic harmonic trap with $\omega_0 \equiv \omega_r = \omega_z = 2\pi \times (9.03(2)\ \text{Hz})$ with a residual asphericity of less than 0.2%. This system was used in previous work to study the monopole mode of a Bose gas above the BEC critical temperature [163], and a detailed description of the apparatus can be found in Ref. [165].

We excite the monopole mode of the system below the BEC critical temperature in the range of approximately 0.75–0.9 T_c. The experimental procedure parallels that of Ref. [163]—beginning from a system at equilibrium, the trap frequency is sinusoidally modulated at a driving frequency $\omega_D \approx 2\pi \times 18$–$19$ Hz for four periods with an amplitude $\epsilon \approx 0.1$:

$$\omega(t) = [1 + \epsilon \sin(\omega_D t)]\, \omega_0. \tag{10.12}$$

After driving, we find that the peak TF radius of the condensate is 10–15% larger than the equi-

[‡] The experiment was conducted by D. S. Lobser under the supervision of H. J. Lewandowski and E. A. Cornell. The author of this dissertation made use of the experimental data as part of the work published in Ref. [139].

librium value for all of the experimental data sets. The system is then allowed to freely evolve in the static isotropic trap for a time t before six nondestructive phase-contrast images record the integrated column density of the cloud at intervals of 10 ms or 17 ms, sampling between 1 and 1.5 oscillation periods of the monopole mode. This experimental procedure is repeated between 2–4 times for each t, and for times up to $t \approx 1.5$ s.

Each phase-contrast image is analyzed using a 2D bimodal fit to the atomic column density. The fitting function is the sum of a Gaussian and integrated TF function [188]:

$$\begin{aligned} n_{\rm col}(x,z) &= A_G \exp\left[-\left(\frac{x-x_c}{\sigma_{G,x}}\right)^2 - \left(\frac{z-z_c}{\sigma_{G,z}}\right)^2\right] \\ &+ A_{TF}\left[1-\left(\frac{x-x_c}{\sigma_{TF,x}}\right)^2 - \left(\frac{z-z_c}{\sigma_{TF,z}}\right)^2\right]^{3/2} \\ &+ C_{\rm col}, \end{aligned} \tag{10.13}$$

where A_G and A_{TF} are the amplitudes of the Gaussian and TF functions, respectively, x_c and z_c are the center points of the cloud, $\sigma_{G,i}$ are the Gaussian widths, $\sigma_{TF,i}$ are the TF widths, and $C_{\rm col}$ is a constant offset. Note that the TF function is defined to be zero if the argument in brackets is negative.

The dynamics of the condensate monopole mode are captured by the spherically symmetric quantity

$$\sigma_M^2 = \left(\sigma_{TF,x}^2 + \sigma_{TF,y}^2 + \sigma_{TF,z}^2\right)/3. \tag{10.14}$$

During the data runs for this experiment, images were consistently taken in the xz plane. In earlier measurements described in Ref. [163], data were also taken along the xy plane, but technical difficulties were encountered with the imaging system along this axis during the course of the experiments discussed here. However, the limited data available from the xy plane suggests that the cloud was highly symmetric [165]. Therefore, we set $\sigma_{TF,y} = \sigma_{TF,z}$ in Eq. (10.14) when calculating the amplitude of the condensate monopole mode. Although we observe excitation of other collective modes (dipole and quadrupole), we find that the key features of the experimental results for the monopole mode are independent of whether this assumption is made or $\sigma_{TF,y}$ is simply excluded

from Eq. (10.14).

We determine the instantaneous amplitude of the condensate monopole mode by fitting a fixed frequency sine wave to each set of six consecutive time points. The fitting function is of the form

$$g_\sigma(t) = A_\sigma \cos(2\pi\nu t) + B_\sigma \sin(2\pi\nu t) + C_\sigma, \tag{10.15}$$

where $\nu = 19$ Hz, and A_σ, B_σ, and C_σ are fit parameters. This functional form is chosen because we are concerned with the amplitude of the mode, not the frequency, which enables a straightforward linear regression analysis for computing A_σ, B_σ, and C_σ. Finally, we present the data in the form of a fractional amplitude given by

$$A_M = \frac{A_\sigma^2 + B_\sigma^2}{C_\sigma^2}, \tag{10.16}$$

where A_σ, B_σ, and C_σ correspond to the fit parameters of Eq. (10.15). The results of this analysis are shown in Fig. 10.3, where time $t = 0$ is defined as the point at which the modulation of the trap frequency ceases.

A central feature of the data is that the amplitude of the condensate monopole mode does not decay exponentially. Across the five data sets, there is a consistent collapse in the amplitude of the monopole mode between $t = 0.3$–0.5 s, and a partial revival around $t = 0.7$–0.9 s. Motivated by the results of the coupled-modes analysis, we fit the data to an envelope function that represents the superposition of two sinusoidal modes, and we include an overall exponential damping factor to represent the loss of amplitude with time:

$$g_{\rm e}(t) = A_{\rm e} \cos\left(\frac{\Delta\omega}{2}t\right)^2 e^{-\Gamma_{\rm e} t}, \tag{10.17}$$

where $A_{\rm e}$ is the initial amplitude, $\Delta\omega$ is the beat frequency, and $\Gamma_{\rm e}$ is the damping rate of the envelope. The results of this fit are overlaid with the data in Fig. 10.3. From the fit, we find $\Delta\omega/\omega_0 \sim 0.13$ on average, and damping rates in the range $\Gamma_{\rm e} \sim 1.5$–3.5 s^{-1}. The observed beat frequency is less than $\Delta\omega/\omega_0 \sim 0.2$ as expected from the coupled-modes analysis. We attribute this disagreement to the naive form of the fitting function, which assumes that the two sinusoidal modes damp at the same rate, respond equally to the trap frequency perturbation, and have no

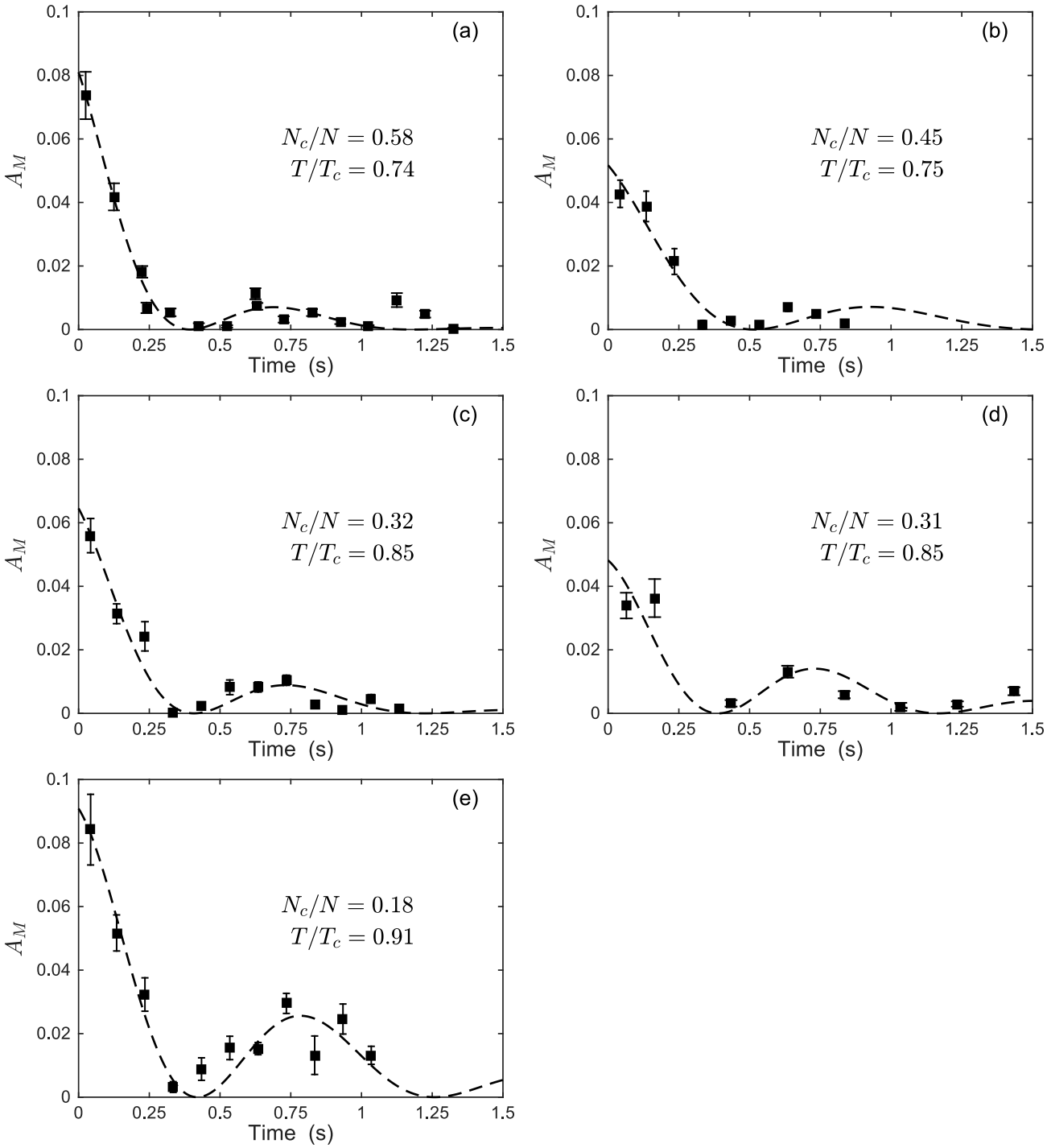

Figure 10.3: Amplitude of the monopole mode oscillation (squares) for atom numbers of (a) $N = 8.9 \times 10^5$, (b) $N = 9.7 \times 10^5$, (c) $N = 6.7 \times 10^5$, (d) $N = 5.4 \times 10^5$, and (e) $N = 7.9 \times 10^5$. Each frame is labeled with the condensate fraction (N_c/N) and temperature (T/T_c). Error bars represent the statistical uncertainty of multiple realizations of the experiment at each time point. The dashed lines are a fit of the data to Eq. (10.17), which represents the envelope function for the superposition of two sinusoids. From the fit it is found that the beat frequency is $\Delta\omega/\omega_0 \sim 0.13$ on average and the damping rate lies in the range $\Gamma_e \sim 1.5$–3.5 s^{-1}. Reproduced from Ref. [139].

phase difference between them. These assumptions are investigated further in the next section where the two sinusoidal modes are identified with the in-phase and out-of-phase modes predicted by the coupled-modes analysis.

Before moving on, it is important to note that in Ref. [164] it was shown that anharmonic corrections to the trap geometry were likely responsible for the anomalous exponential damping of the monopole mode observed above the critical temperature [163]. As shown in Ref. [163], this damping is < 0.2 s^{-1} for clouds with a full width at half maximum (FWHM) of < 125 μm. In this work, the FWHM of the cloud below the critical temperature satisfies this criterion; thus, we neglect anharmonic corrections to the trap geometry as the observed damping rate is approximately an order of magnitude larger.

10.3 Collisional Dynamics

We now investigate the damping observed in the experimental data through numerical simulations within the ZNG formalism. The coupled-modes analysis ignores collisions and exchange of particles between the two components, as well as nonlinear mean-field effects. However, below the critical temperature, these interactions between the condensate and noncondensate can shift the frequencies of collective modes and cause damping. Collisions that exchange energy and particles between the two components of the gas cause collisional damping [171, 173], whereas mean-field effects lead to Landau damping (see Refs. [189–196] for further discussion) and Beliaev damping [197]. Landau damping describes a process where a collective mode decays due to its interaction with a thermal distribution of excitations, and it is expected to dominate at higher temperatures approaching the critical temperature. On the other hand, Beliaev damping is a process where a collective mode decays into two lower energy excitations, which is suppressed for the lowest energy collective modes of a trapped gas due to the discretization of energy levels. Thus, the Beliaev process is absent for the monopole mode, and is therefore excluded from our analysis in this paper.

10.3.1 Simulation of the experiment

To model the experiment, we simulate a gas of $N = 8 \times 10^5$ ^{87}Rb atoms in a spherically symmetric harmonic trap with $\omega_0 = 2\pi \times 9$ Hz. Using the algorithm outlined in Ref. [171], we generate equilibrium initial states of the condensate and noncondensate for temperatures ranging from 0.1–0.9 T_c.[§] We then directly simulate the excitation of the monopole mode as in the experiment by sinusoidally modulating the frequency of the trapping potential at $\omega_D = 2\omega_0$ for four periods. We find that our results are essentially unchanged for drive frequencies of $(1 + \sqrt{5}/2)\omega_0$ or $\sqrt{5}\omega_0$. We use trap frequency modulation amplitudes of $\epsilon = 0.02$, 0.03, or 0.04, and then allow the system to evolve freely for $t = 2$ s. We find that this range of ϵ excites the monopole mode of the condensate with an amplitude comparable to that observed in the experiment (i.e. 10–15% peak increase in the TF radius of the condensate from equilibrium). We note that these values are somewhat less than the quoted experimental value of $\epsilon \approx 0.1$, and speculate that this discrepancy is a result of multiple collective modes being excited in the experiment due to the difficulty of driving the trap perfectly spherically. This is in contrast to the simulations where only the monopole mode is excited, and therefore less energy is required to be added to the system to achieve the same level of excitation of the condensate.

We record the mean-square radius of the condensate as a function of time, along with snapshots of the individual density profiles. Although the experimental data sets have total atom numbers that range between about 6×10^5 and 1×10^6, we find simulations for 8×10^5 atoms represent the features of interest, namely the collapse and revival behavior and damping rate. In order to compare directly with the experimental data, we generate 2D column densities from the simulation results, and determine the TF radii using the same bimodal fitting routine described in Sec. 10.2. Equation (10.14) is used to calculate the amplitude of the condensate monopole mode, and Eq. (10.15) is fit to single periods of the oscillation corresponding to a window of approximately 53 ms. The results of this analysis are overlaid with the experimental data in Fig. 10.4 for the three

[§] As $T \to T_c$ the numerical method for calculating the equilibrium state of the gas becomes unstable, and 0.9 T_c is an empirical upper bound.

different values of ϵ. The timescale of the first collapse and revival observed in the simulation results show good agreement with the experiment.

10.3.2 Extraction of damping rates

The prediction of the coupled-modes analysis and results of the ZNG simulations show good agreement with the collapse and revival behavior observed in the experimental data (see Figs. 10.3 and 10.4). In addition, the damping observed in the results of the ZNG simulations agrees well with experimental observations. Therefore, due to the limited and noisy experimental data available, we use the results of the ZNG simulations instead of experimental data to get an estimate of the damping rates for the in-phase and out-of-phase eigenmodes predicted by the coupled-modes analysis.

We fit the simulated evolution of the condensate mean-square radius, $\langle R_c^2 \rangle = \int d\mathbf{r}\ r^2 n_c(\mathbf{r})$, by the sum of two sine waves with decaying amplitudes

$$\begin{aligned} g_c(t) &= A_1 \sin(2\pi\nu_1 t + \phi_1) e^{-\Gamma_1 t} \\ &\quad + A_2 \sin(2\pi\nu_2 t + \phi_2) e^{-\Gamma_2 t} + C_c, \end{aligned} \tag{10.18}$$

where A_i, ν_i, ϕ_i, and Γ_i are the amplitudes, frequencies, phases, and damping rates, respectively, of the two eigenmodes, and C_c is a constant offset. Figure 10.5 shows typical results of this fitting procedure for simulation results with a trap frequency modulation amplitude of $\epsilon = 0.03$. Time $t = 0$ is defined as the point at which the modulation of the trap frequency ceases. We choose to fit to the mean-square radius of the condensate as its time evolution is most sensitive to the presence of both eigenmodes across the temperature range investigated. The mean-square radius of the total density becomes dominated by the noncondensate at higher temperatures, and any signature of a second eigenmode is lost. Similar behavior is observed in the evolution of the noncondensate mean-square radius.

The mode frequencies extracted from this fitting procedure show excellent agreement with the results of the coupled-modes analysis across the temperature range simulated. Simulation results

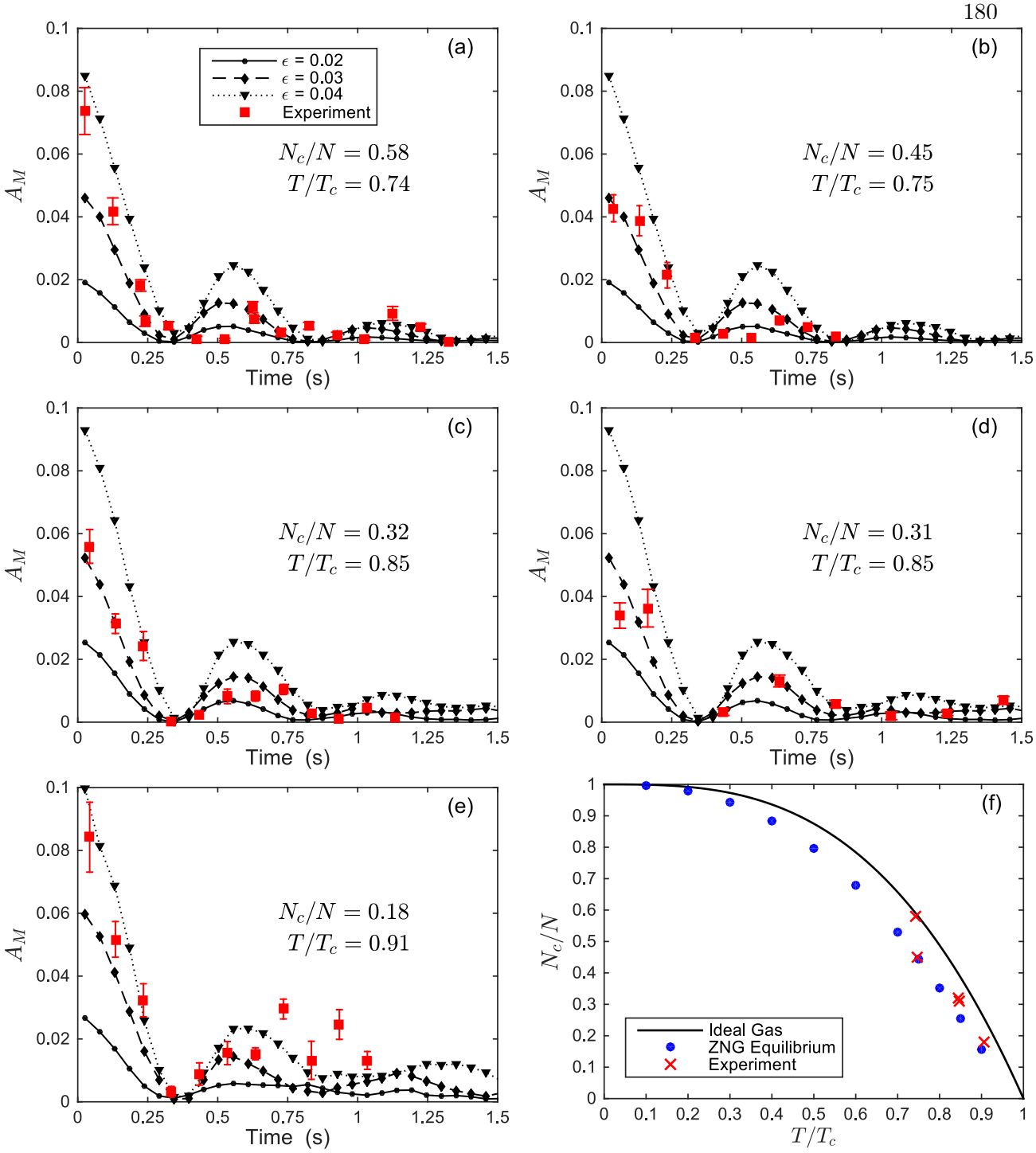

Figure 10.4: (Color online) Amplitude of the monopole mode oscillation for experimental atom numbers of (a) $N = 8.9 \times 10^5$, (b) $N = 9.7 \times 10^5$, (c) $N = 6.7 \times 10^5$, (d) $N = 5.4 \times 10^5$, and (e) $N = 7.9 \times 10^5$. Each frame is labeled with the condensate fraction (N_c/N) and temperature (T/T_c), and the legend denotes the different modulation amplitudes used in the ZNG simulations. Error bars on the experimental data represent the statistical uncertainty of multiple realizations of the experiment at each time point. (f) Condensed fraction vs temperature for the ideal Bose gas, $N_c/N = 1 - (T/T_c)^3$ (solid line), the equilibrium state of the ZNG simulations (blue points), and the experimental data (red crosses). All simulations are performed with $N = 8 \times 10^5$ atoms. Reproduced from Ref. [139].

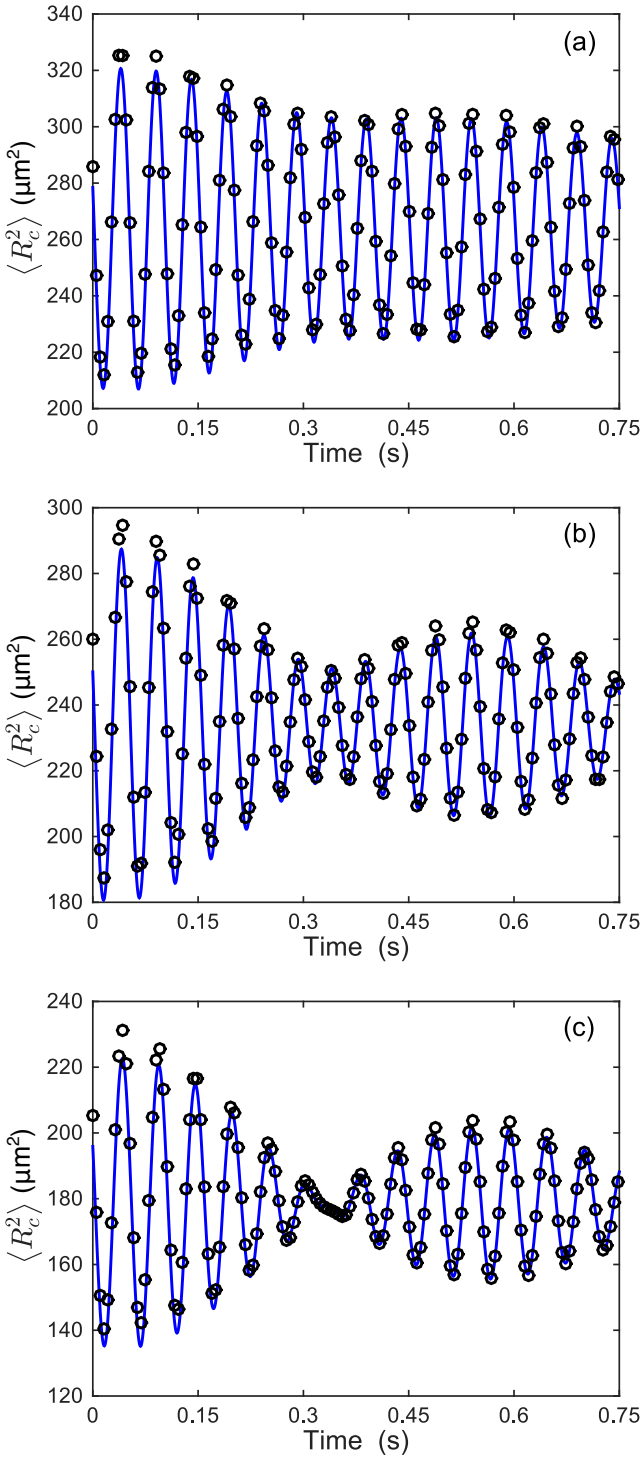

Figure 10.5: (Color online) Simulated mean-square radius of the condensate density for a trap frequency modulation amplitude of $\epsilon = 0.03$ at (a) $T = 0.4\ T_c$, (b) $0.6\ T_c$, and (c) $0.8\ T_c$ (black circles) and resulting fit of Eq. (10.18) (blue line). The density of simulated points has been reduced for clarity. Reproduced from Ref. [139].

at temperatures of $T = 0.1\ T_c$ and $0.2\ T_c$ are fit with a single decaying sinusoid due to the absence of a second mode. This also agrees with the prediction of the coupled-modes analysis, where only a single mode responds to a trap frequency perturbation for $T \leq 0.2\ T_c$ (see Fig. 10.2). A notable feature in Fig. 10.5 is a downward shift of the fast oscillations of $\langle R_c^2 \rangle$ (i.e., carrier frequency) with increasing temperature, an effect also observed in Ref. [173] for the monopole mode. As the temperature of the system increases the out-of-phase mode begins to get excited in conjunction with the in-phase mode, and the fast oscillations shift to a lower frequency because they represent a weighted average of the two independent mode frequencies.

The damping rate of each mode determined from the fitting procedure is shown in Fig. 10.6 as a function of temperature. In the temperature range of the experiment, there is a mismatch of the damping rates between the two eigenmodes. This mismatch, along with the beating between the two modes, captures the behavior seen experimentally of strong collapse and subsequent revival of the condensate oscillation. At lower temperatures, the in-phase mode dominates and the out-of-phase mode is strongly damped, and the inverse is true at higher temperatures. Thus, the in-phase mode appears to be dominated by the condensate while the out-of-phase mode consists primarily of the noncondensate.

Based on the results of the coupled-modes analysis, one may suspect that the particular drive frequency used to excite the system has a large effect on the nature of the response due to the presence of two resonant excitation frequencies. However, results from ZNG simulations showed little dependence on the drive frequency, which can be attributed to the presence of damping. Damping in the system effectively broadens the resonances such that both modes are appreciably excited when the system is driven in the range $2\omega_0$ to $\sqrt{5}\omega_0$. Thus, the main characteristics of the condensate collapse-revival behavior are relatively insensitive to the particular drive frequency.

10.4 Summary

In conclusion, we have experimentally observed non-exponential collapse and subsequent revival of the monopole mode of a finite temperature BEC in an isotropic magnetic trap. A coupled-

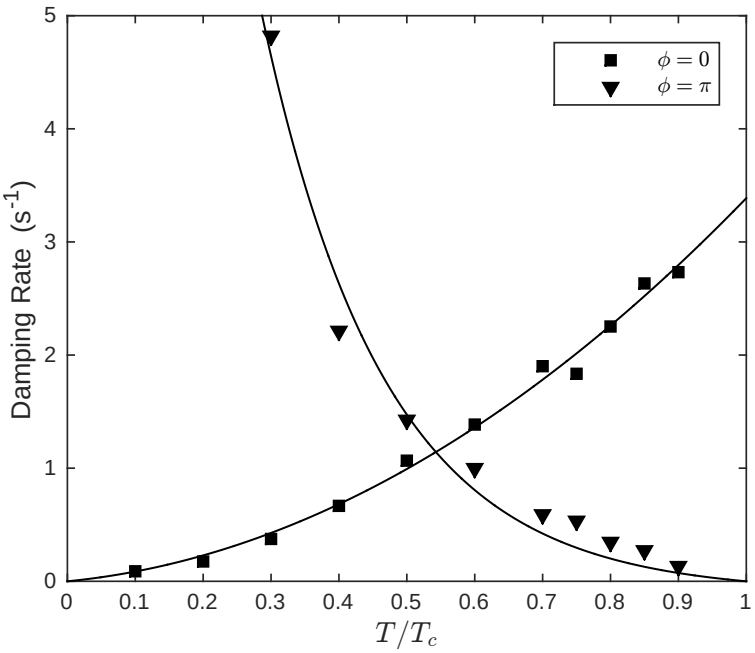

Figure 10.6: Damping rate of the in-phase (squares) and out-of-phase (triangles) mode as a result of fitting Eq. (10.18) to the simulated evolution of $\langle R_c^2 \rangle$ at each temperature for a trap frequency modulation amplitude of $\epsilon = 0.03$. The solid lines are guides to the eye. Representative fits are shown in Fig. 10.5. Reproduced from Ref. [139].

modes analysis was used to study the linear response of the system to external perturbation, the results of which are the identification of two eigenmodes of the system corresponding to in-phase and out-of-phase oscillations of the condensate and non-condensate. These modes appear to be collisionless analogues to the first and second sound modes as previously discussed in Ref. [150]. Simultaneous excitation of these two modes results in the observed collapse and partial revival of the condensate monopole mode, which has a timescale compatible with the mismatch in the eigenfrequencies. Damping of the oscillations was also observed experimentally, and simulations within the ZNG formalism resulted in good agreement with the data.

Chapter 11

Conclusion to Part 2

11.1 Summary

The second part of this dissertation has investigated the dynamics of the monopole mode of a degenerate Bose gas confined in an isotropic harmonic trap. Previous to the work described here, experiments investigating the collective mode spectrum of degenerate Bose gases were confined to anisotropic trapping geometries, and predictions about the dynamics of collective modes in spherical symmetry could not be proven. Thus, fundamental comparisons between different theoretical predictions for mode frequencies and damping rates as a function of temperature had not been made.

In Chapter 8, the theoretical background for the ZNG method was outlined. It was emphasized that the ZNG method treats excitations about the condensed state semiclassically in the Hartree-Fock limit, and completely neglects quantum fluctuations like Bogoliubov quasi-particle excitations. Therefore, the ZNG method is not applicable to the study of many physical phenomena; however, it is expected to be a valid approach to the problem investigated in this dissertation. As shown in Chapter 10, the ZNG method was able to accurately reproduce experimental observations in a regime close to the BEC transition temperature.

In Chapter 9, a detailed discussion of a numerical solution to the ZNG equations in spherical symmetry was given. We outlined the solution of the GGPE using the Crank-Nicolson method, as well as the solution of the QBE using a modified DSMC method that included both mean-field interactions and collisional interactions between the condensate and non-condensate. In addition,

explicit details were given on the Monte Carlo sampling method used to incorporate the effects of collisions, as well as on how to generate equilibrium states and perform a full dynamical simulation of the ZNG equations. Finally, the developed spherically symmetric ZNG code was compared directly to previously codes in the literature, and excellent agreement was found.

In Chapter 10, we demonstrated the experimental observation of non-exponential collapse and subsequent revival of the monopole mode of a finite temperature BEC in an isotropic harmonic trap. A coupled-modes analysis was used to study the linear response of the system to external perturbation, the results of which were the identification of two eigenmodes of the system corresponding to in-phase and out-of-phase oscillations of the condensate and non-condensate. These modes appear to be collisionless analogues of the first and second sound modes as previously discussed in Ref. [150]. Simultaneous excitation of these two modes resulted in the observed collapse and partial revival of the condensate monopole mode, which has a timescale compatible with the mismatch in the eigenfrequencies. Damping of the oscillations was also observed experimentally, and simulations within the ZNG formalism resulted in good agreement with the data.

11.2 Future Outlook

In moving forward from the work described in Part 2 of this dissertation, it would be interesting to obtain more detailed experimental results that cover a larger range of temperatures below the BEC transition temperature. This would allow direct analysis of the damping rates and mode frequencies as a function of temperature, which could then be directly compared to existing theories such as the ZNG method or the classical field method. Besides additional experimental results, it would be interesting to investigate modification of the ZNG or classical field methods to include some of the missing physics. In regards to the ZNG method, this would involve going beyond the Hartree-Fock and local density approximations for the treatment of the excitations about the condensed state and their interactions. In regards to the classical field method, modifications would include a way of describing excitations beyond the Bogoliubov quasi-particle limit; therefore, it would be necessary to couple this method with a QBE in a similar fashion to the ZNG method.

Bibliography

[1] J. C. Védrine, Catalysts **7**, 341 (2017).

[2] W. H. Wollaston, Philosophical Transactions of the Royal Society of London **92**, 365 (1802).

[3] J. Fraunhofer, Annalen der Physik **56**, 264 (1817).

[4] K. G., Annalen der Physik **185**, 148 (1860).

[5] K. G. and B. R., Annalen der Physik **186**, 161 (1860).

[6] K. G. and B. R., Annalen der Physik **189**, 337 (1861).

[7] C. Abney and L.-C. Festing, Philosophical Transactions of the Royal Society of London **172**, 887 (1881).

[8] B. M. and O. R., Annalen der Physik **389**, 457 (1927).

[9] M. D. Harmony, Accounts of Chemical Research **25**, 321 (1992).

[10] D. W. Pratt, Annual Review of Physical Chemistry **49**, 481 (1998).

[11] K. C. Cossel, E. M. Waxman, I. A. Finneran, G. A. Blake, J. Ye, and N. R. Newbury, Journal of the Optical Society of America B **34**, 104 (2017).

[12] S. T. Cundiff and J. Ye, Reviews of Modern Physics **75**, 325 (2003).

[13] M. Thorpe and J. Ye, Applied Physics B **91**, 397 (2008).

[14] C. R. Petersen, U. Møller, I. Kubat, B. Zhou, S. Dupont, J. Ramsay, T. Benson, S. Sujecki, N. Abdel-Moneim, Z. Tang, D. Furniss, A. Seddon, and O. Bang, Nature Photonics **8**, 830 (2014).

[15] I. Pupeza, D. Sánchez, J. Zhang, N. Lilienfein, M. Seidel, N. Karpowicz, T. Paasch-Colberg, I. Znakovskaya, M. Pescher, W. Schweinberger, V. Pervak, E. Fill, O. Pronin, Z. Wei, F. Krausz, A. Apolonski, and J. Biegert, Nature Photonics **9**, 721 (2015).

[16] J. Faist, G. Villares, G. Scalari, M. Rösch, C. Bonzon, A. Hugi, and M. Beck, Nanophotonics **5**, 272 (2016).

[17] J. Ye, L.-S. Ma, and J. L. Hall, Journal of the Optical Society of America B **15**, 6 (1998).

[18] L.-S. Ma, J. Ye, P. Dubé, and J. L. Hall, Journal of the Optical Society of America B **16**, 2255 (1999).

[19] J. M. Hollas, *High Resolution Spectroscopy*, 2nd ed. (John Wiley and Sons, New York, 1998).

[20] J. Brown and A. Carrington, *Rotational Spectroscopy of Diatomic Molecules* (Cambridge University Press, Cambridge, 2003).

[21] J. R. Heath, A. L. Cooksy, M. H. Gruebele, C. A. Schmuttenmaer, and R. J. Saykally, Science **244**, 564 LP (1989).

[22] H. Piest, G. von Helden, and G. Meijer, The Journal of Chemical Physics **110**, 2010 (1999).

[23] F. Dong, S. Davis, and D. J. Nesbitt, The Journal of Physical Chemistry A **110**, 3059 (2006).

[24] B. E. Brumfield, J. T. Stewart, and B. J. McCall, The Journal of Physical Chemistry Letters **3**, 1985 (2012).

[25] G. Scoles, *Atomic and Molecular Beam Methods I* (Oxford University Press, New York, 1988).

[26] J. T. Brice, T. Liang, P. L. Raston, A. B. McCoy, and G. E. Douberly, The Journal of Chemical Physics **145**, 124310 (2016).

[27] H. Pauly, *Atom, Molecule, and Cluster Beams I* (Springer-Verlag, New York, 2000).

[28] M. A. Duncan, Review of Scientific Instruments **83**, 041101 (2012).

[29] N. R. Hutzler, H.-I. Lu, and J. M. Doyle, Chemical Reviews **112**, 4803 (2012).

[30] S. E. Maxwell, N. Brahms, R. DeCarvalho, D. R. Glenn, J. S. Helton, S. V. Nguyen, D. Patterson, J. Petricka, D. DeMille, and J. M. Doyle, Physical Review Letters **95**, 173201 (2005).

[31] N. R. Hutzler, M. F. Parsons, Y. V. Gurevich, P. W. Hess, E. Petrik, B. Spaun, A. C. Vutha, D. DeMille, G. Gabrielse, J. M. Doyle, and D. DeMille, Physical Chemistry Chemical Physics **13**, 18976 (2011).

[32] J. F. Barry, E. S. Shuman, D. DeMille, P. W. Hess, E. Petrik, B. Spaun, A. C. Vutha, D. DeMille, G. Gabrielse, J. M. Doyle, and D. DeMille, Physical Chemistry Chemical Physics **13**, 18936 (2011).

[33] S. M. Skoff, R. J. Hendricks, C. D. J. Sinclair, J. J. Hudson, D. M. Segal, B. E. Sauer, E. A. Hinds, and M. R. Tarbutt, Physical Review A **83**, 023418 (2011).

[34] W. Bu, T. Chen, G. Lv, and B. Yan, Physical Review A **95**, 032701 (2017).

[35] G. Z. Iwata, R. L. McNally, and T. Zelevinsky, Physical Review A **96**, 022509 (2017).

[36] L. D. van Buuren, C. Sommer, M. Motsch, S. Pohle, M. Schenk, J. Bayerl, P. W. H. Pinkse, and G. Rempe, Physical Review Letters **102**, 033001 (2009).

[37] C. Sommer, L. D. van Buuren, M. Motsch, S. Pohle, J. Bayerl, P. W. H. Pinkse, G. Rempe, J. Petricka, D. DeMille, and J. M. Doyle, Faraday Discussions **142**, 203 (2009).

[38] L. Santamaria, V. Di Sarno, I. Ricciardi, M. De Rosa, S. Mosca, G. Santambrogio, P. Maddaloni, and P. De Natale, The Astrophysical Journal **801**, 50 (2015).

[39] X. Li, L. Xu, Y. Yin, S. Xu, Y. Xia, and J. Yin, Physical Review A **93**, 063407 (2016).

[40] B. Spaun, P. B. Changala, D. Patterson, B. J. Bjork, O. H. Heckl, J. M. Doyle, and J. Ye, Nature **533**, 517 (2016).

[41] S. K. Tokunaga, R. J. Hendricks, M. R. Tarbutt, and B. Darquié, New Journal of Physics **19**, 053006 (2017).

[42] P. Asselin, Y. Berger, T. R. Huet, L. Margulès, R. Motiyenko, R. J. Hendricks, M. R. Tarbutt, S. K. Tokunaga, and B. Darquié, Physical Chemistry Chemical Physics **19**, 4576 (2017).

[43] C. J. E. Straatsma, M. I. Fabrikant, G. E. Douberly, and H. J. Lewandowski, The Journal of Chemical Physics **147**, 124201 (2017).

[44] N. E. Bulleid, S. M. Skoff, R. J. Hendricks, B. E. Sauer, E. A. Hinds, M. R. Tarbutt, J. E. Stalnaker, M. Zolotorev, G. Gabrielse, J. M. Doyle, and D. DeMille, Physical Chemistry Chemical Physics **15**, 12299 (2013).

[45] P. J. Pritchard, *Fox and McDonald's Introduction to Fluid Mechanics*, 8th ed. (John Wiley and Sons, Hoboken, 2011).

[46] Y. Sone, *Molecular Gas Dynamics - Theory, Techniques, and Applications* (Birkhäuser, Boston, 2007).

[47] J. F. O'Hanlon, *A User's Guide to Vacuum Technology*, 3rd ed. (John Wiley and Sons, Hoboken, 2003) pp. 25–33.

[48] J. Farrar, Y. Lee, V. Goldman, and M. Klein, Chemical Physics Letters **19**, 359 (1973).

[49] V. Singh, A. K. Samanta, N. Roth, D. Gusa, T. Ossenbrüggen, I. Rubinsky, D. A. Horke, and J. Küpper, Physical Review A **97**, 032704 (2018).

[50] R. DeCarvalho, J. Doyle, B. Friedrich, T. Guillet, J. Kim, D. Patterson, and J. Weinstein, The European Physical Journal D **7**, 289 (1999).

[51] L. Landau and E. Teller, Phys. Z. Sow. **10**, 34 (1936).

[52] G. Sanna and G. Tomassetti, *Introduction to Molecular Beams Gas Dynamics* (Imperial College Press, London, 2005).

[53] E. E. Nikitin and J. Troe, Phys. Chem. Chem. Phys. **10**, 1483 (2008).

[54] P. Colarusso, B. Guo, K.-Q. Zhang, and P. Bernath, Journal of Molecular Spectroscopy **175**, 158 (1996).

[55] B. Guo, K. Zhang, and P. Bernath, Journal of Molecular Spectroscopy **170**, 59 (1995).

[56] J. B. Hasted, *Physics of Atomic Collisions*, 2nd ed. (Elsevier, New York, 1972).

[57] A. O. Sushkov and D. Budker, Physical Review A **77**, 042707 (2008).

[58] M.-J. Lu, K. S. Hardman, J. D. Weinstein, and B. Zygelman, Physical Review A **77**, 060701 (2008).

[59] M.-J. Lu and J. D. Weinstein, New Journal of Physics **11**, 055015 (2009).

[60] S. S. Harilal, C. V. Bindhu, M. S. Tillack, F. Najmabadi, and A. C. Gaeris, Journal of Applied Physics **93**, 2380 (2003).

[61] N. Farid, S. S. Harilal, H. Ding, and A. Hassanein, Journal of Applied Physics **115**, 033107 (2014).

[62] D. M. Lubman, C. T. Rettner, and R. N. Zare, The Journal of Physical Chemistry **86**, 1129 (1982).

[63] H. Murphy, *The Effects of Source Geometry on Free Jet Expansions*, Ph.D. thesis, University of California, San Diego (1984).

[64] H. C. W. Beijerinck and N. F. Verster, Physica B+C **111**, 327 (1981).

[65] T. G. Dietz, M. A. Duncan, D. E. Powers, and R. E. Smalley, The Journal of Chemical Physics **74**, 6511 (1981).

[66] V. E. Bondybey and J. H. English, The Journal of Chemical Physics **74**, 6978 (1981).

[67] P. F. Bernath, *Spectra of Atoms and Molecules*, 2nd ed. (Oxford University Press, New York, 2005).

[68] D. A. Steck, "Rubidium 87 D Line Data," (2003).

[69] K. Huang, *Statistical Mechanics*, 2nd ed. (John Wiley & Sons, New York, 1987).

[70] P. R. Griffiths and J. A. de Haseth, *Fourier Transform Infrared Spectrometry* (John Wiley and Sons, New York, 1986).

[71] L. Mertz, Infrared Physics **7**, 17 (1967).

[72] A. S. Filler, Journal of the Optical Society of America **54**, 762 (1964).

[73] R. H. Norton and R. Beer, Journal of the Optical Society of America **66**, 259 (1976).

[74] J. K. Kauppinen, D. J. Moffatt, D. G. Cameron, and H. H. Mantsch, Applied Optics **20**, 1866 (1981).

[75] R. J. Anderson and P. R. Griffiths, Analytical Chemistry **47**, 2339 (1975).

[76] R. J. Anderson and P. R. Griffiths, Analytical Chemistry **50**, 1804 (1978).

[77] S. F. Parker and P. B. Tooke, Spectrochimica Acta Part A: Molecular and Biomolecular Spectroscopy **53**, 2245 (1997).

[78] G. Jalsovszky, Journal of Molecular Structure **114**, 127 (1984).

[79] E. V. Loewenstein, in *Aspen International Conference on Fourier Spectroscopy*, edited by G. A. Vanasse, A. T. Stair, and D. J. Baker (1970) pp. 3–18.

[80] R. J. Nordstrom, in *Fourier, Hadamard, and Hilbert Transforms in Chemistry* (Plenum Publishing, New York, 1982) pp. 421–451.

[81] H. E. Hallam and G. F. Scrimshaw, in *Vibrational Spectroscopy of Trapped Species* (John Wiley and Sons, New York, 1973) pp. 11–66.

[82] I. R. Dunkin, *Matrix-isolation techniques: a practical approach* (Oxford University Press, Oxford, 1998).

[83] L. J. Schoen, D. E. Man, C. M. Knobler, and D. White, The Journal of Chemical Physics **37**, 1146 (1962).

[84] R. F. Curl, F. Capasso, C. Gmachl, A. A. Kosterev, B. McManus, R. Lewicki, M. Pusharsky, G. Wysocki, and F. K. Tittel, Chemical Physics Letters **487**, 1 (2010).

[85] J. Faist, F. Capasso, D. L. Sivco, C. Sirtori, A. L. Hutchinson, and A. Y. Cho, Science **264**, 553 LP (1994).

[86] F. Capasso, C. Gmachl, R. Paiella, A. Tredicucci, A. Hutchinson, D. Sivco, J. Baillargeon, A. Cho, and H. Liu, IEEE Journal of Selected Topics in Quantum Electronics **6**, 931 (2000).

[87] C. Gmachl, F. Capasso, D. L. Sivco, and A. Y. Cho, Reports on Progress in Physics **64**, 1533 (2001).

[88] G. C. Bjorklund, Optics Letters **5**, 15 (1980).

[89] L. Tombez, F. Cappelli, S. Schilt, G. Di Domenico, S. Bartalini, and D. Hofstetter, Applied Physics Letters **103**, 031111 (2013).

[90] X. Chao, J. B. Jeffries, and R. K. Hanson, Applied Physics B **106**, 987 (2012).

[91] H. Li, G. B. Rieker, X. Liu, J. B. Jeffries, and R. K. Hanson, Applied Optics **45**, 1052 (2006).

[92] P. Kluczynski and O. Axner, Applied Optics **38**, 5803 (1999).

[93] S. Schilt, L. Thévenaz, and P. Robert, Applied Optics **42**, 6728 (2003).

[94] R. Arndt, Journal of Applied Physics **36**, 2522 (1965).

[95] P. Kluczynski, J. Gustafsson, Å. M. Lindberg, and O. Axner, Spectrochimica Acta Part B: Atomic Spectroscopy **56**, 1277 (2001).

[96] P. C. D. Hobbs, Proc. SPIE 1376 , 216 (1991).

[97] K. L. Haller and P. C. D. Hobbs, Proc. SPIE 1435 , 298 (1991).

[98] P. C. D. Hobbs, Applied Optics **36**, 903 (1997).

[99] A. Van Orden and R. J. Saykally, Chemical Reviews **98**, 2313 (1998).

[100] J. R. Heath and R. J. Saykally, The Journal of Chemical Physics **94**, 1724 (1991).

[101] P. Neubauer-Guenther, T. Giesen, U. Berndt, G. Fuchs, and G. Winnewisser, Spectrochimica Acta Part A: Molecular and Biomolecular Spectroscopy **59**, 431 (2003).

[102] L. Belau, S. E. Wheeler, B. W. Ticknor, M. Ahmed, S. R. Leone, W. D. Allen, H. F. Schaefer III, and M. A. Duncan, Journal of the American Chemical Society **129**, 10229 (2007).

[103] W. Weltner, P. N. Walsh, and C. L. Angell, The Journal of Chemical Physics **40**, 1299 (1964).

[104] W. Weltner and D. McLeod, The Journal of Chemical Physics **40**, 1305 (1964).

[105] K. R. Thompson, R. L. DeKock, and W. J. Weltner, Journal of the American Chemical Society **93**, 4688 (1971).

[106] L. N. Shen and W. R. M. Graham, The Journal of Chemical Physics **91**, 5115 (1989).

[107] J. Szczepanski and M. Vala, The Journal of Physical Chemistry **95**, 2792 (1991).

[108] A. M. Smith, J. Agreiter, M. Härtle, C. Engel, and V. E. Bondybey, Chemical Physics **189**, 315 (1994).

[109] R. H. Kranze, P. A. Withey, C. M. L. Rittby, and W. R. M. Graham, The Journal of Chemical Physics **103**, 6841 (1995).

[110] J. Szczepanski, S. Ekern, C. Chapo, and M. Vala, Chemical Physics **211**, 359 (1996).

[111] R. H. Kranze, C. M. L. Rittby, and W. R. M. Graham, The Journal of Chemical Physics **105**, 5313 (1996).

[112] P. Freivogel, M. Grutter, D. Forney, and J. P. Maier, Chemical Physics **216**, 401 (1997).

[113] L. Lapinski and M. Vala, Chemical Physics Letters **300**, 195 (1999).

[114] X. D. Ding, S. L. Wang, C. M. L. Rittby, and W. R. M. Graham, The Journal of Physical Chemistry **112**, 5113 (2000).

[115] B. Kern, D. Strelnikov, P. Weis, A. Böttcher, and M. M. Kappes, The Journal of Physical Chemistry A **117**, 8251 (2013).

[116] J. Szczepanski, S. Ekern, and M. Vala, The Journal of Physical Chemistry A **101**, 1841 (1997).

[117] J. Hutter, H. P. Luethi, and F. Diederich, Journal of the American Chemical Society **116**, 750 (1994).

[118] J. Szczepanski, R. Pellow, and M. Vala, Z. Naturforsch. **47a**, 595 (1992).

[119] M. Grutter, P. Freivogel, D. Forney, and J. P. Maier, The Journal of Chemical Physics **107**, 5356 (1997).

[120] M. E. Jacox, Chemical Society Reviews **31**, 108 (2002).

[121] C. L. Kingsbury, S. J. Mehrman, and J. M. Takacs, Current Organic Chemistry **3**, 497 (1999).

[122] C. N. R. Rao, Annual Review of Physical Chemistry **40**, 291 (1989).

[123] W. Weltner, Science **155**, 155 (1967).

[124] A. J. Merer, Annual Review of Physical Chemistry **40**, 407 (1989).

[125] R. S. Ram, J. Liévin, G. Li, T. Hirao, and P. F. Bernath, Chemical Physics Letters **343**, 437 (2001).

[126] A. Gatterer and S. G. Krishnamurty, Nature **169**, 543 (1952).

[127] W. Weltner and D. McLeod, Journal of Molecular Spectroscopy **17**, 276 (1965).

[128] D. W. Green and K. M. Ervin, Journal of Molecular Spectroscopy **89**, 145 (1981).

[129] A. Samoilova, Y. Efremov, and L. Gurvich, Journal of Molecular Spectroscopy **86**, 1 (1981).

[130] M. Lorenz and V. E. Bondybey, Chemical Physics **241**, 127 (1999).

[131] C. J. Nelin and C. W. Bauschlicher, Chemical Physics Letters **118**, 221 (1985).

[132] R. S. Ram, J. Liévin, and P. F. Bernath, Journal of Molecular Spectroscopy **256**, 216 (2009).

[133] G. Herzberg, *Molecular Spectra and Molecular Structure - I. Spectra of Diatomic Molecules*, 2nd ed. (D. Van Nostrand Company, Inc., Princeton, 1950).

[134] W. D. Bare, P. F. Souter, and L. Andrews, The Journal of Physical Chemistry A **102**, 8279 (1998).

[135] M. Zhou and L. Andrews, The Journal of Chemical Physics **111**, 4230 (1999).

[136] P. Brosset, R. Dahoo, B. Gauthier-Roy, L. Abouaf-Marguin, and A. Lakhlifi, Chemical Physics **172**, 315 (1993).

[137] K. R. Asmis, Physical Chemistry Chemical Physics **14**, 9270 (2012).

[138] P. Bocherel, L. B. Herbert, B. R. Rowe, I. R. Sims, I. W. M. Smith, and D. Travers, The Journal of Physical Chemistry **100**, 3063 (1996).

[139] C. J. E. Straatsma, V. E. Colussi, M. J. Davis, D. S. Lobser, M. J. Holland, D. Z. Anderson, H. J. Lewandowski, and E. A. Cornell, Physical Review A **94**, 043640 (2016).

[140] M. H. Anderson, J. Ensher, M. R. Matthews, C. E. Wieman, and E. A. Cornell, Science **269**, 198 (1995).

[141] K. B. Davis, M. O. Mewes, M. R. Andrews, N. J. van Druten, D. S. Durfee, D. M. Stamper-Kurn, and W. Ketterle, Phys. Rev. Lett. **75**, 3969 (1995).

[142] D. S. Jin, J. Ensher, M. R. Matthews, C. E. Wieman, and E. A. Cornell, Phys. Rev. Lett. **77**, 420 (1996).

[143] M. O. Mewes, M. R. Andrews, N. J. van Druten, D. M. Stamper-Kurn, D. S. Durfee, C. G. Townsend, and W. Ketterle, Phys. Rev. Lett. **77** (1996).

[144] M. Edwards, P. A. Ruprecht, K. Burnett, R. J. Dodd, and C. W. Clark, Phys. Rev. Lett. **77**, 1671 (1996).

[145] S. Stringari, Phys. Rev. Lett. **77**, 2360 (1996).

[146] D. S. Jin, M. R. Matthews, J. Ensher, C. E. Wieman, and E. A. Cornell, Phys. Rev. Lett. **78**, 764 (1997).

[147] D. M. Stamper-Kurn, H.-J. Miesner, S. Inouye, M. R. Andrews, and W. Ketterle, Phys. Rev. Lett. **81**, 500 (1998).

[148] O. Maragò, G. Hechenblaikner, E. Hodby, and C. Foot, Phys. Rev. Lett. **86**, 3938 (2001).

[149] F. Chevy, V. Bretin, P. Rosenbusch, K. W. Madison, and J. Dalibard, Phys. Rev. Lett. **88**, 250402 (2002).

[150] M. J. Bijlsma and H. T. C. Stoof, Phys. Rev. A **60**, 3973 (1999).

[151] U. Al Khawaja and H. T. C. Stoof, Phys. Rev. A **62**, 053602 (2000).

[152] E. Zaremba, A. Griffin, and T. Nikuni, Phys. Rev. A **57**, 4695 (1998).

[153] V. Shenoy and T.-L. Ho, Phys. Rev. Lett. **80**, 3895 (1998).

[154] G. M. Kavoulakis, C. J. Pethick, and H. Smith, Phys. Rev. A **57**, 2938 (1998).

[155] B. Jackson and E. Zaremba, Phys. Rev. Lett. **88**, 180402 (2002).

[156] B. Jackson and E. Zaremba, Laser Phys. **12**, 93 (2002).

[157] B. Jackson and E. Zaremba, Laser Phys. **13**, 1004 (2003).

[158] S. A. Morgan, J. Phys. B.: At. Mol. Opt. Phys. **33**, 3847 (2000).

[159] M. Rusch, S. A. Morgan, D. A. W. Hutchinson, and K. Burnett, Phys. Rev. Lett. **85**, 4844 (2000).

[160] S. A. Morgan, M. Rusch, D. A. W. Hutchinson, and K. Burnett, Phys. Rev. Lett. **91**, 250403 (2003).

[161] S. A. Morgan, Phys. Rev. A **69**, 023609 (2004).

[162] S. A. Morgan, Phys. Rev. A **72**, 043609 (2005).

[163] D. S. Lobser, A. E. S. Barentine, E. A. Cornell, and H. J. Lewandowski, Nat. Phys. **11**, 1009 (2015).

[164] V. E. Colussi, C. J. E. Straatsma, D. Z. Anderson, and M. J. Holland, New Journal of Physics **17**, 103029 (2015).

[165] D. S. Lobser, *Observation of a Persistent Non-Equilibrium State in an Extremely Isotropic Harmonic Potential*, Ph.D. thesis, University of Colorado (2015).

[166] C. J. Pethick and H. Smith, *Bose-Einstein Condensation in Dilute Gases*, 2nd ed. (Cambridge University Press, Cambridge, 2008).

[167] A. L. Fetter and J. D. Walecka, *Quantum Theory of Many-Particle Systems* (Dover Publications, Mineola, 1971).

[168] N. P. Proukakis and B. Jackson, J. Phys. B.: At. Mol. Opt. Phys. **41**, 203002 (2008).

[169] T. R. Kirkpatrick and J. R. Dorfmann, J. Low Temp. Phys. **58**, 301 (1985).

[170] E. Zaremba, T. Nikuni, and A. Griffin, J. Low Temp. Phys. **116**, 227 (1999).

[171] A. Griffin, T. Nikuni, and E. Zaremba, *Bose-Condensed Gases at Finite Temperature* (Cambridge University Press, New York, 2009).

[172] S. Giorgini, L. P. Pitaevskii, and S. Stringari, J. Low Temp. Phys. **109**, 309 (1997).

[173] B. Jackson and E. Zaremba, Phys. Rev. A **66**, 033606 (2002).

[174] M. D. Feit, J. J. A. Fleck, and A. Steiger, J. Comput. Phys. **47**, 412 (1982).

[175] W. H. Press, S. A. Teukolsky, W. T. Vetterling, and B. P. Flannery, *Numerical Recipes in Fortran 77 – The Art of Scientific Computing*, 2nd ed. (Cambridge University Press, New York, 1992).

[176] G. A. Bird, *Molecular Gas Dynamics and the Direct Simulation of Gas Flows*, 2nd ed. (Clarendon, Oxford, 1994).

[177] J. J. Sakurai and J. Napolitano, *Modern Quantum Mechanics*, 2nd ed. (Addison-Wesley, Redwood City, 2011).

[178] G. Strang, SIAM J. Numer. Anal. **5**, 506 (1968).

[179] H. Goldstein, C. Poole, and J. Safko, *Classical Mechanics*, 3rd ed. (Addison-Wesley, Redwood City, 2000).

[180] C. K. Birdsall and A. B. Langdon, *Plasma Physics via Computer Simulation* (Taylor and Francis, Boca Raton, 2004).

[181] D. J. Larson, D. W. Hewett, and A. B. Langdon, Comput. Phys. Commun. **90**, 260 (1995).

[182] J. P. Verboncoeur, J. Comput. Phys. **174**, 421 (2001).

[183] C. Cornet and D. T. K. Kwok, J. Comput. Phys. **225**, 808 (2007).

[184] A. J. MacLeod, Computers in Physics **11**, 385 (1997).

[185] J. Märkle, *Hybrid systems at finite temperatures*, Ph.D. thesis, Universität Tübingen (2014).

[186] D. Guéry-Odelin, F. Zambelli, J. Dalibard, and S. Stringari, Phys. Rev. A **60**, 4851 (1999).

[187] W. Petrich, M. H. Anderson, J. R. Ensher, and E. A. Cornell, Phys. Rev. Lett. **74**, 3352 (1995).

[188] W. Ketterle, D. S. Durfee, and D. M. Stamper-Kurn, in *Bose-Einstein Condensation in Atomic Gases*, Proceedings of the International School of Physics "Enrico Fermi", edited by M. Inguscio, S. Stringari, and C. E. Wieman (1999) pp. 67–176.

[189] P. C. Hohenberg and P. C. Martin, Ann. Phys. **34**, 291 (1965).

[190] P. Szépfalusy and I. Kondor, Ann. Phys. **82**, 1 (1974).

[191] W. V. Liu, Phys. Rev. Lett. **79**, 4056 (1997).

[192] L. P. Pitaevskii and S. Stringari, Phys. Lett. **235**, 398 (1997).

[193] P. O. Fedichev, G. V. Shlyapnikov, and J. T. M. Walraven, Phys. Rev. Lett. **80**, 2269 (1998).

[194] M. Guilleumas and L. P. Pitaevskii, Phys. Rev. A **61**, 013602 (1999).

[195] K. Das and T. Bergeman, Phys. Rev. A **64**, 013613 (2001).

[196] B. Jackson and E. Zaremba, New J. Phys. **5**, 88 (2003).

[197] S. T. Beliaev, Zh. Eksp. Teor. Fiz. **34**, 433 (1958)